Study of B -> K pi pi gamma dacays with the Babar Experiment: the photon helicity and the resonant structure of the K pi pi system

S. Akar

THÈSE DE DOCTORAT
DE L'UNIVERSITÉ PIERRE ET MARIE CURIE

présentée par

Simon Akar

Pour obtenir le grade de

DOCTEUR DE L'UNIVERSITÉ PIERRE ET MARIE CURIE

Spécialité :

Particules, Noyaux, Cosmologie (ED 517)

Études des désintégrations $B \to K\pi\pi\gamma$ avec l'expérience *BABAR* : hélicité du photon et structure résonante du système $K\pi\pi$

Study of $B \to K\pi\pi\gamma$ decays with the BABAR Experiment: the photon helicity and the resonant structure of the $K\pi\pi$ system

Soutenue le 30 septembre 2013 devant le jury composé de:

M.	Eli	BEN-HAIM	Directeur de thèse
M.	Frédéric	BLANC	Rapporteur
Mme.	Emi	KOU	Rapporteur
M.	Stéphane	MONTEIL	Examinateur
M.	Karim	TRABELSI	Examinateur
M.	Pascal	VINCENT	Président du jury

À Bertrand, Pierre et Henri,
trois héritages fondateurs.

Thus to be independent of public opinion
is the first formal condition of achieving
anything great or rational
wether in life or in science.

G.W.F HEGEL

Taken from a Port Charlotte bottle,
aged 10 years heavily-peated
Islay coastal single malt.

Remerciements

Au début, on ne remarque pas toujours assez l'importance, la nécessité même, d'être correctement entouré et soutenu au cours de ces fameuses trois années qui, si tout se passe bien, se terminent une coupe de champagne à la main, chargé de beaucoup de fatigue mais surtout d'une grande fierté de faire maintenant partie du club. Donc quand bien même seul mon nom figure en première page de cette thèse, il est maintenant temps de corriger cette quasi-imposture tant les soutiens dont j'ai bénéficiés ont été déterminants à la réussite de ma thèse.

L'exercice pratiqué ici n'étant pas trivial, et puisque qu'il est plus aisé de faire remonter des souvenirs récents, je vais donc l'aborder avec simplicité, c'est-à-dire en commencant par la fin. Avant de débuter ce recensement et puisqu'il est probable, voire certain, que malgré mes efforts certaines personnes échappent à ma vigilance, je vais commencer par m'adresser à tous ces anonymes qui ont, consciemment ou non, lors de rencontres diverses, contribué à l'achèvement de cette thèse. À vous tous je veux dire merci !

Ensuite je tiens à remercier l'ensemble des membres du jury d'avoir fait le déplacement, parfois depuis l'autre bout du monde, afin d'évaluer mon travail. Je remercie le président du jury, Pascal Vincent, d'avoir accepté cette tâche, Frédéric Blanc et Emi Kou, rapporteurs, d'avoir lu d'un regard aussi efficace et attentif ces sept chapitres, et enfin Stéphane Monteil et Karim Trabelsi, pour leurs commentaires avisés et leurs remarques bienveillantes.

Je tiens à remercier chaleureusement l'ensemble des membres, actuels et anciens, du groupe de physique du B du LPNHE. Je remercie mon prédécesseur, Simon Sitt, qui a toujours su trouver le temps de m'aider au début de ma thèse alors que lui-même était en train de terminer la sienne. Merci également à Jacques Chauveau, co-directeur de l'école doctorale, qui a toujours su se rendre disponible afin de discuter de mes travaux de recherche. Sans oublier Francesco Polci, Aurélien Martens, Diego Milanes, Matthew Charles, Gerard Bonneaud, Maurice Benayoun, Pascal David et Luigi Delbuono qui m'ont aidé chacun à leur facon. Cette liste ne saurait être complète sans la présence de Giovanni Calderini, Giovani Marchiori, José Ocariz et Lydia Roos dont l'expertise m'a beaucoup apportée.

Lors de ma thèse j'ai à plusieurs occasions eu l'opportunité de me rendre à SLAC en Californie où j'ai croisé un grand nombre de personnes qui méritent toutes ma gratitude. Ainsi je voudrais remercier Bill Dunwoodie et Brian Meadows pour leur écoute et leurs conseils avisés. Je voudrais également remercier Dana Lindemann qui m'a conseillé sur bien des points. Les grandes collaborations scientifique étant ainsi faites, j'ai également croisé à chacun de mes séjours à SLAC, et uniquement là-bas, Nicolas Arnaud, travaillant au LAL

d'Orsay, près de Paris donc. Il a toujours eu pour moi un regard bienveillant et je l'en remercie très sincèrement. Je remercie aussi Ann O'Hearn et Ruben chez qui j'ai logé à chacun de mes séjours en Californie pour leur accueil toujours extrêmement chaleureux.

J'ai également eu la chance de pouvoir interagir avec plusieurs théoriciens du LAL et du LPT d'Orsay durant ces trois années. Je tiens ici à témoigner de ma plus grande gratitude envers Emi Kou qui m'a permis, de par sa véritable implication, de mieux comprendre une immense partie des subtilités liées à mes travaux de recherche. Je tiens également à remercier Patrick Roudeau et Alain le Yaouanc pour leur attention et leurs conseils précieux.

Merci à Christophe Balland d'avoir assumé son rôle de parrain de la meilleur facon qu'il soit : c'est-à-dire avec écoute, attention et bienveillance. Nos conversations ont été particulièrement utiles puisqu'elles m'ont permis de prendre régulièrement le recul nécessaire afin de mieux percevoir mon travail.

Merci à toutes les équipes techniques du LPNHE. Merci à l'ensemble du personnel de l'administration, à Magali Carlosse, Véronique Joisin, Bernard Caraco, Souad Rey, Sylvie Soulard, Jocelyne Meurgey et Annick Guilloteau. Merci à tous les membres des services généraux, à Michael Roynel et Franck Leclercq. Merci aux membres du service informatique, Francois Legrand, Thomas Audo, Victor Mendoza et Patricia Warin-Charpentier. Merci enfin au pôle communication, Isabelle Cossin et Laurence Marquet.

Ces remerciements ne sauraient être complets sans la présence, déterminante, des professeurs qui m'ont transmis non seulement un savoir mais surtout une passion. Parmi eux, je voudrais remercier Eli Ben-Haim, Sophie Trincaz-Duvoid, Jean-Paul Tavernet, Achille Stocchi, Jean-Pierre Rozet et Jérome Tignon. Je voudrais également remercier Sandro De Cecco et Jean-Pierre Engel qui m'ont encadré et initié au métier de chercheur lors de différents stages. Aussi loin que je m'en rappelle, mon professeur de Physique-Chimie en première et terminal, Véronique Perrard, est la première personne à m'avoir enseigné le goût de la physique ainsi que la rigueur intellectuelle qui lui est associée. Merci à elle.

Parmi les personnes qui ont beaucoup compté, il y en a trois à qui je voudrais rappeler toute mon amitié. Olivier avec qui j'ai partagé mon bureau, Flora avec qui j'ai partagé de beaux moments de cinéma et Laura qui m'a fait partager sa bonne humeur et son enthousiasme quasi permanent. J'ai surtout partagé avec eux tous les moments, joyeux et douloureux, qui jalonnent le chemin du doctorat. Merci à vous trois, d'avoir été, chacun à votre facon, d'une présence déterminante.

Bien-sûr il y a également ma famille, un peu plus extérieure à toute cette aventure, qui m'a également été d'un grand soutien. Ainsi je voudrais remercier ma soeur Juliette, mon père, Antoine, qui s'est toujours fortement intéressé d'abord à mes études et puis à mon travail de thèse. Je remercie ma mère, Francoise, qui m'avait dit, lorsque j'étais encore tout jeune, que l'important n'était pas forcément d'être le premier, mais surtout de faire ce qu'il te plait. Merci pour ce sage conseil. Je voudrais également remercier Marie et Jérome pour leur chaleur humaine ainsi que pour leur attention envers moi.

Certaines personnes ont joué un rôle particulièrement important. Ainsi je veux remercier Delphine, avec qui j'ai appréhendé cette ville de Paris et qui a partagé avec moi la majeure partie de mes angoisses, de mes joies et de mes rêves. Je la remercie aussi pour son soutien avant et pendant une grande partie de ma thèse. Je lui souhaite avec toute mon affection la

plus grande réussite possible.

Je veux remercier Vera qui a trouvé le courage de me supporter pendant les moments les plus intenses des trois années de thèse, c'est-à-dire durant les six derniers mois. Elle n'a pas hésité à relire et à corriger des chapitres entiers, et ce jusque tard dans la nuit. Son incroyable tendresse m'a permis de prendre les grandes bouffées d'oxygène nécessaires à la conclusion de ce projet. Merci infiniment à toi Vera.

Plus que toute autre personne, je veux ici adresser toute ma gratitude et ma reconnaissance à celui qui a encadré mon travail durant ces trois années. J'ai eu le privilège de rencontrer Eli Ben-Haim tout d'abord comme professeur en première et deuxième année de Master. Durant cette période, j'ai déjà pu entrevoir ce qui m'a été confirmé plus tard. Eli est doté d'une grande patience ainsi que d'une superbe volonté de transmettre son savoir. Il a toujours su trouver le temps nécessaire afin de me guider, tout en me laissant apprivoiser par moi-même les divers aspects de mes travaux. En plus ses qualités pédagogiques et de chercheur indéniables, il a également toujours fait preuve d'un soutien sans faille. Avant de choisir mon sujet de thèse, plusieurs personnes m'ont dit qu'au delà du sujet, le choix du directeur était essentiel, primordial même. Sur ce point, si je devais recommencer, je ne changerai rien. Je lui dois énormément. Merci Eli. Merci pour tout !

Marseille, 16 décembre 2013

Contents

List of Figures

List of Tables

Introduction

The current knowledge on the fundamental interactions describing physics at the subatomic scale is comprised in the Standard Model (SM) of strong and electroweak interactions. Gravitation, whose contribution to microscopic phenomena is negligible compared to the ones from both strong and electroweak interactions, is not included in the SM since it still fails to be described by quantum field theories. In the last decades Standard Model predictions have been extensively tested, and even though several questions remain without answer, no contradictory experimental result arises to date.

Before the start of the B Factories, *BABAR* in SLAC National Laboratory California, and Belle at KEK, in Japan, the quark flavor sector described by electroweak interactions, from which emerges the essential phenomenon of CP violation, was one of the least tested. The first observation of CP violation in weak interactions was performed in 1964 in decays of neutral K mesons. During the same decade, Andrei Sakharov [1] showed that CP violation was one of the necessary conditions in order to explain why the Universe evolved from its initial matter-antimatter symmetric state to the one that exists today. However, the mechanism allowing for CP violation in the SM is not sufficient to explain the observed asymmetry between matter and antimatter, which could indicate that the SM is an effective model for a more fundamental theory.

The absence of results coming from *direct* searches of New Physics (NP) effects performed in high-energy colliders, indicates that if such NP exist, corresponding effects would arise beyond the electroweak scale. Some specific decay processes, referred to as penguin diagrams and further described in Sec. 1.4, in which CP violation occurs and that are accessible at low-energy colliders such as it is the case in the B factories, could allow to probe NP effects *via indirect* searches.

In this context, the "radiative penguin" transition $b \to s\gamma$ which proceeds *via* an electroweak-interaction loop diagram is a promising process; it underlies the decays $B \to X_s\gamma$, where X_s is a hadronic final state.

In B^0 ($\overline{B}^0$) transitions with radiated photons, the SM predicts a right (left) helicity of these photons. A hadronic correction of order $\mathcal{O}(|m_s/m_b|^2)$ needs to be taken into account, introducing a small left (right) handed component. Measurement of the photon polarization would be a strong test of the SM, since non-SM processes such as supersymmetry can introduce diagrams with different polarization.

As the polarization of the photon cannot be directly measured, different experimental methods exist that give access to this information through other phenomena. In the present thesis, in order to gather information on the photon helicity we exploit the mixing-induced

CP asymmetry, $\mathcal{S}$, in $B^0 \to K^0_S\rho^0\gamma$ decays. This quantity is predicted by the SM to be small in decay modes of the type $B \to f_{CP}\gamma$ gamma, where f_{CP} is a *CP* eigenstate, like $K^0_S\rho^0$. This is due to the correlation between the final-state photon helicity to the flavor of the decaying B-meson, as explained above, and to the fact that different (thus non-interfering) final states do not contribute to $\mathcal{S}$. The analysis of this mode is described in Chapter 7. Since deviations from the SM predictions would indicate contributions from NP processes, the results obtained can be used to set constraints on parameters of NP models.

Decays to $K\pi\pi\gamma$ can also display an interesting hadronic structure: they have contributions from several kaonic resonances decaying to $K\pi\pi$. The decays of these resonances themselves exhibits a resonant structure, with $K^*\pi$, $K\rho$, and $(K\pi)^*_0\pi$ combinations, where $(K\pi)^*_0$ corresponds to $(K\pi)$ S-wave. Five kaonic resonances contribute to the $K\pi\pi$ invariant mass range below $1.8\,\mathrm{GeV}/c^2$, that is considered in the present analysis.

The structure of the $K\pi\pi$ system is not well measured, and can be crucial for probing the photon helicity. Indeed, it has been shown [2] that the photon polarization may be measured in $B \to K^+\pi^-\pi^0\gamma$ and $B \to K^0_S\pi^+\pi^0\gamma$ decays. In these decays, interference between $K^{*0}\pi^0$ and $K^{*+}\pi^-$ processes or between $K^{*+}\pi^0$ and $K^{*0}\pi^+$ can produce decay distributions sensitive to the photon polarization. The overall decay rate does not depend on the photon polarization, but the decay rate variation with θ_d is related to the polarization, where θ_d is the angle between the $K\pi\pi$ decay plane normal and the photon direction.

In the present thesis we measure the $m_{K\pi\pi}$ and $m_{K\pi}$ spectra in $B^+ \to K^+\pi^-\pi^+\gamma$ decays, as described in Chapter 6, and extract information about the $K\pi\pi$ resonant structure. An amplitude analysis of these two spectra is then performed. The results are used, assuming Isospin symmetry, to extract the mixing-induced *CP* parameters of the $B^0 \to K^0_S\pi^+\pi^-\gamma$ process from the analysis of $B^0 \to K^0_S\rho^0\gamma$ decays without an explicit amplitude analysis.

Belle has previously reported a time-dependent *CP* asymmetry measurement of $B^0 \to K^0_S\rho^0\gamma$ decays [3]. Similar measurements with $B^0 \to K^0_S\pi^0\gamma$ decays have been reported by *BABAR* [4] and Belle [5]. At this time no evidence of NP has been observed: all time dependent *CP* asymmetry measurements yield *CP* asymmetry parameters that is compatible with SM predictions. More generally, radiative penguin B decays have been observed in exclusive two-body final states, where X_s is $K^+\pi^-$ or $K^0_S\pi^0$, as well as in exclusive three-body final states such as $B \to K^+\pi^+\pi^-\gamma$ and $B \to K^0_S\pi^-\pi^+\gamma$ [6].

Part I

Theoretical overview and brief experimental status

Chapter 1

Flavor physics and *CP* violation in the Standard Model

Contents

The Standard Model of particle physics is a quantum field theory describing the interactions of all observed elementary particles. The SM is a gauge theory based on the gauge group $SU(3)_c \otimes SU(2)_L \otimes U(1)_Y$, including the strong interaction symmetry group $SU(3)_c$, and the electroweak interaction group $SU(2)_L \otimes U(1)_Y$.

In the SM framework, *CP* violation originates from the existence of an irreducible phase that appears in the Lagrangian describing the charged current decays of quarks. This is a consequence of the complex coupling constants between the flavor sector in the weak interactions and of the mass terms for the quarks. In the SM, masses of particles are brought by a dynamical mechanism, known as the Higgs mechanism [7]. Recent observations of a new particle [8, 9], very likely to be the Higgs boson, bring strong indications for the existence of such a mechanism.

1.1 Weak interactions in the flavor sector

In the SM, the matter fields corresponding to the spin-1/2 particles are put in doublets of $SU(2)_L$, while the corresponding right-handed fields transform as singlets under $SU(2)_L$. Q_L^i, u_R^i and d_R^i are the quarks fields, where the index i label the family or generation and the subscripts L and R denote left- and right-handed fields, respectively, such as

$$\psi_L = P_L\psi \ , \quad \psi_R = P_R\psi \ , \tag{1.1}$$

where P_L and P_R are the projection operators

$$P_L = \frac{1}{2}\left(1-\gamma_5\right) \ , \quad P_R = \frac{1}{2}\left(1+\gamma_5\right) \ . \tag{1.2}$$

The quarks acquire mass through their Yukawa couplings to the Higgs field ϕ:

$$\mathcal{L}_{\text{Yukawa}} = -Y_u^{ij}\overline{Q_L^i}\epsilon\phi^* u_R^j - Y_d^{ij}\overline{Q_L^i}\phi d_R^j + \text{h.c.} \ , \tag{1.3}$$

where the $Y_{u,d}$ are 3×3 complex matrices, the indices i and j label the generations, and ϵ is the antisymmetric tensor. In Eq. 1.3 the terms corresponding to leptons have been dropped for simplicity, being analogous to those of the quarks.

Since the Higgs field has a vacuum expectation value, $\langle\phi\rangle = (0, v/\sqrt{2})$, the Yukawa couplings give rise to the 3×3 quarks mass matrices:

$$M_u^{ij} = \left(v/\sqrt{2}\right) Y_u^{ij} \ , \quad M_d^{ij} = \left(v/\sqrt{2}\right) Y_d^{ij} \ . \tag{1.4}$$

Since the matrices M couple the left-handed component of each quark Q_L^i with the right-handed projections of all flavors, they are non-diagonal in the flavor basis. The mass eigenstates being the one that propagate in space and time, the matrices M must be diagonalized. Any matrix M can be brought into a diagonal form by separate unitary transformations on the left and right, respectively

$$M \to \mathcal{U}_L M_{\text{diag}} \mathcal{U}_R^\dagger \ , \tag{1.5}$$

where $\mathcal{U}_L$ and $\mathcal{U}_R$ are unitary and M_{diag} is real, diagonal and non-negative. For the quark fields, this is done by changing from the flavor to the mass basis, the unitary transformation being

$$\begin{aligned} u_L &= \mathcal{U}_L^u u'_L \ , \quad u_R = \mathcal{U}_R^u u'_R \ , \\ d_L &= \mathcal{U}_L^d d'_L \ , \quad d_R = \mathcal{U}_R^d d'_R \ , \end{aligned} \tag{1.6}$$

where u and d are three-component column vectors representing the *up*- and *down*-type quarks in flavor space, respectively, and the primed fields represent the corresponding mass eigenstates. In this case, the transformation matrices $\mathcal{U}$ are chosen such as

$$\mathcal{U}_R^{u\dagger} M_u \mathcal{U}_L^u \ = \ \begin{pmatrix} m_u & 0 & 0 \\ 0 & m_c & 0 \\ 0 & 0 & m_t \end{pmatrix} \ ,$$

$$\mathcal{U}_R^{d\dagger} M_d \mathcal{U}_L^d = \begin{pmatrix} m_d & 0 & 0 \\ 0 & m_s & 0 \\ 0 & 0 & m_b \end{pmatrix} . \tag{1.7}$$

This change from flavor to the mass basis requires different transformations of the two parts of each Q_L doublet:

$$\begin{pmatrix} u_L \\ d_L \end{pmatrix} = \begin{pmatrix} \mathcal{U}_L^u u'_L \\ \mathcal{U}_L^d d'_L \end{pmatrix} = \mathcal{U}_L^u \begin{pmatrix} u'_L \\ \mathcal{U}_R^{u\dagger} \mathcal{U}_L^d d'_L \end{pmatrix} . \tag{1.8}$$

When expressing the SM Lagrangian in terms of the primed mass-eigenstate fields, the quark kinetic terms remain unchanged. The Z and γ boson couplings are also unaffected. As a consequence no flavor-changing neutral current (FCNC) processes are allowed at the tree level (defined in Sec. 1.4) in the SM. On the other hand, in the part of the charged-current Lagrangian describing the couplings of the $W^\pm$ bosons to the quarks, the transformation leaves the couplings unchanged by $\mathcal{U}_L^u$, but not by $\mathcal{U}_R^{u\dagger}\mathcal{U}_L^d$:

$$\frac{g}{\sqrt{2}} \overline{u}_L \gamma^\mu d_L W_\mu^+ = \frac{g}{\sqrt{2}} \overline{u'}_L \gamma^\mu V_{\mathrm{CKM}} d'_L W_\mu^+ , \tag{1.9}$$

where g is the $SU(2)_L$ coupling constant and W_μ^+ is the $SU(2)_L$ gauge field. In this representation, quarks from different flavors are coupled through the complex matrix $V_{\mathrm{CKM}} \equiv \mathcal{U}_R^{u\dagger}\mathcal{U}_L^d$, named after Cabbibo, Kobayashi and Maskawa [10, 11]. As a result, the SM predicts the existence of flavor-changing charged currents at the tree level.

1.2 Quark mixing and the CKM matrix

In the general case of N quark families, the $2N^2$ real parameters of the complex $N \times N$ matrix V_{CKM}, can be reduced using properties of the V_{CKM} matrix and the quarks fields. Indeed, due to the unitarity conditions applying to the former, the number of parameters are reduced to N^2, and by another $2N-1$ degrees of freedom when individual phase redefinitions ($q_{Lj} \to e^{i\phi_j^q} q_{Lj}$) for the $2N$ quark fields are considered. All this leaves $(N-1)(N-2)/2$ irreducible phases, and turns out to be 0 for $N = 2$ and 1 for $N = 3$. As Kobayashi and Maskawa noticed, this irreducible phase in a three-generation model would be the origin of all CP violation in the SM (see Section 1.3.2).

Although this mechanism allows for CP violation, it is not a necessary feature of the SM. Thus, in the case where two quarks of the same charge had equal masses, or the value of one of the mixing angles was equal to zero or $\pi/2$, or even the value of the irreducible phase itself was zero, the number of parameters could be reduced even further and CP violation would no longer be manifest.

Since the V_{CKM} matrix was formulated for the first time, several parametrizations have been proposed. One of such parametrization is the so called 'Standard parametrization" proposed by Chau and Keung, and which is obtained as the product of three (complex)

rotation matrices and a overall phase,

$$V_{\rm CKM} = \begin{pmatrix} c_{12}c_{13} & s_{12}c_{13} & s_{13}e^{-i\delta} \\ -s_{12}c_{23} - c_{12}s_{23}s_{13}e^{i\delta} & c_{12}c_{23} - s_{12}s_{23}s_{13}e^{i\delta} & s_{23}c_{13} \\ s_{12}s_{23} - c_{12}c_{23}s_{13}e^{i\delta} & -c_{12}s_{23} - s_{12}c_{23}s_{13}e^{i\delta} & c_{23}c_{13} \end{pmatrix} , \tag{1.10}$$

where $c_{ij} = \cos\theta_{ij}$, $s_{ij} = \sin\theta_{ij}$ for $i < j = 1, 2, 3$, the θ_{ij} are the rotation angles between families, and δ is the irreducible phase.

Thanks to many experimental results, it has been established that a hierarchy among the matrix elements exists and that the matrix is dominated by its diagonal terms. In other words, transitions among quarks from different flavor doublets are suppressed, compared to the ones among quarks of the same generation. A useful parameterization that emphasizes the hierarchical, nearly diagonal structure of the matrix, is due to Wolfenstein [12]:

$$V_{\rm CKM} = \begin{pmatrix} V_{ud} & V_{us} & V_{ub} \\ V_{cd} & V_{cs} & V_{cb} \\ V_{td} & V_{ts} & V_{tb} \end{pmatrix} \simeq \begin{pmatrix} 1 - \frac{1}{2}\lambda^2 & \lambda & \lambda^3 A\left(\rho - i\eta\right) \\ -\lambda & 1 - \frac{1}{2}\lambda^2 & \lambda^2 A \\ \lambda^3 A\left(1 - \rho - i\eta\right) & -\lambda^2 A & 1 \end{pmatrix} + \mathcal{O}\left(\lambda^4\right) , \tag{1.11}$$

which is based on a Taylor development where λ is the expansion parameter, known to be small from experimental data, i.e. $\lambda \simeq |V_{us}| \sim 0.22$, and A, ρ and η are all of order 1. In the Wolfenstein parametrization η contains the *CP* violation information, i.e. *CP* violation occurs when $\eta \neq 0$. To all orders in λ, the exact Wolfenstein parameterization can be defined as,

$$s_{12} \equiv \lambda , \tag{1.12}$$
$$s_{23} \equiv \lambda^2 A , \tag{1.13}$$
$$s_{13}e^{-i\delta} \equiv \lambda^3 A\left(\rho - i\eta\right) . \tag{1.14}$$

This definition is useful because it allows an elegant improvement of the accuracy of the original Wolfenstein parameterization. In particular, up to the order $\mathcal{O}(\lambda^6)$, one get

$$V_{us} = \lambda , \quad V_{cb} = \lambda^2 A , \quad V_{ub} = \lambda^3 A\left(\rho - i\eta\right) , \tag{1.15}$$

$$V_{td} = \lambda^3 A\left(1 - \overline{\rho} - i\overline{\eta}\right) , \tag{1.16}$$

$$\Im(V_{cd}) = -\lambda^5 A^2 \eta , \quad \Im(V_{ts}) = -\lambda^4 A\eta , \tag{1.17}$$

where

$$\overline{\rho} = \rho(1 - \lambda^2/2) , \quad \overline{\eta} = \eta(1 - \lambda^2/2) . \tag{1.18}$$

One of the major physics goal of the B Factories was to improve the experimental constraints on the elements of $V_{\rm CKM}$. Relations among these elements can be derived from the

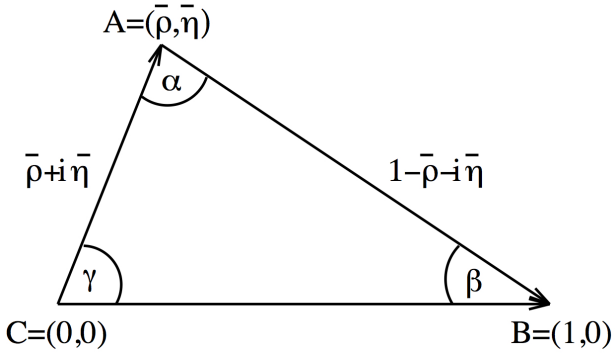

Figure 1.1: Pictorial representation, dubbed "Unitarity Triangle", of the relation $V_{ud}V_{ub}^* + V_{cd}V_{cb}^* + V_{td}V_{tb}^* = 0$ derived from the unitarity of the CKM matrix. Each of the terms can be viewed as a vector in the complex plane. Their sum being equal to zero then implies that they have to form a (closed) triangle in the Argand plane. The base of the triangle has been aligned with the horizontal (real) axis by dividing the equation by $V_{cd}V_{cb}^*$.

unitarity condition of the matrix $V_{\rm CKM}^\dagger V_{\rm CKM} = \mathbb{1}$. Three of them are of particular interest for the study of CP violation, as they more sensitive to the irreducible phase

$$V_{ud}V_{us}^* + V_{cd}V_{cs}^* + V_{td}V_{ts}^* = 0\ , \tag{1.19}$$
$$V_{us}V_{ub}^* + V_{cs}V_{cb}^* + V_{ts}V_{tb}^* = 0\ , \tag{1.20}$$
$$V_{ud}V_{ub}^* + V_{cd}V_{cb}^* + V_{td}V_{tb}^* = 0\ . \tag{1.21}$$

Each term in these relations can be interpreted geometrically as a vector in the complex plane. This way, each equation above can be visualized as a triangle in the Argand plane, known as the *unitarity triangles*. The first two triangles are related to the CKM matrix elements that governs the $K^0 - \overline{K}^0$ and $B_s^0 - \overline{B}_s^0$ systems, respectively. For each of those triangles one side is much shorter than the other two, and so they almost collapse to a line. This would give an intuitive understanding of why CP violation is small in the leading K and B_s decays. On the other hand, for the triangle corresponding to the relation given in Eq. 1.21, the sides are of the same order of magnitude. It is in this third triangle, related to the $B_d^0 - \overline{B}_d^0$ system, that the most exciting physics of CP violation lies. Indeed, the openness of this triangle predicts large CP asymmetries in B_d decays, which are the ones accessible at the B Factories[1]. Note that all the unitarity triangles are equal in area. Equation 1.21 can be written in another way. Once divided by $V_{cd}V_{cb}^*$, it becomes

$$\frac{V_{ud}V_{ub}^*}{V_{cd}V_{cb}^*} + 1 + \frac{V_{td}V_{tb}^*}{V_{cd}V_{cb}^*} = 0\ . \tag{1.22}$$

In this convention one of the side of this triangle is aligned to the real axis of the Argand plane. The resulting pictorial representation is a unitarity triangle whose apex is determined

[1] Belle collected a data sample of $124.4\,\text{fb}^{-1}$ at the $\Upsilon(5S)$, allowing to study the B_s properties.

by the $\overline{\rho}$ and $\overline{\eta}$ parameters, or equivalently, the irreducible phase (see Figure 1.1). In this representation, the lengths of the sides are given by

$$\overline{CB} = 1 \,, \tag{1.23}$$

$$\overline{AB} = \left|\frac{V_{td}V_{tb}^*}{V_{cd}V_{cb}^*}\right| = \sqrt{(1-\overline{\rho})^2+\overline{\eta}^2} = \frac{1}{\lambda}\left|\frac{V_{td}}{V_{cb}}\right| \,, \tag{1.24}$$

$$\overline{AC} = \left|\frac{V_{ud}V_{ub}^*}{V_{cd}V_{cb}^*}\right| = \sqrt{\overline{\rho}^2+\overline{\eta}^2} = \left(1-\frac{\lambda^2}{2}\right)\frac{1}{\lambda}\left|\frac{V_{ub}}{V_{cb}}\right| \,, \tag{1.25}$$

while the angles are given by

$$\beta = \arg\left(\frac{V_{td}V_{tb}^*}{V_{cd}V_{cb}^*}\right) = \arctan\left(\frac{\overline{\eta}}{1-\overline{\rho}}\right) \,, \tag{1.26}$$

$$\gamma = \arg\left(\frac{V_{ud}V_{ub}^*}{V_{cd}V_{cb}^*}\right) = \arctan\left(\frac{\overline{\eta}}{\overline{\rho}}\right) \,, \tag{1.27}$$

$$\pi = \alpha+\beta+\gamma \,. \tag{1.28}$$

A good way to test the SM is to overconstrain the unitarity triangle parameters by making as many independent measurements of the sides and the angles of the triangle as possible. To date, the experimental status seems to indicate that the Standard Model provides, up to the available precision, a good description of *CP* violation in the quark flavor sector (Figure 1.2).

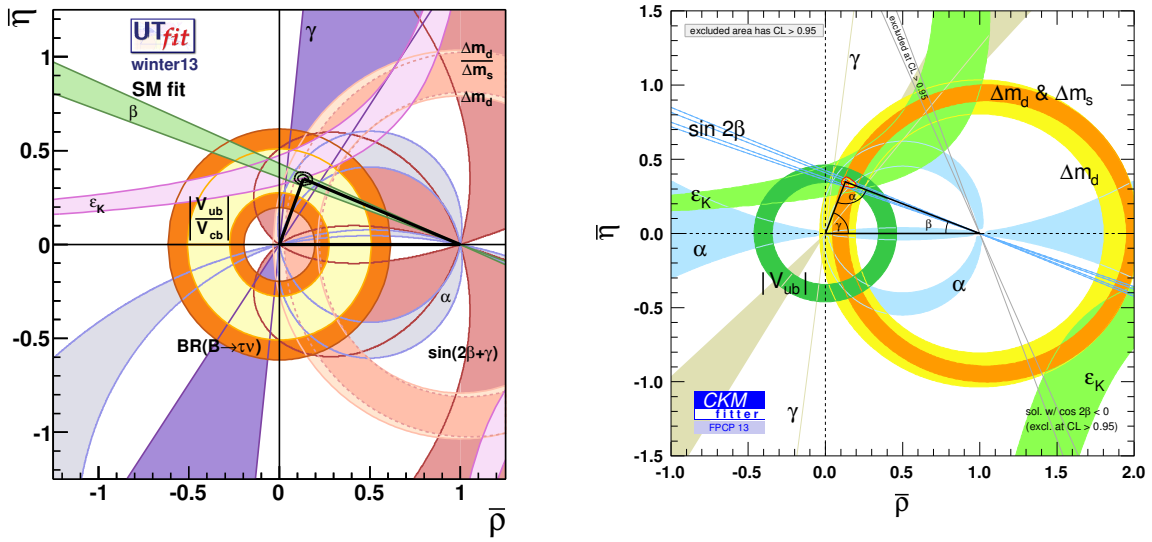

Figure 1.2: Pictorial representation of the current experimental constraints on the sides and angles of the unitarity triangle, by the CKMfitter group [13] (right), updated with the results available in spring 2013, and by the UTFit group [14] (left) updated with the results available in winter 2013. The bands representing each experimental measurement or bound are seen to be in very good agreement with each other, all of them overlapping around the apex of the triangle drawn.

1.3 Mixing and CP violation in the B meson system

This section treats the quantum mechanical properties of the neutral B-meson system, which are model independent. These properties are related to CP violation observables, and use features of the flavor and weak-interaction structure of the Standard Model. Three different kinds of CP violation, resulting from different processes, are to be distinguished, as they allow to extract different CP-violating quantities.

1.3.1 Mixing of neutral B mesons

A neutral meson state and its CP conjugate decay due to weak interactions. In order to describe the neutral meson system it is important to distinguish between different representations. On one hand, the neutral meson can be described by two flavor eigenstates, each with a definite quark content, which are useful for understanding particle production and decay processes. On the other hand, the neutral meson can be described by the two eigenstates of the Hamiltonian (mass eigenstates), with definite mass and lifetime, which are the states that propagate in space and time. Mass eigenstates are not flavor eigenstates, and so flavor eigenstates get mixed as they propagate. Since CP symmetry is broken in the SM, the mass and CP eigenstates can differ.

The phenomenon of mixing, referring here to the process where a neutral meson turns into its antiparticle via a process involving two charged currents, has been observed in kaons [15], B_d and B_s mesons [16–18], and also, D mesons [19–21].

Let us now consider an arbitrary combination of the neutral B-meson flavor eigenstates[2]:

$$a(t)\left|B^0\right\rangle + b(t)\left|\overline{B}^0\right\rangle \ , \tag{1.29}$$

which is governed by the time-dependent SchroÃàdinger equation

$$i\frac{d}{dt}\begin{pmatrix} a(t) \\ b(t) \end{pmatrix} = \mathrm{H}\begin{pmatrix} a(t) \\ b(t) \end{pmatrix} \equiv (M - i\Gamma)\begin{pmatrix} a(t) \\ b(t) \end{pmatrix} \ , \tag{1.30}$$

where M and Γ are two 2×2 hermitian matrices known as mass and decay matrices, respectively. The assumption of CPT invariance constrains the Hamiltonian and imposes to the diagonal elements: $M_{11} = M_{22} = M$ and $\Gamma_{11} = \Gamma_{22} = \Gamma$. The off-diagonal terms, M_{12} and Γ_{12} are particularly important in the discussion of CP violation, since $\arg(M_{12}/\Gamma_{12}) = 0$ would be implied in the case of CP conservation. The mass matrix of the Hamiltonian describes the oscillation between flavor eigenstates, where the diagonal terms in M are dominated by the flavor eigenstates masses, and the off-diagonal ones represent the transitions *via* virtual intermediate states. The diagonal terms of the decay part of the Hamiltonian describe the flavor eigenstates decays to different final states, i.e. $B^0 \to f$ and $\overline{B}^0 \to \overline{f}$, while the off-diagonal terms describe transitions *via* real intermediate states. Figure 1.3 shows the Feynman diagrams representing the weak transitions between B^0 and $\overline{B}^0$, also referred to as $B^0\overline{B}^0$ mixing. Such transitions lead to the inclusion of the three up-type quarks in the loop,

[2]The flavor eigenstates of the neutral B meson are defined as $B^0 = \overline{b}d$ and $\overline{B}^0 = \overline{d}b$

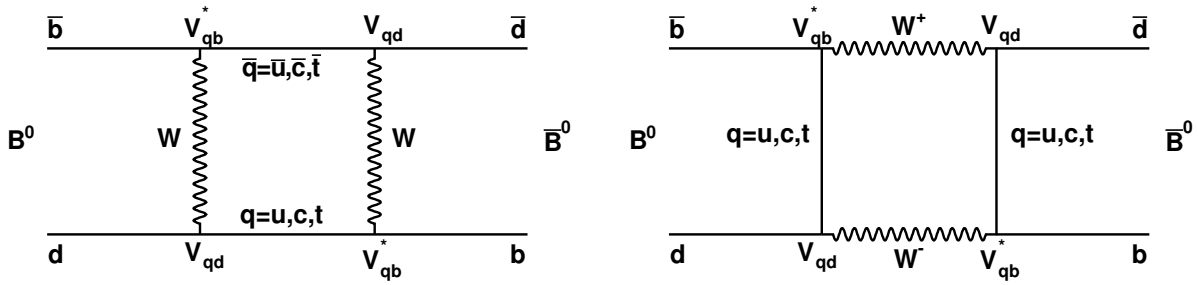

Figure 1.3: Diagrams describing the mixing phenomenon for neutral B mesons via a second-order weak transition.

since all of them couple via a CKM factor that is proportional to λ^6. However, integration of the internal degrees of freedom (the up-type quarks and the W) yields an expression that weighs the contribution of each quark by the ratio of its mass to that of the weak boson [22]. Thus, the up and charm quarks contribution are suppressed, and an evaluation of the corresponding CKM factors (see (**??**)) readily gives a phase of $(V_{td}V_{tb}^*)^2 \sim e^{-i2\beta}$. In other words, the B^0 states that oscillate into $\overline{B}^0$ pick up an extra -2β phase, called the *mixing angle*, with respect to the B^0 states that do not oscillate. This phase is measurable whenever both flavors decay to a common state.

Diagonalizing the Hamiltonian, H, leads to the expression of the mass eigenstates of the neutral B meson system, which consist in a superposition of the B^0 and $\overline{B}^0$ flavor eigenstates, such as

$$|B_L\rangle = p\,|B^0\rangle + q\,|\overline{B}^0\rangle \ , \tag{1.31}$$

$$|B_H\rangle = p\,|B^0\rangle - q\,|\overline{B}^0\rangle \ , \tag{1.32}$$

where the index $L(H)$ refers to the lighter (heavier) mass eigenstate and the complex coefficients p and q are constrained by a normalization condition

$$|p|^2 + |q|^2 = 1 \ . \tag{1.33}$$

The mass and width difference between the neutral B mesons are defined as follows,

$$\Delta m_d \equiv M_H - M_L \ , \quad \Delta\Gamma \equiv \Gamma_H - \Gamma_L \ , \tag{1.34}$$

so that Δm_d is positive by definition. Finding the eigenstates of Eq. 1.30 the following relations are derived

$$(\Delta m_d)^2 - \frac{1}{4}(\Delta\Gamma)^2 = 4\left(|M_{12}|^2 - \frac{1}{4}|\Gamma_{12}|^2\right) \ , \tag{1.35}$$

$$\Delta m_d \Delta\Gamma = 4\Re\left(M_{12}\Gamma_{12}^*\right) \ , \tag{1.36}$$

and the ratio q/p is finally given by

$$\frac{q}{p} = -\frac{\Delta m_d - \frac{i}{2}\Delta\Gamma}{2\left(M_{12} - \frac{i}{2}\Gamma_{12}\right)} \ . \tag{1.37}$$

For the B_d mesons, the difference in width, $\Delta\Gamma_{B_d}$, is expected to be small compared to Γ_{B_d}. Indeed, $\Delta\Gamma_{B_d}$ value is produced by decay amplitudes of channels common to B^0 and $\overline{B}^0$, with corresponding branching fractions at the level of 10^{-3}. And since many channels contribute with different signs, their sum is not expected to exceed the individual level, hence $\Delta\Gamma_{B_d}/\Gamma_{B_d} \sim \mathcal{O}(10^{-2})$. From the considerations above, one should note that $\Delta\Gamma_{B_d} \ll \Gamma_{B_d}$ is model-independent. Moreover, the B_d oscillation parameter x_d has been measured [23], such as

$$x_d \equiv \frac{\Delta m_d}{\Gamma_{B_d}} = 0.775 \pm 0.006 \ , \tag{1.38}$$

which implies then, model-independently, $\Delta\Gamma_{B_d} \ll \Delta m_d$. As a consequence, using Eqs. 1.35 to 1.37, one gets

$$|\Gamma_{12}| \ll |M_{12}| \ , \quad \text{and } |q/p| \ \sim 1 \ . \tag{1.39}$$

Consider a state which is created at time $t = 0$ as an initially pure $B^0(\overline{B}^0)$, denoted by $\left|B^0_{\text{phys}}\right\rangle$ ($\left|\overline{B}^0_{\text{phys}}\right\rangle$). The time evolution of these states can be described by the eigenvalues of the Hamiltonian and the q and p parameters such as

$$\left|B^0_{\text{phys}}(t)\right\rangle = g_+(t)\left|B^0\right\rangle + \frac{q}{p} g_-(t)\left|\overline{B}^0\right\rangle \ , \tag{1.40}$$

$$\left|\overline{B}^0_{\text{phys}}(t)\right\rangle = g_+(t)\left|\overline{B}^0\right\rangle + \frac{p}{q} g_-(t)\left|B^0\right\rangle \ , \tag{1.41}$$

where

$$g_+(t) = e^{-\frac{i}{2}(M_H+M_L)t} e^{-\frac{\Gamma}{2}t} \cos\left(\frac{\Delta m_d t}{2}\right) \ , \tag{1.42}$$

$$g_-(t) = e^{-\frac{i}{2}(M_H+M_L)t} e^{-\frac{\Gamma}{2}t} i \sin\left(\frac{\Delta m_d t}{2}\right) \ . \tag{1.43}$$

Due to the close values of the neutral B meson lifetime, $\tau = (1.530 \pm 0.009)\,\text{ps}$, and the frequency of oscillation, $\Delta m_d = (0.507 \pm 0.005)\,\text{ps}^{-1}$ [24], the amplitude for the mixing process is rather large. Accordingly, the integrated probability of oscillation is sizeable [25]:

$$\chi_d = \frac{(\tau\Delta m_d)^2}{2(1+(\tau\Delta m_d)^2)} = 0.1878 \pm 0.0024 \ , \tag{1.44}$$

which confers mixing a prominent role. An immediate consequence are the large time-dependent *CP* asymmetries that mixing produces, and that are discussed in the next section.

1.3.2 *CP* violation in the B mesons

As previously discussed, the phases in the Standard Model coupling constants is responsible for all *CP*-violating effects. The possible manifestation of these effects may have a few aspects:

- ***CP* violation in decay**, which occurs when the amplitude for a decay and its *CP* conjugate process have different magnitudes;

- ***CP* violation in mixing**, which occurs when the neutral mass eigenstates and the *CP* eigenstates are not identical;
- ***CP* violation in the interference between decays with and without mixing**, which occurs when the B^0 and $\overline{B}^0$ mesons can decay into the same common final state.

Before presenting in more details each type of *CP* violation in B decays, let us first introduce some useful notations for the B transition amplitudes.

The $B(\overline{B})$ meson decay amplitude to a final state $f(\overline{f})$, denoted by $A_f(\overline{A}_{\overline{f}})$, is written as

$$A_f = \langle f|\mathrm{H}|B\rangle \ , \quad \overline{A}_{\overline{f}} = \left\langle \overline{f}|\mathrm{H}|\overline{B}\right\rangle \ . \tag{1.45}$$

There are two types of phases that may appear in A_f and $(\overline{A}_{\overline{f}})$. The first type is referred to as *CP-odd* phases, or *weak* phases. They are related to the weak-interaction part of the Lagrangian, whose relevant terms are exactly the same for a process and for its *CP*-conjugate except that the multiplicative constants become complex-conjugated [22], thus breaking the *CP* symmetry of the terms they form part of. In contrast, the phases generated by *CP*-invariant terms in the Lagrangian, such as those from QCD, are the same for the two processes, and are known as *CP-even* phases, or *strong* phases.

1.3.2.1 *CP* violation in decay

Consider first a quantum-mechanical amplitude with *CP*-odd and *CP*-even phases ϕ and δ, respectively. According to the remarks above, the amplitude transforms under *CP* as

$$Ae^{i(\delta+\phi)} \xrightarrow{CP} Ae^{i(\delta-\phi)} \ . \tag{1.46}$$

However, phases are not directly observable, so even though these two amplitudes are different, the rates for the processes they describe are the same. Since only relative phases have physical meaning, more than one amplitude is needed for *CP*-violating asymmetries.

Consider now a process that is made of different contributions. The total amplitude is then the sum of all of them

$$A_f = \sum_j A_j e^{i\delta_j} e^{i\phi_j} \ , \tag{1.47}$$

$$\overline{A}_{\overline{f}} = e^{2i\xi_f - \xi_B} \sum_j A_j e^{i\delta_j} e^{-i\phi_j} \ , \tag{1.48}$$

where A_j is the modulus of the contributing amplitude, δ_j and ϕ_j their *CP*-even and *CP*-odd phases, respectively. The phases ξ_B and ξ_f are arbitrary, and their transformations have no physical effect, since they are related to the quark flavor symmetries of the strong interactions. When taking the module of the ratio between the two total amplitudes, one obtains a convention-independent quantity

$$\left|\frac{\overline{A}_{\overline{f}}}{A_f}\right| = \left|\frac{\sum_j A_j e^{i\delta_j} e^{-i\phi_j}}{\sum_j A_j e^{i\delta_j} e^{i\phi_j}}\right| \ . \tag{1.49}$$

In the case where the *CP* symmetry is conserved, the weak phases ϕ_j are all equal. It is then trivial to see that in the opposite case

$$\left|\frac{\overline{A}_{\overline{f}}}{A_f}\right| \neq 1 \quad \Longrightarrow \quad CP \text{ violation} \; . \tag{1.50}$$

This type of *CP* violation is also referred to as *direct CP violation*, and results from the interference among various terms in the decay amplitude. In this case the difference in the rates is

$$|A_f|^2 - \left|\overline{A}_{\overline{f}}\right|^2 = -2\sum_{i,j} |A_i|\,|A_j| \sin\left(\delta_i - \delta_j\right) \sin\left(\phi_i - \phi_j\right) \; . \tag{1.51}$$

Thus, for such direct *CP* asymmetries to appear, two or more amplitudes must contribute to the process with different *CP*-odd and *CP*-even phases. A common definition of the *CP* asymmetry is

$$\mathcal{A}_{CP} = \frac{\Gamma\left(\overline{B} \to \overline{f}\right) - \Gamma\left(B \to f\right)}{\Gamma\left(\overline{B} \to \overline{f}\right) + \Gamma\left(B \to f\right)} \; , \tag{1.52}$$

which applies to both cases of neutral or charged B mesons. Indeed, direct *CP* violation is the only one possible for the charged modes. In the case of neutral modes, *CP* violation in decays can occur among the other two types of *CP* violation effects as described below.

1.3.2.2 *CP* violation in mixing

Another type of *CP* violation comes from the fact that the neutral B mesons can oscillate into its *CP* conjugate, as described in Sec.1.3.1. Indeed, since the mass and the *CP* eigenstates are not identical in the case of neutral B mesons, an asymmetry arises between their transition probabilities, $B^0 \to \overline{B}^0$ and $\overline{B}^0 \to B^0$. One can express these differences using the convention-free quantity $|q/p|$, since it is related to the matrix elements $M_{12} - \frac{i}{2}\Gamma_{12}$ and $M_{12}^* - \frac{i}{2}\Gamma_{12}^*$, describing the $B^0 \to \overline{B}^0$ and $\overline{B}^0 \to B^0$ transitions, respectively:

$$\left|\frac{q}{p}\right|^2 = \left|\frac{M_{12}^* - \frac{i}{2}\Gamma_{12}^*}{M_{12} - \frac{i}{2}\Gamma_{12}}\right| \; . \tag{1.53}$$

If *CP* was conserved, the relative phase between M_{12} and Γ_{12} would vanish. Then Eq. 1.53 implies

$$\left|\frac{q}{p}\right| \neq 1 \quad \Longrightarrow \quad CP \text{ violation} \; . \tag{1.54}$$

This type of *CP* violation is also known as indirect *CP* violation. It has been first observed in 1964 [26] in the neutral kaon system. In the neutral B_d system, effects of *CP* violation in mixing is expected to be small, $\mathcal{O}(10^{-4})$ [27], and very negligible with respect to the sensitivity of the B factories, thus making $|q/p| \sim 1$ a good approximation.

1.3.2.3 *CP* violation in the interferences between decays with and without mixing

Finally, another possibility for *CP* violation, also referred to as *CP* violation in mixing and decay, is the one foreseen by Bigi, Carter, Sanda and others [28–30]. It occurs whenever

$$\Gamma(B^0 \to f) \neq \Gamma(\overline{B}^0 \to f) \ , \tag{1.55}$$

where f is a final state accessible to both B^0 and $\overline{B}^0$, a condition that is satisfied if f is a *CP* eigenstate. It is of primary importance in the decays of neutral B mesons, in which *CP* violation arises as a consequence of the interference between the amplitudes $A(B^0 \to f_{CP})$ and $A(B^0 \to \overline{B}^0 \to f_{CP})$. It has to be noticed that, before the start of the B Factories, LEP had already put some constraints on the *CP* violation parameters in the B meson sector, which have been significantly improved by the results obtained at the B Factories. Note that *CP* violation in the mixing and in the decay of the $K^0 - \overline{K}^0$ system [26, 31], had also been observed before the start of the B Factories.

A quantity similar to the one used to measure purely direct *CP* violation, given in Eq. 1.52, could be applied in order to measure the *CP* violation here. However, in this case the flavor of neutral B mesons is not straightforward to determine since, precisely, their flavors change over time. At the B Factories, the flavor determination is facilitated by the fact that the B mesons are produced from the decay of the $\Upsilon(4S)$ resonance, i.e. $\Upsilon(4S) \to B\overline{B}$, therefore forming an *entangled* pair of mesons. Such states are predicted by quantum mechanics by the famous "EPR paradox" [32, 33], where at instant t, the probability of one of the mesons to be a particle equals the probability for the other meson to be an antiparticle. Thus, if it is possible to determine the flavor of one of the B mesons at time t, the flavor of the other meson can be inferred to be the opposite at that exact same instant, and evolves afterwards independently by means of mixing. This is experimentally known as *flavor tagging* (see Figure 2.3). The flavor of a given B meson, B_{rec}, is determined from the observation of the other meson, B_{tag}, decaying into a state that unambiguously establishes its flavor. A sufficiently precise measurement of the time elapsed between the two decays, Δt, is also required in order to account for the probability for a given B meson state to oscillate (see Sec. 1.3.1).

With these considerations, the *CP* asymmetry as defined in Eq. 1.52 can be redefined in a time-dependent way

$$\mathcal{A}_{CP}(\Delta t) = \frac{\Gamma\left(B_{\text{tag}=B^0}(\Delta t) \to f_{CP}\right) - \Gamma\left(B_{\text{tag}=\overline{B}^0}(\Delta t) \to f_{CP}\right)}{\Gamma\left(B_{\text{tag}=B^0}(\Delta t) \to f_{CP}\right) + \Gamma\left(B_{\text{tag}=\overline{B}^0}(\Delta t) \to f_{CP}\right)} \ . \tag{1.56}$$

In the case where no experimental biases are taken into account, such as the probability of wrongly determining the flavor of the B_{tag} meson (called mistagging), the amplitudes for the processes $B^0_{\text{phys}}(\Delta t) \to f_{CP}$ and $\overline{B}^0_{\text{phys}}(\Delta t) \to f_{CP}$ are given by

$$\left\langle f_{CP} \left| \mathrm{H} \right| B^0_{\text{phys}}(\Delta t) \right\rangle = \eta_{CP} A_{f_{CP}} \left(g_+(\Delta t) + \lambda_{f_{CP}} g_-(\Delta t) \right) \ , \tag{1.57}$$

$$\left\langle \overline{f}_{CP} \left| \mathrm{H} \right| \overline{B}^0_{\text{phys}}(\Delta t) \right\rangle = \eta_{CP} \frac{p}{q} A_{f_{CP}} \left(g_-(\Delta t) + \lambda_{f_{CP}} g_+(\Delta t) \right) \ , \tag{1.58}$$

where η_{CP} is the CP eigenvalue of the final state f_{CP}, $g_+(\Delta t)$ and $g_-(\Delta t)$ are given by Eqs. 1.42 and 1.43, respectively, and where

$$\lambda_{f_{CP}} = \eta_{CP} \frac{q}{p} \frac{\overline{A}_{\overline{f}_{CP}}}{A_{f_{CP}}} \tag{1.59}$$

is the convention free quantity carrying the CP violation information.

It is also useful to construct the expression of the time-dependent decay rate as a function of the tag q_{tag} and the time difference Δt

$$f_{q_{\text{tag}}}(\Delta t) = \frac{e^{-|\Delta t|/\tau}}{4\tau} \left[1 + q_{\text{tag}} \left(\mathcal{S} \sin(\Delta m_d \Delta t) - \mathcal{C} \cos(\Delta m_d \Delta t)\right)\right] , \tag{1.60}$$

where $q_{\text{tag}} = +1(-1)$ when the B_{tag} is identified as a B^0 ($\overline{B}^0$), and from which the asymmetry from CP violation in mixing and decay is:

$$\mathcal{A}_{CP}(\Delta t) = \mathcal{S} \sin(\Delta m_d \Delta t) - \mathcal{C} \cos(\Delta m_d \Delta t) , \tag{1.61}$$

where

$$\mathcal{S} = \frac{2\Im(\lambda_{f_{CP}})}{1 + |\lambda_{f_{CP}}|^2} , \quad \mathcal{C} = \frac{1 - |\lambda_{f_{CP}}|^2}{1 + |\lambda_{f_{CP}}|^2} . \tag{1.62}$$

The coefficient $\mathcal{S}$ is different from zero when CP violation in mixing and decay occurs, whereas the coefficient $\mathcal{C}$, in case it is non zero, is an indication of direct CP violation. When taking into account experimental effects, Eq. 1.60 may be re-written in terms of the tagging dilution factors $\langle \mathcal{D} \rangle$ and $\Delta\mathcal{D}/2$ (see Section 7.1.1 for definitions and a detailed discussion), accounting for the probability for a B meson to be mistagged

$$f_{q_{\text{tag}}}(\Delta t) = \frac{e^{-|\Delta t|/\tau}}{4\tau} \left[1 + q_{\text{tag}} \frac{\Delta\mathcal{D}}{2} + q_{\text{tag}} \langle \mathcal{D} \rangle \left(\mathcal{S} \sin(\Delta m_d \Delta t) - \mathcal{C} \cos(\Delta m_d \Delta t)\right)\right] , \tag{1.63}$$

from which $\mathcal{A}_{CP}(\Delta t)$ becomes now:

$$\mathcal{A}_{CP}(\Delta t) = \langle \mathcal{D} \rangle \left(\mathcal{S} \sin(\Delta m_d \Delta t) - \mathcal{C} \cos(\Delta m_d \Delta t)\right) . \tag{1.64}$$

Looking at Eqs. 1.61 and 1.62 it clearly appears that CP violation will occur in the case where

$$\lambda_{f_{CP}} \neq 1 . \tag{1.65}$$

Note that in both cases of CP violation in decay and of CP violation in mixing the previous relation on $\lambda_{f_{CP}}$ is verified for $|\overline{A}_{\overline{f}}/A_f| \neq 1$ and $|q/p| \neq 1$, respectively. However, in the present case, even if $|\overline{A}_{\overline{f}}/A_f| = |q/p| = 1$, CP violation could still occur through

$$|\lambda_{f_{CP}}| = 1 , \quad \Im(\lambda_{f_{CP}}) \neq 0 . \tag{1.66}$$

If there is only one SM contribution to the amplitudes A_f and $\overline{A}_{\overline{f}}$, the expectations are that $\mathcal{S} = -\eta_{CP} \sin(2\beta)$ and $\mathcal{C} = 0$. Deviations from that imply the existence of unaccounted amplitudes that, depending on the characteristics of the mode, could originate from theoretical uncertainties in the Standard Model contributions, or could be an indication of physics beyond the SM.

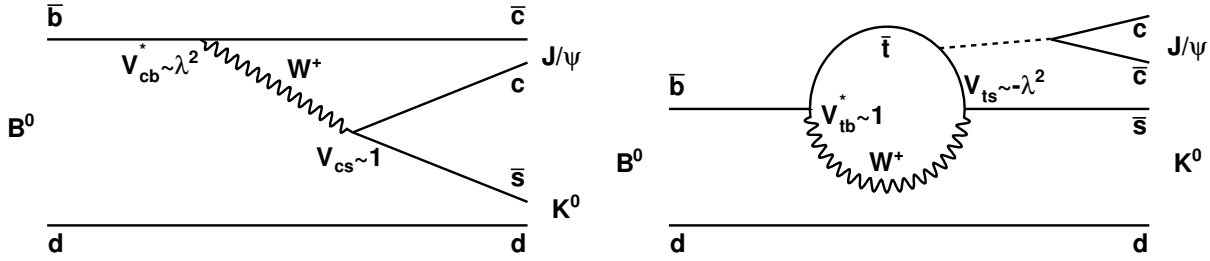

Figure 1.4: Feynman diagrams for the amplitudes contributing to the $B^0 \to J/\psi K^0_S$ decay. Left: tree level diagram. Right: Penguin diagram, where the contribution of the light, u and c, quarks have been neglected. The dotted line corresponds to the exchange of three gluons, necessary to produce a $c\bar{c}$ pair.

1.4 Trees and Penguins

In a quantum field theory, on which is based the SM, in order to describe a given decay process, one needs to include all the possible contributing amplitudes. Each amplitude does not necessarily contribute at the same level, thus it is useful to apply a hierarchical ranking. It often happens that only the two first-order contributions to the total amplitude are sufficient to make theoretical predictions that are precise enough to be compared to experimental results.

For instance, in the so-called "golden mode" $B^0 \to J/\psi K^0_S$, in which the final state is a *CP* eigenstate that makes it sensitive to *CP* violation in mixing and decay, not only one amplitude is allowed. One of the contributing amplitudes, in which the W boson is emitted and absorbed by the same quark line, is called a "loop" or, more often, a "penguin" diagram, whereas the other, is said to be a "tree-level", or simply "tree", diagram (see Figure 1.4). In the penguin diagram, the internal loop, which is formed by the W boson and a combination of up-type quarks, is dominated by the top quark due to its large mass compared to up and charmed quarks. In the hypothetical presence of new physics, new heavy particles could traverse the loop and provide new *CP*-odd phases that could dramatically enhance (or suppress) the amplitude [22, 34]. As shown in Figure 1.5 candidates for such particles are for instance charged Higgs or squarks and gluinos from a super symmetric model.

In the considered example, the CKM factors in both amplitudes carry the same phases, as can easily be seen thanks to the powers of λ and phases that have been written next to the CKM terms on the figure. However, as in many other decays, the penguin diagram is suppressed compared to the tree diagram [35], which have SM couplings. Thus, SM contributions in the loop dominates over possible effects from non-SM couplings and a clean interpretation for the time-dependent asymmetry is obtained: $\mathcal{A}_{CP}(\Delta t) = \sin 2\beta \sin(\Delta m_d \Delta t)$. The measurement of *CP* violation in this channel constitutes one of the main achievements of the B Factories. It plays the role of a benchmark with which to compare measurements of $\sin 2\beta$, e.g. in $b \to q\bar{q}s$ transitions, possibly affected by new physics.

In a general way, tree diagrams are usually cleaner in their theoretical interpretation

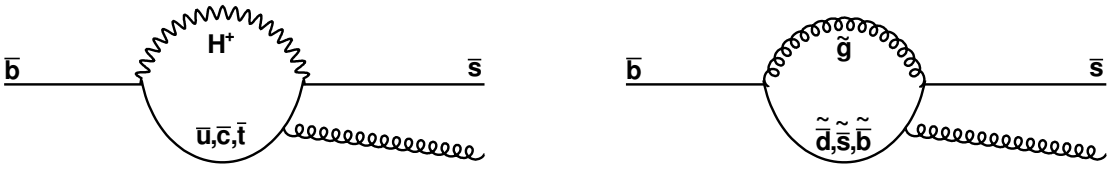

Figure 1.5: Diagrams demonstrating the potential for new physics sensitivity in $b \to s$ penguin diagrams. On the left, a charged Higgs, predicted by the MSSM, enters the loop possibly carrying a complex coupling constant. On the right, the loop is formed by a gluino and (anti)squarks, enhancing the SM amplitude. Supersymmetry has potentially large effects on flavor observables, since squarks may change flavor while propagating, e.g, the loop on the right could be produced by a gluino and a bottom squark that turns into a strange squark in the middle of the loop [22].

than penguin diagrams. However, in some specific transition modes, the tree diagrams can be suppressed compared to penguin diagrams, as it is the case for $b \to s\gamma$ transitions. Furthermore, since SM parameters are now well constrained, any deviations due to unknown physics should be small compared to SM predictions. Such modes are therefore particularly interesting in the indirect search for new physics at the electroweak scale, due to the absence of a tree contribution which could overshadow effects from possible new physics. They are also complementary to direct searches performed in high-energy colliders such as in hadronic colliders like the LHC.

Chapter 2

The photon polarization in radiative B decays and the $K_1(1270)$ resonance

Contents

Study of FCNC processes, such as $b \to s\gamma$ transitions, can provide strong constraints on NP. In the SM, the Glashow-Iliopoulos-Maini (GIM) mechanism [36] implies that FCNC processes are forbidden at the tree level and only occurs through a loop or box diagrams, where heavy virtual particles can propagate. Since the presence of such heavy particles influences the predicted values of physical observables, the study of $b \to s\gamma$ processes could reveal the existence of yet unknown particles introduced by NP models.

The SM predicts that photons emitted in $b \to s\gamma$ decays are left-handed, up to small corrections of order m_s/m_b (see Sec. 2.1), while being right-handed in $\bar{b} \to \bar{s}\gamma$. In several models beyond the SM the photon in $b \to s\gamma$ acquires an appreciable right-handed component due to the exchange of a heavy fermion in the electroweak loop process. The branching ratio of inclusive $B \to X_s\gamma$ process is currently experimentally known up to a quite high level of precision ($\mathcal{B}(B \to X_s\gamma)_{\text{exp.}} = (3.43 \pm 0.21 \pm 0.07) \times 10^{-4}$ [23]) and agrees reasonably well with the SM predictions obtained at the next-to-next-to-leading order in QCD ($\mathcal{B}(B \to X_s\gamma)_{\text{th.}} = (3.15 \pm 0.23) \times 10^{-4}$ [37]). On the other hand, as detailed in Sec. 2.2, up to date, no evidence

exists for the helicity of the photons in exclusive decays. In some NP models [38–40], the right-handed component may be comparable in magnitude to the left-handed component, without affecting the SM prediction for the inclusive radiative decay rate, which motivates independent measurements of the photon helicity in several exclusive radiative decay modes.

2.1 The photon polarization

In the SM, the quark level $b \to s\gamma$ vertex is given (without QCD corrections) by:

$$\bar{s}\Gamma_{\mu}^{b\to s\gamma} b = \frac{e}{(4\pi)^2}\frac{g^2}{2M_W^2} V_{ts}^* V_{tb} F_2 \bar{s} i\sigma_{\mu\nu} q^{\nu} \left(m_b P_R + m_s P_L\right) b \ , \tag{2.1}$$

where $q = q_b - q_s$ with q_b and q_s the four-momenta of the b and s quarks, respectively, F_2 is the loop function, whose expression can be found in [41], P_L and P_R are the projection operators as defined in Eq. 1.2, V_{ts} and V_{tb} are the leading CKM matrix elements appearing in the loop diagram, and $\sigma_{\mu\nu}$ are the commutators of the Dirac γ 4×4 matrices.

Once fixing the three momentum direction such as $q^{\mu} = (|\mathbf{q}|, 0, 0, |\mathbf{q}|)$ in the b quark rest frame, and defining the right- and left-handed polarization vectors as

$$\epsilon_{R,L}^{\mu} = \mp\frac{1}{\sqrt{2}} \begin{pmatrix} 0 \\ 1 \\ \pm i \\ 0 \end{pmatrix} \ , \tag{2.2}$$

it is possible to compute the helicity amplitude and to demonstrate that

$$\bar{s}_L i\sigma_{\mu\nu} q^{\nu} b_R \epsilon_R^{\mu *} = \bar{s}_R i\sigma_{\mu\nu} q^{\nu} b_L \epsilon_L^{\mu *} = 0 \ . \tag{2.3}$$

From Eq. 2.3 one can see that the first (second) term in Eq. 2.1 are non-zero only when multiplying the $b \to s\gamma$ vertex by the left (right)-handed polarization vector. This shows

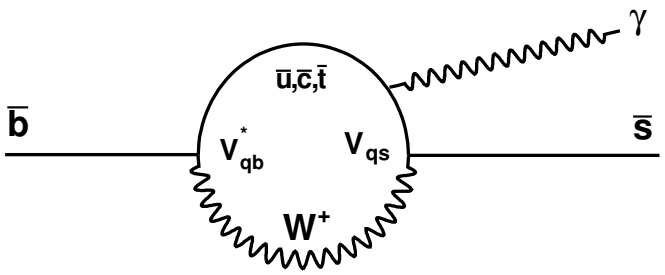

Figure 2.1: Feynman diagram of $\bar{b} \to \bar{s}\gamma$ transition in the SM. The loop being dominated by the top quark, the weak couplings are given by $|V_{qb}^*| \sim 1$ and $|V_{qs}| \sim \lambda^2$. In this transition, since the $\bar{b} \to \bar{s}\gamma$ transition is a two-body back-to-back decay in the $\bar{b}$ rest frame, and due to the helicity conservation the photon must be right-handed, while being left-handed in $b \to s\gamma$.

that the term proportional to m_b in Eq. 2.1 describes $b \to s\gamma_L$ transitions, while the term proportional to m_s describes $b \to s\gamma_R$ transitions. Therefore, due to the fact that the b quark is much heavier than the s quark (i.e. $m_s/m_b \sim 0.02$), the SM predicts that photons emitted in $b \to s\gamma$ decays are predominantly left-handed. In a similar manner, photons emitted in $\overline{b} \to \overline{s}\gamma$ decays are predominantly right-handed. Figure 2.1 shows the Feynman diagram of the quark level $\overline{b} \to \overline{s}\gamma$ transition in the SM.

When considering cascade decays of the type $B \to K_{\rm res}\gamma \to K\pi\pi\gamma$, the weak $B \to K_{\rm res}\gamma$ amplitudes involving left- and right-handed photons, denoted c_L and c_R, respectively, need to include QCD corrections compare to the quark level transition described above. For $b \to s\gamma$ process, QCD corrections can typically be described using an effective Hamiltonian defined as

$$\mathrm{H}_{\rm eff} = -\frac{4G_F}{\sqrt{2}} V_{ts}^* V_{tb} \sum_{i=1}^{8} C_i(\mu)\mathcal{O}_i(\mu) + C_i'(\mu)\mathcal{O}_i'(\mu) \ , \tag{2.4}$$

where the C_i and $\mathcal{O}_i$ are, respectively, the short-distance Wilson coefficients and local long-distance operators related to $b \to s\gamma_L$ transitions, the primed operators being related to $b \to s\gamma_R$ transitions. G_F is the Fermi constant, which is related to the coupling constant of the weak interaction (g) and the mass of the W boson (M_W) such as $G_F \propto g^2/M_W^2$.

One can make an intuitive interpretation of $\mathrm{H}_{\rm eff}$. The picture of a decaying hadrons with masses of order $\mathcal{O}(m_b)$, is more properly described by effective point-like vertices which are represented by the local operators $\mathcal{O}_i$. The Wilson coefficients C_i can then be regarded as coupling constants associated with these effective vertices. Thus $\mathrm{H}_{\rm eff}$ is simply a series of effective vertices multiplied by effective coupling constants C_i.

The μ dependence is the renormalization scale whose value can be chosen arbitrarily. It serves to separate the physics contributions to a given decay amplitude into short-distance contributions at scales higher than μ and long-distance contributions corresponding to scales lower than μ. It is customary to choose μ to be of the order of the mass of the decaying hadron, in the present case m_b.

The leading contribution to $\mathrm{H}_{\rm eff}$ comes here from the electro-magnetic operator, $\mathcal{O}_{7\gamma}$, describing the photon penguin diagram, and which is defined as

$$\mathcal{O}_{7\gamma} = \frac{e}{16\pi^2} m_b \overline{s}_L \sigma_{\mu\nu} b_R F^{\mu\nu} \ , \tag{2.5}$$

where $F^{\mu\nu}$ denotes the electromagnetic field strength tensor, while the primed electro-magnetic penguin operator $\mathcal{O}'_{7\gamma}$ is defined as

$$\mathcal{O}'_{7\gamma} = \frac{e}{16\pi^2} m_b \overline{s}_R \sigma_{\mu\nu} b_L F^{\mu\nu} \ . \tag{2.6}$$

Note that when only considering the contribution of the dominant $\mathcal{O}_{7\gamma}$ operator in $\mathrm{H}_{\rm eff}$, and making the Fourier transform $-\sigma^{\mu\nu}F_{\mu\nu} \to 2i\sigma_{\mu\nu}q^\nu$, the effective hamiltonian is equivalent to the first term in Eq. 2.1.

The other operators, with subleading contributions, are the current-current operators $\mathcal{O}_1$ and $\mathcal{O}_2$, corresponding to diagrams where two quark lines exchange a W boson; the QCD penguin operators $\mathcal{O}_3$ to $\mathcal{O}_6$, corresponding to the same diagrams with an additional

gluon exchange between the two quark lines; the chromomagnetic gluon penguin operator $\mathcal{O}_8$ corresponding to loop diagrams where a gluon is emitted from the virtual up-type quark line.

In the SM, primed operators related to $b \to s\gamma_R$ transitions with $i \leq 6$ are predicted to have no contribution. Thus, only $\mathcal{O}'_{7\gamma}$ and $\mathcal{O}'_8$ contribute, but are negligible since $C'_{7\gamma}$ and C'_8 Wilson coefficients are suppressed compared to $C_{7\gamma}$ and C_8 such as

$$\frac{C'_{7\gamma}}{C_{7\gamma}} = \frac{C'_8}{C_8} = \frac{m_s}{m_b} \sim 0.02 \ . \tag{2.7}$$

Since in $\mathrm{H_{eff}}$ the $\mathcal{O}_{7\gamma}$ operator is dominant at the leading order, it is possible to absorb the subleading contribution from $\mathcal{O}_{i\neq 7}$ into an effective $C^{\mathrm{eff}}_{7\gamma}$ coefficient such as the amplitude of $b \to s\gamma$ can be written

$$\mathcal{M}(b \to s\gamma)_{\mathrm{LO}} = \langle f|\mathrm{H_{eff}}|i\rangle = -\frac{4G_F}{\sqrt{2}} V^*_{ts}V_{tb} \left(C^{(0)\mathrm{eff}}_{7\gamma}(\mu) \langle f|\mathcal{O}_{7\gamma}|i\rangle + C'^{(0)\mathrm{eff}}_{7\gamma}(\mu) \langle f|\mathcal{O}'_{7\gamma}|i\rangle \right) , \tag{2.8}$$

where i and f denotes the hadronic initial and final states, respectively, and $\langle f|\mathcal{O}_{7\gamma}|i\rangle$ are the hadronic matrix elements of $\mathcal{O}_{7\gamma}$ between i and f. The coefficient $C^{(0)\mathrm{eff}}_{7\gamma}(\mu)$ denotes the leading logarithmic expression to $C^{\mathrm{eff}}_{7\gamma}$. The matrix elements summarize the physics contributions to the amplitude $\mathcal{M}(b \to s\gamma)$ from scales lower than μ, often chosen as of the order m_b.

Theoretical calculations have shown that, even though the contribution of the subleading operators was small, they can not be completely neglected. Indeed from Ref. [42] a significantly larger value of $C^{(0)\mathrm{eff}}_{7\gamma}$ compared to $C^{(0)}_{7\gamma}$ is obtained. The observed enhancement is due to short-distance QCD corrections, which appear to be large for the $b \to s\gamma$ process.

Recent developments were made in computing the perturbative QCD corrections to the matrix element part [43, 44]. From these developments, it appeared that contributions of higher order diagrams in the SM could possibly enhance opposite photon polarization (i.e. right-handed photons in $b \to s\gamma$). Many efforts to evaluate such effect have been made in the case of $B \to K^*\gamma$ decays [43–46]. Calculations from Refs. [45, 46] indicate an opposite photon helicity contamination up to 10%. However, these predictions appear to be strongly model dependent and do not agree with each other. Some suggest much smaller values of the contamination from opposite sign helicity photons. In some cases, right-handed photons contribution is even found to be reduced by $\sim$ 20% [47, 48] with respect to the leading m_s/m_b term. Thus, it clearly appears that further theoretical works are required to give a more rigorous conclusion.

Several NP models introduce contributions to the $b \to s\gamma$ process such as the proportion of right-handed photons could be significantly enhanced. As previously emphasized, many of such NP models allow for a large contribution of right-handed photons, which result is a large coefficient to the right-handed electro-magnetic operator $\mathcal{O}'_{7\gamma}$, without affecting the SM prediction of the inclusive $B \to X_s\gamma$ branching ratio.

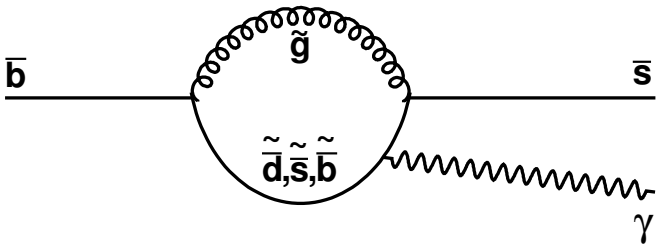

Figure 2.2: One of the Feynman diagrams of $\bar{b} \to \bar{s}\gamma$ transition in MSSM. The loop is formed by a gluino, the SUSY partner of a gluon, and (anti)squarks. In the SM the right-handed contribution are suppressed by a factor m_s/m_b due to the left-handed coupling of W to quarks, while in MSSM this suppression can be reduced due to right-handed couplings appearing in the loop: undiscovered heavy fermions f contributing to the penguin loop would provide an enhancement of m_f/m_b to the helicity-flip amplitude.

Supersymmetric (SUSY) models are an example of NP models that bring extra source of flavor violation. One such model is the Minimal Supersymmetric Standard Model (MSSM), which is a minimal supersymmetric extension of the SM. The MSSM introduce superpartners to each SM particle and two Higgs doublets. For instance, the superpartners to quarks are called the squarks. Since there is no theoretical constraint on the mass of these hypothetical new particles, the only constraints come from experiments. Until now, no evidence of such superpartners was found in direct searches at existing high-energy collider experiments. As a consequence, new particles from NP models, such as MSSM, are required to be very heavy compared to SM particles. The masses and mixing parameters are generated through the soft supersymmetric breaking mechanism [49].

Once the mechanism of the SUSY breaking specified, it is possible to express, the *soft breaking part*[1] of the Lagrangian in MSSM. After the spontaneous symmetry breaking, it appears that the squark mass can come from any combination of left- and right-handed couplings. Since the squark mass matrices and the couplings are not diagonal in the quark basis, the squark propagator can change flavor and chirality. In particular, the chirality can be flipped on the squark propagator in the loop of $b \to s\gamma$, which can lead to a right-handed photon emission. One Feynman diagram of such process in MSSM is shown in Fig 2.2.

[1]In MSSM, the structure of the Lagrangian is similar to the one of the SM. The part of the MSSM Lagrangian corresponding to the Yukawa couplings is called the soft breaking part, which consists of mass terms for scalar fields (namely the left- and right-handed squark and slepton fields and the two Higgs fields), Higgs mixing terms, trilinear scalar couplings and gaugino (the superpartners of gauge bosons) mass terms.

2.2 Physical observables and experimental status

As the photon polarization is not directly measurable, several methods have been proposed in order to measure it in $b \to s\gamma$ processes. A few of them are briefly described in this Section.

2.2.1 Mixing-induced CP asymmetry

One method to probe the photon helicity is to perform an indirect measurement *via* a time-dependent CP asymmetry analysis in neutral B mesons. This strategy is the one adopted in the present thesis.

In the case of the radiative decay of a neutral B meson to a hadronic CP eigenstate f_{CP}, $B^0(t) \to f_{CP}\gamma$, where the B meson state is identified (tagged) as a B^0 (rather than a $\overline{B}^0$) at time $t = 0$, the time-dependent CP asymmetry is given by [50]

$$\begin{aligned} \mathcal{A}_{CP}(t) &= \frac{\Gamma(\overline{B}^0(t) \to f_{CP}\gamma) - \Gamma(B^0(t) \to f_{CP}\gamma)}{\Gamma(\overline{B}^0(t) \to f_{CP}\gamma) + \Gamma(B^0(t) \to f_{CP}\gamma)} && (2.9) \\ &\simeq -\xi \sin(2\psi) \sin(\phi_M - \phi_L - \phi_R) \sin(\Delta \mathrm{M} t) && (2.10) \\ &= \mathcal{S}_{f_{CP}} \sin(\Delta \mathrm{M} t) \ , && (2.11) \end{aligned}$$

where $\mathcal{S}_{f_{CP}}$ is the mixing-induced CP violation parameter, $\xi \equiv CP(f_{CP}) = \pm 1$ and

$$\begin{aligned} \Gamma(B^0(t) \to f_{CP}\gamma) &= |\mathcal{M}_L(t)|^2 + |\mathcal{M}_R(t)|^2 \ , \\ \Gamma(\overline{B}^0(t) \to f_{CP}\gamma) &= \left|\overline{\mathcal{M}}_L(t)\right|^2 + \left|\overline{\mathcal{M}}_R(t)\right|^2 \ , \end{aligned} \qquad (2.12)$$

with $\mathcal{M}_L$ and $\mathcal{M}_R$ corresponding to the total amplitudes involving left- and right-handed photons, respectively. In order to obtain Eq. 2.10, both direct CP violation ($\mathcal{C}_{f_{CP}}$) and the small width difference, compared to the mass difference between the B meson mass eigenstates, are neglected.

In Eq. 2.10, $\sin(2\psi)$ parametrizes the relative amount of left- and right-handed photons and is defined as

$$\sin(2\psi) \equiv \frac{2|\mathcal{M}_L \mathcal{M}_R|}{|\mathcal{M}_L|^2 + |\mathcal{M}_R|^2} \ ; \qquad (2.13)$$

the phase ϕ_M is the one appearing in the $B^0\overline{B}^0$ mixing such as $\phi_M = 2\beta$ for B_d^0 mesons and is almost zero for B_s^0 mesons; $\phi_{L,R}$ are the relative CP-odd weak phases in the $b \to s\gamma$ process, and are defined as

$$\phi_{L,R} = \sin^{-1}\left(\frac{\Im(\mathcal{M}_{L,R})}{|\mathcal{M}_{L,R}|}\right) \ . \qquad (2.14)$$

In the SM, $\phi_{L,R}$ are predicted to be almost zero ($\mathcal{O}(\lambda^4)$). Since the right-handed amplitude is suppressed in the SM, the time-dependent asymmetry is such as

$$\mathcal{A}_{CP}^{\mathrm{SM}}(t) \sim 0 \ . \qquad (2.15)$$

From this method, it appears that, although an observation of $\mathcal{A}_{CP}(t) \neq 0$ would immediately indicate the existence of NP contributions, it is not possible to determine quantitatively

the ratio $\mathcal{M}_R/\mathcal{M}_L$, which is related to $|C'^{\rm eff}_{7\gamma}/C^{\rm eff}_{7\gamma}|$. Indeed $\mathcal{A}_{CP}(t)$ measures a combination of $\mathcal{M}_R/\mathcal{M}_L$ and the *CP* violating phases in $b \to s\gamma$ as well as in $B\overline{B}$ mixing. Therefore in the case of an experimental result that would measure a deviation of $\mathcal{A}_{CP}(t)$ from its predicted value in the SM, one can only fix the *CP* violating phases $\phi_{M,L,R}$ as given by several NP models in order to discriminate the one that describes the best the observed value of $\mathcal{A}_{CP}(t)$.

Several exclusive radiative decay modes have been studied in time-dependent *CP* violation analyses. Due to experimental constraints, such analyses appear to be very challenging in hadronic colliders, and the best results to date come from the B Factories.

In the $B \to K^0_S\pi^0\gamma$ decay process, where the SM predicts $\mathcal{S} \approx -0.028$ [50], both *BABAR* and Belle have performed measurements of the mixing-induced *CP* asymmetry parameter $\mathcal{S}$, and reported $\mathcal{S}_{K^0_S\pi^0\gamma} = -0.78 \pm 0.59 \pm 0.09$ [4] and $\mathcal{S}_{K^0_S\pi^0\gamma} = -0.10 \pm 0.31 \pm 0.07$ [5], respectively. Moreover in the mass region of the $K^*(892)$, *BABAR* reported $S_{K^*\gamma} = -0.08 \pm 0.31 \pm 0.05$ [51], and Belle $S_{K^*\gamma} = -0.32^{+0.36}_{-0.33} \pm 0.05$ [5]. Note that in the $B^0 \to K^{*0}\gamma$ decays, the LHCb collaboration have reported a precise measurement [52] of the direct *CP* asymmetry, $\mathcal{A}_{CP} = 0.008 \pm 0.017 \pm 0.009$, corresponding to the parameter $\mathcal{C}$ in the time-dependent *CP* asymmetry. This result is in good agreement with the SM predictions and consolidates one of the assumptions made in Eq. 2.10.

Belle has also performed a time-dependent *CP* asymmetry measurement of $B^0 \to K^0_S\rho^0\gamma$ decays, where the SM predicts $\mathcal{S} \approx 0.03$ [53], and reported $\mathcal{S}_{K^0_S\rho\gamma} = 0.11 \pm 0.33^{+0.05}_{-0.09}$ [3].

2.2.2 Other methods

One other method, proposed by Gronau *et al.* [2, 54], allows a direct determination of the photon polarization by studying the angular distribution in the $B \to K_{\rm res}\gamma \to K\pi\pi\gamma$ decay. This method uses the angular correlations among the final hadronic decay products $K\pi\pi$ in order to extract the polarization λ_γ defined as

$$\lambda_\gamma = \frac{|c_R|^2 - |c_L|^2}{|c_R|^2 + |c_L|^2} \,, \tag{2.16}$$

where c_L and c_R are the amplitudes involving left- and right-handed photons, as described in the previous Section. They are related to the Wilson coefficients such as

$$c_R = g_+^{K_{\rm res}} C^{(0)\rm eff}_{7\gamma} \,, \quad c_L = g_+^{K_{\rm res}} C'^{(0)\rm eff}_{7\gamma} \,, \tag{2.17}$$

where $g_+^{K_{\rm res}}$ are hadronic form factors at $q^2 = 0$, which have been computed using several models [55–60]. Since in the SM the photon in B decays is dominantly right-handed, it implies $|c_L|^2 \ll |c_R|^2$, such that $\lambda_\gamma \approx 1$ holds for radiative B decays, while $\lambda_\gamma \approx -1$ applies to radiative $\overline{B}$ decays. The determination of λ_γ is done *via* the measure of an observable called the up-down asymmetry $A_{\rm ud}$ representing the asymmetry between the measured signal rates with photons emitted above and below the $K\pi\pi$ decay plane in the $K_{\rm res}$ reference frame.

The LHCb collaboration recently reported the first measurement of the up-down asymmetry in $B^\pm \to K^\pm\pi^\pm\pi^\mp$ decays giving $A_{\rm ud} = -0.085 \pm 0.019({\rm stat}) \pm 0.003({\rm syst})$ [61]. This

result is 4.6σ away from zero, showing evidence for photon polarization in $b \to s\gamma$ transitions. However, the current theoretical status do not allow to link directly $A_{\rm ud}$ to λ_γ, in which case a value for the photon polarization can be determined from this result.

Another angular analysis method is based on the angular distribution of the four-body final state in the $B^0 \to K^{*0}(\to K^-\pi^+)\ell^+\ell^-$ decay in the low $\ell^+\ell^-$ invariant mass region [62]. Many observables involving different combinations of K^* spin amplitudes, which are related to the c_L and c_R amplitudes, and therefore to the $C_{7\gamma}$ and $C'_{7\gamma}$ Wilson coefficients, can be studied.

The latest experimental results were reported by the LHCb collaboration in the analysis of $B \to K^* e^+e^-$ [63] and by the LHCb [64] and CMS [65] collaborations in the analysis of $B \to K^*\mu^+\mu^-$. No enhancement of the emission of right-handed photons in $b \to s\gamma$ process have been observed, and all these results are in good agreement with SM predictions.

2.3 Status of the $K_1(1270)$ resonance description

In the present thesis, the mixing-induced CP asymmetry parameter $\mathcal{S}_{K^0_S\rho\gamma}$ is determined from the effective value of $\mathcal{S}$ ($\mathcal{S}_{K^0_S\pi^+\pi^-\gamma}$), which is extracted from a time-dependent analysis of $B^0 \to K^0_S\pi^+\pi^-\gamma$ decays. $\mathcal{S}_{K^0_S\rho\gamma}$ is related to $\mathcal{S}_{K^0_S\pi^+\pi^-\gamma}$, by a dilution factor $\mathcal{D}_{K^0_S\rho\gamma}$ depending on the amplitudes of intermediate hadronic resonances appearing in the decays of the kaonic resonances in the cascade $B \to K_{\rm res}\gamma \to K\pi\pi\gamma$. From the five kaonic resonances in the $K\pi\pi$ invariant mass range below $1.8\,\mathrm{GeV}/c^2$, the dominant contribution is expected to originate from the axial-vector resonance $K_1(1270)$ [24]. Therefore a good understanding of the $K_1(1270)$ properties is useful in order to correctly model the $K\pi\pi$ resonant structure.

In this section we give a brief overview of the status on the $K_1(1270)$ resonance description. For a more complete description, see [48].

2.3.1 Axial-vector K_1 resonances

The resonances $K_1(1270)$ and $K_1(1400)$, close in mass, were disentangled for the first time in 1977 at SLAC [66] and a few years later by the ACCMOR collaboration at CERN [67], in experiments on the diffractive production of the $1^+(K\pi\pi)$ system in the $Kp \to K\pi\pi p$ reaction. The fact that the relative ratios of the two dominant decay modes, $K^*\pi$ and $K\rho$, are different between the $K_1(1270)$ and the $K_1(1400)$ resonances, i.e. the $K\rho(K^*\pi)$ channel of $K_1(1270)(K_1(1400))$ is dominant, indicates that the two strange axial-vector resonances are the mixtures of non mass eigenstates K_{1A} and K_{1B}. Using conventions from [68], the mass eigenstates can then be defined as

$$|K_1(1270)\rangle = |K_{1A}\rangle \sin\theta_{K_1} + |K_{1B}\rangle \cos\theta_{K_1} \ , \tag{2.18}$$

$$|K_1(1400)\rangle = |K_{1A}\rangle \cos\theta_{K_1} - |K_{1B}\rangle \sin\theta_{K_1} \ , \tag{2.19}$$

where θ_{K_1} is the mixing angle. In some theoretical predictions [68], two possible solutions were found for the value of the mixing angle: $\theta_{K_1} \approx 33°$ or $57°$.

The first experimental measurement of the mixing angle was performed at SLAC [66] from the couplings to the $K^*\pi$ and $K\rho$ channels, and gave $\theta_{K_1} = (41 \pm 4)°$. Results from the partial wave analysis done by the ACCMOR collaboration yielded $\theta_{K_1} = (64 \pm 8)°$ and $\theta_{K_1} = (54 \pm 4)°$ for the low and high momentum transfer to the recoiling proton, respectively[2].

Results from τ decays in the $K_1(1270)$ or the $K_1(1400)$ resonances and a neutrino, from experiments at LEP, indicate that the production of $K_1(1270)$ is favored with respect to that of $K_1(1400)$ [69–71]. The mixing angle determined by CLEO [71] is consistent with the predictions given by [68].

More recently, the Belle collaboration also reported the observation of the $K_1(1270)$ and the $K_1(1400)$ resonances in radiative B decays [6]. They observed that the branching fraction of the decay $B \to K_1(1400)\gamma$ was very suppressed compared to that of $B \to K_1(1270)\gamma$; $\mathcal{B}(B^+ \to K_1(1270)^+\gamma) = (4.3 \pm 0.9(\text{stat.}) \pm 0.9(\text{syst.})) \times 10^{-5}$, while only an upper limit was reported for $K_1(1400)$: $\mathcal{B}(B^+ \to K_1(1400)^+\gamma) < 1.5 \times 10^{-5}$ at 90% CL. In this context, a detailed study of the $B \to K_1(1270)\gamma$ and $B \to K_1(1400)\gamma$ decays in the light-cone QCD sum rules approach was performed [72]. The predicted branching fractions, $\mathcal{B}(B^+ \to K_1(1270)^+\gamma)$ and $\mathcal{B}(B^+ \to K_1(1400)^+\gamma)$ are in agreement with the Belle measurement.

In the present analysis, the values of the branching fractions of $B \to K_{\text{res}}\gamma$ decays is important. Indeed in a preliminary stage of the analysis we rely on existing measurements and theoretical estimations of these branching fractions to model the signal.

2.3.2 The $K\pi$ S-wave in $K_1(1270)$ decays

Some contradictions appear in the literature the branching fractions of the $K_1(1270)$ decay modes. The PDG gives [24]:

- $\mathcal{B}(K_1(1270) \to K\rho) = 0.42 \pm 0.06$;
- $\mathcal{B}(K_1(1270) \to K_0^*(1430)\pi) = 0.28 \pm 0.04$;
- $\mathcal{B}(K_1(1270) \to K^*\pi) = 0.16 \pm 0.05$;
- $\mathcal{B}(K_1(1270) \to K\omega) = 0.11 \pm 0.02$;

as well as a small contribution of the $Kf_0(1370)$ channel. All these branching fractions are extracted from the results from ACCMOR. Looking at the $K_0^*(1430)\pi$ channel, one can have doubts about the PDG interpretation of the ACCMOR results. Indeed, in the original paper [67], a reference is made to a strongly coupled peak in the "scalar + π" channel around the mass $M_{K\pi\pi} \sim 1270\,\text{MeV}/c^2$, but there is no reference to the scalar being the $K_0^*(1430)$ resonance. In the ACCMOR paper, the scalar meson is parametrized with a mass M of $\simeq 1.25\,\text{GeV}/c^2$ and a large width of $\Gamma \simeq 600\,\text{MeV}/c^2$, and can be treated as a continuum

[2]Note that different conventions were used to define the K_1 mass eigenstates (see Eqs. 2.18 and 2.19) by the two groups. Therefore, adopting conventions from [68] implies that $\theta_{K_1} = \theta_{K_1}^{\text{ACCMOR}} = 90° - \theta_{K_1}^{\text{SLAC}}$.

$(K\pi)_{\mathrm{S-wave}}$ component.

The Belle collaboration performed an analysis of $B \to J/\psi\,(\psi')K\pi\pi$ decays [73], and measured the branching fractions of $B^+ \to J/\psi\,K^+\pi^+\pi^-$ and $B^+ \to \psi' K^+\pi^+\pi^-$. In both decay modes, since the $K\pi\pi$ final state originates from various K_{res} and as the $K_1(1270)$ turned out to be dominant, a detailed study of $K_1(1270) \to K\pi\pi$ was also done. The branching fraction of the $K_0^*(1430)\pi$ channel was measured to be $\mathcal{B}(K_1(1270) \to K_0^*(1430)\pi) \simeq 2\%$, which is much smaller than the value given by the PDG. Note that in the Belle analysis the $K_0^*(1430)\pi$ channel is described as a scalar resonance of mass $M_{K_0^*(1430)} = (1425 \pm 50)\,\mathrm{MeV}/c^2$ and width $\Gamma_{K_0^*(1430)} = (270 \pm 80)\,\mathrm{MeV}/c^2$ using a Relativistic Breit-Wigner line shape, which is different from the scalar meson parametrization used in the ACCMOR analysis. However, they did not observe any other "lower scalar + π" component in the decay of $K_1(1270)$, the "missing" branching fraction being mainly absorbed by an enhancement of the $K\rho$ channel.

From the comments above, the presence of $K_1(1270) \to (K\pi)_0^*\pi$ decays, where $(K\pi)_0^*$ denotes a very wide scalar meson, should be considered when studying $K_1(1270) \to K\pi\pi$ decays. One candidate is the $K_0^*(800)$ [74], also referred to as κ. Finally, one surprising fact, as noticed by [67], is that there is no evidence for the presence of a $\kappa\pi$ channel in the $K_1(1400)$ decay.

2.3.3 Width of the $K_1(1270)$

When the mass of one resonance at the peak is close to a decay threshold, such as in the $K_1(1270) \to K\rho$ decay, different definitions of the resonance width are no longer equivalent. One definition is the width at the peak, $\Gamma(M_{\mathrm{peak}})$, that can be predicted using the K-matrix formalism [75]. Another definition is the full width at half maximum, $\Gamma_{K_1}(M)$, of the Breit-Wigner distribution. In the latter case, the width appears to be smaller than in the former case. Indeed the ACCMOR collaboration measured the $K_1(1270)$ width to be $\Gamma_{K_1(1270)} = 90 \pm 8\,\mathrm{MeV}/c^2$ [67], in which case it is assumed to correspond to the full width at half maximum. On the other hand, the theoretical calculation of Ref. [67], using the K-matrix couplings, gives a value of the width at the peak of the order $\Gamma_{K_1(1270)} \approx 200\,\mathrm{MeV}/c^2$. This prediction contains a sum over all possible intermediate states including $\kappa\pi$.

In the analysis of $B \to J/\psi\,(\psi')K\pi\pi$ decays, Belle also studied the parameters of the $K_1(1270)$ resonance, by floating its mass and width in an additional fit to the $B^+ \to J/\psi\,K^+\pi^+\pi^-$ data. The averaged mass given by the PDG is $M_{K_1(1270)} = (1272 \pm 7)\,\mathrm{MeV}/c^2$, which is very close to the one reported by the ACCMOR collaboration ($M_{K_1(1270)} = (1270 \pm 10)\,\mathrm{MeV}/c^2$). Belle observed a smaller mass, $M_{K_1(1270)} = (1248.1 \pm 3.3(\mathrm{stat.}) \pm 1.4(\mathrm{syst.}))\,\mathrm{MeV}/c^2$, and a larger width $\Gamma_{K_1(1270)} = (119.5 \pm 5.2(\mathrm{stat.}) \pm 6.7(\mathrm{syst.}))\,\mathrm{MeV}/c^2$ compared to ACCMOR measurement. Note that since the total width depends on the contributions of the decay modes, these results are correlated to the fact that in Belle analysis, the "scalar + π" channel is almost absent, increasing the proportion of $K^*\pi$ and $K\rho$. However, the floated width is much smaller than $200\,\mathrm{MeV}/c^2$ as would be expected from the calculation using the

K-matrix formalism.

As a conclusion, one should keep in mind that the measured values of the $K_1(1270)$ width are smaller than the expected one obtained by theory, and should therefore consider, if possible, not to fix this parameter in analyses involving $K_1(1270) \to K\pi\pi$ decays.

Part II

BABAR and PEP-II

Overview

As previously discussed in Chapter 1, *CP* violation phenomena lead to particularly large asymmetries in the case of the B^0 mesons (composed of a bottom antiquark and a light d quark) decaying to states common to both B^0 and $\overline{B}^0$. In addition, for these mesons, the period of these particle-antiparticle oscillations was comparable to their lifetimes [16, 76], which mean that the interfering amplitudes are of the same order, and make the B system the best choice to study *CP* violation. However, the same phenomenon also impeded the experimental determination of the flavour (i.e. B^0 or $\overline{B}^0$) of the particle in decay, a *sine qua non* to compare the decay rates of both flavours. The proposed solution involved using pairs of B^0-$\overline{B}^0$ mesons produced in the quantum mechanical state of entanglement, one of them decaying to the channel of interest, and the other one to a final state that uniquely determines its flavour (a *flavour eigenstate*). The entanglement implies that, at the precise moment of the decay of the latter, the former meson would be its antiparticle, and that its flavour at decay time could be determined as well by evolving its known state in time (*tagging*). Thus, measuring *CP* asymmetries between the B mesons requires simultaneous reconstruction of the decay products of both B mesons and measurement of the time difference between their decays (see Figure 2.3 and Section 7.1.1 for more details).

The lifetime of the B mesons (~ 1.5 ps) make impractical any such measurements using symmetric e^+e^- colliders, since the small distances travelled in the detector would be washed out by the resolution of the instrument. Therefore, Pier Oddone had the idea of building an *asymmetric* e^+e^- collider, in which the centre-of-mass, and hence any particles produced, would move in the laboratory frame with a relativistic boost large enough to extend those distances into the measurable range [77]. The *BABAR* and Belle experiments were built based on this idea, associated to e^+e^- asymmetric colliders (PEP-II and KEKB, respectively) with the centre-of-mass energy tuned to the $\Upsilon(4S)$ resonance, which decays almost uniquely to $B^0_d\bar{B}^0_d$ and $B^+_uB^-_u$ pairs with equal probabilities. The advantages over a hadronic collider are substantial, a number of factors contributing to the much cleaner environment and hence to better event reconstruction: the low multiplicity of the events (with an average of 11 charged tracks per event), the relatively large signal-to-background ratio ($\sigma_{B\bar{B}}/\sigma_{\text{total hadronic}} \simeq 0.28$), the possibility of reconstructing photons and π^0 and a physics rate low enough (~ 10 Hz) for the detector not be overwhelmed by data during its dead time [78]. Furthermore, the precise knowledge of the kinematical state of the e^+e^- system allows for a complete reconstruction of the event and naturally provides us with background discriminating variables (Section 5.3). In addition, running at the $\Upsilon(4S)$ resonance and using the advantage of quantum entanglement, greatly helps in the tagging process by forcing the two particles to remain

a particle-antiparticle pair for as long as both exist. In a hadronic environment, such a statement is no longer true and the tagging efficiencies fall dramatically for two reasons: first, the higher track multiplicity is an obstacle to finding the particle whose charge uniquely tags the flavour of $B_{\rm tag}$; second, determining the flavour of $B_{\rm rec}$ requires establishing the flavour of $B_{\rm tag}$, evolving it back to the production point, and then forward to the $B_{\rm rec}$ decay vertex, thus depending strongly on the accuracy in the inference of the production point.

These properties, together with a large data sample consisting of $\sim 10^8$ $B\overline{B}$ pairs, are the necessary ingredients for *BABAR*'s main physics goals: precisely measuring the *CP* violating time-dependent asymmetries and constraining the CKM matrix elements. Secondary physics interests are rare B decays, such as the subject of this thesis, charm and τ physics, and QCD and two-photon physics. Other quantum electrodynamic processes, such as muon pair production, are mostly filtered due to their large cross-sections, some of them being used for calibration and luminosity measurement purposes. Specifically, the integrated luminosity is calculated to great accuracy by examining the accumulated samples of $e^+e^- \to e^+e^-(\gamma)$, $e^+e^- \to \mu^+\mu^-(\gamma)$ and $e^+e^- \to \gamma\gamma$, processes for which the cross-sections are extremely well understood thanks to QED.

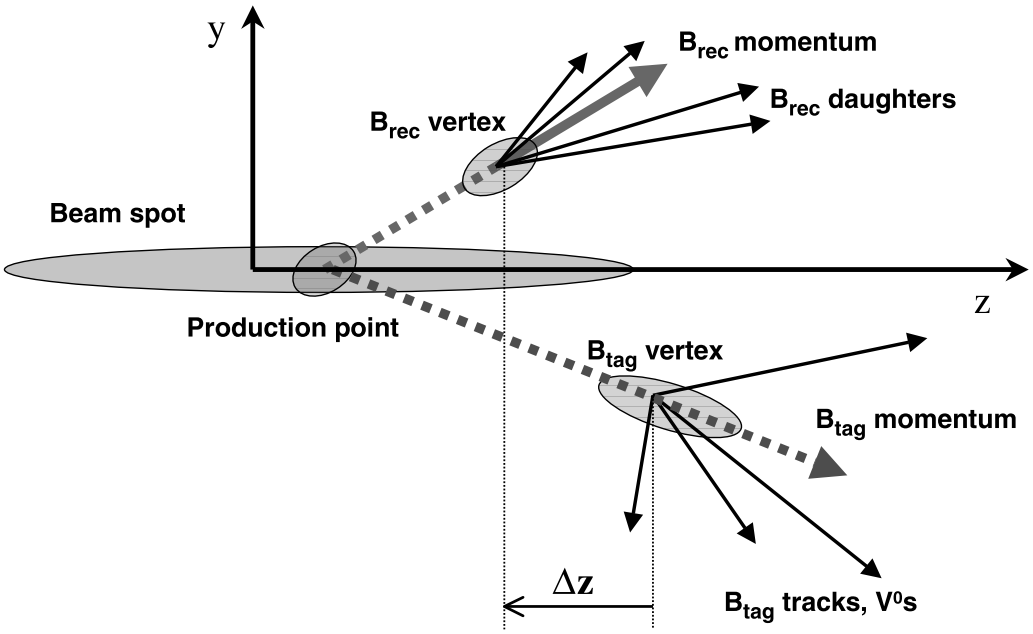

Figure 2.3: In many processes of interest, $B_{\rm rec}$ decays to a channel that can be reached by both a B^0 or a $\overline{B}^0$. Evaluation of the *CP* violating asymmetries requires knowing the flavour of the B meson at its decay time. This is achieved by identifying the decay channel of the other B meson, $B_{\rm tag}$, often only partially reconstructed. If B_{tag} decays into a state that uniquely determines the flavour of its parent particle, e.g. $B^0 \to D^* + X$, then the knowledge of the difference between the decay times of both B's allows us to infer the flavour of B_{rec}. The time elapsed between the two decays can be calculated from the distance Δz measured between the two B decay vertices along the beam direction, z.

The constraints posed to the accelerator and detector configurations by the difficulties of time-dependent analyses as well as the high luminosities needed to achieve the physic goals are discussed in Chapters 3 and 4, respectively.

Chapter 3

An asymmetric e^+e^- collider: PEP-II

Contents

For the time-dependent *CP* violating asymmetries arising in neutral B mesons to be measured, an asymmetric collider is required. The boost of the B mesons in the laboratory frame allows the distance between the decay vertices of the two mesons to be measured, from which the time between the decays of the two particles can be inferred.

The asymmetry is achieved by injecting into the PEP-II storage rings 9.0 GeV e^- and 3.1 GeV e^+ beams which, upon collision, result in a boost of $\beta\gamma = 0.56$ along the e^- beam direction in the laboratory frame for the centre-of-mass of the particles produced. The centre-of-mass energy is tuned to the $\Upsilon(4S)$ mass, 10.58 GeV, for 90% of the running time, the remaining 10% being set 40 MeV below the resonance peak. The first sample, known as the *On-Peak* sample, contains the $B\overline{B}$ events, whereas the second one, called the *Off-Peak* sample, is recorded for background characterization purposes. The light quark processes $e^+e^- \to q\overline{q}$, $q = u, d, s, c$ which constitute the most prominent background to the $B\overline{B}$ events are the only hadronic reactions allowed below the $\Upsilon(4S)$ threshold.

The injection is carried out using the two mile long Stanford Linear Accelerator, which diverts a fraction of the accelerated electrons to produce positrons in collision with a high-Z stationary target. These are then directed back to the linear accelerator to be brought to their nominal energy before entering the storage rings. Once there, the electrons and the positrons, which circulate in bunches along physically separated rings, are collided in one Interaction Region, in which the *BABAR* detector is located.

3.1 The *LINAC* and the storage ring

PEP-II is made of two storage rings of 2.2 Km of circumference in which the collision takes place. Fig 3.1 shows an schematic view of the PEP-II collider and the LINAC accelerator. The LINAC (LINear ACcelerator) constitutes the PEP-II injection system. It is 3 Km long and accelerates the particles up to their nominal energies. The LINAC is a facility also used for other purposes, being able to produce beams with energies up to 50 GeV. The electrons and positrons used by PEP-II only use part of the accelerator capabilities. These electrons and positrons produced in the LINAC are accelerated until their nominal energies, and then injected to PEP-II storage rings placed at the end of the linear accelerator. Once there, the electrons and positrons, which circulate in bunches in separate rings, are made to collide at the IP, around which the *BABAR* detector is located.

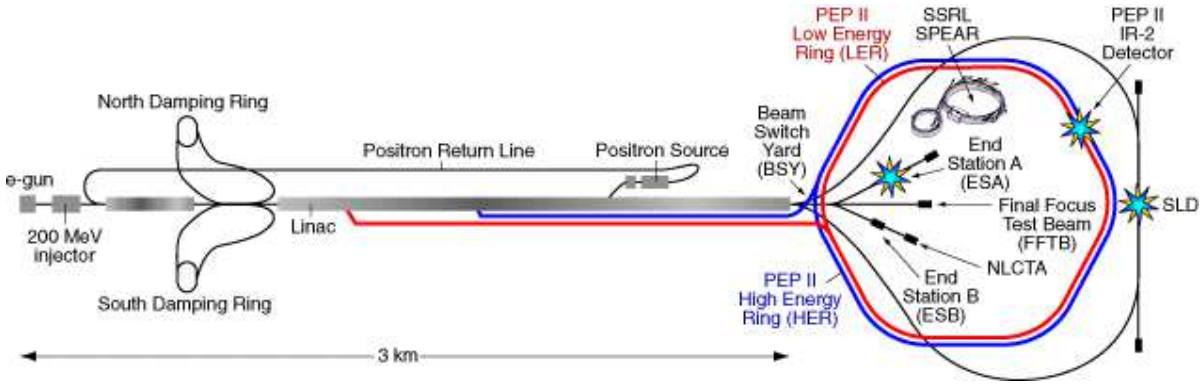

Figure 3.1: The linear accelerator at SLAC and the PEP-II collider.

The High Energy Ring (HER) produces electron beams with 9.0 GeV of energy, while the Low Energy Ring (LER), delivers positrons with an energy of 3.1 GeV, which upon collision, result in a boost of $\beta\gamma \sim 0.56$ along the e^- beam direction in the laboratory frame. This boost allows the measurement of the $B_{\rm rec}/B_{\rm tag}$ mesons time difference (see Sec. 7.1.2). The parameters for these storage rings are summarized on Tab. 3.1.

3.2 The interaction region

The Interaction Region is heavily instrumented with magnets that focus the beams before the collision, directs them so that there is no crossing angle between them, and finally separates them before a given bunch of particles collides with a second bunch from the other beam (see Figure 3.2). The quadrupole magnets labelled QD and QF, situated outside the *BABAR* detector, focus the high and low energy beams. The dipoles labelled B1 are responsible for bringing the beams together and separating them immediately afterwards. This is the reason why they need to be close to the interaction point; in fact, within the detector volume.

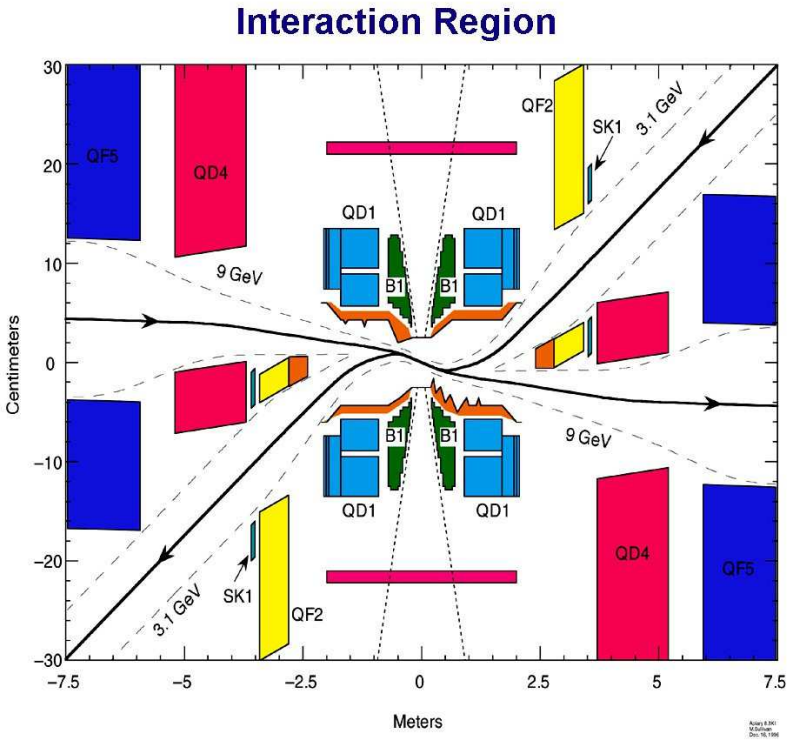

Figure 3.2: Schematic view of the Interaction Region. Observe the strong bending needed to make the two beams collide head-on, that results in the most prominent machine background: synchroton radiation.

3.3 Machine backgrounds

Accelerator backgrounds may degrade the detector performance and must thus be prevented, since they may cause sustained radiation damage and prolonged dead times where the detector subsystems readout is inactive. The main origin of these backgrounds is the synchrotron radiation around the IP, followed by the beam particles interaction with the residual gas in the storage rings and the electromagnetic showers generated in beam-beam collisions. A serious background can find it's origin in synchrotron radiation in the nearby dipoles, the $Q1$ quadrupoles and $B1$ dipoles. Beam orbits, vacuum-pipe apertures and synchrotron radiations masks have been conceived in a way that leads the majority of these photons to a distant dump and before they can enter the *BABAR* acceptance the remnants are submitted to various scatters.

Eventually beam particles may escape the acceptance of the ring and hit the beam pipe, thus causing electromagnetic showers that disseminate on the detector. Such events are caused by beam-gas bremsstrahlung and Coulomb scattering of residual gas molecules. To avoid this there are vacuum pumps that ensure the residual pressure to a minimal level and collimators that remove beam tails generated by betatron oscillations and beam-gas interactions. Aside from the DIRC, the main cause of radiation damage in the SVT and the major

source of background in all detectors systems is beam-gas scattering. Radiative Bhabha scattering leads to low energy electrons or positrons that hit aperture limitations within a few meters of the IP and spray *BABAR* with electromagnetic showers. This background is proportional to the instantaneous luminosity, hence being the prevailing background in the DIRC.

3.4 The injection system

In 1999, when *BABAR* started, the electrons and positrons were injected in the storage rings in bunches of 109 particles with a frequency between $(1 - 30)$Hz and a mean time spacing of 4 ns. In a normal operation the injection was made every $(40 - 50)$ min. These periods of injection (of ~ 5 min) generated intense backgrounds in *BABAR*. Also, the injection induced dead time, as it was necessary to ramp down the high voltages of detector systems for protection purposes. The result was that data taking was periodically suspended. Moreover, not only the recorded luminosity was not optimal, but the beam currents continuously decreased. From 2004 a system of continuous injection was settled, the trickle injection, where a new injection is just performed if the instantaneous luminosity falls below a pre-established threshold, and can be made continuously at a low rate. At first this was obtained for the LER, with a gain in luminosity of 35% and afterwards applied in the HER, resulting in an extra gain of 12%. The main disagreement of this new method consists in it's difficulty to limit the backgrounds created by the injection. But it was demonstrated through various tests that these backgrounds could be kept to a manageable level and thus the trickle injection has since it's implementation become the default operation.

3.5 Performance

Within it's first year of running, PEP-II achieved it's design luminosity and accelerator parameter objectives, having since never stopped improving them. Table 3.1 shows the design objectives and the latest records achieved. The machine stopped running at the $\Upsilon(4S)$ peak in September 2007, having recorded a total of $432.9\,\mathrm{fb}^{-1}$ integrated luminosity. After that, the data taking was performed at the $\Upsilon(2S)$ and $\Upsilon(3S)$ resonances (which are located at 10.023 GeV and 10.355 GeV [24], respectively), finishing with integrated luminosities of $20.3\,\mathrm{fb}^{-1}$ and $14.5\,\mathrm{fb}^{-1}$, respectively. The best instantaneous luminosity reached a value of $1.2 \times 10^{34}\,\mathrm{cm}^{-2}s^{-1}$.

Table 3.1: PEP-II design parameters, and best achieved.

Parameter	Design	Best achieved
HER current (A)	0.75	2.07
LER current (A)	2.14	3.21
Luminosity ($10^{33}\,\mathrm{cm}^{-2}s^{-1}$)	3.0	12.07

Chapter 4

The *BABAR* Detector

Contents

CP-violation study as described at the beginning of this chapter lead to an asymmetric collider, and therefore, since a uniform acceptance in the centre-of-mass system is preferred, to an asymmetric detector as well. The main physics goals as well as physics under study place additional stringent constraints on the detector. In this section, we state the main resulting requirements on the *BABAR* detector, describing each subsystem and its performance in the next sections.

The detector must comply with the following requirements:

- A high reconstruction efficiency for charged tracks and photons of momenta above 60 MeV/c and 20 MeV/c, respectively.
- Good photon energy and angular resolutions, in order to reconstruct and discriminate π^0 and η particles and for radiative decays.
- Very good momentum resolution of charged particles in the momentum range 60 MeV/c to 4 GeV/c for signal-background separation.

- Excellent vertex resolution, to measure the typical distances associated to a time-dependent analysis, $\beta\gamma c\tau_{B^0} \lesssim 250\mu m$.
- Excellent hadron and lepton identification capabilities, as these are crucial to the tagging procedure. In particular, electrons and muons should be reliably identified, and hadrons such as p, K, π should be distinguished.
- Dead times as short as possible, so that higher luminosities can be handled.
- Components resisting to radiation, in order for the efficiencies of the subsystems to operate reliably under high background conditions over the lifetime of the experiment.

The final design of the detector, installed around the interaction point (IP) of the PEP-II collider, was built to achieve these goals. It is a classic almost 4π acceptance detector, which consists of five subsystems: the silicon vertex tracker (SVT), used to measure angles and positions of charged particles coming from the displaced vertices of the B mesons and other particles with similar lifetimes; the drift chamber (DCH), whose purpose is the measurement of momentum of charged particles; the detector of internally reflected Čerenkov light (DIRC), whose input for particle identification is essential (in particular K/π separation); the electromagnetic calorimeter (EMC) made of CsI crystals, that allows to measure the energies of photons and electrons; and the flux return (IFR), which serves as muon detector and as a primitive hadronic calorimeter. The three subsystems are surrounded by a superconducting solenoid, which generate in a uniform axial 1.5 T magnetic field necessary to measure the transverse momentum from the curvature of the tracks. Figure 4.1 shows the whole detector, specifying each subsystem.

To maximize the geometrical acceptance for the boosted $\Upsilon(4S)$ decays, the detector is shifted relative to the IP by $37cm$ in the direction of the LER. The convention adopted in *BABAR* for the coordinate system follows a standard spherical-polar coordinate system centred on the IP, the z axis being parallel to the e^- beam direction, and θ and ϕ being the usual polar and azimuthal angles, with a coverage extends to 350 mrad and 400 mrad in the forward and backward directions, respectively. The cartesian axes form a right-handed system with the x axis pointing outwards from the PEP-II ring and the y axis pointing upwards.

4.1 The Silicon Vertex Tracker (SVT)

Physics requirements

The SVT [79] is located just outside the beam pipe, at around 3 cm from its centre, and has been designed to provide a precise reconstruction of the decay vertices near the IP. This is critical for the measurement of the time-difference between B and $\overline{B}$ decays, and that of the flight distances of D mesons and τ leptons. To achieve the necessary resolution in Δt, a resolution of 80 μm must be attained in z for single-vertex measurements. In the xy plane, distances of $\sim 100\,\mu m$ must be resolved for the correct reconstruction of secondary vertices such as those from D and τ decays.

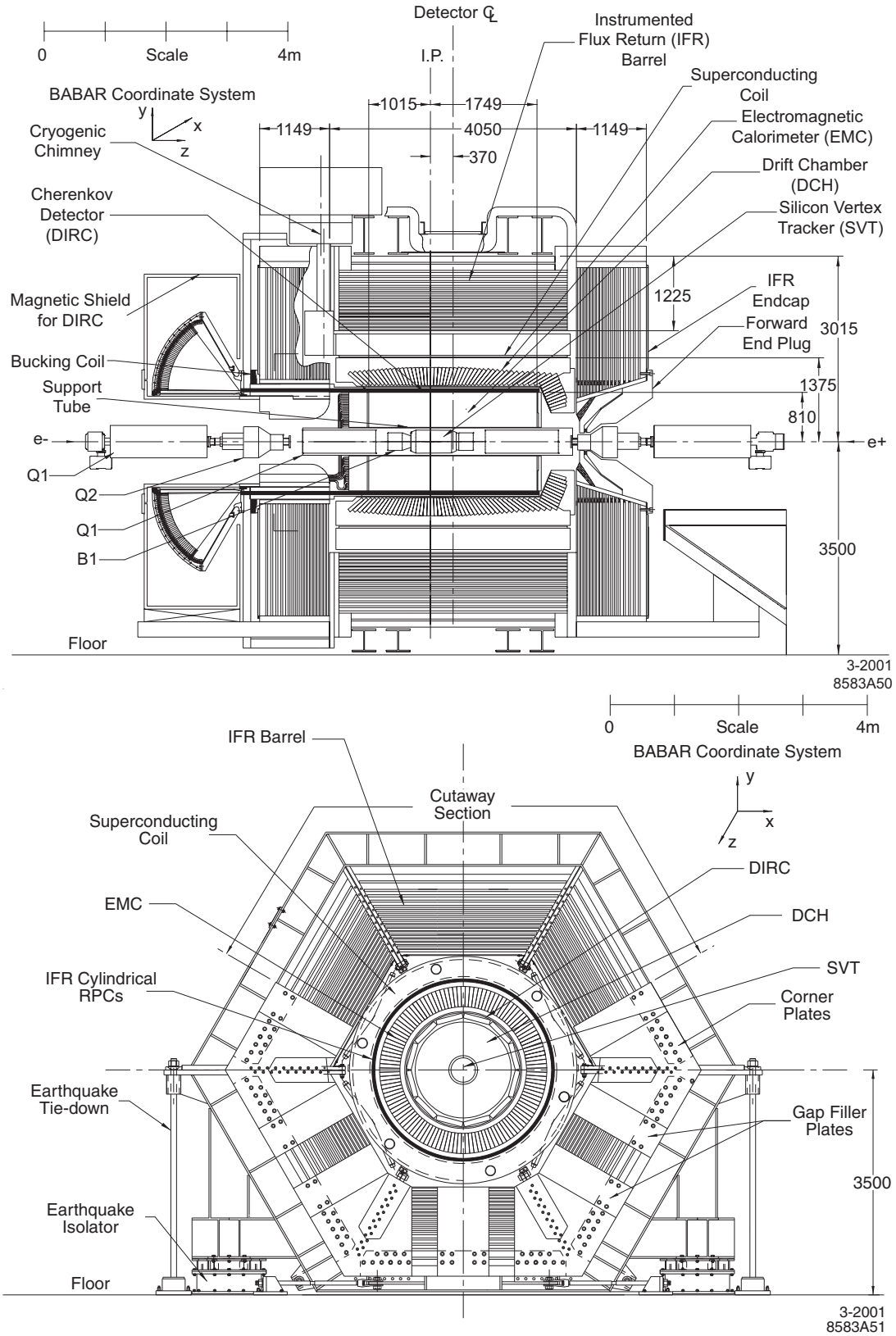

Figure 4.1: Lateral (top) and front (bottom) view of the detector, with all the subsystems clearly indicated.

The SVT is also provides precise reconstruction of trajectories of charged particles and tracking of low momentum particles, since for $p_t < 120\,\mathrm{MeV}/c$ they are unlikely to reach the drift chamber or produce enough hits in it. This is fundamental for the reconstruction of the D^* decay into a low momentum pion and a D meson, which is important in itself and for tagging purposes.

Finally, the SVT also plays a role in particle identification through its own measurement of ionization energy loss $\mathrm{d}E/\mathrm{d}x$, and by giving the best determination of the polar angle of high momentum tracks, which is a necessary input to fully exploit the DIRC.

Design

Although maximum coverage is desirable, the B1 dipoles situated inside the detector (see Fig. 3.2) and some support structures limit the SVT acceptance to the polar angles $20.1° < \theta < 150.2°$, which still comprises 90% of the solid angle in the centre-of-mass system. Another constraint on the SVT design is that it must be able to withstand the irradiation associated with being so close to the beam pipe, while still keeping the amount of material as low as possible to avoid multiple Coulomb scattering.

The SVT consists of five concentric layers ($300\,\mu$m thickness each) of double-sided silicon strips (see Fig. 4.2), where the strips on opposite sides of each sensor are mutually orthogonal, thus providing the two coordinates at the impact location in ϕ and z, respectively, for each hit.

The first three layers are composed of 6 modules each, slightly tilted to provide complete coverage. Layers 4 and 5, having 16 and 18 modules respectively, produce the overlap between neighboring strips, in order to avoid dead zones in ϕ, by alternating the radii at which they are located. The three inner layers, having each 6 modules, give the position and angle information for the measurement of the decay vertex position. In contrast the strips in the two outermost layers are at a much larger radii and arch-shaped in order to reduce the material a track goes through while providing complete coverage. The two innermost layers are particularly important in determining the polar angle of a track, while the role of the two outermost is to help in matching tracks to those found by the DCH. The third layer provides extra information for low momentum tracks that may not reach the drift chamber. Each of the five layers module contains from 4 to 8 silicon detectors and has its own readout electronics. In total, the SVT has 340 silicon detectors covering a area of $0.96m^2$, with a total of 150,000 readout channels.

To be able to meet the resolution goals, the local and global alignment of the SVT is crucial. On a daily base and each time the SVT configuration changes, calibrations are performed in absence of circulating beams. The local alignment, of the different modules relative to each other, is only necessary after accesses to the detector. It is carried out by fitting tracks from cosmic rays and $e^+e^- \to \mu^+\mu^-$ events. Global alignment, of the SVT with respect to the rest of the detector, is done at the beginning of each run, by minimizing the differences between the SVT and DCH tracks in a small sample of events. Due to the very small distance of the SVT components with respect to the beam pipe, this detector is significantly affected by radiation. In order to protect the detector, designed to resist to a

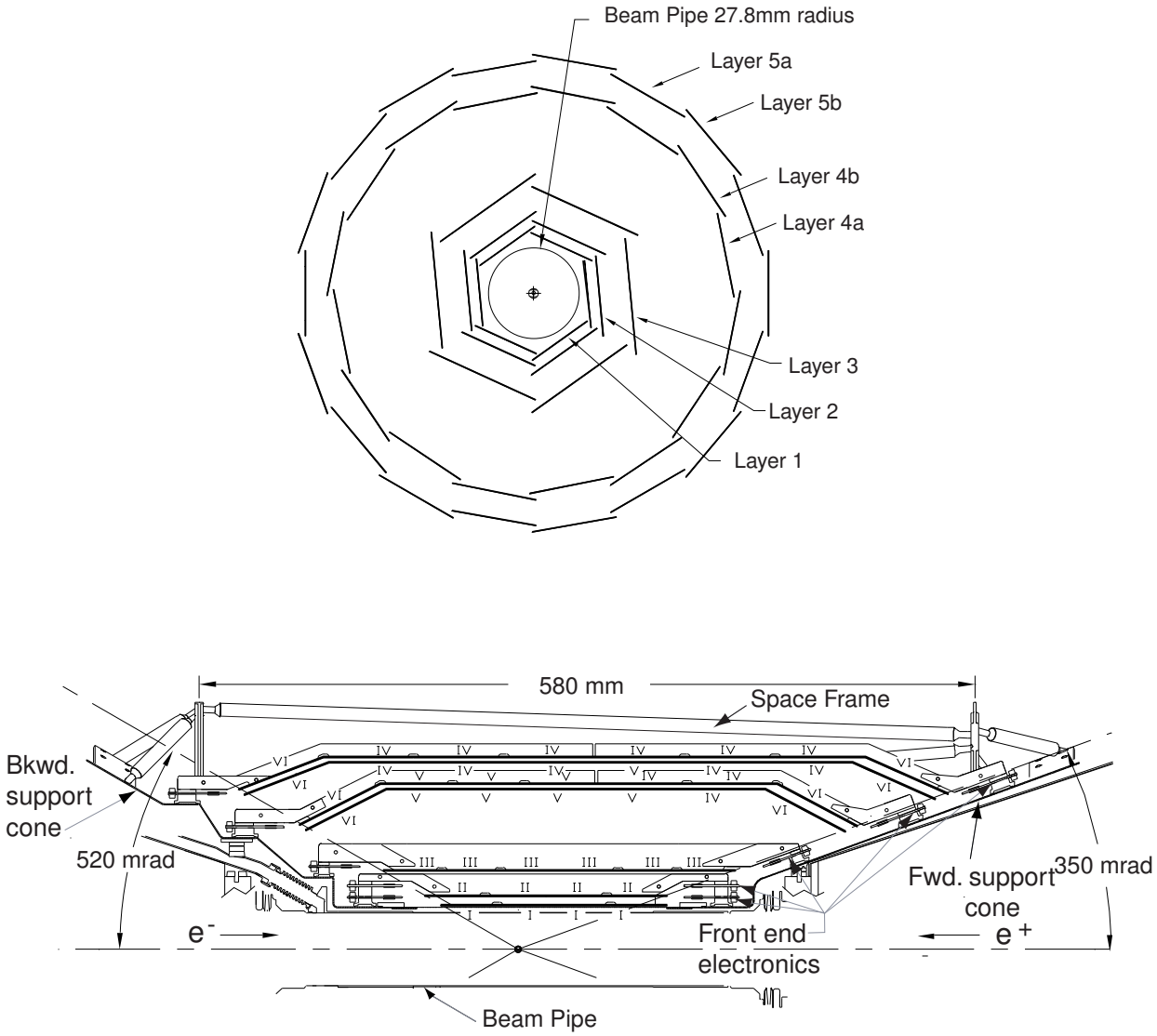

Figure 4.2: End (top) and side (bottom) views of the Silicon Vertex Tracker, in which the five layer structure and the arch shape of the outer layers can be appreciated.

maximum of 5Mrad of integrated radiation dose, from high backgrounds, a customized online protection system, called SVTRAD was used. It permits *BABAR* to stop automatically the beams when the instantaneous or integrated radiation doses go above predefined thresholds.

Performance

The average track efficiency reconstruction of the SVT as measured in data on $e^+e^- \to \mu^+\mu^-$ events is 97%, after excluding the defective strips. The efficiency of low momentum tracking in the SVT enables to perform demanding physics analyses such as *BABAR*'s result on $D^0 - \overline{D}^0$ mixing [19], in which extraordinarily large samples of D^* mesons decaying to a charged pion and a D meson are needed in order to tag the flavour of the neutral meson and detect the minute oscillation.

The spatial resolution of the SVT hits can be evaluated by fitting high momentum tracks without the hit in the layer under inspection and comparing the hit with the intersection of the fitted track. The residuals are divided by the uncertainty on the track determination to get the resolution. This is found to be better than $40\mu m$, implying a vertex resolution better than $70\mu m$. The resolution on the ionization energy loss $\mathrm{d}E/\mathrm{d}x$ measurements is approximately 14%. A 2σ separation between kaons and pions can be achieved up to a momentum of 500 MeV/c, and between kaons and protons below 1 GeV/c.

4.2 The Drift Chamber (DCH)

Physics requirements

The drift chamber [80, 81] is the main tracking system in the *BABAR* detector. The principal purpose of the DCH is the efficient detection of charged particles and the measurement of their angles and momenta (over a wide range of $0.12 < p_t < 5.0\,\mathrm{GeV}/c$) with high precision. This allows, with momentum and spatial resolution of $\sigma_{p_t}/p_t < 0.3\%$ and $140\mu m$, respectively, to reconstruct exclusive B and D meson decays with low background. It provides one of the main inputs to the Level-1 trigger and plays a key role in the extrapolation of tracks into the DIRC, EMC and IFR. Thus, the solid angle coverage must be as complete as possible whilst minimizing the amount of material that the particles have to traverse.

The reconstruction of decay and interaction vertices of long-lived particles outside the SVT volume, like the K^0_S (present in the final state of the decay channel studied in this thesis, and in many other channels studied in time-dependent analyses), relies solely on the DCH.

The vertexing of long-lived particles outside the SVT volume, such as K^0_S particles present in the golden mode and in one of the channel studied in this thesis, as well as in many other final states studied with time-dependent analyses, relies solely on the DCH. It requires the drift chamber to measure longitudinal positions to better than 1 mm.

Finally, the DCH also bears the responsibility for particle identification using the measurement of the ionization energy loss $\mathrm{d}E/\mathrm{d}x$, for which the DIRC is not effective, and for tracks that fall outside the acceptance of the latter in the forward region. The achieved

design resolution of about 7% allows to separate kaons from pions up to momentum of 700 MeV/c.

Design

The DCH is a 276 cm long cylinder located immediately outside the SVT, with inner and outer radii of 23.6 and 80.9 cm, respectively. Figure 4.3 shows a longitudinal section of the DCH, where the middle of the chamber in z is located asymmetrically with respect the IP to increase the centre-of-mass acceptance, being offset by ~ 370 mm in the HER direction. It is bounded in the radial direction by the support tube (the DIRC) at its inner (outer) radius. It is formed from 40 layers of hexagonal drift cells (for a total of 7104 cells). The cells consist of a sense wire in the centre, with a diameter of $20\mu m$ and kept at 1930 V, surrounded by 6 field wires, of 80 and $120\mu m$ diameters, that are grounded. The layers are grouped by four into ten superlayers, with different stereo angles. The stereo angle is defined as the angle between the cells wires and the z-axis, in a revolution plane around the z-axis. The stereo angles of the superlayers alternate between axial (null stereo angle: A) and stereo (non-null stereo angle: U,V) pairs, in the order AUVAUVAUVA. A mixture of helium and isobutane in a ratio 4:1 fills the chamber, with additional small amounts of water vapor (0.3%) to extend the lifetime of the device. Altogether, the whole volume of gas and the wires represent only 0.28% of a radiation length for tracks with normal incidence.

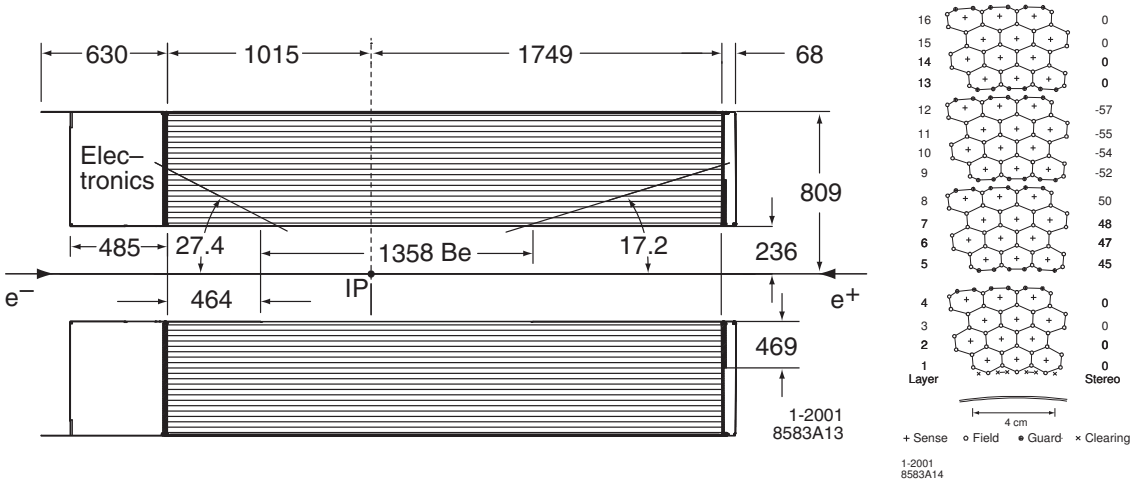

Figure 4.3: Side view of the drift chamber (left) and cell layout in first four superlayers (right). The angle in mrad of the stereo layers with the z axis is written on the right of each layer.

Performance

Some of the molecules in the gas are ionized by the charged particles traversing the chamber. The charges then start drifting due to the electric field, which is locally quasi-cylindrical around each sense wire. Collisions with further gas molecules result in a gain of $\sim 5 \times 10^4$.

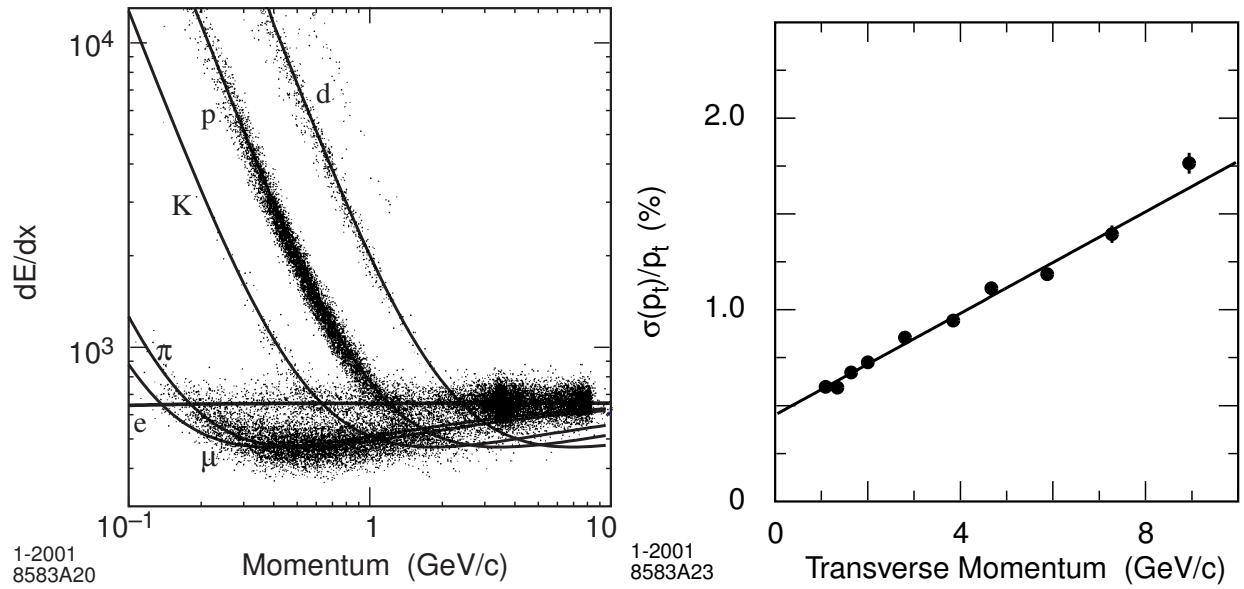

Figure 4.4: On the left, DCH dE/dx measurements and the Bethe-Bloch predictions [82]. On the right, the resolution on p_t as calculated from cosmic ray events that fall within the acceptance of the SVT and the DCH [82].

The time taken for the charge to arrive at the wire translates into a distance from the wire. That drift time, however, requires cell-by-cell calibration, which is performed by fitting high momentum $\mu^+\mu^-$ and e^+e^- tracks while omitting the cell being calibrated. The total charge deposited, which is used to calculate dE/dx, also needs calibration.

The sample of tracks that goes through the DCH and the SVT, the two tracking devices, allows the estimation of the track reconstruction efficiency. The proportion of tracks reconstructed in the DCH over those observed in the SVT is of $(96 \pm 1)\%$, once the fake SVT tracks have been adjusted.

The dE/dx value for a given track is calculated as the truncated mean of the 80% lowest measurements dE/dx measurements for the track, since these follow a Landau distribution whose mean diverges. Figure 4.4 shows the dE/dx measurements in the DCH as a function of the momentum, and the corresponding Bethe-Bloch expectations [24]. A good separation between pions and kaons is achieved below 0.7 GeV/c momentum, above which the DIRC has the main responsibility for particle identification. This is also demonstrated in practice in *BABAR*'s last measurement of $B^0 \to h^+h^-$ (where $h = K, \pi$) [83], where the DCH is used to provide particle identification of forward tracks falling outside the acceptance of the DIRC[1]. The dE/dx resolution on electrons is 7.5%, almost at the design value (7%). The resolution on p_t is, as shown in Fig.4.4, very close to the design value too.

[1]Unlike in this example, most analyses in *BABAR* which require particle identification do not use the information from each subdetector separately, and instead draw on a combination of information from the DIRC and the DCH and SVT dE/dx measurements, as described in Sec. 5.2.3.

4.3 The Detector of Internally Reflected Čerenkov Light (DIRC)

Physics requirements

As the *BABAR*physics program consists of measuring *CP* violating asymmetries in a variety of channels, identifying particles is crucial. In neutral modes, it is necessary to define the flavour of the other B in the event in order to measure these asymmetries. This definition is obtained by correlating the charges of certain particles with the flavour of the parent meson. Since these correlations are conditioned by the particle species, these must be identified (see Sec. 7.1.1). Also, as similar channels, like $B^0 \to K^+\pi^-$ and $B^0 \to \pi^+\pi^-$, have different asymmetries it is essential to avoid contamination in the isolation of final states.

More specifically, above 700 MeV/c, the drift chamber is no longer able to distinguish kaons from pions, which the DIRC aims to separate at 4σ significance up to a momentum of 4.2 GeV/c. For the muons, the DIRC must complement the IFR, whose effectiveness falls for momenta below 750 MeV/c.

Finally, the DIRC must be small, not only due to it's location - between the drift chamber and inside the calorimeter - but also in order to minimize the size of this latter one (as the calorimeter is the most expensive part of the detector), amounting to only a fraction of the radiation length (see below).

Design

When a particle travels faster than the speed of light in the medium that surrounds it, $v/c = \beta \geq 1/n$, it emits Čerenkov photons at an angle $\cos\theta_C = 1/n\beta$ with the direction of the particle. Hence, provided that its trajectory is known accurately enough, a measurement of the direction of these photons establishes the speed of the particle. Given the space constraints sketched above, the instrumentation to detect them must lie outside the main body of the detector. Internal reflection on a plane surface is used to preserve the angle of these photons while directing them towards the photomultiplier tubes (see Fig. 4.5). Forward moving photons are reflected in a mirror, allowing the DIRC instrumentation to occupy only the less populated backward end of the detector.

The photons are confined by bars of quartz ($n = 1.474$) of 17mm thick and 35mm wide but reaching 4.9m long. In a normally incident particle, they totalize 17% of a radiation length.In the backward end of the detector, the photons go through a wedge-shaped quartz piece and then into a water filled expansion region, known as the standoff box, after which they meet the photomultiplier tubes. The role of the wedge is to reflect photons arriving at large angles, thereby reducing the area of the standoff box that needs to be instrumented at the cost of introducing ambiguities in the angle.

There are 10752 photomultiplier tubes, surrounded by "light catchers" that amplify the detection area. Finally, the standoff box is magnetically shielded to avoid disturbances in the tubes.

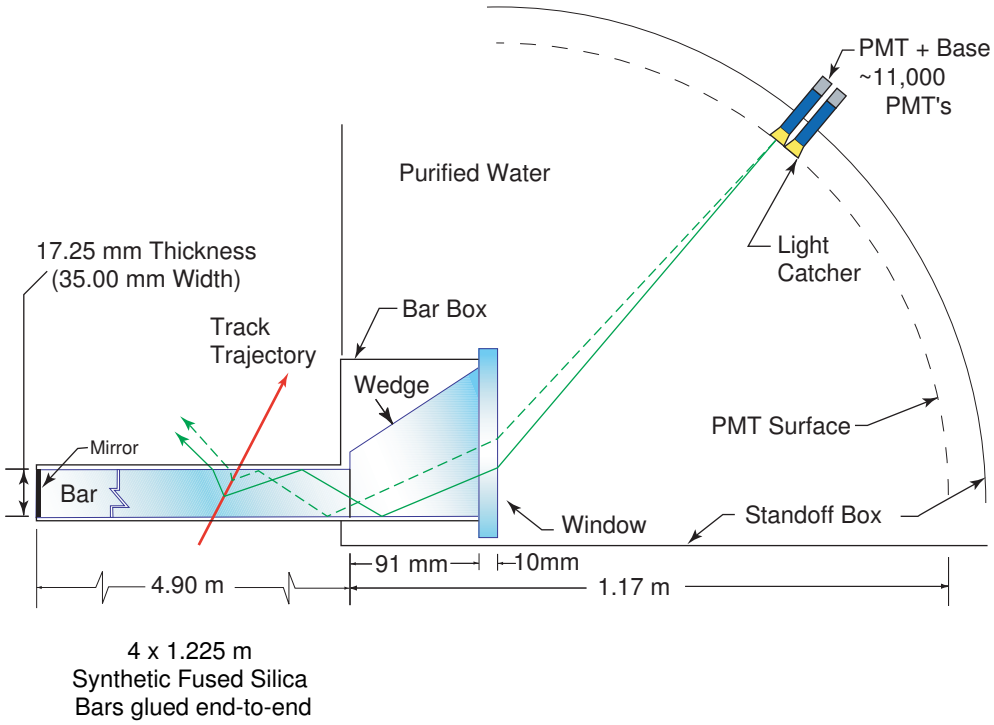

Figure 4.5: Diagram illustrating the operating principles of the DIRC.

Performance

The angle and time resolution can be calibrated from dimuon events. The Čerenkov angle resolution for a track turns out to be 2.5 mrad, giving over 4σ separation at 3 GeV/c (see Fig. 4.6). Figure 4.6 also shows the mass peak of the decay $\overline{D}^0 \to K^+\pi^-$ with and without the kaon/pion separation provided by the DIRC.

4.4 The Electromagnetic Calorimeter (EMC)

Physics requirements

A number of *CP* eigenstates within *BABAR*'s physics goals contain π^0's in the final state. Many others involve η particles or photons directly, such as $b \to s\gamma$, in which the spectrum is quite hard. Some QED processes, such as $e^+e^- \to e^+e^-\gamma$ or $e^+e^- \to \gamma\gamma$ are also important for calibration or luminosity measurement purposes. Therefore, *BABAR* must be able to reconstruct photons over a wide range of energies, from 20 MeV up to 4 GeV.

The EMC is the only system being able to supply precise information on particle identification and must thus identify electrons accurately, as they are relevant in flavour tagging and semi-leptonic B decays.

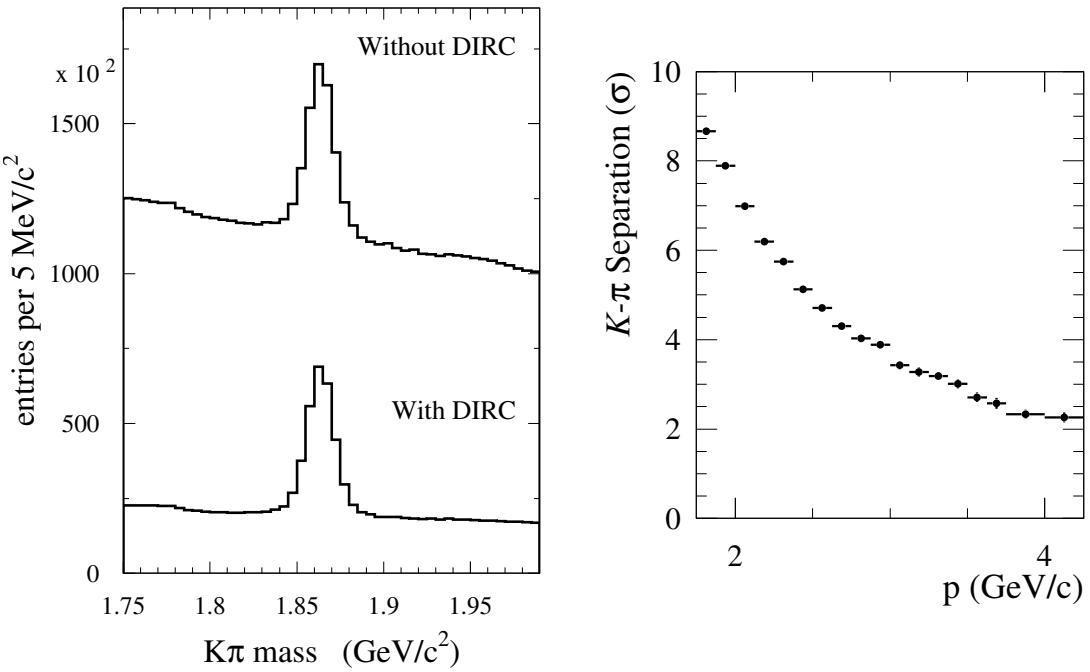

Figure 4.6: Plots illustrating the DIRC capabilities for kaon-pion separation [82]. On the left, the reconstructed $\overline{D}^0$ mass with and without the PID information provided by the DIRC. On the right, the separation of kaons and pions achieved by the DIRC in standard deviations.

Design

The EMC is formed from 6580 Thallium doped Caesium Iodide crystals arranged in a barrel and a forward endcap . The material was chosen due to its high light yield and small Molière radius, which imply good energy and angular resolutions, respectively. The crystal size varies from 16 radiation lengths in the backward direction to 17.5 radiation lengths in the forward endcap, since these receive impacts from the more energetic Lorentz-boosted particles. The crystals are tilted in such a way that they face the interaction point. Their exposed area is $\sim 5\,\mathrm{cm}^2$ (c.f. their Molière radius, 3.8 cm), so a typical electromagnetic shower will spread over several crystals. Figure 4.7 shows a schematic view of the subdetector.

Performance

It is necessary to establish the relation between the light yield and the energy deposited in the crystal as well as the between the cluster energy and the total energy of the incident particle, in order to calibrate the electromagnetic calorimeter. From one crystal to another there is a variation of the light yield dependence on the energy, that radiation damage may change over time. It is calibrated for low energies using 6.13 MeV photons from a radioactive source, and in the high energy range by using Bhabha scattering events, for which the polar angle precisely determines the energy of the particle. The cluster energy must be calibrated due to crystal leakage and absorption of energy by the material at the front of the crystals or between them. This is applied during the offline reconstruction and is derived from samples

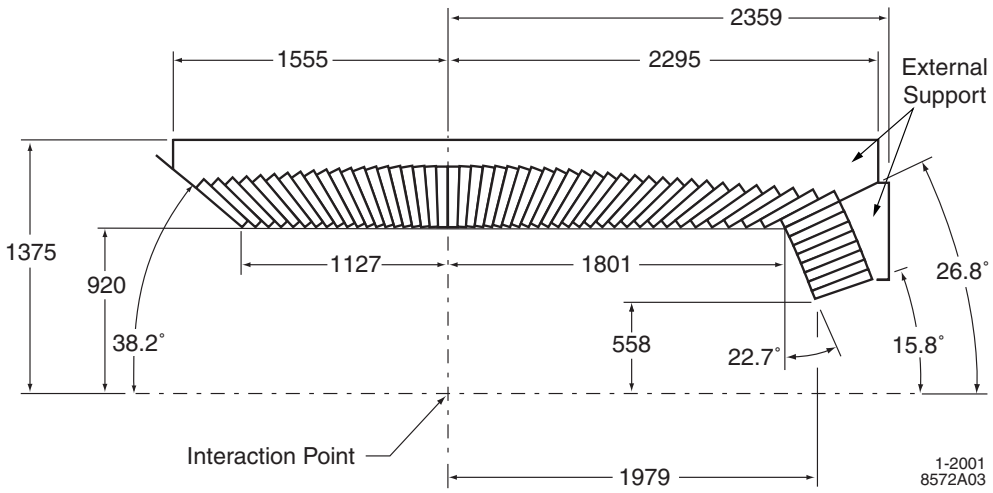

Figure 4.7: Side view on the Electromagnetic Calorimeter.

of π^0 and η mesons.

The photon energy and angular resolutions of the EMC are also extracted from the calibrations, and are found to be parameterized, respectively (see Fig. 4.8), by

$$\frac{\sigma_E}{E} = \frac{a}{(E(\,\mathrm{GeV}))^{1/4}} \oplus b \tag{4.1}$$

$$\sigma_\theta = \sigma_\phi = \frac{c}{E(\,\mathrm{GeV})} + d\,, \tag{4.2}$$

where the first sum is in quadrature, and $a = (2.3 \pm 0.3)\%$, $b = (1.85 \pm 0.12)\%$, $c = 3.87 \pm 0.07$ and $d = 0.00 \pm 0.04$.

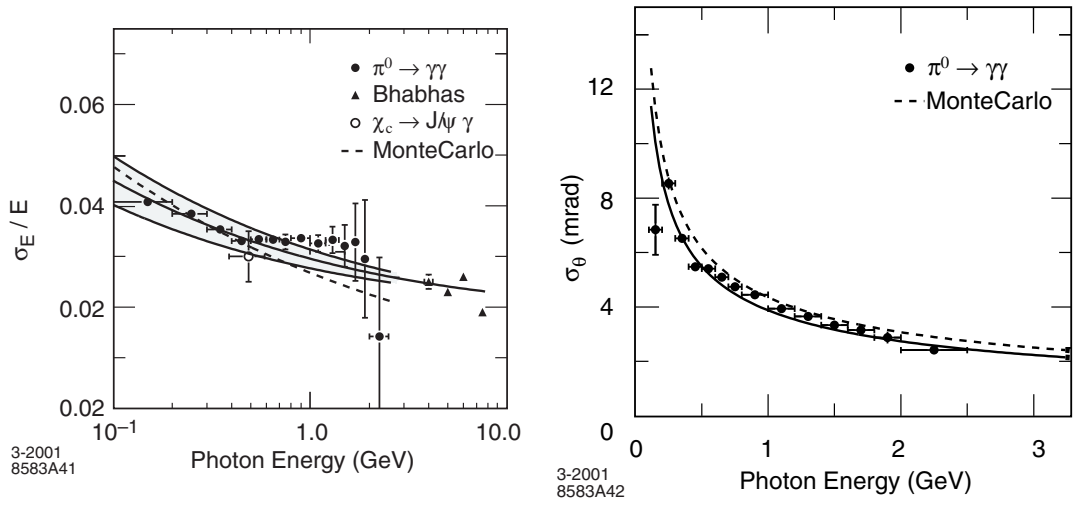

Figure 4.8: Photon energy (left) and angular (right) resolutions achieved by the electromagnetic calorimeter [82].

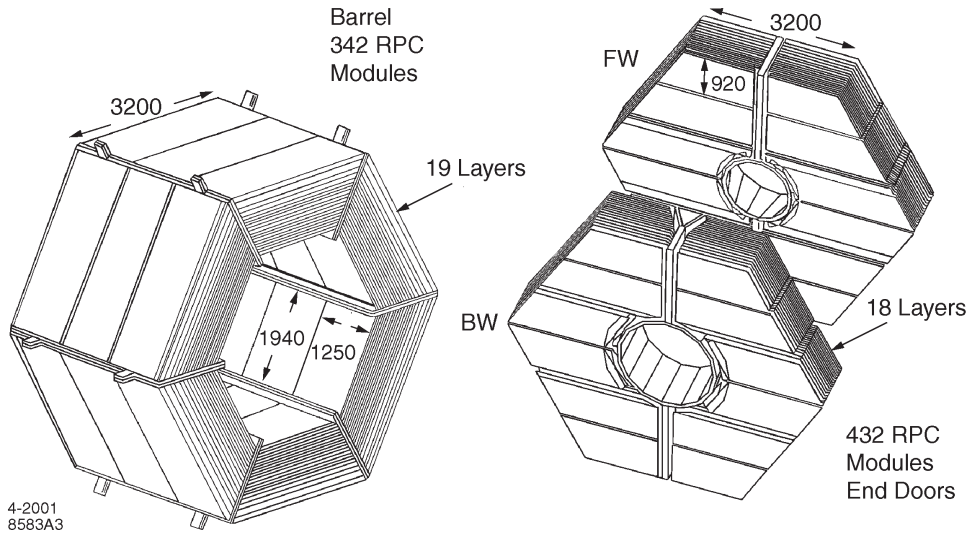

Figure 4.9: Schematic view of the IFR, with the barrel on the left and the forward (FW) and backward (BW) endcaps on the right.

4.5 The Instrumented Flux Return (IFR)

Physics requirements

The golden mode, $J/\psi\, K^0_S$, involves muons, as the J/ψ is reconstructed in the channels e^+e^- and $\mu^+\mu^-$. Their detection is also essential for semi-leptonic physics and for the tagging algorithms. Particle identification information on muons is desirable for momenta from about 1 GeV/c.

Muons are heavier than electrons, making bremsstrahlung a far less effective energy loss mechanism for them. Since they have relatively long lifetimes and do not participate in nuclear interactions either, they are very penetrating particles. Therefore, the best choice is to place a dedicated subdetector outside the rest of the instruments.

In *BABAR*, the outer part of the detector plays the role of the flux return for the solenoid, at the same time as it provides a support structure. Interleaved between the steel plates of the flux return, instruments can be placed to turn it into a muon detector and a primitive hadron calorimeter, in charge of detecting neutral hadrons, mainly K^0_L. These feature in a number of modes of interest, due to them having an opposite CP eigenvalue to the best experimentally suited modes containing a K^0_S.

Design

The steel of the flux return, which is distributed in layers of increasing thickness from the inner to the outer sides, serves the purpose of filtering the muons and absorbing the neutral hadrons. Between the steel sheets, in the barrel and the endcaps, there are 19 and 18 gaps, respectively, which host the instrumentation. These are shown in Figure 4.9, where the

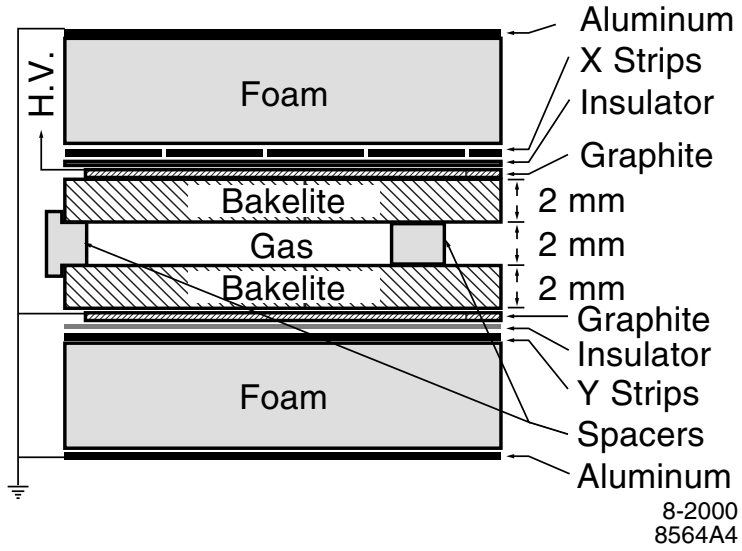

Figure 4.10: Resistive plate chamber design.

almost complete coverage of the detector is also apparent. The arrangement of these gaps, and the thickness of each of the layers was carefully chosen after dedicated MC studies to optimize the physics capabilities.

In these gaps, resistive plate chambers were installed. Two cylindrical RPCs were also placed between the EMC and the magnet to detect particles leaving the EMC and link any EMC clusters to IFR energy deposits.

The resistive plate chambers (see Fig. 4.10) consist of two graphite electrodes separated by two 2 mm thick sheets of bakelite, and in between these, another 2 mm gap filled with a mixture of gases: argon, freon and isobutane in the proportions 57:39:4. Readout strips are located next to the graphite, separated from it only by a film of insulator. They are placed orthogonally (hence the labels "X strip " and "Y strip" in the figure), providing three-dimensional positional information when combined with the distance of the RPC to the interaction point. The apparatus works as a capacitor, with one of the graphite electrodes grounded and the other one set to an 8 kV voltage. The passage of a charged particle or a hadronic shower do not cause a discharge, but induce temporary changes in the charge accumulated at each electrode, that are capacitatively read by the readout strips.

Performance

During *BABAR*'s first year of running, an 8% pion misidentification probability was found for a 90% muon efficiency.

The calibration of the angular resolution and efficiency of the detection of neutral hadrons was studied through the process $e^+e^- \to \phi\gamma \to K^0_S K^0_L \gamma$, and yielded efficiencies between 20 and 40%, and angular resolutions around 60 mrad for K^0_L that did not interact in the EMC.

When the latter also provided information, the resolution was twice as good.

However, shortly after installation, the performance of the RPC was observed to degrade quickly, with the muon efficiency dropping at an average rate of 1.2% per month and growing numbers of plates being declared "dead" (efficiencies less than 10%). The RPCs in the endcaps were replaced by new RPCs built with more stringent quality constraints, except for the first five, in whose brass was placed to improve pion rejection. A different solution was adopted for the barrel RPCs. These were substituted by limited streamer tubes.

Limited streamer tubes

The principle of operation of limited streamer tubes is similar to that of the RPCs. In the case of *BABAR*, a conducting wire with a $100\mu m$ diameter is placed in a long resistive cell (the "tube"), with a section of $15 \times 17\,\mathrm{mm}^2$, the wire playing the role of the anode, and the tube, of the cathode. The volume between them is filled with a gas that is ionized upon the passage of a charged particle or the spread of a hadronic shower, altering the charge distribution in the cylindrical capacitor. The signal can then be read either by external strips attached to both sides, or from the wires directly. In *BABAR*, the latter method is used to measure the ϕ coordinate, and the former, to read the z coordinate.

Their efficiency is monitored by using dimuon events and cosmic rays, finding an average of 90%, without any noticeable degradation trend over time.

4.6 The Trigger system

The aim of the trigger is to reduce the potential number of events per second reconstructed by the detector, which is essentially determined by the frequency of bunch crossing, to a manageable level of events that can be recorded. Of course, the goal of the trigger is to reject badly reconstructed events and background while retaining as much signal as possible.

In *BABAR*, that is achieved through a two-stage trigger, composed of the level-1 trigger (L1T), implemented in hardware, and the level-3 trigger, which is carried out by software, and after which all surviving events are recorded.

Level-1 trigger

The level-1 trigger consists of a global trigger (GLT) that combines the input from several individual triggers linked to the different subsystems of the detector, and accepts events at rates around 1 kHz, its limit being 2 kHz. The individual triggers feeding the global one are the DCH trigger (DCT), the EMC trigger (EMT) and the IFR trigger (IFT). These are continuously producing abstract data (*primitives*) describing the objects found by the subdetectors they are associated to, and are passed to the GLT. The global trigger then tries to match them to any of 24 *trigger lines* that represent events of interest, and if the timing of the trigger signal coincides with one bunch crossing, the fast control and timing system issues an *accept* signal. It is at this point that some classes of physics events, such as typical

QED processes that are used only in calibration, are scaled down, making their acceptance less likely.

The DCT produces its primitives by looking for sequential DCH hits in neighboring cells. These are then joined if possible to construct either short tracks, that traverse only a few superlayers, and long ones, that reach the end of the chamber. Axial superlayers are also examined looking for segments consistent with tracks with transverse momenta greater than 800 MeV/c.

The EMT sums the energy deposited on 40 strips along the ϕ polar angle, and finds a peak whose energy is compared to thresholds for different physics processes: minimum ionizing particle cluster ($E > 120$ MeV), intermediate energy cluster ($E > 307$ MeV), high energy electron or photon ($E > 768$ MeV), minimum ionizing particle in forward endcap ($E > 100$ MeV) and backward high energy cluster ($E > 922$ MeV).

The IFT primitives are just single clusters or back-to-back coincidences. These select cosmic ray events for calibration purposes, and $\mu^+\mu^-$ events.

The different trigger subsystems are optimized to select high multiplicity, multi-hadronic events, resulting in efficiencies over 99% for $B\overline{B}$ events for both the DCT and the EMT individually, and over 99.9% when combined.

Level-3 trigger

The level-3 trigger must reduce by $\gtrsim 10$ the number of events accepted by the L1T. It is implemented in software and run in computing farms, which allow the use of information from all the subdetectors. Examples are the rejection events with tracks not originating from the interaction point, as these are likely to be machine background, or events whose timing does not match a bunch crossing.

Level-3 trigger lines may also be prescaled to reduce the rate of less interesting physics events, such as Bhabha scatterings. Calculation of efficiencies requires accepting events that do not satisfy any of the level-3 criteria. These are known as *L1 passthrough* events.

4.7 Data acquisition

By data acquisition (DAQ) system we refer to the overall architecture by which the detector, the triggers and the computing structure are governed. The diagram in Fig. 4.11 schematically depicts it. The front end electronics process and digitize the signals coming from the detector and passes them to the level-1 trigger and the data flow buffers. If an accept signal is issued by the fast control and timing, the event is passed to the level-3 trigger, which also performs some basic data quality monitoring. Finally, if the event is accepted by the L3T, it is written to disk, where it will be passed to the online prompt reconstruction software in a matter of days. The DAQ is also responsible for recording the detector conditions, that will be used in the production of simulated data to better reproduce the running conditions (see Section 5.1.1).

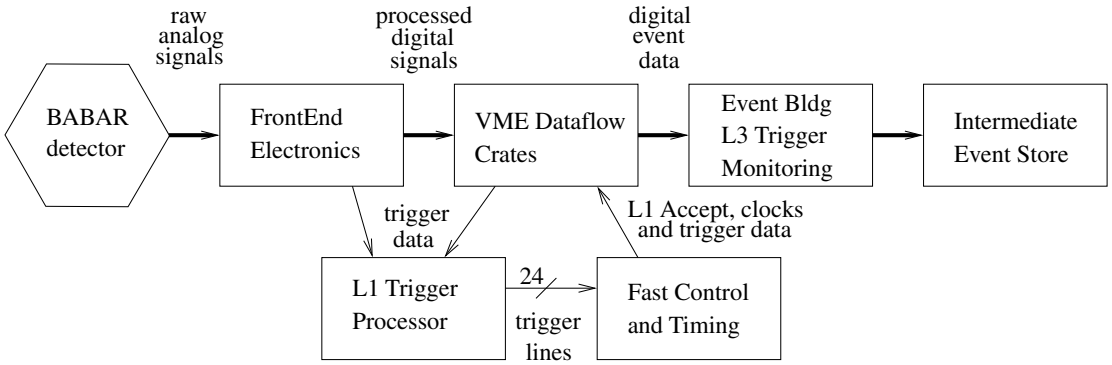

Figure 4.11: Schematic explanation of the interplay between the detector, the triggers and the first stages of the reconstruction process, known globally as the data acquisition system.

4.8 Online prompt reconstruction

After a data sample, typically consisting of around an hour of experiment running, has been logged on to disk, it goes through a prompt calibration processing, during which some of the calibration methods mentioned earlier in the chapter are run, and part of the data quality monitoring is performed. Following that, the data continue to event reconstruction, where tracks and clusters are found, and particle identification information (PID) is calculated. An event, by then essentially a collection of tracks, EMC clusters and IFR clusters, is stored in a database that will be accessed by the analysts reconstruction code to form *candidates* for events of a given decay channel (see Sec. 5.2). Once all these quantities have been calculated, a more detailed data quality check is made.

Part III

Analysis

Analysis overview

The main goal of the study presented in this thesis is to extract the time dependent *CP* asymmetry parameters, $\mathcal{S}_{K^0_S\rho\gamma}$ and $\mathcal{C}_{K^0_S\rho\gamma}$, from $B^0 \to K^0_S\rho^0\gamma$ decays. However, due to the large natural width of the $\rho^0(770)$, a non negligible amount of $B^0 \to K^{*\pm}(K^0_S\pi^\pm)\pi^\mp\gamma$ events, which do not contribute to $\mathcal{S}_{K^0_S\rho\gamma}$, are expected to lie under the $\rho^0(770)$ resonance. These events will therefore dilute $\mathcal{S}_{K^0_S\rho\gamma}$. We can define a dilution factor $\mathcal{D}_{K^0_S\rho\gamma}$ such as

$$\mathcal{D}_{K^0_S\rho\gamma} = \frac{\mathcal{S}_{K^0_S\pi^+\pi^-\gamma}}{\mathcal{S}_{K^0_S\rho\gamma}},$$

where $\mathcal{S}_{K^0_S\pi^+\pi^-\gamma}$ is the effective value of the mixing induced *CP* asymmetry measured for the whole dataset. Since in the time-dependent analysis a small number of signal events is expected, it is difficult to discriminate $B^0 \to K^{*\pm}(K^0_S\pi^\pm)\pi^\mp\gamma$ from $B^0 \to K^0_S\rho^0(\pi^\mp\pi^\pm)\gamma$ decays. Hence the dilution factor needs to be obtained by other means. To do that, the amplitudes of the different resonant modes are extracted in the charged decay channel $B^+ \to K^+\pi^-\pi^+\gamma$, which has more signal events and is related to $B^0 \to K^0_S\pi^+\pi^-\gamma$ by Isospin symmetry. Assuming that the resonant amplitudes are the same in both modes, the dilution factor is calculated from those of $B^+ \to K^+\pi^-\pi^+\gamma$. Moreover, the branching fractions of the $B \to K_{\rm res}\gamma$ decays are not well measured. We also use the charged decay channel $B^+ \to K^+\pi^-\pi^+\gamma$ to extract the amplitudes of modes with different kaonic resonance.

The analysis work presented in this thesis is divided in two chapters:
Chapter 6 presents the analysis of $B^+ \to K^+\pi^-\pi^+\gamma$ decays. This analysis is done in four steps. First the signal $K\pi\pi$, $K\pi$ and $\pi\pi$ invariant mass spectra are extracted, using a background-subtracted method, from a fit to three discriminating variables. In a second step the relative contributions of each kaonic resonance are computed from the corresponding amplitudes extracted from a fit to the $m_{K\pi\pi}$ spectrum. Then, using as input the $K_{\rm res}$ relative contributions extracted in the previous step, the amplitudes of the intermediate states contributing to the $K\pi\pi$ final state are extracted from a fit to the $m_{K\pi}$ invariant mass spectrum. In a final step, the analytical expression of the dilution factor in terms of the intermediate state amplitudes is presented in detail and the dilution factor value is then given.
Chapter 7 presents the time-dependent analysis of $B^0 \to K^0_S\pi^+\pi^-\gamma$ decays. This analysis allows to extract the value of the effective *CP* asymmetry parameters, $\mathcal{S}_{K^0_S\pi^+\pi^-\gamma}$ and $\mathcal{C}_{K^0_S\pi^+\pi^-\gamma}$. The mixing-induced *CP* parameter of $B^0 \to K^0_S\rho^0\gamma$ decays, $\mathcal{S}_{K^0_S\rho\gamma}$, is finally given, using the value of $\mathcal{D}_{K^0_S\rho\gamma}$ extracted from the charged channel analysis.

Since both analyses are performed using common High Energy Physics analyses tools and methods, these are first detailed in Chapter 5.

In the rest of the document, when specific decays are quoted, charged conjugation is always implied, unless explicitly specified.

Chapter 5

Data samples and analysis techniques

Contents

In this Chapter, we describe in detail some tools and methods commonly used in High Energy Physics analyses, such as simulation of data (see Section 5.1), event reconstruction (Section 5.2), signal and background discrimination (Section 5.3) and maximum likelihood fits (Section 5.4).

5.1 Monte Carlo and data samples

5.1.1 Monte Carlo samples

Simulated data, usually referred to as Monte-Carlo (MC) data, are essential to understand detector effects (e.g. mis-reconstruction of signal and reconstruction efficiencies), backgrounds and systematic effects that could affect the analysis procedure. To simulate the physics mechanisms that operate in e^+e^- collisions within *BABAR*'s energy regime, events are first generated with the `EvtGen` package [84], which gives an accurate representation of phenomena such as mixing and interference (necessary for the correct modeling of *CP*-violation) or the angular distributions of the decay products in non-trivial situations, such as pseudoscalar-to-vector-vector decays. The vast majority of B decays are generated using `EvtGen`, however, the remaining generic B decays to hadronic final states, for which there is no specific model, and continuum events ($e^+e^- \to q\bar{q}, \quad q = u, d, s, c$) are produced via an interface to `JETSET` [85].

Then, in order to account for the interaction of the generated-event decay products with the detector as they propagate through it, the latter are simulated by a customized software based on `GEANT 4` [86], which requires a detailed model of the instrument, both in geometric and material terms. Processes like rescattering or photon conversions, for instance, as well as a detailed account of the energy that is lost and deposited by the particles in the different parts of the detector (e.g. silicon strips in SVT, gas and wires in DCH and crystal in EMC) are simulated at this stage.

In the following stage, each of these interactions (or *hits*) are used to simulate the data read out by the electronics, trigger and DAQ system. Typical electronic noise and machine backgrounds characterizing a certain period of running of the experiment are taken into account. The latter are obtained by recording real events, at regular intervals, with a random trigger, which are then aggregated to simulated events.

In a last stage, the simulated electronic output is processed with the same version of *BABAR* reconstruction software that is used on real data.

The MC samples used to characterize signal and background, and to optimize the selection in the charged and the time-dependent analyses are given in Tabs. 5.1 and 5.2, respectively. Two different types of MC samples are used to study backgrounds from B-meson decays (B backgrounds): generic $B\overline{B}$ MC and exclusive MC, whereas only exclusive MC samples are used to study signal events. The exclusive signal MC samples with different kaonic resonances decaying to $K\pi\pi$ are combined according to cocktail weights, as described in Secs. 6.1 and 7.2 for the charged and the time-dependent analysis, respectively. The

generic $B\overline{B}$ MC corresponds, approximately, to an integrated luminosity of three times that of the data sample. It comprises and is composed of a cocktail of $e^+e^- \to \Upsilon(4S) \to B\overline{B}$ events, where the B mesons decay to all their known and predicted decay modes. The relative abundances of different decay channels are set to the experimental branching fractions [23, 24], when available, or to theoretical predictions.

Table 5.1: MC samples used to characterize signal and background events in the charged analysis. In the decay process description, when "gen." is quoted, it means the corresponding particle is allowed to decay to any known possible final state.

Studied event category	Decay process	$N_{B\bar{B}}$ generated ($\times 10^6$)
Signal	$B^+ \to K_1(1270)^+\gamma$ $K_1(1270)^+ \to$ gen.	7.886
	$B^+ \to K_1(1400)^+\gamma$ $K_1(1400)^+ \to$ gen.	1.286
	$B^+ \to K_2^*(1430)^+\gamma$ $K_2^*(1430)^+ \to$ gen.	2.467
	$B^+ \to K^*(1410)^+\gamma$ $K^*(1410)^+ \to$ gen.	1.365
	$B^+ \to K^*(1680)^+\gamma$ $K^*(1680)^+ \to$ gen.	0.650
Background	$B^+B^- \to$ gen.	708.8
	$B^0\overline{B}^0 \to$ gen.	718.3
	$B^0 \to X_{sd}\gamma$ $X_{sd} \to$ gen.	0.650
	$B^+ \to X_{su}\gamma$ $X_{su} \to$ gen.	0.650
	$B^0 \to K^{*0}\gamma$ $K^{*0} \to$ gen.	4.580
	$B^+ \to K^{*+}\gamma$ $K^{*+} \to$ gen.	4.658
	$B^0 \to K^{*0}\eta$ $\eta \to \gamma\gamma$ $K^{*0} \to K^+\pi^-$	0.650
	$B^+ \to a_1^+\pi^0\gamma$ $a_1^+ \to \rho^0\pi^+$	0.216
	$B^+ \to K^{*0}\pi^+\pi^0\gamma$ $K^{*0} \to K^+\pi^-$	0.153

Table 5.2: MC samples used to characterize signal and background events in the time-dependent analysis. In the decay process description, when "gen." is quoted, it means the corresponding particle is allowed to decay to any known possible final state.

Studied event category	Decay process	$N_{B\bar{B}}$ generated ($\times 10^6$)
Signal	$B^0 \to K_1(1270)^0\gamma$ $K_1(1270)^0 \to$ gen.	7.295
	$B^0 \to K_1(1400)^0\gamma$ $K_1(1400)^0 \to$ gen.	1.176
	$B^0 \to K_2^*(1430)^0\gamma$ $K_2^*(1430)^0 \to$ gen.	2.653
	$B^0 \to K^*(1410)^0\gamma$ $K^*(1410)^0 \to$ gen.	3.493
	$B^0 \to K^*(1680)^0\gamma$ $K^*(1680)^0 \to$ gen.	10.806
Background	$B^+B^- \to$ gen.	708.8
	$B^0\overline{B}^0 \to$ gen.	718.3
	$B^0 \to X_{sd}\gamma$ $X_{sd} \to$ gen.	0.650
	$B^+ \to X_{su}\gamma$ $X_{su} \to$ gen.	0.650
	$B^0 \to K^{*0}\gamma$ $K^{*0} \to$ gen.	4.580
	$B^+ \to K^{*+}\gamma$ $K^{*+} \to$ gen.	4.658

5.1.2 *On-Peak* and *Off-Peak* data samples

The data sample used in both analyses presented in this thesis is the final *BABAR* dataset that consist of 470.9±2.8 million $B\bar{B}$ pairs corresponding to an integrated luminosity of 429.0 fb^{-1} at the $\Upsilon(4S)$, and is referred to as the *On-Peak* data sample. In addition, during dedicated running periods, 44.8 fb^{-1} of data were collected at 40 MeV below the $\Upsilon(4S)$ resonance. It is referred to as the *Off-Peak* data sample. As previously mentioned this small data sample is useful to characterize specific background, called continuum, where no $B\overline{B}$ pair is produced, and that often constitutes the largest background (in term of number of events) in *BABAR* analyses. Both the *On-* and *Off-Peak* data samples are divided in six sub-data samples, or *Runs*. Each one corresponding to a period of continuous data taking, lasting typically some ten months. The data sample is summarized in Tab. 5.3.

Table 5.3: Run by run integrated luminosity and $B\overline{B}$ number of events in the data.

Sample	*On Peak* (fb^{-1})	$N_{B\overline{B}}$ ($\times 10^6$)	$\sigma^{stat.+syst.}_{N_{B\overline{B}}}$ ($\times 10^6$)	*Off Peak* (fb^{-1})
Run 1	20.60	22.56	0.14	2.62
Run 2	62.07	68.42	0.41	7.03
Run 3	32.67	35.76	0.22	2.50
Run 4	100.78	111.39	0.67	10.23
Run 5	133.85	147.58	0.89	14.55
Run 6	79.03	85.18	0.51	7.89
Total	429.0	470.91	2.84	44.81

5.2 Reconstruction

The reconstruction of events is performed in two steps. First, the Offline Prompt Reconstruction is performed. During this step, the goal is to find tracks and to reconstruct calorimeter clusters from hits in the DCH and the SVT, and crystals with energy deposits in the EMC, respectively. Čerenkov photons and $\mathrm{d}E/\mathrm{d}x$ information are also processed during this stage and used to form "particle identification selectors". In a second step, the reconstruction process allows the reconstruction of objects that are not directly detected, but can be inferred from the properties of their decay products. B and D mesons are good examples of such composite objects. The corresponding candidates are obtained from the combination of tracks and neutral objects, consistent with the desired meson. This allows the vertexing of the B meson and the Δt measurement to be made.

5.2.1 Tracking algorithms

Charged tracks follow helicoidal trajectories due to the axial magnetic field in which the inner parts of the detector are immersed. They can be described by five parameters that are fitted using a Kalman filter technique [87]. The five parameters are defined at the point of closest approach (POCA) to the z-axis:

- d_0, the distance to the z-axis in the xy plane
- z_0, the coordinate along the z-axis
- ϕ_0, the azimuthal angle of the plane containing the POCA and the z-axis
- λ, the dip angle of the track with respect to the transverse (xy) plane. It is related to the cylindrical polar angle θ via $\theta = \pi/2 - \lambda$
- ω, the (signed) curvature of the track, whose sign and magnitude are related, respectively, to the charge of the associated particle and its transverse momentum, $\omega \propto 1/p_t$.

The Kalman filter algorithm uses an iterative and recursive fit technique, where each vertex is fitted independently. That way the changes in the parameters are propagated to the neighboring vertices. This procedure results in a global fit, where corrections to account for fine details can be done, thanks to the local character of each step of the algorithm. These details correspond to the material distribution of the detector, the slight inhomogeneities of the magnetic field or the energy loss of low momentum tracks.

The algorithm starts from the DCH hits found by the $L3$ trigger to form a primary track; further hits are added if they are consistent with this primary track. Afterwards, a search is made, using the remaining hits in the DCH, for tracks that may not be originated from the beamspot (e.g. K^0_S that lived long enough to decay outside the SVT), or that may not be energetic enough to traverse the whole chamber. Finally, SVT hits are examined and added to the existing DCH tracks if consistent, and are otherwise searched to locate any low momentum, SVT-only tracks. All the reconstructed tracks are further classified and stored in lists according to different selection criteria. The pion candidates, in both analyses presented in this thesis, are taken from the standard `GoodTracksLoose` list, with the quality requirements:

- $p_t > 0.1\,\mathrm{GeV}/c$
- $p < 10.0\,\mathrm{GeV}/c$
- a minimum of 12 hits in the DCH
- $d_0 < 1.5$ cm
- $|z_0| < 10$ cm

Note that the K^0_S candidates, are formed from any two oppositely charged tracks that often do not meet the `GoodTracksLoose` requirements above. The details on the K^0_S selection requirements are given in Secs. 5.2.4 and 7.3.1.1.

5.2.2 Calorimeter algorithms

Particles flying through the EMC typically result in *showers*, spreading over several neighboring crystals, and which form clusters of energy deposit. Such clusters may be due to the interaction of more than one particle and hence present energy distributions with more than one maximum, each of them being referred as a *bump*. The EMC reconstruction algorithm purpose is to search and find these maxima, to extract the right shape of the clusters, and to finally identify and correctly assign the energy of the flying particles.

In order to achieve these goals, the algorithm starts by looking for "seed" crystals with energy deposits greater than 10 MeV. Then, clusters are formed adding surrounding crystals containing above 1 MeV themselves, or adjacent crystals with an energy greater than 3 MeV. Local bumps are found using standard methods [88]. For a given maximum, a weight (ω_j) is assigned to each crystal depending on the ratio of the distance from the crystal to the maximum, its deposited energy (E_j) and the Molière radius. The bump energy is then

estimated from the weighted sum of the energy deposits over all the crystals in the cluster, as $E_{\text{bump}} = \sum_j E_j \omega_j$.

In a last step, tracks are projected onto the inner face of the EMC, and if they are consistent with one of the considered bumps, they are linked to a single charged particle in the following reconstruction routines. The remaining bumps are assumed to be neutral objects.

5.2.3 Particle identification

In order to achieve the physics goals, it is crucial to correctly track and identify the charged, long-lived particles in the *BABAR* detector. Such particles are: electrons, muons, pions, kaons and protons. This reconstruction step is achieved by exploiting the different ways those particles interact with each part of the detector. Information from all subdetectors (SVT, DCH, DIRC, EMC and IFR) is used to construct a PDF (see Section 5.4) that represents the likelihood of a particle to belong to a given species. Electrons and muons PDFs are obtained from information collected in the Electromagnetic Calorimeter and the Instrumented Flux Return, respectively. In the case of protons, their production is rare compared to other particles in *BABAR* and is of no interest for the analyses presented in this thesis.

For the kaon-pion separation, the likelihood for kaon and pion hypotheses is constructed as the product of the PDFs from the SVT, the DCH and the DIRC for the given particle hypothesis, where the first two contribute with $\mathrm{d}E/\mathrm{d}x$ measurements and the last one, with the angle (θ_c) with respect to the track at which Čerenkov photons are emitted in the quartz bars of the DIRC.

For both the DCH and the SVT, the measured energy losses of each track are compared with the Bethe-Bloch [24] expectations by forming the pulls (see Section 5.4), and are parameterized with a gaussian and a gaussian with asymmetric widths, respectively. In the case of the DIRC, in which the relevant quantities suffer from long non-gaussian tails that prevent the use of a similar method, a binned likelihood obtained from MC is used instead. This likelihood depends on θ_c and on the number of photons. The latter, being a function of the momentum and type of the particle, helps to improve the identification of low momentum tracks.

Once the likelihoods for the different particle hypotheses have been calculated, cuts on their values are applied, and the track is entered into different lists according to the criteria satisfied: `SuperLoose, VeryLoose, Loose, Tight, VeryTight` and `SuperTight` for pions, and `NotPion, VeryLoose, Loose, Tight` and `VeryTight` in the case of kaons. For both analyses described in this thesis, pions in the `SuperLoose` list are selected (see Secs. 6.2 and 7.3) and charged kaons in the `Loose` list are selected in the charged-mode analysis (see Secs. 6.2). In the case of pions, the efficiency of such a requirement is above 95% in most of the kinematical range, and the kaon misidentification rate is around $5-15\%$ depending on the momentum, while in the case of kaons, the efficiency is above 85% in most of the kinematical range and the pion misidentification rate is around $2-7\%$ [89]. Due to additional cuts on background discriminating variables, we expect a negligible kaon and/or pion contaminations in our samples.

5.2.4 Vertexing

Candidates for composite particles are first formed from all the possible combinations of tracks and neutral particles matching their decay products. These candidates are then vertexed according to some kinematical criteria. For example, in the reconstruction of the $B^0 \to K^0_S\pi^+\pi^-\gamma$ decays, intermediate states like ρ^0 or $K^{*+}(892)$, whose decays are governed by the strong force, have such short lifetimes that their decay vertex can be assumed to match the vertex of the B meson. In the present analyses, only the K^0_S and the B candidates are assumed to be long lived and are assigned to a decay vertex. Candidates for K^0_S mesons are formed from all possible oppositely charged tracks in the event assumed to be pions, with a total center-of-mass energy within $25\,\mathrm{MeV}/c^2$ of the K^0_S mass [24]. This selection of K^0_S candidates is referred as `KsDefault` list.

Using the `TreeFitter` package [90], the assumed decay vertices of K^0_S and B candidates are calculated with a geometric fit, in which daughter-tracks are required to emerge from a common vertex. This procedure is performed through a global fit to the whole decay chain by applying the Kalman filter technique. In order to estimate the interaction point, a fit to all tracks in the event is performed. Its result is used as a starting point in the iterative procedure for the B vertex reconstruction.

For the B vertexing, constraints may be applied in the fit to reduce detector resolution effects. Hence a first vertexing fit is performed constraining the B candidate to have the nominal B-meson mass [24], from which the event shape variables are calculated. A second vertexing fit is made with no mass-constraint; the discriminant kinematical variables m_{ES} and ΔE are extracted from it (see Section 5.3).

5.3 Discriminating variables

The small branching fractions of the radiative B decay modes studied in this thesis[1], namely $B^+ \to K^+\pi^-\pi^+\gamma$ and $B^0 \to K^0_S\pi^+\pi^-\gamma$, compared to the large cross sections of some undesired processes such as continuum background ($e^+e^- \to q\bar{q}$, $q = u, d, s, c$ where $\sigma_{q\bar{q}} \sim 3.2 \times \sigma_{b\bar{b}}$), entails the use of background-rejecting variables. In both analyses, three event species are distinguished in the data: signal events ($B^+ \to K^+\pi^-\pi^+\gamma$ or $B^0 \to K^0_S\pi^+\pi^-\gamma$), continuum events (representing the dominant background) and several B-backgrounds corresponding to B-meson decays that differ from the signal.

By exploiting the differences between the distributions of some variables in signal and backgrounds, it is possible to achieve a statistical separation between them. Two approaches may be used in order to take advantage of these differences. In the case where the background peaks at a different point than signal for a certain variable, a *cut* on this variable may be applied. The rejection of all events lying on one side of the cut value enriches the sample with signal events. Another approach consists of accepting all events, and assigning each of them a weight or probability of belonging to each species according to the value of the considered discriminating variable. In both analyses presented in this thesis, a mixed strategy has been followed: loose cuts are applied on the three discriminating variables, m_{ES}, ΔE and the a

[1] $\mathcal{B}(B^+ \to K^+\pi^-\pi^+\gamma) = (2.76 \pm 0.22) \times 10^{-5}$ and $\mathcal{B}\left(B^0 \to K^0_S\pi^+\pi^-\gamma\right) = (1.95 \pm 0.22) \times 10^{-5}$ [24]

combination of event shape variables, and their distributions are then used in the fit. These three variables are described in detail in the following sections. Other variables, not present in the fit, on which cuts are applied, are used in the event selection step of both analyses. They are described in Secs. 6.2 and 7.3.

5.3.1 Kinematic variables

Taking advantage of the well know initial state, e^+e^-, at the B Factories, combined to the fact the $B\overline{B}$ pair is produced *via* the decay of the $\Upsilon(4S)$ resonance, two kinematical variables can be constructed in order to discriminate signal from continuum and B-background events. Namely, these two variables are the energy difference ΔE (Sec. 5.3.1.1) and the energy-substituted mass $m_{\rm ES}$ (Sec. 5.3.1.2), which are usually largely uncorrelated [91].

5.3.1.1 The energy difference ΔE

The energy difference, ΔE, can be expressed in a Lorentz-invariant form as

$$\Delta E = (2q_B q_0 - s)/2\sqrt{s} \ , \tag{5.1}$$

where q_B and $q_0 = q_{e^+} + q_{e^-} = (E_0, \mathbf{p}_0)$ are the Lorentz vectors representing the momentum of the B-meson candidate and of the initial e^+e^- system, and $\sqrt{s} = 2E^*_{\rm beam}$ denotes the CM energy. In the CM frame, ΔE can be expressed as

$$\Delta E = E^*_B - \sqrt{s}/2 \ , \tag{5.2}$$

where E^*_B is the reconstructed energy of the B candidate without applying any constraint. Since ΔE is by construction related to the mass hypotheses for each of the tracks, its distribution will strongly depend on the nature of the final state particles. For instance, in the case where a kaon is misidentified as a pion, its reconstructed energy, and consequently that of the B candidate, will be smaller than expected, and the event will be shifted towards negative values of ΔE. On the other hand, the distribution for correctly reconstructed signal events will peak at zero. This makes ΔE especially helpful in isolating backgrounds from misreconstructed B decays. Moreover, since continuum events do not originate from B decays, their distribution in this variable is expected to be linear in the whole dynamical range, excluding acceptance effects and phase space.

The ΔE distribution receives a sizable contribution from the beam energy spread, but is generally dominated by detector energy resolution, especially in the case for modes involving neutral particles. In modes with no neutral particles in the final state, the resolution for the ΔE variable is $\sim 15\,\text{MeV}$, while in the present analysis it is of the order of $\sim 20 - 25\,\text{MeV}$.

5.3.1.2 The energy-substituted mass $m_{\rm ES}$

The other kinematic variable, the energy-substituted mass $m_{\rm ES}$ can be expressed, in the laboratory frame, as

$$m_{\rm ES} = \sqrt{(s/2 + \mathbf{p}_0 \cdot \mathbf{p}_B)^2/E_0^2 - \mathbf{p}_B^2} \ . \tag{5.3}$$

In the CM frame the three momentum of the e^+e^- system equals to zero, and $m_{\rm ES}$ can be expressed in this case as

$$m_{\rm ES} = \sqrt{E^*_{\rm beam} - \mathbf{p}^{*2}_B}\ , \tag{5.4}$$

where $\mathbf{p}^{*2}_B$ is the CM momentum of the B candidate. Since the candidate is formed from a number of tracks and neutral objects whose energies are not as accurately measured as are the beam conditions, the B-candidate energy is here substituted by $E^*_{\rm beam}$. This allows to improve the mass resolution by using our knowledge of the initial kinematics. Due to the annihilation of the electron and the positron, which creates a $B\overline{B}$ pair, and to the fact that the masses of the particle and of the antiparticle are equal, we have

$$q^2_B = q^2_{\overline{B}} = (q_0 - q_B)^2 = q^2_0 + q^2_B - 2q_0q_B \ \Rightarrow\ 0 = q^2_0 - 2q_0q_B \ \Rightarrow\ s/2 = -E_0E_B + \mathbf{p}_0\cdot\mathbf{p}_B$$
$$\Rightarrow\ m_B = \sqrt{E^2_B - \vec{p}^{\,2}_B} = \sqrt{\left(\tfrac{s/2 - \mathbf{p}_0\cdot\mathbf{p}_B}{E_0}\right)^2 - \mathbf{p}^2_B} = m_{\rm ES}.$$

Thus, for signal events, $m_{\rm ES}$ yields the mass of the B meson and shows a clean peak. For continuum events, composed of light quarks, the only way of reaching the B rest mass is by artificially associating random tracks. As a consequence, the distribution of this kind of events displays the slowly varying shape that one could expect from their combinatoric nature.

In modes with no neutral particles in the final state, the resolution for the $m_{\rm ES}$ variable is $\sim 3\,\mathrm{MeV}/c^2$, and do not exceed $10\,\mathrm{MeV}/c^2$ in the present analysis.

The parameterizations used for the distributions of ΔE and $m_{\rm ES}$, for signal and backgrounds, are given in Secs. 6.5.3 and 7.6.3 for the charged and time-dependent analyses, respectively. Plots of both variables for signal and backgrounds can be seen in Figs. 6.10 and 6.16 to 6.22 for the charged channel analysis and in Figs. 7.4 and 7.8 to 7.15 for the time-dependent analysis, respectively.

5.3.2 Event-shape variables

Due to the underlying kinematics of the decay products in $e^+e^- \to \Upsilon(4S) \to B\overline{B}$ and $e^+e^- \to q\bar{q}$, $q = u, d, s, c$ processes, strong differences arise in the angular correlations among the produced daughters in $B\overline{B}$ and continuum events.

In continuum events, a small amount of the initial energy is invested in the rest masses of the quarks. As a result most of the available center-of-mass energy will be carried as kinetic energy, which implies that the event will have a two-jet-like structure and will roughly follow a $(1 + \cos^2\theta)$ dependence, where θ is the center-of-mass angle of a jet with respect to the beam axis. This is as predicted by lowest order Feynman QED diagram for an $e^+e^- \to f\bar{f}$, where f is a spin-1/2 fermion.

On the contrary, $B\overline{B}$ events are characterized by the decay of the spin-1 $\Upsilon(4S)$ resonance into two spin-0 B mesons, resulting in a $\sin^2\theta$ distribution, where θ is the angle between the B direction and the z-axis. In addition, since the reaction is barely allowed kinematically, the B mesons have in average very low momenta in CM frame, $\sim 340\,\mathrm{MeV}/c$, which is smaller than the typical momenta of their daughters, $\sim$ 1-2 GeV/c. This implies that the

decay products of a B meson will not follow its flight direction. Furthermore, the B-meson being a pseudoscalar, it decays isotropically and the distributions of its daughters will be approximately spherical in the $\Upsilon(4S)$ CM frame .

Taking advantage of the differences described above, some variables, called event-shape or topological variables, are useful for the separation between these two event species. Since B-background is coming from $B\overline{B}$ events, the event-shape variables will not allow to efficiently separate it from signal events. In that case discrimination can only be obtained using the kinematical variables $m_{\rm ES}$ and ΔE.

In the definitions below, some variables take advantage not only of the B candidate daughters, but also of tracks coming from the other B meson in the event. Hence, it is useful to distinguish between the reconstructed-B side of the event, and the Rest Of the Event (ROE). The latter being defined as the ensemble of all the tracks and neutral objects that do not make up the B candidate.

5.3.2.1 Angle between the B momentum and the beam axis

One of the event-shape variables is the cosine of the angle between the CM B candidate direction and the z axis, $\theta_{B_{mom}}$. As described above, the distribution of this variable for signal is a parabolic: $\sin^2\theta_{B_{mom}} = 1 - \cos^2\theta_{B_{mom}}$. For continuum events, in contrast, the B candidates can only be formed from random combinations of tracks, which implies that $\cos\theta_{B_{mom}}$ will have random values and will therefore follow (without taking into account any acceptance effects) a flat distribution.

5.3.2.2 Thrust Axis variables

The thrust of an ensemble of particles is defined as the direction, $\hat{\rm t}$, in which the sum, $\hat{T}$, of the projections of the momenta of the particles is maximized:

$$\hat{T} = \max\left(\frac{\sum_i \left|\hat{\rm t}_i \cdot \mathbf{p}_i^*\right|}{\sum_i \left|\mathbf{p}_i^*\right|}\right), \tag{5.5}$$

where the index i runs over all the particles in the ensemble. For $B\overline{B}$ events, $\hat{T}$ takes almost random values, as the events are mostly isotropic. For $q\overline{q}$ events, on the other hand, $\hat{T}$ follows the direction of the formed jets, and is therefore strongly directional.

Several variables can be defined employing the thrust axis, such as the cosine of the angle between the thrust axis of the B candidate and the z axis, $\cos\theta_{\hat{T}}$, or the cosine of the angle between the thrust axes of the B candidate and the rest of the event, $\cos\theta_{\hat{T}}^{ROE}$.

5.3.2.3 The ROE and momentum-weighted polynomials

Additional variables can be defined taking advantage of the differences in the angular distributions between $B\overline{B}$ ($\propto \sin^2\theta$) and continuum ($\propto 1 + \cos^2\theta$) events. When the whole allowed phase space of a multi-body decay is explored, the signal-side angular information cannot be used without biasing the data sample. In that case, the fact that the other B

in the event behaves statistically, but independently, in the same way is fully exploited to separate between signal and continuum events. Indeed, the tracks from the ROE should exhibit a very small correlation with the kinematical variables, since these are constructed using only signal-side information. Possible correlations are at the first order, assumed to be negligible.

In order to characterize the angular correlations of the ROE, we can define the momentum-weighted Legendre polynomials as

$$L_0 = \sum_i^{ROE} \mathbf{p}_i \ , \tag{5.6}$$

$$L_1 = \sum_i^{ROE} \mathbf{p}_i \cos\theta_i \ , \tag{5.7}$$

$$L_2 = \sum_i^{ROE} \mathbf{p}_i \frac{1}{2}\left(3\cos^2\theta_i - 1\right) \ , \tag{5.8}$$

where $\mathbf{p}_i$ and θ_i are the momentum and the angle, with respect to the thrust axis of the B candidate, of the i-th particle in the ROE. The expectation values of these variables in both signal and background show that the L_0 and L_2 have the largest separation power. This is due to the fact that the corresponding expectation values are non-zero and different for the two species, while the expectation value of L_1 is zero for both species. The ratio of the two polynomials, L_2/L_0, also shows a good separation between signal and continuum.

Other variables, also based on information coming from the ROE, called Fox-Wolfram moments, may help the separation between $B\overline{B}$ and continuum events. They are defined as follows:

$$\mathrm{FW}(l) = \sum_{ij} |\mathbf{p}_i||\mathbf{p}_j|\mathrm{P}_l(\cos(\theta_{ij})), \tag{5.9}$$

where the summation is over all final state particles in the ROE, $\mathbf{p}_i$ and $\mathbf{p}_j$ are momenta of the particles i and j, θ_{ij} is the angle between them and $\mathrm{P}_l(x)$ are the Legendre polynomials of order l. We can construct the ratio, R_2, between the 2-nd and 0-th Fox-Wolfram moments of the ROE, which exhibits a large separation power. This quantity taking values in the range $[0, 1]$ is indicative of the collimation ("jettiness") of an event topology. In the case of a $q\overline{q}$ event, R_2 expected values are closer to 1, which indicates a jet-like event. In contrast, for $B\overline{B}$ events, values of R_2 are expected to be closer to 0, indication of a nearly isotropic event.

5.3.3 Fisher discriminant

Since the event-shape variables described above exploit different aspects of the same physical principle, some correlations might appear among them. This implies that it may be difficult to find the best set of cuts among these variables during an optimization procedure.

As an alternative, a unique quantity defined as a linear combination of several discriminating variables x_i, can take full advantage of all the variables under consideration and their

correlations to maximize the separation power. The Fisher discriminant ($\mathcal{F}$) [92] is designed to do precisely that and is defined as

$$\mathcal{F} = \sum_i a_i x_i = \mathbf{a}^T \mathbf{x} \ , \tag{5.10}$$

where $\mathbf{a}^T$ is a line vector. The a_i coefficients are found by maximizing the separation between the signal and background distributions. This is defined to be

$$D(\mathbf{a}) = \frac{(\overline{\mathcal{F}}_S - \overline{\mathcal{F}}_B)^2}{\sigma_S^2 + \sigma_B^2} \ , \tag{5.11}$$

$\overline{\mathcal{F}}_j$ being the mean of the distribution of the species j, and σ_j^2 the variances, where the index j denotes either signal or background. Writing these in terms of the means $\boldsymbol{\mu}_j$ and covariance matrices V_j of the variables,

$$\overline{\mathcal{F}}_j = \mathbf{a}^T \boldsymbol{\mu}_j, \quad \sigma_j^2 = \mathbf{a}^T \mathrm{V}_j \mathbf{a} \ , \tag{5.12}$$

we get

$$D(\mathbf{a}) = \frac{\mathbf{a}^T (\boldsymbol{\mu}_S - \boldsymbol{\mu}_B)(\boldsymbol{\mu}_S - \boldsymbol{\mu}_B)^T \mathbf{a}}{\mathbf{a}^T (\mathrm{V}_S + \mathrm{V}_B) \mathbf{a}} \ , \tag{5.13}$$

which can be maximized by differentiating and equating to zero, giving

$$\mathbf{a} = (\mathrm{V}_S + \mathrm{V}_B)^{-1} (\boldsymbol{\mu}_S - \boldsymbol{\mu}_B). \tag{5.14}$$

Thus, by using signal and background control samples, such as signal MC and off-resonance data, the coefficients $\mathbf{a}$ can be calculated.

The Fisher discriminant is used in both analyses presented in this thesis. A study was first performed for the charged channel, to find an optimal choice of background discriminating variables. Due to the very similar final states (the only difference being the presence of a K_S^0 instead of a charged kaon in the neutral channel analysis), the optimal set of variables, consisting of six variables, is identical in both analyses. As a preliminary stage to the optimization other additional event-shape variables were tried and rejected, due to strong correlations among them, in favor of:

- absolute value of the cosine of the angle between the momentum of the B candidate and the beam (z) axis in the CM frame, $|\cos\theta_{B_{mom}}|$;
- cosine of the angle between the B thrust axis and the z axis, $\cos\theta_{\hat{T}}$;
- cosine of the angle between the B thrust axis and the ROE, $\cos\theta_{\hat{T}}^{ROE}$;
- 0-th order Legendre polynomials moments of the ROE, L_0;
- ratio between the 2-nd and the 0-th order momentum-weighted Legendre polynomials moments of the ROE, L_2/L_0;

- ratio between the 2-nd and 0-th order Fox-Wolfram moments of the ROE, R_2.

For this set of variables comparisons between the performance of the Fisher discriminant, a Neural Network (NN) [93] and a Boosted Decision Tree (BDT) [94] were also made. It was found that the BDT and the NN where slightly more performant: at 90% of signal efficiency, the continuum rejection was of 73% and $\sim$ 76% for the Fisher and both the NN and BDT, respectively. However, due to the gaussian behavior of the Fisher discriminant distributions compared to the more complicated ones of the BDT and the NN, we chose to keep the Fisher discriminant, in order to use parametric descriptions for it in the fit.

The parameterizations used to describe this variable for signal and backgrounds are given in Secs. 6.5.3 and 7.6.3 for the charged-mode and neutral-mode time-dependent analyses, respectively. Plots of this variable for signal and backgrounds can be seen in Figs. 6.10 and 6.16 to 6.22 for the charged channel analysis and in Figs. 7.4 and 7.8 to 7.15 for the time-dependent analysis, respectively.

5.4 The maximum likelihood fit

Often, in particle physics, one of the main goals is to extract parameters of interest for a given event category (usually signal) in a data sample containing several event species (i.e. signal and various backgrounds). Since it is almost never possible to completely separate signal from other contributions by applying cuts, another method may be used. Therefore taking advantage of the different behaviors between signal and background categories in several discriminating variables, the maximum likelihood fitting method is used. In this case it is even more interesting to apply loose cuts on the discriminating variables, since it allows keep a reasonable large number of events in the MC samples in order to parametrize their distributions more accurately.

Indeed, this powerful method enables to estimate the parameters that characterize the distribution of certain variables in the data sample [93, 95]. The distribution represents the values taken by a random variable x and can usually be described by a function $\mathcal{P}(x, \mathbf{a})$ whose shape is characterized by a set of parameters $\mathbf{a}$. In the case where this function is normalized, it is said to be a Probability Density Function (PDF) for x. In order to extract the best possible estimations for the values of the parameters $\mathbf{a}$, given a set of N measurements of the random variable, the maximum likelihood method seeks the values of $\mathbf{a}$ that maximize the *likelihood function*:

$$\mathcal{L}(\mathbf{a}) = \prod_{i=1}^{N} \mathcal{P}(x_i, \mathbf{a}) \ . \tag{5.15}$$

In other words, the likelihood function represents the probability of drawing the N measurements of x given a certain set of values for the parameters $\mathbf{a}$. Consequently, optimizing this probability should yield the parameter values that best describe the sample.

In a realistic analysis, the likelihood function can be quite complicated due to the presence of several event species ("hypotheses") with different distributions as well as several random

variables to be described:

$$\mathcal{P}\left(i, \mathbf{a}\right) = \sum_{j=1}^{M} \mathcal{P}_j\left(x_i, y_i; \mathbf{a}\right) \ , \tag{5.16}$$

where M is the number of hypotheses, x_i and y_i are two random variables in the i-th experiment. In the case where there is no correlation among the variables x_i and y_i, the PDF can be written as

$$\mathcal{P}\left(i, \mathbf{a}\right) = \sum_{j=1}^{M} \mathcal{Q}_j\left(x_i; \mathbf{a}_{\mathcal{Q}}\right) \mathcal{R}_j\left(y_i; \mathbf{a}_{\mathcal{R}}\right) \ . \tag{5.17}$$

Otherwise, one needs to take them into account through multi-dimensional PDFs that depend on the correlated variables.

In order to simplify the computation of the likelihood function during the optimization procedure, the expression given in (**??**) is not usually applied as written. Instead, a minimization of the negative logarithmic likelihood function (NLL) is performed

$$\text{NLL} = -\ln \mathcal{L} = -\sum_{i=1}^{N} \ln \mathcal{P}\left(x_i, \mathbf{a}\right), \tag{5.18}$$

where the sum of logarithms is far more manageable in terms of machine precision than the original product. Two packages are used for the likelihood fitting in this thesis. The first one is based on the `Laura++` package [96] and the second is based on the `RooFit` package [97]. Both are interfaced to `Minuit` [98, 99] through `ROOT` [100].

5.4.1 Extended maximum likelihood fit

Usually, the number of events is also unknown, and needs to be incorporated in the likelihood function. As a consequence, the previous definition needs to be modified in order to include the probability, given by the Poisson distribution, of having N occurrences when ν is the expected value:

$$\mathcal{L}\left(\nu, \mathbf{a}\right) = \frac{e^{-\nu}\nu^N}{N!} \prod_{i=1}^{N} \mathcal{P}\left(x_i, \mathbf{a}\right) = \frac{e^{-\nu}}{N!} \prod_{i=1}^{N} \nu\mathcal{P}\left(x_i, \mathbf{a}\right) \ . \tag{5.19}$$

which, can be generalized for M hypotheses by

$$\mathcal{L}\left(\mathbf{n}, \mathbf{a}\right) = \frac{e^{-\sum_{k=1}^{M} n_k}}{N!} \prod_{i=1}^{N} \left(\sum_{j=1}^{M} n_j \mathcal{P}_j\left(x_i, \mathbf{a}\right) \right) \ , \tag{5.20}$$

where n_j is the number of events for the hypothesis j.

In both analyses presented in this thesis, the initial parameters $\mathbf{a}$ are extracted either from MC simulation or *Off-Peak* data. It may happen that some of them need to be fixed

in the minimization procedure, depending on the fit ability to extract them, which is tested through validation tests, as described in Sec. 5.4.3. The minimum found in the fitting procedure may or may not be global and therefore, we need to check the behavior of results when performing several fits using random initial values of each parameter. If the minimum stays stable, we consider it to be global. In some cases, the shape of the likelihood as a fraction of a particular variable is also obtained as described in Sec. 6.6.2.

The variables used in the fit are the two kinematical variables ($m_{\rm ES}$ and ΔE) and the Fisher discriminant in both analyses. In the time-dependent analysis, Δt (whose model is described in Sec. 7.1) is used in addition.

5.4.2 Error estimations

In `Minuit` the statistical errors estimation is performed by default using the `HESSE` routine, which calculates the matrix of second derivatives of the likelihood function with respect to the parameters evaluated at the maximum and inverts it to get the error matrix:

$$\left(V^{-1}\right)_{ij} = - \left. \frac{\partial^2 \log \mathcal{L}}{\partial a_i \partial a_j} \right|_{\mathbf{a}=\mathbf{a}^0} \tag{5.21}$$

where $\mathbf{a}^0$ are the values returned by the fit. Due to the assumptions that are made here, such as infinite data sample and a gaussian behavior of the likelihood function in the parameter space, the error estimations may result in an underestimate of the errors.

Another method to extract error estimations can also be used in `Minuit`: the `MINOS` routine, which uses more resources than `HESSE`, allows to estimate the one standard deviation (σ) errors using the variation of the likelihood as a function of the parameter values. This "scan" method consists of defining the errors σ_i by the points $a_i^0 \pm \sigma_i$ in which the logarithm of the likelihood drops by 1/2:

$$\begin{aligned} \mathrm{NLL}\left(a_i^0 + \sigma_i\right) &= \mathrm{NLL}\left(a_i^0\right) + \tfrac{1}{2} = \mathrm{NLL}_{\max} + \tfrac{1}{2} \ , & (5.22) \\ \mathrm{NLL}\left(a_i^0 - \sigma_i\right) &= \mathrm{NLL}\left(a_i^0\right) + \tfrac{1}{2} = \mathrm{NLL}_{\max} + \tfrac{1}{2} \ . & (5.23) \end{aligned}$$

In the case where the likelihood function has gaussian behavior, the error is of the width of the gaussian.

In the rest of the document, when reporting fit results the `HESSE` routine is used to estimate the errors, unless otherwise specified.

5.4.3 Toy Monte Carlo

In order to test the robustness of the fit model, before extracting the parameter of interest in the data, validation tests are performed by means of the "toy MC" studies, using generated "toy samples" or pseudo experiments. These allow, using "pull" distributions, to estimate the potential biases that can arise from the model. In order to get a realistic estimation of these biases, each toy sample, must be statistically equivalent to the real data sample. In other words, the different categories present in the fit model must have yields and characteristics

corresponding to these expected in data. The pull of a free parameter a in the i-th pseudo experiment is defined as:

$$pull_i = \frac{a_i^{fit} - a_i^{true}}{\sigma_i^{fit}} \ , \tag{5.24}$$

where a_i^{fit} and σ_i^{fit} correspond to the fitted value of a parameter and its fit-error, respectively. In case the parameter is unbiased, the corresponding pull distribution is a gaussian of zero mean and unity width. Otherwise, the pull distribution gives the bias in units of the statistical error.

Two types of toy studies are used in the present thesis: *pure* and *embedded*. Pure toys consist in generating pseudo experiments using the fit model itself. They allow to determine which PDF parameters can be varied in the fit, and are sensitive, for instance to biases due to small number of events. Embedded toy studies use reconstructed MC events for signal and certain backgrounds, embedded within generated samples for the other categories. They are sensitive to reconstruction effects, such as correlations between variables. We ensure that for each embedded category, a MC event does not appear twice, and thus the limitation of these studies is the number of statistically independent MC samples that can be used to construct the pull distribution. Significant biases observed in these studies could then be corrected in the fit to data.

5.4.4 The ${}_s\mathcal{P}lot$ technique

The ${}_s\mathcal{P}lot$ technique corresponds to a background subtracting method fully described in Ref. [101]. It takes place in the context of a unbinned extended maximum likelihood fit, making use of the discriminating variables denoted y. We can express the log likelihood as:

$$\mathcal{L} = \sum_{e=1}^{N} \ln \left(\sum_{i=1}^{\mathrm{N_s}} N_i f_i(y_e) \right) - \sum_{i=1}^{\mathrm{N_s}} N_i \ , \tag{5.25}$$

where N is the total number of events considered, $\mathrm{N_s}$ is the number of species populating the data sample, N_i is the number of events expected on the average for the i^{th} species, y represents the set of discriminating variables, which can be correlated with each other and $f_i(y_e)$ is the value of the Probability Density Function of y for the i^{th} species and for event e. Let us define another variable x, whose distributions are unknown for a particular source of events, and which is uncorrelated with y.

The aim of the ${}_s\mathcal{P}lot$ formalism is to unfold the true distribution, $\mathbf{M}_{\mathrm{n}}(x)$, of a the variable x for events of the n^{th} species (any one of the $\mathrm{N_s}$ species), from the sole knowledge of the PDFs of the discriminating variables f_i. The advantage of the ${}_s\mathcal{P}lot$ technique is to allow building histograms in x keeping all signal events while removing all background events, and propagating the statistical uncertainties per bin in x. Therefore, this method is more powerful than simpler methods consisting of placing cuts to enhance signal, mainly because this reduces the number of signal events and does not completely filter out backgrounds events.

When considering two sets of uncorrelated variables x and y, the total PDFs $f_i(x,y)$ all factorize into products $\mathbf{M}_{\rm i}(x)f_i(y)$. A fit having been performed to determine the yields N_i for all species, one can define, for all events, a weight (called ${}_s$Weight) defined by:

$$ {}_s\mathcal{P}_{\rm n}(y_e) = \frac{\sum_{j=1}^{\rm N_s} \mathbf{V}_{{\rm n}j} f_j(y_e)}{\sum_{k=1}^{\rm N_s} N_k f_k(y_e)} \ , \tag{5.26} $$

where $\mathbf{V}_{{\rm n}j}$ is the covariance matrix, such as its inverse, $\mathbf{V}^{-1}_{{\rm n}j}$, is related to the second derivatives of $-\mathcal{L}$:

$$ \mathbf{V}^{-1}_{{\rm n}j} = \frac{\partial^2(-\mathcal{L})}{\partial N_{\rm n} \partial N_{\rm j}} \ . \tag{5.27} $$

These ${}_s$Weights can be used to build an estimate, denoted ${}_s\tilde{\rm M}_{\rm n}$, of the x-distribution of the species labelled n (signal or background):

$$ N_{\rm n}\ {}_s\tilde{\rm M}_{\rm n}(\bar{x})\delta x \equiv \sum_{e \subset \delta x} {}_s\mathcal{P}_{\rm n}(y_e) \ , \tag{5.28} $$

where the sum runs over the events for which the x value lies in the bin centered on $\bar{x}$ and of total width δx. The fact that the covariance matrix $\mathbf{V}_{{\rm n}j}$ explicitly enters the ${}_s$Weight definition implies that locally the ${}_s\mathcal{P}lot$ histogram can be negative, due to the fact that the ${}_s$Weights are not positive definite. Nevertheless, the ${}_s\mathcal{P}lot$ histogram reproduces, on average, the true binned distribution of variable x:

$$ \left\langle N_{\rm n}\ {}_s\tilde{\rm M}_{\rm n}(x) \right\rangle = N_{\rm n}\mathbf{M}_{\rm n}(x) \ . \tag{5.29} $$

The ${}_s\mathcal{P}lot$ formalism implies some nice properties, such as that each x-distributions is properly normalized. The sum over the x-bins of $N_{\rm n}\ {}_s\tilde{\rm M}_{\rm n}\delta x$ is equal to $N_{\rm n}$. Moreover, in each bin, the sum over all species of the expected numbers of events equals to the number of events actually observed.

Some limitations of the ${}_s\mathcal{P}lot$ formalism need to mentioned. For instance, as already emphasized, in order to correctly reproduce the true $N_{\rm n}\mathbf{M}_{\rm n}(x)$ distribution, the variable x must be uncorrelated with the discriminating variables y. Moreover, the procedure described above is only valid in the case where the yields, N_i, of all event categories present in the fit are let free to vary. Otherwise, the ${}_s\mathcal{P}lot$ formalism can to be extended, and corrections to the $\left\langle N_{\rm n}\ {}_s\tilde{\rm M}_{\rm n}(x) \right\rangle$ must be applied in order to reproduce the true $N_{\rm n}\mathbf{M}_{\rm n}(x)$ distribution, as described in appendix B of Ref. [101]. One must then distinguish two cases: either the x-distributions of the fixed categories are well known, using other sources of information, or not. In the former case, the correction procedure is rather straight forward. However, this is not often the case, and the x-distributions of the fixed categories are usually taken from MC, and therefore cannot be fully trusted. The extended ${}_s\mathcal{P}lot$ can still be applied in this last case, but the statistical price to pay can be prohibitive.

Chapter 6

Analysis of $B^+ \to K^+\pi^-\pi^+\gamma$ decays: study of the $K\pi\pi$ resonant structure

Contents

The main purpose of the charged-channel analysis is to extract the dilution factor $\mathcal{D}_{K^0_S\rho\gamma}$, assuming Isospin asymmetry, as described in detail in Sec. 6.8. Its expression is related to the amplitudes of the three resonant modes, and the interferences among them, contributing to the $K\pi\pi$ final state. Namely these modes are the $K\rho^0(770)$ and the $K^{*0}(892)\pi$ P-waves as well as the $(K\pi)^0\pi$ S-wave. Their amplitudes and the corresponding interferences among them are extracted from a fit to the signal-TM[1] $m_{K\pi}$ spectrum (see Sec. 6.7). The $m_{K\pi}$ fit model relies on the relative fractions of each kaonic resonance contributing to our signal. Lacking better source of information, these are, in a preliminary stage of the analysis, taken from existing measurements and from theoretical estimations as described in Sec. 6.1. In order to extract these quantities from the data, we first perform a fit to the $m_{K\pi\pi}$ spectrum (see Sec. 6.6), from which we extract the amplitudes of each of the considered kaonic resonance. Both the $m_{K\pi}$ and $m_{K\pi\pi}$ spectra for signal-TM events are extracted from a fit to $m_{\rm ES}$, ΔE and the Fisher discriminant detailed in Sec. 6.5, using the ${}_s\mathcal{P}lot$ technique.

6.1 Signal Monte Carlo cocktail

Several different resonances may contribute to the $K^+\pi^-\pi^+$ spectrum. We model our signal with a cocktail of the exclusive MC samples listed in Tab. 5.1.

Each of the channels is weighted according to the branching fractions given below (Tab. 6.1, 6.2). The measured branching fractions in Tab. 6.1 are taken from Ref. [23]. The other ones having not been measured, we take ansatz values estimated from theoretical papers. For the mode $B \to K_1(1400)\gamma$, Belle published the upper limit $\mathcal{B}(B \to K_1(1400)\gamma) < 15.0 \times 10^{-6}$; we use 8.0×10^{-6}, which corresponds to typical values predicted by Ref. [102, 103]. Lacking better information, and as done in the previous *BABAR* analysis [104], we take the same rate for $\mathcal{B}(B \to K^*(1410)\gamma)$. Finally, for $\mathcal{B}(B \to K^*(1680)\gamma)$ we take, as suggested by theoretical estimations (Ref. [102, 103]), a smaller branching fraction: 2.0×10^{-6}. These branching fractions are applied in the cocktail used to study the signal probability density functions

[1] detailed in Sec. 6.3

Table 6.1: Assumed branching fractions for the signal cocktail.

Signal mode	Assumed $\mathcal{B}(10^{-6})$	$\sigma_{\mathcal{B}}$ (10^{-6})	Reference
$B \to K_1(1270)\gamma$	43.0	1.2	Measured [23]
$B \to K_1(1400)\gamma$	8.0	$\emptyset$	Theoretical (estimation)
$B \to K^*(1410)\gamma$	8.0	$\emptyset$	Theoretical (estimation)
$B \to K_2^*(1430)\gamma$	14.5	4.3	Measured [23]
$B \to K^*(1680)\gamma$	2.0	$\emptyset$	Theoretical (estimation)

Table 6.2: Assumed branching fractions for decays of kaonic resonances into our signal mode.

Signal mode	Assumed $\mathcal{B}(10^{-2})$	$\sigma_{\mathcal{B}}^{Exp.}$ (10^{-2})
$K_1(1270)^+ \to K^+\pi^-\pi^+$	32.85	11.6
$K_1(1400)^+ \to K^+\pi^-\pi^+$	42.19	13.4
$K^*(1410)^+ \to K^+\pi^-\pi^+$	40.52	$\emptyset$
$K_2^*(1430)^+ \to K^+\pi^-\pi^+$	13.92	1.45
$K^*(1680)^+ \to K^+\pi^-\pi^+$	23.76	3.07

Table 6.3: Assumed branching fractions for decays of B mesons into our signal mode and their relatives weights. More accurate values for the relative weight are extracted from a fit to the data, and used thereafter (see Sec. 6.6).

Signal mode	Assumed $\mathcal{B}$ (10^{-6})	$\sigma_{\mathcal{B}}^{Exp.}$ (10^{-6})	Relative Weights	σ_{RW}
$B^+ \to K_1(1270)^+(K^+\pi^-\pi^+)\gamma$	14.1	2.86	0.608	0.145
$B^+ \to K_1(1400)^+(K^+\pi^-\pi^+)\gamma$	3.38	$\emptyset$	0.145	$\emptyset$
$B^+ \to K^*(1410)^+(K^+\pi^-\pi^+)\gamma$	3.24	$\emptyset$	0.140	$\emptyset$
$B^+ \to K_2^*(1430)^+(K^+\pi^-\pi^+)\gamma$	2.02	0.08	0.087	0.011
$B^+ \to K^*(1680)^+(K^+\pi^-\pi^+)\gamma$	0.47	$\emptyset$	0.020	$\emptyset$
$B^+ \to K^+\pi^-\pi^+\gamma$ + c.c.	23.2	2.9	1.0	0.08

(PDFs) and in validation tests. More accurate values are then extracted from the fit to data (see Sec. 6.6.2) and used thereafter.

Furthermore, to compute the weights we multiply the above numbers by the decay branching fractions corresponding to all contributing resonant and non-resonant modes, listed in Ref. [24]. Table 6.2 summarizes the overall branching fraction of each kaonic resonance into our signal mode. Note that in the case of $K^*(1410)$ decays, the only measured decay branching fraction is $\mathcal{B}(K^*(1410) \to K\pi) = 6.6 \times 10^{-2}$, other branching frac-

tions being reported as upper limits ($\mathcal{B}(K^*(1410) \to K\rho) < 7 \times 10^{-2}$) or lower limits ($\mathcal{B}(K^*(1410) \to K^*\pi) > 40 \times 10^{-2}$). Therefore, we fix the $\mathcal{B}(K^*(1410) \to K\rho)$ value to its upper limit and take the fraction not accounted neither by $K\pi$ nor by $K\rho$ intermediate states as the $\mathcal{B}(K^*(1410) \to K^*\pi)$ value. Table 6.3 summarizes the different weights applied for the signal cocktail. Finally, we apply a global scale to the entire cocktail to make it equivalent to the integrated luminosity of our On-Resonant data sample.

6.2 Event Selection

For candidate selection from MC and data samples, a skim is first applied, as described in Sec. 6.2.1. In a second stage, several selection cuts are used (Sec. 6.2.2).

At the first order, the candidate selection for the present analysis relies on the selection criteria from the previous *BABAR* analysis [104] that considered several $K\pi\pi\gamma$ modes. Then we modify these criteria to optimize the sensitivity to $B^+ \to K^+\pi^-\pi^+\gamma$ events. This optimization procedure is described in Sec. 6.2.3. Some signal events, after event selection, contain multiple candidates. Section 6.2.4 describes the technique applied for multiple candidate selection.

6.2.1 Skim

In order to reduce the data sample, a skim is applied before any other selection criteria. It generally consists of loose requirements, which can be used by several different analyses. In the present analysis, we use the `BtoXGamma` skim available in the *BABAR* code. It is applied to both data and MC samples. This skim selects events passing the `BGFMultiHadron` [105] filter that requires at least three tracks in the `RecoGoodTracksLoose` list, which are matching the EMC clusters. The skim also requires a high-energy photon, consistent with a radiative B decay, and that the CM energy of the highest-energy photon candidate in the event falls between 1.5 and 3.5 GeV, corresponding to the range of the photon energy spectrum in radiative B decays, as taken from semi-inclusive analyses of $B \to X_s\gamma$ decays (see Refs. [106, 107] and references therein).

6.2.2 Selection cuts

Some of the selection variables used in the present analysis have already been described in Chapter 5. Additional selection variables, which are described below, are also used in order to enrich the data sample in signal events.

6.2.2.1 High-energy photon selection

The high-energy photons, which are taken from the `GoodPhotonLoose` list, are further required to pass the following selection criteria:

- No dead or noisy crystals in the cluster;

- $-0.74 < \cos\theta_\gamma < 0.93$, where θ_γ corresponds to the angle with respect to the beam of the EMC cluster centroid in the lab frame (i.e. the polar angle);

- The three-dimensional distance between the centroid of the EMC cluster and the centroid of the nearest cluster is greater than 25 cm. This isolation requirement suppresses photons from π^0 and η decays;

6.2.2.2 Vetos of π^0 and η

As in our signal mode we have a high energy photon, most of our photon background originates from misreconstructed π^0 and η-mesons. Indeed, these fake photons either come from asymmetric decays of π^0 and η (one of the photons takes most of the energy of the decaying particle) or from merged decays (the decaying particle has a high momentum in the CM frame therefore the two outgoing photons cannot be properly separated in the EMC). To reduce these backgrounds, the photon candidate γ_1 is associated with all other photons γ_2 in `CalorNeutral` list. Then we construct the π^0 and η likelihood functions, defined as

$$\mathcal{LR} = \frac{p(m_{\gamma_1\gamma_2}, E_{\gamma_2}|\theta)}{p(m_{\gamma_1\gamma_2}, E_{\gamma_2}|K^+\pi^+\pi^-\gamma) + p(m_{\gamma_1\gamma_2}, E_{\gamma_2}|\theta)}, \tag{6.1}$$

where θ is either π^0 or η, and p is a probability density function in terms of $m_{\gamma_1\gamma_2}$, and the energy of γ_2 in the lab frame, E_{γ_2}. The π^0 (η) $\mathcal{LR}$ is between zero and one, and the larger the value is, the more likely it is that γ_1 comes from the π^0 (η) decay. Details on the $\mathcal{LR}$ construction can be find elsewhere [108]. Figures 6.1 and 6.2 show the π^0 and η likelihood function distributions, respectively. We select the events satisfying:

- $\mathcal{LR}_{\pi^0} < 0.86$,

- $\mathcal{LR}_{\eta} < 0.957$.

The cut values where optimized using the procedure described in Sec. 6.2.3. The cut on $\mathcal{LR}_{\pi^0}$, if applied before any other cuts, retains $\sim$ 93% of signal events, while it rejects $\sim$ 83% of continuum events and $\sim$ 63% of B-background events. The cut on $\mathcal{LR}_{\eta}$, if applied before any other cuts, retains $\sim$ 95% of signal events, while it rejects $\sim$ 87% of continuum events and $\sim$ 10% of B-background events.

Vetoes are also applied on photon candidates invariant mass, $m_{\gamma_1(e^+e^-)}$, when one photon converts to an (e^+e^-) pair by interacting with the detector. Here we select the events satisfying:

- $|m_{\gamma_1(e^+e^-)} - m_{\pi^0}| > 25\,\mathrm{MeV}/c^2$,

- $|m_{\gamma_1(e^+e^-)} - m_{\eta}| > 50\,\mathrm{MeV}/c^2$.

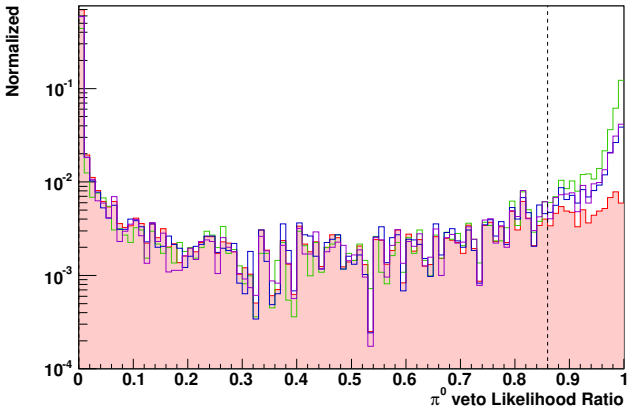

Figure 6.1: Normalized distributions of π^0 Likelihood ratio for signal MC events (red area), *Off-Peak* data (green), generic B^+B^- backgrounds (blue) and generic $B^0\overline{B}^0$ backgrounds (violet). The vertical dashed line shows the corresponding selection cut. All other selection cuts have been applied.

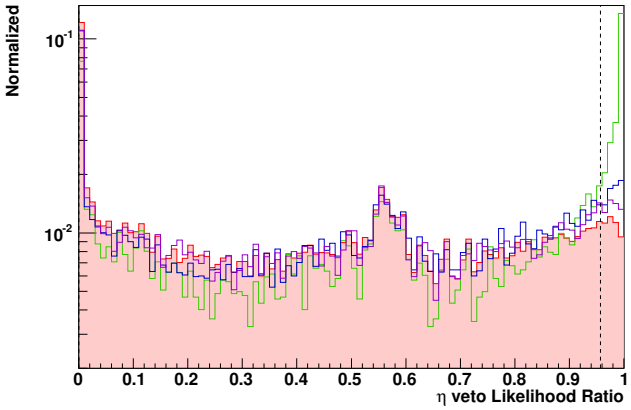

Figure 6.2: Normalized distributions of η Likelihood ratio for signal MC events (red area), *Off-Peak* data (green), generic B^+B^- backgrounds (blue) and generic $B^0\overline{B}^0$ backgrounds (violet). The vertical dashed line shows the corresponding selection cut. All other selection cuts have been applied.

6.2.2.3 Photon-merged π^0 consistency

To discriminate between merged π^0-mesons and photons, we use a standard *BABAR* algorithm [109]. The latter calculates the likelihood for the EMC deposit to be a π^0 or a γ by evaluating, for a given hypothesis $h = \pi^0$ or $h = \gamma$, the expression:

$$\mathcal{L}_h = \frac{M_h^2 - E^2(S - S_\gamma)}{\sigma(M_h^2)}$$

where S is the second moment of the energy deposit and M_h^2 is the invariant mass of the energy deposit under the hypothesis h. We select the events satisfying $\mathcal{L}_h < 0.00031$. This

cut, if applied before any other cuts, retains $\sim 97\%$ of signal events, while it rejects $\sim 9\%$ of continuum events and $\sim 4\%$ of B-background events.

6.2.2.4 Invariant mass of the $K^+\pi^-\pi^+$ system

In the present analysis, we do not expect the $K^+\pi^-\pi^+$ resonance mass region above $1.8\,\mathrm{GeV}/c^2$ to contain a large fraction of signal events, while we expect a significant number of background events, as shown in Fig. 6.3. Therefore, we restrict the $K^+\pi^-\pi^+$ resonance mass to the region $m_{K\pi\pi} < 1.8\,\mathrm{GeV}/c^2$.

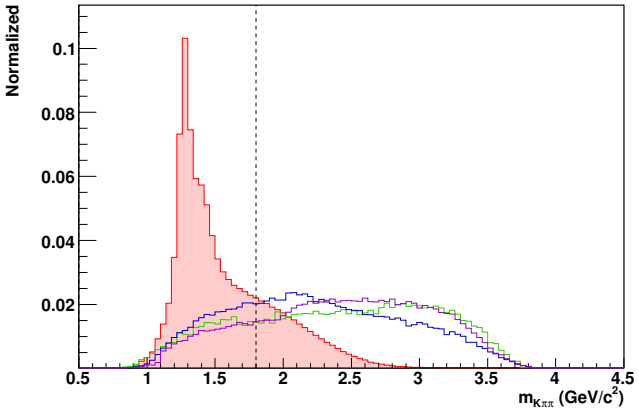

Figure 6.3: Normalized distributions of $m_{K\pi\pi}$ for signal MC events (red area), *Off-Peak* data (green), generic B^+B^- backgrounds (blue) and generic $B^0\overline{B}^0$ backgrounds (violet). The vertical dashed line shows the corresponding selection cut. All other selection cuts have been applied.

6.2.2.5 Kinematic variables

Three kinematic cuts are applied. The first one, a basic sanity check, selects events with total energy less than 20 GeV. In addition, we require m_{ES} and ΔE to be:

- $m_{\mathrm{ES}} > 5.20\,\mathrm{GeV}/c^2$;
- $|\Delta E| < 0.2\,\mathrm{GeV}$.

Figure 6.4 shows the discriminating power of these last two variables.

6.2.2.6 Kaon PID

The K^+ candidates are required to satisfy the `LooseKMKaon` selector. The K^+ track is also required to satisfy the `GoodTracksLoose`.

6.2.2.7 Pion PID

Both of the $\pi^\pm$ candidates are required to satisfy the `SuperLooseKMPion` selector. The $\pi^\pm$ track are also required to satisfy the `GoodTracksLoose`.

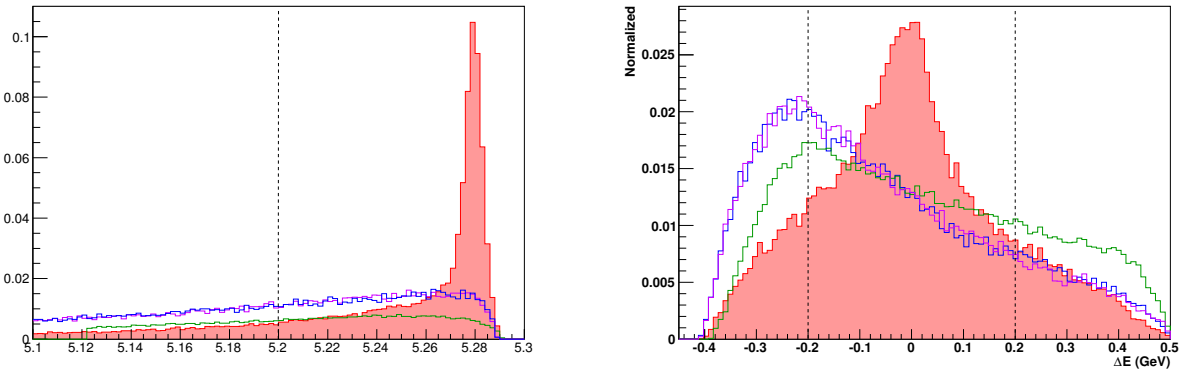

m_{ES} ΔE

Figure 6.4: Normalized distributions of the two kinematical variables entering into the fit model, m_{ES} (left) and ΔE (right) for signal MC events (red area), *Off-Peak* data (green), generic B^+B^- backgrounds (blue) and generic $B^0\overline{B}^0$ backgrounds (violet). Note that in the case of m_{ES}, the *Off-Peak* distribution is shifted towards lower values of $\sim 0.02\,\mathrm{GeV}/c^2$ compared to the other contributions. This is due to the fact that the corresponding data are taken at a CM energy about 40 MeV below the $\Upsilon(4S)$ resonance peak mass. The vertical dashed lines show the selection cut applied. All other selection cuts have been applied.

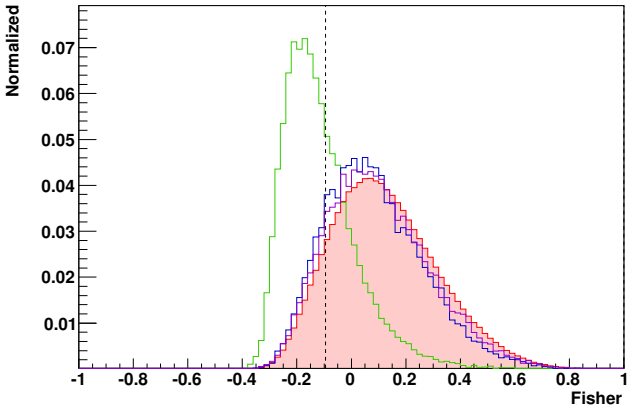

Figure 6.5: Normalized distributions of Fisher discriminant for signal MC events (red area), *Off-Peak* data (green), generic B^+B^- backgrounds (blue) and generic $B^0\overline{B}^0$ backgrounds (violet). The vertical dashed line shows the corresponding selection cut. All other selection cuts have been applied.

6.2.2.8 Event shape variable: Fisher discriminant

As described in Sec. 5.3.3 a unique variable, combining the information from six event shape variables, is used in the present analysis. Figure 6.5 shows the distributions of the Fisher discriminant for $K^+\pi^+\pi^-\gamma$ signal MC and different backgrounds (*Off-Peak* data, B^+B^- and $B^0\overline{B}^0$ generic MC). Figure 6.6 gives the linear correlations among the six event shape variables used to build the Fisher discriminant. We observe no strong correlations for the signal event category. Since the Fisher discriminant is used in the maximum likelihood fit, the applied

cut value is not optimized using the optimization procedure described in Sec. 6.2.3. We select candidates with a Fisher discriminant output value greater than -0.095. This cut is chosen in order to retain, if applied before any other cut, $\sim 90\%$ of signal events. This allows to reject $\sim 60\%$ of continuum events and $\sim 10\%$ of B-background events.

6.2.2.9 Vertex selection

As described in Sec. 5.2.4, the B candidates are formed by fitting the vertex of all the final state particles, using tracks or cluster information in case of charged particles or the photon,

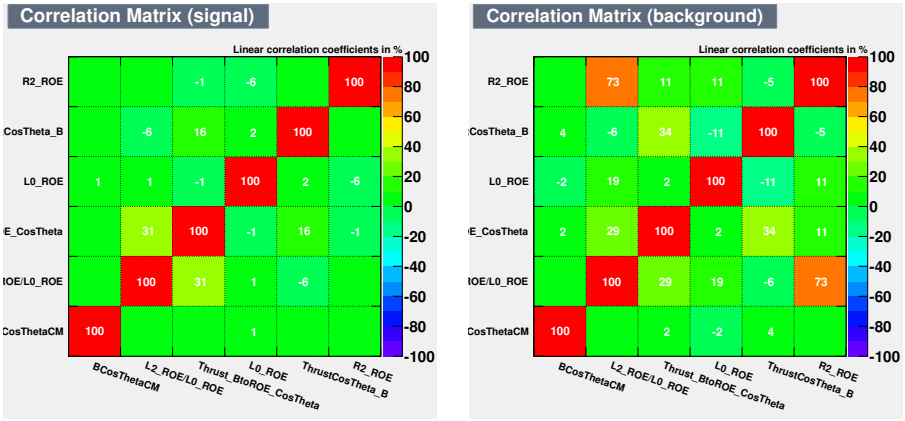

(a) (b)

Figure 6.6: Linear correlations between the variables used in the Fisher discriminant, for signal and continuum background events in (a) and (b), respectively.

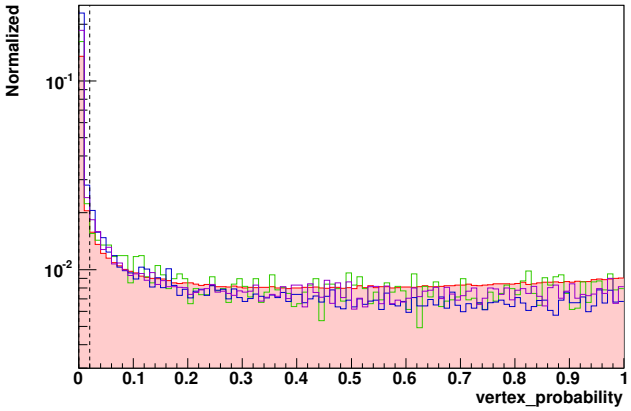

Figure 6.7: Normalized distributions of vertex probability for tracks from the B candidates decay for signal MC events (red area), *Off-Peak* data (green), generic B^+B^- backgrounds (blue) and generic $B^0\overline{B}^0$ backgrounds (violet). The vertical dashed line shows the corresponding selection cut. All other selection cuts have been applied.

respectively. The fit on the decay products of the reconstructed B is performed with a beam spot constraint, where the B candidate trajectory is reconstructed using information from the assumed beam position and the B decay vertex. Although the high-energy photon is included in the fit in order to get higher constraints on the B candidate kinematics, it will not contribute to the vertex information (unless the photon has converted).

In order to reduce combinatoric backgrounds, a cut on the vertex probability, which results from the vertex fit, is applied. Figure 6.7, in a logarithmic y-axis scale, shows that the discriminating point is near zero. From the optimization procedure, described below, we select candidates with a vertex probability greater than 0.0199.

6.2.3 Cut Optimization

The cut optimization was done using the `BumpHunter` algorithm [110] of the `StatPatternRecognition` package. The optimization consists in maximizing the figure of merit (FOM) defined as $S/\sqrt{S+B}$, where S is the yield of truth-matched (TM) signal MC and B is the total yield of backgrounds. Note that both S and B are normalized to the luminosity in the data. The signal yield is estimated from exclusive MC samples, weighted using the cocktail weights given in Tab. 6.2. The total yield of backgrounds (B) corresponds to the sum of the continuum and two (neutral and charged) B-backgrounds contributions. The continuum yield is estimated from the number of events in the *Off-Peak* data sample (after applying the other selection cuts) scaled by a factor 12.3 as described in Sec. 6.4.2. The two B-background yields are taken from the number of events in the neutral and generic $B\overline{B}$ MC samples (after applying the other selection cuts) and scaled by factors 0.31 and 0.29, respectively.

The optimization was done using a set of 7 variables, listed below, in the fit region, for which `BumpHunter` was able to find optimum values in order to maximize the FOM.

- PhotonMergedPi0Consistency, $\mathcal{L}_h$
- Pi0VetoLikelihoodRatio, $\mathcal{LR}_{\pi^0}$
- EtaVetoLikelihoodRatio, $\mathcal{LR}_{\eta}$
- Daug1TrackPID_KSelectorKM, Kaon PID
- Daug2TrackPID_PiSelectorKM, Pion PID
- Daug3TrackPID_PiSelectorKM, Pion PID
- BvtxProbChi2, vertex probability

Figure 6.8 shows there are no significant correlations between the variables used in the cut optimization. The value of the FOM is $S/\sqrt{S+B} \sim 4.66$ after optimization.

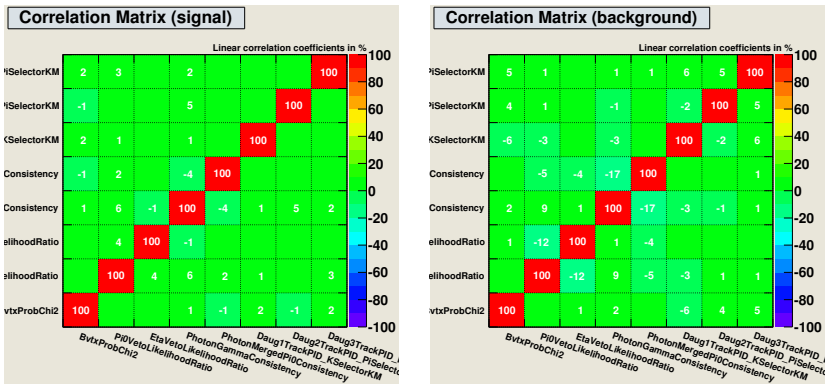

(a) (b)

Figure 6.8: Correlations between the variables used in the cut optimization, for signal and background events in (a) and (b), respectively.

6.2.4 Multiple candidate selection

In this section, we describe the technique used to select a single candidate in events where more than one is reconstructed and passes the selection criteria. We only consider candidates that have already passed all selection cuts described earlier in this chapter. The average number of candidates per event is $\sim$ 1.4, for both signal and B-backgrounds, while the maximum number of candidate can be of 6 or 7 per event.

In order to select the best candidate, we compared a naive random selection to a "best-

Table 6.4: Multiple candidate selection efficiency of all kaonic resonances contributing to our signal mode, for the fit region in $m_{\rm ES}$ ΔE and the Fisher discriminant. Multiple candidate selection efficiency is the ratio of signal-TM events on MC events containing at least one candidate (either TM candidate or not), after all other candidate selection cuts, the fit region cut, and multiple candidate selection.

Signal mode	MCS technique	MCS Efficiency (%)
$K_1(1270)^+$	BvtxProbChi2	90.89 ± 0.56
	Random	85.58 ± 0.53
$K_1(1400)^+$	BvtxProbChi2	90.68 ± 0.52
	Random	84.86 ± 0.50
$K^*(1410)^+$	BvtxProbChi2	91.00 ± 0.56
	Random	85.29 ± 0.53
$K_2^*(1430)^+$	BvtxProbChi2	90.21 ± 0.92
	Random	84.82 ± 0.88
$K^*(1680)^+$	BvtxProbChi2	93.22 ± 0.91
	Random	88.07 ± 0.88

B-vertex-probability" selection. The multiple candidate selection efficiency is defined as the yield of TM signal MC candidates after the dedicated selection, divided by the number of signal MC events in which the TM candidate passes all other cuts. Signal events in which the correct $K^+\pi^+\pi^-\gamma$ combination is not reconstructed at all do not enter into this efficiency, nor do background processes, since for these we do not care which candidate is chosen. Table. 6.4 shows the multiple candidate selection efficiency for both techniques.

We choose to use BvtxProbChi2 as selecting variable for multiple candidate selection, to maximize the multiple candidate selection selection. Note that we also checked that the variable used for the multiple candidate selection was not correlated to the fit variables.

6.2.5 Efficiency

Table 6.5 details, for each of the applied selection criteria, the efficiency in TM signal MC. The reconstruction efficiency, before any cut, is also indicated. In addition, Tab. 6.6 gives the total efficiency once multiple candidate selection is applied. Moreover, Tab. 6.7 shows that the overall efficiencies are comparable between resonances. This observation excludes the $K^*(1680)$, for which the overall efficiency is smaller. This is due to the large width ($\Gamma = 322 \pm 110$ MeV/c^2) of this resonance combined with a pole mass of $m_0 = 1717 \pm 27$ MeV/c^2, near the $K^+\pi^-\pi^+$ invariant mass cut (i.e. $m_{K\pi\pi} < 1.8$ GeV/c^2). This cut is responsible for the significant decrease in efficiency for the $K^*(1680)$.

Table 6.5: Absolute, last- and first-cut efficiencies of candidate selection cuts in TM signal MC. The absolute efficiency is obtained from the product of all the preceding cut efficiencies in the table, including the corresponding one. The reconstruction efficiency is obtained from the ratio between the number of generated and reconstructed events, before any of the cuts is applied. The last- (first-)cut efficiency is the efficiency of the corresponding cut when applied after (before) all the other cuts. Events that satisfy the condition on the cut value are selected. Mass and time cuts are expressed in GeV/c^2 and ps, respectively.

Cut	Value	Absolute efficiency	Last-cut efficiency	First-cut efficiency
Reconstruction	$\emptyset$	0.542	$\emptyset$	$\emptyset$
$m_{K\pi\pi}$	$x < 1.8$	0.517	0.806	0.948
$\mathcal{LR}_{\pi^0}$	$x < 0.86$	0.470	0.907	0.932
$\mathcal{LR}_{\eta}$	$x < 0.957$	0.446	0.947	0.954
$\lvert m_{\gamma_1(e^+e^-)} - m_{\pi^0}\rvert$	$x < 0.025$	0.446	> 0.999	> 0.999
$\lvert m_{\gamma_1(e^+e^-)} - m_{\eta}\rvert$	$x < 0.050$	0.446	> 0.999	> 0.999
B vertex probability	$0.0199 < x$	0.398	0.866	0.917
ΔE	$-0.2 \leq x \leq 0.2$	0.375	0.902	0.936
$m_{\rm ES}$	$5.2 < x$	0.375	0.866	> 0.999
Fisher	$x > -0.095$	0.339	0.878	0.911
$\mathrm{B}_{\Delta t}$	$-20 \leq x \leq 20$	0.337	0.967	> 0.999
$\mathrm{B}_{\sigma_{\Delta t}}$	$x < 2.5$	0.331	0.953	0.983
B vertex status	$x = 0$	0.331	0.985	> 0.999
B tag vertex status	$x = 0$	0.330	0.975	0.998
$\cos\theta_\gamma$	$-0.74 \leq x \leq 0.93$	0.330	> 0.999	> 0.999
Photon bump distance	$25 < x$	0.313	0.920	0.962
Photon track distance	$25 < x$	0.292	0.907	0.937
Photon merged π^0 consistency	$x < 0.00031$	0.283	0.964	0.968
K^+ PID	`LooseKMKaon`	0.234	0.726	0.852
π_1 PID	`SuperLooseKMPion`	0.232	0.945	0.994
π_2 PID	`SuperLooseKMPion`	0.231	0.982	0.994

Table 6.6: Individual and absolute efficiency (product of all the preceding cut efficiencies in the table, including the corresponding one) of candidate selection cuts in TM signal MC.

Cut	Efficiency	Absolute efficiency
Reconstruction	0.542	0.542
Candidate selection	0.426	0.231
MCS	0.909	0.210

Table 6.7: Overall efficiency of TM candidates by resonance in signal MC. The efficiency of $K^*(1680)$ resonance is smaller due to the cut applied on the $K^+\pi^-\pi^+$ invariant mass (i.e. $m_{K\pi\pi} < 1.8$ GeV/c^2). Uncertainties come from MC statistics.

Resonance	$K_1(1270)$	$K_1(1400)$	$K^*(1410)$	$K_2^*(1430)$	$K^*(1680)$
Overal efficiency	0.2130 ± 0.0006	0.2110 ± 0.0013	0.1926 ± 0.0013	0.2092 ± 0.0016	0.1276 ± 0.0020

6.3 Signal study

In this section we present the study of signal events and their separation in two categories: TM and self-cross-feed (SCF). The corresponding PDFs are presented in Sec. 6.5.1.

6.3.1 Truth matching

Qualifying an event as TM or SCF is generally based on MC truth information. As a first criterion (C1 in the following), events are considered as TM when all reconstructed B daughters match the MC truth daughters, and SCF otherwise. This criterion results in wrongly assigning some TM events to the SCF category, mainly in the following cases:

- Photon conversion: the photon has converted into a e^+e^- pair, therefore its particle ID does not match anymore a photon.
- Pion decay: the pion decayed into a muon and a neutrino, therefore its particle ID does not match anymore a pion.
- Kaon/Pion swap: the kaon has been identified as the pion and vice versa[2].

Figure 6.9 shows the fit variables distributions of the TM events wrongly assigned to the SCF category. Table 6.8 gives the relative fraction of events concerned by these three sources of contamination. Finally events are considered as TM if they satisfy the criterion C1 or one of the main cases of mistake listed previously, and SCF otherwise.

[2]It has been realized at an advanced stage of the analysis that the case of Kaon/Pion swap was in fact corresponding to true SCF. Possible effects on the physical parameters extracted in the present analysis due to assigning such events to the signal-TM event category have been studied. These effects were found to be not significant, therefore they are treated as systematic uncertainties (see Sec. 6.9.1.6).

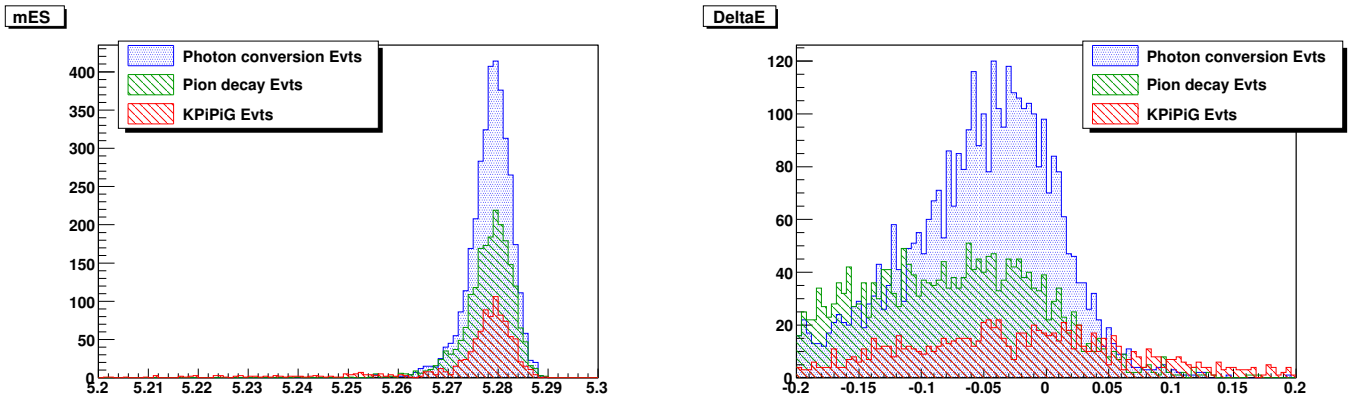

$m_{\rm ES}$ ΔE

Figure 6.9: Distributions of TM events, wrongly assigned to the SCF category, in the two kinematical variables entering the final fit ($m_{\rm ES}$ and ΔE). Photon conversions are presented in blue, the pion decays in green, and the kaon/pion swap in red.

Table 6.8: Fractions of wrongly assigned TM events to the SCF category compared to the total number of events (f_1) as well as to the number of SCF events (f_2), before correction, for each source of contamination.

Contamination source	f_1 (%)	f_2 (%)
Photon conversion	1.41	5.77
Pion decay	0.82	3.35
Kaon/Pion swap	0.37	1.53
Total	2.60	10.65

Table 6.9: $B^+ \to K^+\pi^-\pi^+\gamma$ signal estimated yields for the final *BABAR* Run1-6 dataset. The uncertainties on the estimated yields are dominated by the uncertainties on the branching fractions taken from Refs. [23, 24]. The uncertainties on the fractions come from MC statistics.

Category	Estimated yield	Fraction
Signal TM	2295 ± 306	0.7699 ± 0.0031
Signal SCF	686 ± 91	0.2301 ± 0.0052
Total Signal	2981 ± 397	$\emptyset$

6.3.2 Expected yields

The total signal yield, is estimated multiplying the total number of B mesons expected in the final *BABAR* dataset by the estimated branching fractions of each mode given in Tab. 6.3,

and then by adding the resulting numbers. Then the TM and SCF yields are estimated using the amount of each category extracted from the MC, as given in Tab. 6.9.

6.4 Backgrounds study

As previously mentioned, the backgrounds in the present analysis are of two different types: B backgrounds (discussed in Sec. 6.4.1) and continuum background (discussed in Sec. 6.4.2). Section 6.4.3 gives the expected yields of each background category. The resulting PDFs are presented in Sec. 6.5.2.

6.4.1 B backgrounds

6.4.1.1 General procedure

Using the generic MC samples, corresponding approximately to an integrated luminosity of three times that of the data sample (see Tab. 5.1) we exclude the signal events using MC truth information. We then apply our selection criteria and list all the remaining decay modes by decreasing order of number of events. The ones with the largest expected yields are then studied using the corresponding exclusive MC sample, whose corresponding luminosities are given in Tab. 5.1.

As expected, we observe that the main backgrounds originate from $b \to s\gamma$ processes. As they have, like signal events, a high energy photon in the final state, we consider them as the most dangerous source of background. Section 6.4.1.2 details the study of these backgrounds. Other B backgrounds observed in the generic MC events, are discussed in Sec. 6.4.1.3.

6.4.1.2 Radiative $b \to s\gamma$ backgrounds

From the generic MC, we isolate six dominant radiative B backgrounds, listed in Tab. 6.10. As the size of the generic MC sample does not allow to perform an accurate study of these radiative B backgrounds, we use exclusive MC datasets, as described in Sec. 5.1.1.

We separate these six dominant radiative B backgrounds in two groups. The first one is composed of "low multiplicity" decays with only three particles in the final state. Namely, those are the $B \to K\pi\gamma$ decays detailed in Tab. 6.10, where one pion is taken from the other side of the event. All these "low multiplicity" radiative B backgrounds are expected to have comparable distributions in our fit variables. Thus, we combine the $B^0 \to K^{*0}(\to K\pi)\gamma$ and $B^0 \to X_{sd}(\to K\pi)\gamma$ contributions into one category. When doing that, we exclude the contributions coming from X_{sd} for $m_{X_{sd}} < 1.1\,\mathrm{GeV}/c^2$. This takes into account the difficulties of the MC to correctly reproduce data in this range of mass for the X_{sd} decays. However, this mass range is included by the $B^0 \to K^{*0}(\to K\pi)\gamma$ sample. Details on this procedure can be found elsewhere [107]. The same argument holds for the combination of $B^+ \to K^{*+}(\to K\pi)\gamma$ and $B^+ \to X_{su}(\to K\pi)\gamma$ decays.

For the second group of radiative B backgrounds, the "Higher multiplicity" decays of Tab. 6.10, one particle or more has been missed in the reconstruction. Thus, for these modes the final states are semi inclusive, due to the fact that many of the X_{su} or X_{sd} decays

Table 6.10: Radiative backgrounds contributing to $B^+ \to K^+\pi^-\pi^+\gamma$, observed in the generic MC.

Specificity	Decay mode
$B \to K\pi\gamma$	$B^0 \to K^{*0}(\to K\pi)\gamma$
	$B^0 \to X_{sd}(\to K\pi)\gamma$
	$B^+ \to K^{*+}(\to K\pi)\gamma$
	$B^+ \to X_{su}(\to K\pi)\gamma$
Higher multiplicity decay	$B^0 \to X_{sd}(\nrightarrow K\pi)\gamma$
	$B^+ \to X_{su}(\nrightarrow K\pi)\gamma$

contribute to our background. A detailed study of these decays performed in another *BABAR* analysis [107] shows that the model used to generate and decay the X_{su} and X_{sd} states is not fully accurate, and does not reproduce data. More precisely, the relative fractions between the X_s decay modes are not correct, while the inclusive branching fraction of $B \to X_s\gamma$ is properly modeled. Therefore corrective weights, obtained in Ref. [107], are applied separately to each decay mode. The corresponding weights are given in App. B.

For $B^0 \to X_{sd}(\nrightarrow K\pi)\gamma$ and $B^+ \to X_{su}(\nrightarrow K\pi)\gamma$ decays, there is no obvious reason to think that the charged and the neutral modes should have the same distributions in our fit variables. Indeed, these distributions do not show significant differences. To avoid too many categories in our fit model, we finally merge the charged and neutral X_s decay modes into one category.

6.4.1.3 Other B backgrounds

From generic MC sample we also identified non radiative B backgrounds with small contributions in term of estimated number of events, but with distributions that are similar to those of signal.

The first one is $B^0 \to K^{*0}\eta$ mode, which we isolate into one single category. Here, the η decays into a pair of charged pions ($\pi^+\pi^-$) and one photon. The selection cut applied to the high energy photon explains that this background does not contribute much. To model properly the PDFs of this background category we use an exclusive MC sample given in Tab. 5.1.

We also identified other modes with very little expected numbers of events, but with distributions very close to signal in $m_{\rm ES}$. Using exclusive MC we constructed another category including $B^\pm \to a_1^\pm(\to \rho^0\pi^\pm)\pi^0\gamma$ and $B^\pm \to K^{*0}(\to K\pi)\pi^\pm\pi^0\gamma$ decays labelled "Peaking charmless".

Once the main peaking B-backgrounds were identified, i.e. all the B-backgrounds previously cited, they have been removed from the generic B^+B^- and $B^0\overline{B}^0$ MC samples. All the remaining non-peaking contributions were further grouped into one single category labelled "generic B background".

6.4.2 Continuum background

For the continuum background, we use the complete *Off-Peak* dataset of 44.81 fb^{-1} collected by *BABAR*. To estimate the continuum yield, we need to normalize the number of events passing through the selection criteria using two factors, given in Tab. 6.11. The first one is the ratio of integrated luminosity between *On-Peak* and *Off-Peak* data. The second corresponds to a correction due to a shift in $m_{\rm ES}$ of $-20\,{\rm MeV}/c^2$.

Table 6.11: Normalization factor used to estimate the continuum yield.

Normalization factor	Value
Luminosity ratio	9.66
$m_{\rm ES}$ shift	1.27
Total	12.29

6.4.3 Expected background yields

Table 6.12 gives the yields of the different background categories defined in the $B^+ \to K^+\pi^-\pi^+\gamma$ analysis.

Table 6.12: $B^+ \to K^+\pi^-\pi^+\gamma$ background estimated yields for the final *BABAR* Run1-6 dataset.

Continuum ($udsc$)	70983
$B^0 \to X_{sd}(\nrightarrow K\pi)\gamma$ $B^+ \to X_{su}(\nrightarrow K\pi)\gamma$	2872
$B^0 \to K^{*0}(\to K\pi)\gamma$ $B^0 \to X_{sd}(\to K\pi)\gamma$	1930
Generic B-background	1065
$B^+ \to K^{*+}(\to K\pi)\gamma$ $B^+ \to X_{su}(\to K\pi)\gamma$	442
$B^0 \to K^{*0}\eta$	56
$B^\pm \to a_1^\pm(\to \rho^0\pi^\pm)\pi^0\gamma$ $B^\pm \to K^{*0}(\to K\pi)\pi^\pm\pi^0\gamma$	17
Total Bkg	77365

6.5 Fit to $m_{\rm ES}$, ΔE and Fisher

Here we present the fit performed on $m_{\rm ES}$, ΔE and the Fisher discriminant in order to extract the $m_{K\pi\pi}$ and $m_{K\pi}$ ${}_s\mathcal{P}lots$ of the signal-TM category. The fit was performed using the `Laura++` package [96]. Sections 6.5.1 and 6.5.2 detail the PDFs use in the fit model and the correlations between the fit variables for the signal and the backgrounds categories, respectively. Then Sec. 6.5.3 summarizes the fitting functions. Section 6.5.4 presents the validation tests of the fit model. Finally, Sec. 6.5.5 gives the projections and the yields extracted from the fit.

6.5.1 Signal PDFs

Probability density functions for the TM and SCF signal events are constructed using the cocktail of signal MC samples (Tab. 6.3). The TM and SCF PDFs for each discriminating variable entering the fit model are shown in Figs. 6.10 and 6.11, respectively. We can observe that the shape of the ΔE distribution of the SCF is slightly bended and that the linear function used to parametrize the distribution can not account for this feature. Possible effects on the physical parameters extracted in the present analysis due to the ΔE parametrization of the SCF have been studied. These effects were found to be not significant, therefore the are treated as systematic uncertainties (see Sec. 6.9.1.5). The total number of events shown in these figures is normalized to the expected yield, given in Tab. 6.9. Details on the function used to describe the PDFs presented below are available in Appendix A.

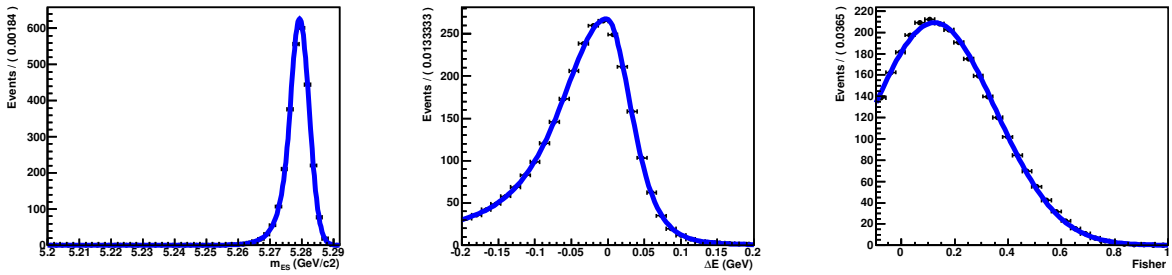

Figure 6.10: Probability density functions for the fit variables $m_{\rm ES}$ (left), ΔE (center) and the Fisher discriminant (right) of signal-TM category. Here the $m_{\rm ES}$ PDF is described by a Crystal Ball function, the ΔE PDF by a Cruijff and the Fisher discriminant PDF by a gaussian. The blue curves represent the PDF distributions, and the black points correspond to MC events.

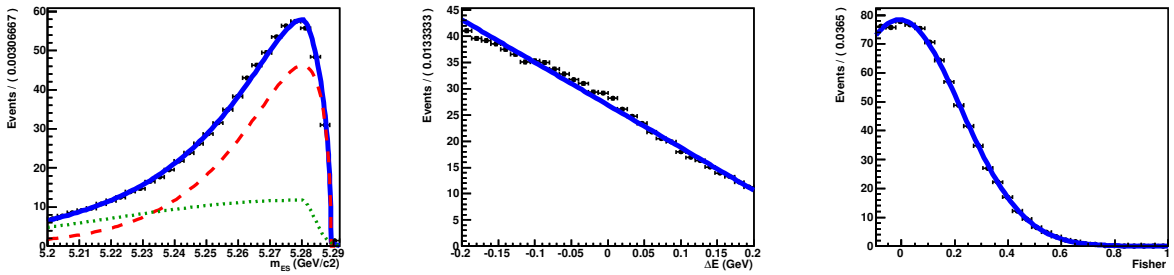

Figure 6.11: Probability density functions for the fit variables $m_{\rm ES}$ (left), ΔE (center) and the Fisher discriminant (right) of signal SCF category. Here the $m_{\rm ES}$ PDF is described by the sum of a Bifurcated Gaussian function (green dotted line) and an Argus (red dashed line), the ΔE PDF by a linear function and the Fisher discriminant PDF by a gaussian. The blue curves represent the PDF distributions, and the black points correspond to MC events.

Correlations among the fit variables for signal events

We checked for possible correlations among our fit variables. No significant correlations were found between the Fisher discriminant and both $m_{\rm ES}$ and ΔE. However between $m_{\rm ES}$ and ΔE, for which correlations may be induced by event reconstruction, some significant correlations were found. A priori we expect to have significant correlations for the signal SCF category. However, it is in the signal-TM component that the stronger correlations appear. We split MC signal events into three bins in $m_{\rm ES}$ and three bins in ΔE. Figures 6.12 and 6.13 show the $m_{\rm ES}$ (ΔE) distributions in ΔE ($m_{\rm ES}$) bins for the signal SCF and TM categories, respectively. From these distributions, we decided to take $m_{\rm ES}$-ΔE correlations into account for signal-TM events. This is done by implementing a two-dimensional PDF for $m_{\rm ES}$-ΔE. As previously shown in Sec. 6.5.1, the $m_{\rm ES}$ and ΔE PDFs were parametrized by 1-dimensional functions. To allow conserving a parametric function for the signal-TM PDFs while accounting for $m_{\rm ES}$-ΔE correlations, we use a two-dimensional conditional PDF. It is constructed as the product of a conditional PDF (Crystal Ball for $m_{\rm ES}$) by a marginal PDF (Cruijff for ΔE). Thus, by construction, the $m_{\rm ES}$ dependence in ΔE is chosen to be explicit while ΔE dependence remains implicit. The Crystal Ball depends on four parameters and is defined as:

$$\mathrm{CB}(x;\mu,\sigma,\alpha,n) = \frac{1}{a}\begin{cases} \left(\frac{n}{\alpha}\right)^n \frac{\exp(-\alpha^2/2)}{((\mu-x)/\sigma+n/\alpha-\alpha)^n} & x \le \mu-\alpha\sigma \\ \exp\left[\frac{1}{2}\left(\frac{x-\mu}{\sigma}\right)^2\right] & x > \mu-\alpha\sigma \end{cases} \tag{6.2}$$

where μ and σ describe a Gaussian, which is truncated on the low side at $\mu-\alpha\sigma$ and joined continuously to a power function with exponent n; $1/a$ is a normalization constant.

The $m_{\rm ES}$ Crystal Ball parameters dependence in ΔE was studied in ten bins (with various sizes) in ΔE, as listed in Tab. 6.13. For each of the ten subsets, we perform an unbinned maximum likelihood fit to extract the Crystal Ball parameters.

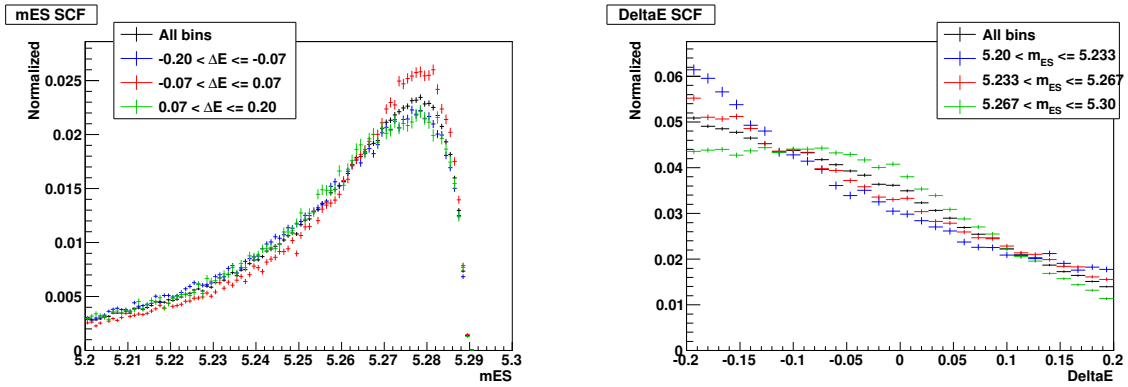

Figure 6.12: $m_{\rm ES}$ (left) and ΔE (right) distributions of SCF events in ΔE and $m_{\rm ES}$ bins, respectively

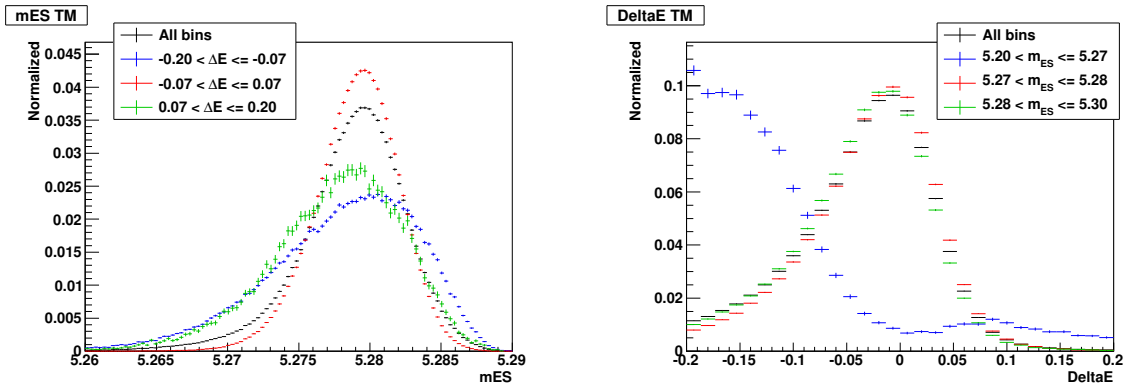

Figure 6.13: $m_{\rm ES}$ (left) and ΔE (right) distributions of TM events in ΔE and $m_{\rm ES}$ bins, respectively

Table 6.13: ΔE bins definition for the $m_{\rm ES}$ Crystal Ball parameters dependence in ΔE.

ΔE bin number	ΔE range (GeV)
0	$[-0.20\,;\,-0.15[$
1	$[-0.15\,;\,-0.10[$
2	$[-0.10\,;\,-0.07[$
3	$[-0.07\,;\,-0.04[$
4	$[-0.04\,;\,-0.01[$
5	$[-0.01\,;\,0.02[$
6	$[0.02\,;\,0.05[$
7	$[0.05\,;\,0.10[$
8	$[0.10\,;\,0.15[$
9	$[0.15\,;\,0.20]$

The following polynomial functions are used to describe the evolution of the Crystal-Ball parameters between ΔE bins:

- μ and σ: second order polynomial function [Fig. 6.14];
- α and n: first order polynomial function [Fig. 6.15].

As a consistency check, we generated toy data samples using this two-dimensional conditional PDF parametrization for each ΔE bin and extracted the Crystal-Ball parameters by a fit. Figures 6.14 and 6.15 show the ΔE-dependent $m_{\rm ES}$ Crystal Ball parameters obtained from both MC and generated toy data samples. As another consistency test, we compared MC

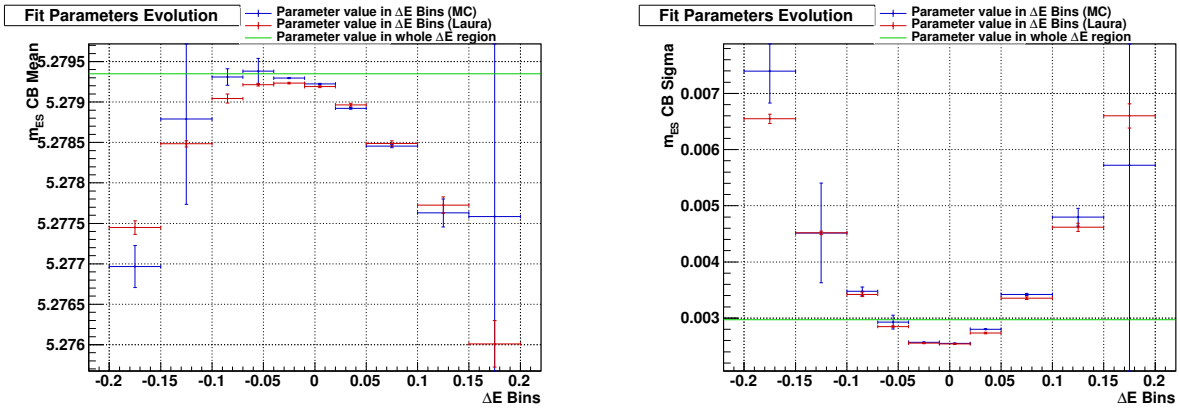

Figure 6.14: $m_{\rm ES}$ Crystal Ball μ (left) and σ (right) parameters evolution in ΔE bins. Blue points correspond to MC sample, red points to a toy sample generated using the two-dimensional conditional PDF, and the green horizontal line corresponds to a 1-dimensional Crystal-Ball PDF without $m_{\rm ES}$-ΔE correlations. The central value of each point is the fitted value of the Crystal Ball parameter, the vertical error bars correspond to the parameter fit error and the horizontal error bars to the size of each ΔE bin.

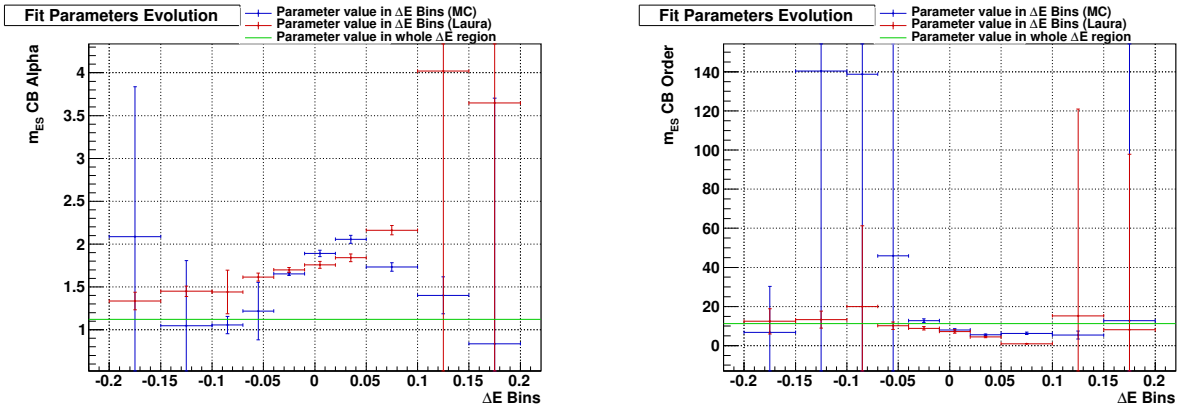

Figure 6.15: $m_{\rm ES}$ Crystal Ball α (left) and n (right) parameters evolution in ΔE bins. Conventions are identical as those of Fig. 6.14.

and generated $m_{\rm ES}$ fit projection distributions for each ΔE subset. Figures D.6 to D.7 in appendix D.2.1, show these fit projections. Even if the Cruijff parameters dependence in $m_{\rm ES}$ bins is not explicitly parametrized we also did consistency tests, comparing the MC and generated ΔE fit projection distributions in each $m_{\rm ES}$ bin. This is not shown in this section, but can be found in appendix D.1.

6.5.2 Background PDFs

Here we present the probability density functions of all the background categories previously defined. They are presented in decreasing order of expected yields, in Figs. 6.16 to 6.22. The total number of events is always normalized to the expected yield for each category. Details on the function used to describe the PDFs presented below are available in Appendix A. Note that when constructing the PDFs for one particular observed B-background mode, we ensure, using MC truth information, that none of the other identified background modes appear in the decay of the other B meson in the event. This procedure ensures that the PDFs corresponding to a given mode are not contaminated by contributions from the other identified background modes.

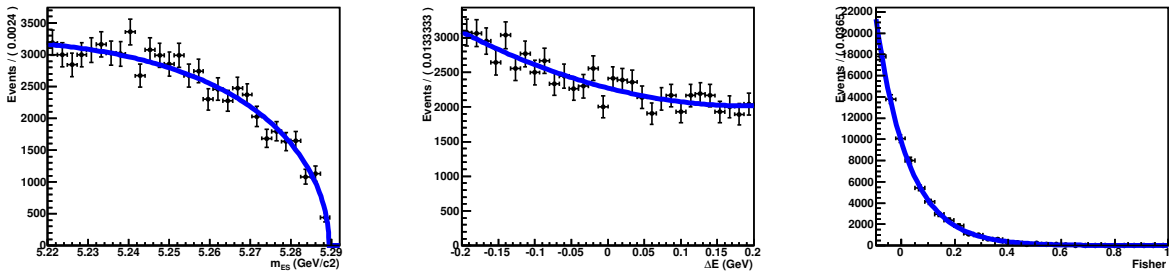

Figure 6.16: Probability density functions for the fit variables $m_{\rm ES}$ (left), ΔE (center) and the Fisher discriminant (right) of continuum ($udsc$) background category. The blue curve represent the PDF distribution, and the black points correspond to MC events. Here the $m_{\rm ES}$ PDF is described by an Argus, the ΔE PDF by an order 2 Chebychev polynomial and the Fisher discriminant by an exponential.

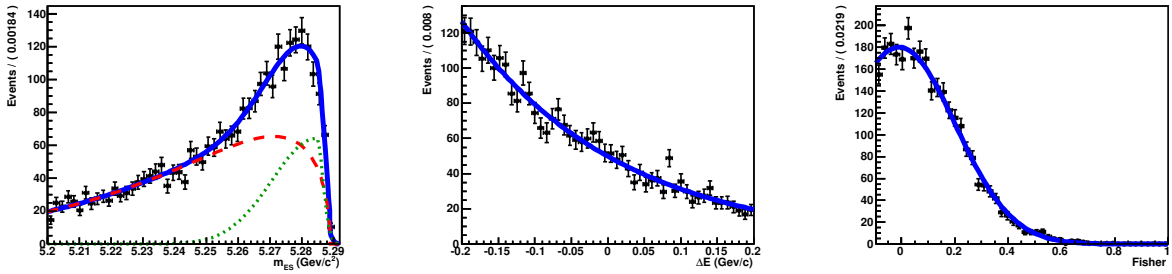

Figure 6.17: PDFs of $B^0 \to X_{sd}(\nrightarrow K\pi)\gamma + B^+ \to X_{su}(\nrightarrow K\pi)\gamma$ B-background category. Conventions are similar to those of Fig. 6.16. Here the $m_{\rm ES}$ PDF is described by the sum of a Cruijff (green dotted line) and an Argus (red dashed line), the ΔE PDF by an exponential and the Fisher discriminant by a gaussian.

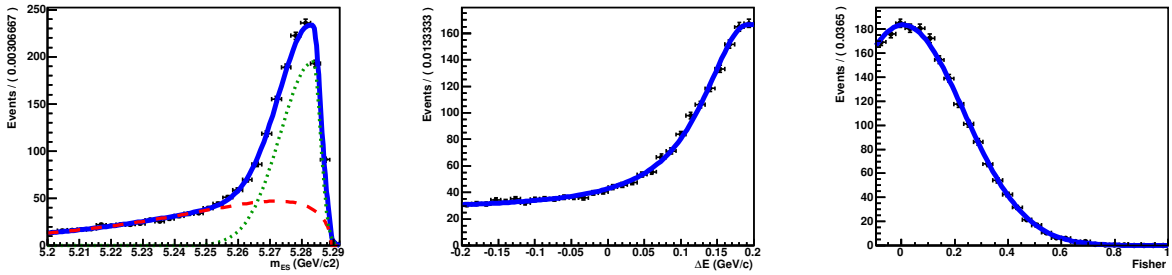

Figure 6.18: PDFs of $B^0 \to K^{*0}(\to K\pi)\gamma + B^0 \to X_{sd}(\to K\pi)\gamma$ background category. Conventions are similar to those of Fig. 6.16. Here the $m_{\rm ES}$ PDF is described by the sum of a Cruijff (green dotted line) and an Argus (red dashed line), the ΔE and the Fisher PDFs discriminant are described by Cruijffs.

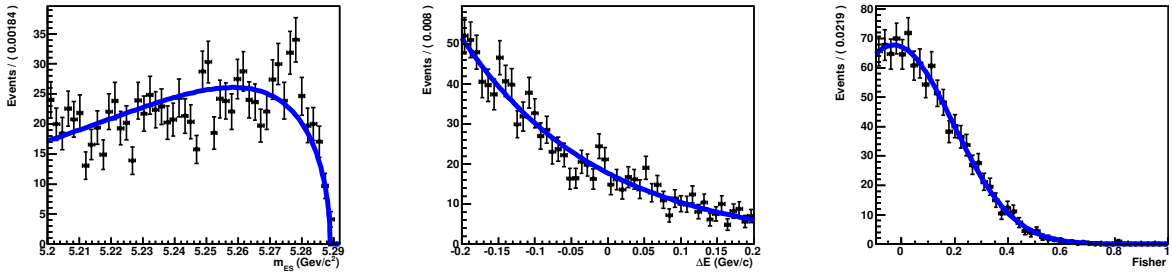

Figure 6.19: PDFs of generic B-background category. Conventions are similar to those of Fig. 6.16. Here the $m_{\rm ES}$ PDF is described by an Argus, the ΔE PDF by an exponential and the Fisher discriminant by a Gaussian.

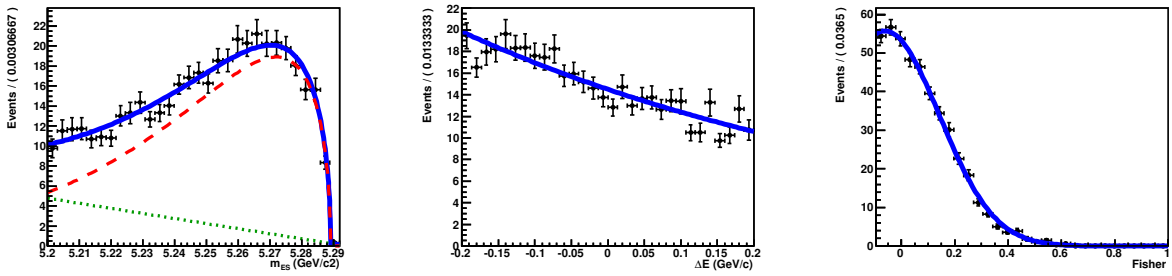

Figure 6.20: PDFs of $B^+ \to K^{*+}(\to K\pi)\gamma + B^+ \to X_{su}(\to K\pi)\gamma$-background category. Conventions are similar to those of Fig. 6.16. Here the $m_{\rm ES}$ PDF is described by the sum of a linear function (green dotted line) and an Argus (red dashed line), the ΔE PDF by exponential function and the Fisher discriminant PDF is described by a Cruijff.

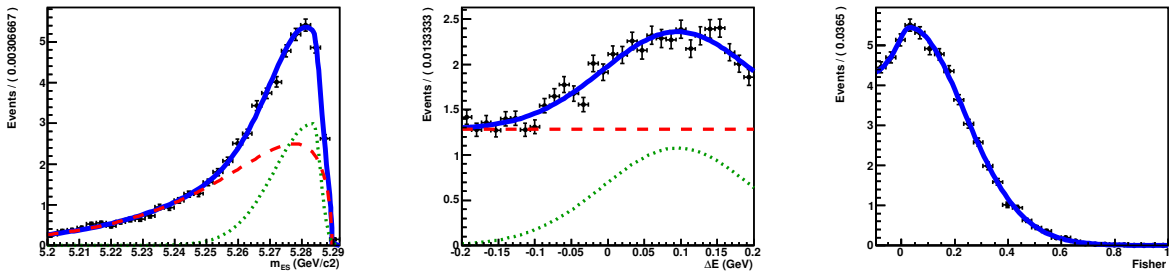

Figure 6.21: PDFs of $B^0 \to K^{*0}\eta$ background category. Conventions are similar to those of Fig. 6.16. Here the $m_{\rm ES}$ PDF is described by the composition of a Cruijff (green dotted line) and an Argus (red dashed line), the ΔE PDF by the composition of a gaussian (green dotted line) and a constant function (red dashed line). The Fisher discriminant PDF is described by a Cruijff.

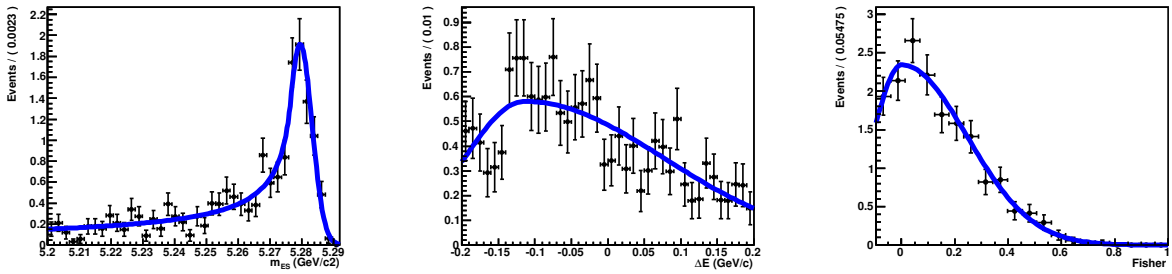

Figure 6.22: PDFs of charmless peaking background category. Conventions are similar to those of Fig. 6.16. Here the $m_{\rm ES}$ PDF is described by a Crystal Ball, the ΔE and the Fisher discriminant PDFs by bifurcated gaussians.

Correlations among the fit variables for background events

As for signal events, we checked for possible correlations between the fit variables. Again, no significant correlations were found between the Fisher discriminant and both $m_{\rm ES}$ and ΔE. We present the study of the correlations between $m_{\rm ES}$ and ΔE for the four main B-background components (in terms of expected yields). Figures 6.23 to 6.26 show $m_{\rm ES}$ (ΔE) distributions in ΔE ($m_{\rm ES}$) bins, for the following B-background categories :

- $B^0 \to X_{sd}(\nrightarrow K\pi)\gamma \; + \; B^+ \to X_{su}(\nrightarrow K\pi)\gamma$ [Fig. 6.23];
- $B^+ \to K^{*+}(\to K\pi)\gamma \; + \; B^+ \to X_{su}(\to K\pi)\gamma$ [Fig. 6.24];
- $B^0 \to K^{*0}(\to K\pi)\gamma \; + \; B^0 \to X_{sd}(\to K\pi)\gamma$ [Fig. 6.25];
- Generic B background [Fig. 6.26].

We do not observe significant $m_{\rm ES}$-ΔE correlations, except for the $B^0 \to K^{*0}(\to K\pi)\gamma \; + \; B^0 \to X_{sd}(\to K\pi)\gamma$ in Fig. 6.24. Thus, we take these correlations into account using a two-dimensional PDF. However, as we do not intend to vary any of the corresponding PDF parameters in the fit to data, we use a non parametric two-dimensional PDF for $m_{\rm ES}$-ΔE. The histogram is taken from a cocktail of MC events.

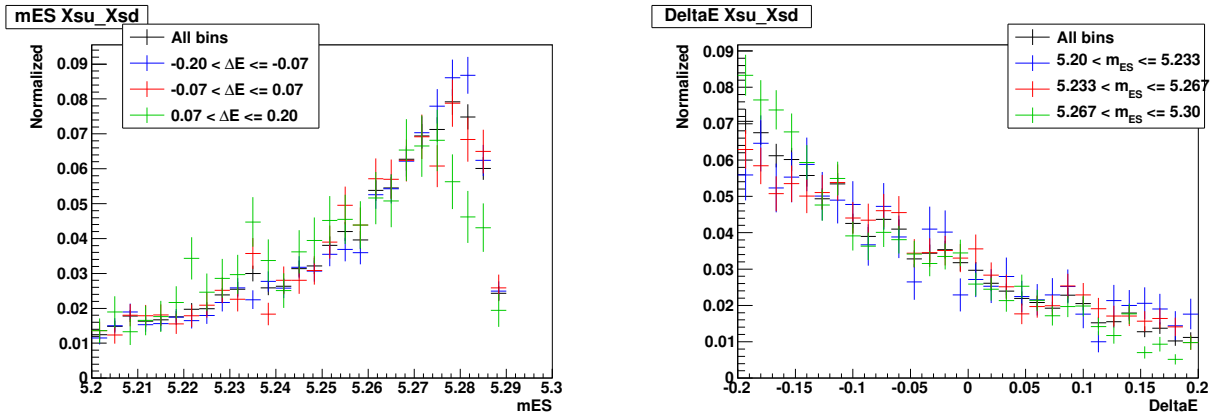

Figure 6.23: $m_{\rm ES}$ (left) and ΔE (right) distributions of $B^0 \to X_{sd}(\nrightarrow K\pi)\gamma \; + \; B^+ \to X_{su}(\nrightarrow K\pi)\gamma$ events in ΔE and $m_{\rm ES}$ bins, respectively

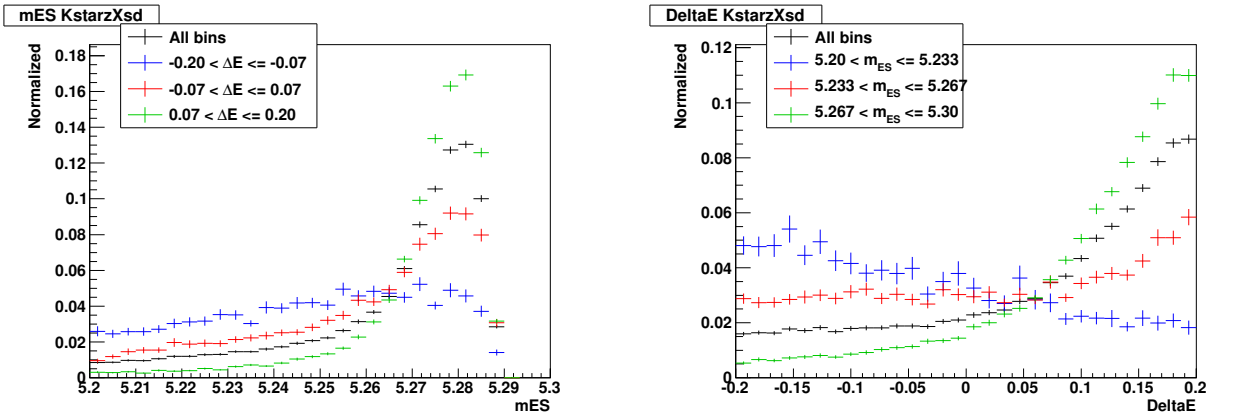

Figure 6.24: $m_{\rm ES}$ (left) and ΔE (right) distributions of $B^0 \to K^{*0}(\to K\pi)\gamma + B^0 \to X_{sd}(\to K\pi)\gamma$ events in ΔE and $m_{\rm ES}$ bins, respectively

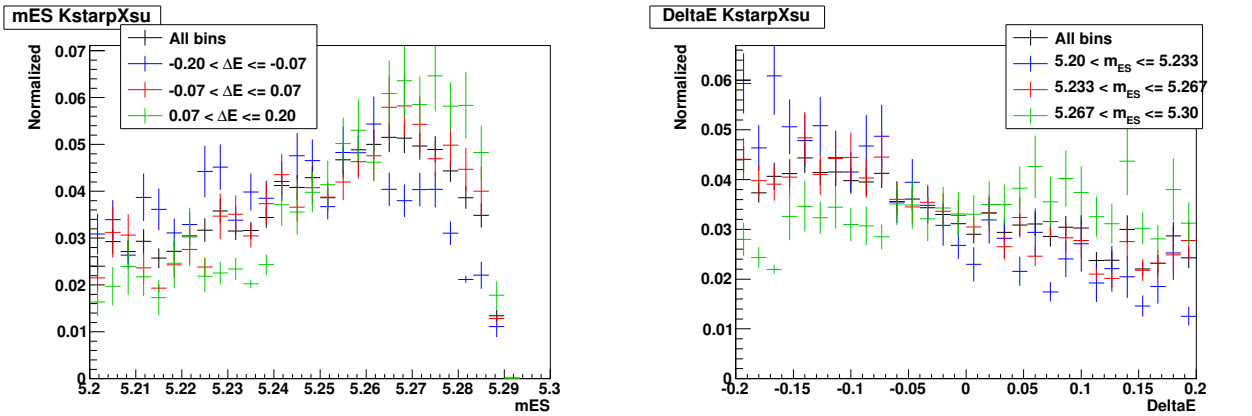

Figure 6.25: $m_{\rm ES}$ (left) and ΔE (right) distributions of $B^+ \to K^{*+}(\to K\pi)\gamma + B^+ \to X_{su}(\to K\pi)\gamma$ events in ΔE and $m_{\rm ES}$ bins, respectively

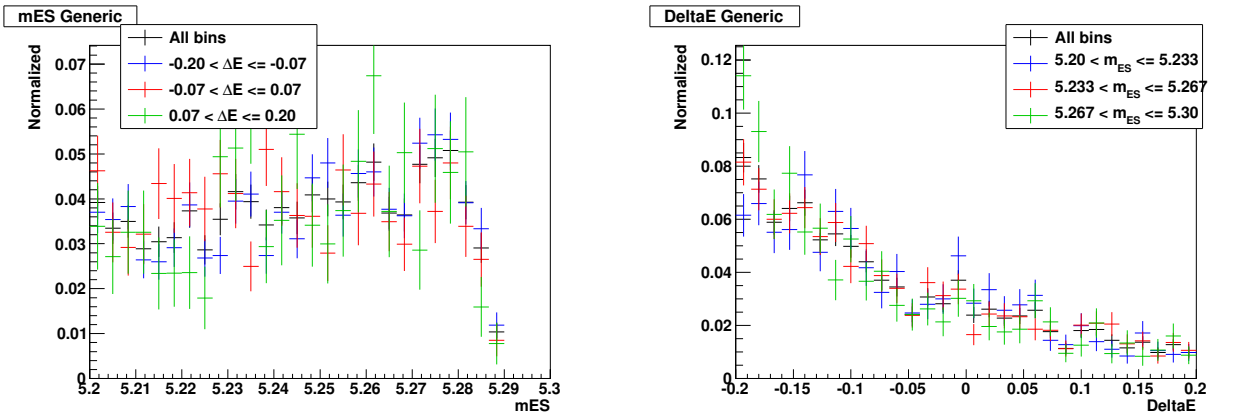

Figure 6.26: $m_{\rm ES}$ (left) and ΔE (right) distributions of generic B background events in ΔE and $m_{\rm ES}$ bins, respectively

6.5.3 Fitting functions

Table 6.14 summarizes the choice of functions used to parametrize the different fit components. Note that for both signal-TM and $B^0 \to K^{*0}(\to K\pi)\gamma$ + $B^0 \to X_{sd}(\to K\pi)\gamma$ categories, the PDF functions are two-dimensional. This is motivated by the correlations that arise between $m_{\rm ES}$ and ΔE, as shown in Secs. 6.5.1 and 6.5.2, respectively.

Table 6.14: Summary of all the fit components and the functions used to parametrize their PDFs.

Fit component	PDF function		
	$m_{\rm ES}$	ΔE	Fisher
Signal TM	Two-dimensional parametric (Crystal Ball – Cruijff)		Gaussian
SCF	Argus + Bifurcated Gaussian	Linear	Gaussian
Continuum $udsc$	Argus	Chebychev ($2^{\rm nd}$ order)	Exponential
$B^0 \to X_{sd}(\not\to K\pi)\gamma$ $B^+ \to X_{su}(\not\to K\pi)\gamma$	Cruijff + Argus	Exponential	Gaussian
$B^0 \to K^{*0}(\to K\pi)\gamma$ $B^0 \to X_{sd}(\to K\pi)\gamma$	Two-dimensional non parametric		Cruijff
$B^+ \to K^{*+}(\to K\pi)\gamma$ $B^+ \to X_{su}(\to K\pi)\gamma$	Argus + Linear	Exponential	Cruijff
Generic B-background	Argus	Exponential	Gaussian
$B^0 \to K^{*0}\eta$	Cruijff + Argus	Gaussian + Constant	Cruijff
Small Charmless Peaking	Crystal Ball	Bifurcated Gaussian	Bifurcated Gaussian

6.5.4 Validation tests

In order to test the robustness of our model before fitting the data, we perform validation tests by means of the toy-MC studies (see Sec. 5.4.3).

6.5.4.1 Pure toy studies

We use our fitter to generate an ensemble of 331 pseudo experiments using the PDFs listed in Tab. 6.14. In each pseudo experiment, the yield of each category is randomly generated from a Poisson distribution (aka "poissonized") corresponding to its expected value (Tabs. 6.9 and 6.12 for signal and background yields, respectively). The values of shape parameters are

extracted from all the MC information available for signal and B background. For continuum background the shape parameters are extracted from Run1-6 *Off-Peak* data sample.

The usual signal description uses a single yield for the total signal, and a fraction of SCF events. However we found out that, using this description, strong correlations appear between the fit parameters. Details about this are given in appendix E.1. We therefore separate the signal-TM and SCF components, using two separated yields in our model. This choice is also due to the fact that we only use the signal-TM component to extract the needed information for the $B^0 \to K^0_S\rho^0\gamma$ analysis.

We use the nominal PDF to fit each of the 331 pseudo-experiments. Due to the large number of shape parameters (greater than 100) we fix many of them, mainly in the background PDFs. Several combinations were tested in order to maximize the number of floated parameters in order to reduce systematic uncertainties without impairing the fit ability to discriminate the different components. As a result, we fix all the B-background shape parameters, as well as some of their yields. Indeed, as some of them have similar PDF shapes, the fitter has difficulties to discriminate them. Namely we fix the $B^+ \to K^{*+}(\to K\pi)\gamma$ + $B^+ \to X_{su}(\to K\pi)\gamma$, $B^0 \to X_{sd}(\nrightarrow K\pi)\gamma$ + $B^+ \to X_{su}(\nrightarrow K\pi)\gamma$, $B^0 \to K^{*0}\eta$ and Peaking charmless yields, letting all the others vary. Furthermore, we fix all the SCF shape parameters as well as the Gaussian parameters of the Fisher discriminant PDF for the

Table 6.15: Means and widths of pull distributions of all the floated parameters entering the model from the pure toy studies.

	Fit variable	Fit Parameter	Pull Mean	Pull Width
Signal TM	$m_{\rm ES}$	CB_μ(Coeff0)	0.079 ± 0.052	0.946 ± 0.037
		CB_μ(Coeff1)	0.035 ± 0.052	0.950 ± 0.037
		CB_μ(Coeff2)	0.009 ± 0.056	1.001 ± 0.039
		CB_σ(Coeff0)	-0.060 ± 0.047	1.085 ± 0.042
		CB_σ(Coeff1)	-0.098 ± 0.054	0.980 ± 0.038
		CB_σ(Coeff2)	-0.116 ± 0.058	1.053 ± 0.041
	ΔE	Cr_μ	0.004 ± 0.048	0.870 ± 0.034
		Cr_{σ_L}	0.067 ± 0.053	0.958 ± 0.037
	Fisher	G_μ	-0.037 ± 0.054	0.991 ± 0.039
		G_σ	-0.012 ± 0.052	0.943 ± 0.037
udsc	$m_{\rm ES}$	Arg_ξ	-0.031 ± 0.054	0.989 ± 0.038
	ΔE	Chebychev(Coeff0)	-0.037 ± 0.056	1.017 ± 0.040
		Chebychev(Coeff1)	-0.090 ± 0.055	1.000 ± 0.039
Yields		Signal TM	0.094 ± 0.059	1.090 ± 0.042
		Continuum *udsc*	0.034 ± 0.057	1.032 ± 0.040
		Generic B-background	-0.063 ± 0.056	1.027 ± 0.040
		$B^0 \to K^{*0}(\to K\pi)\gamma$	0.006 ± 0.054	0.980 ± 0.038
		$B^0 \to X_{sd}(\to K\pi)\gamma$		

continuum *udsc*. For the signal, we found that it is possible to vary the Gaussian parameters of the Fisher discriminant, the Cruijff parameters μ and σ_L and all the evolution coefficients of Crystal Ball parameters μ and σ describing the ΔE polynomial dependence of $m_{\rm ES}$ in the two-dimensional PDF.

Table 6.15 gives the results of the pure toy studies, showing the mean and width of the pull distributions of each floated parameter in our model. We conclude from these results that the model has no intrinsic dysfunction. Note that the fit convergence rate is 100%, and that all the pull distributions are gaussian of means and widths that are compatible, within the statistical uncertainties, with 0 and 1, respectively. Figures 6.27 and 6.28 show the pull distributions for the floated yields in the fit model. Pull distributions of the shape parameters can be found in Appendix E.2.

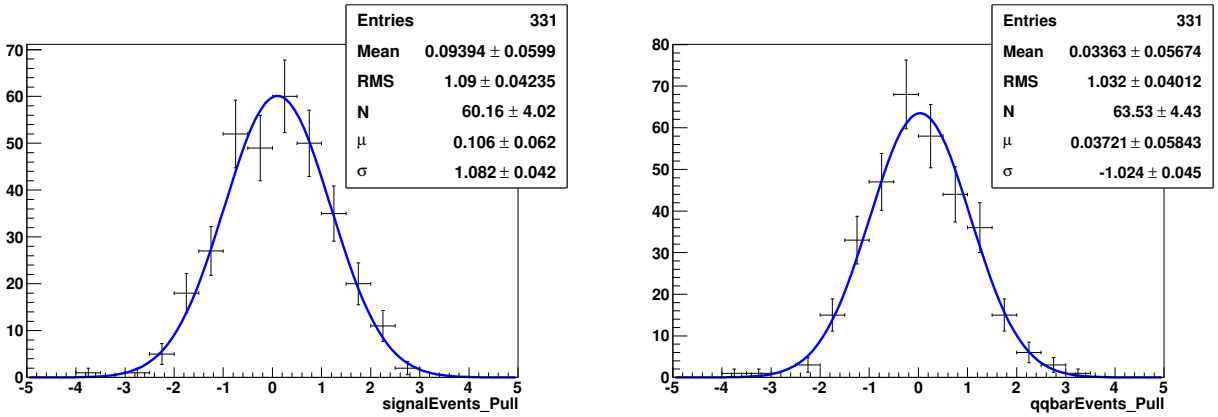

Figure 6.27: Signal-TM (left) and continuum *udsc* (right) yield pull distributions for the pure toy studies with 331 toys, respectively.

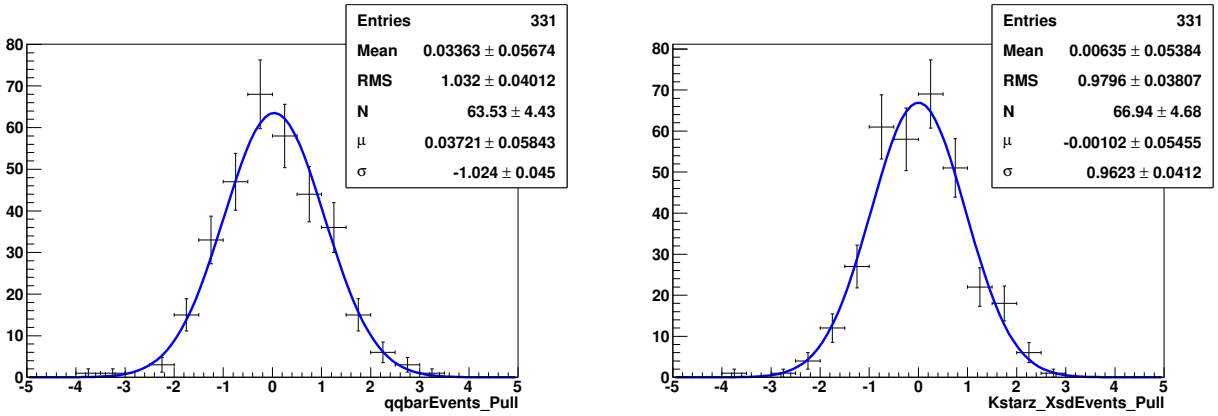

Figure 6.28: Generic B background (left) and $B^0 \to K^{*0}(\to K\pi)\gamma$ + $B^0 \to X_{sd}(\to K\pi)\gamma$ (right) yield pull distributions for the pure toy studies with 331 toys, respectively.

6.5.4.2 Embedded toy studies

In the so called "embedded toys", pseudo experiments are produced by generating events out of the PDFs for the simpler species (background categories with no significant correlation among the fit variables), whereas events for signal (TM and SCF) and B background $B^0 \to K^{*0}(\to K\pi)\gamma$ + $B^0 \to X_{sd}(\to K\pi)\gamma$ are drawn from the fully reconstructed MC samples. 331 of such pseudo experiments are generated, which are then fitted using the same PDFs as in the pure toy studies. The yield of each category is poissonized around their expected value. Table 6.16 gives the results of the embedded toy studies, showing the means and widths of the pull distributions of each floated parameter in the model.

From these results, we conclude that our model has no significant bias on the signal-TM yield. As shown in Sec. 6.5.4.3 no significant biases are found in the relevant mass spectra. We observe some significant biases in the other yields, due to complicated correlations between the corresponding categories, where events migrate from one to others. Some significant biases also appear in shape parameters, but again, this is not of any issue here since this does not affect the signal-TM yield. Therefore, we do not correct for any biases that appear in the embedded pulls. Note that the fit convergence is 100%, and that all the

Table 6.16: Means and widths of pull distributions of all the floated parameters entering the model from the embedded toy studies.

	Fit variable	Fit Parameter	Pull Mean	Pull Width
Signal TM	$m_{\rm ES}$	CB_μ(Coeff0)	0.706 ± 0.057	1.042 ± 0.040
		CB_μ(Coeff1)	-0.338 ± 0.058	1.048 ± 0.040
		CB_μ(Coeff2)	-0.328 ± 0.064	1.180 ± 0.046
		CB_σ(Coeff0)	1.033 ± 0.054	0.983 ± 0.038
		CB_σ(Coeff1)	-0.901 ± 0.053	0.961 ± 0.037
		CB_σ(Coeff2)	-0.681 ± 0.065	1.174 ± 0.046
	ΔE	Cr_μ	-0.061 ± 0.053	0.971 ± 0.038
		Cr_{σ_L}	-0.457 ± 0.063	1.154 ± 0.045
	Fisher	G_μ	0.117 ± 0.057	1.030 ± 0.040
		G_σ	0.116 ± 0.055	0.994 ± 0.039
udsc	$m_{\rm ES}$	Arg_ξ	0.125 ± 0.052	0.948 ± 0.037
	ΔE	Chebychev(Coeff0)	-0.642 ± 0.058	1.056 ± 0.041
		Chebychev(Coeff1)	0.052 ± 0.053	0.957 ± 0.037
Yields		Signal TM	-0.027 ± 0.058	1.050 ± 0.041
		Continuum *udsc*	0.229 ± 0.058	1.054 ± 0.041
		Generic B-background	-0.354 ± 0.057	1.035 ± 0.040
		$B^0 \to K^{*0}(\to K\pi)\gamma$	-0.026 ± 0.055	1.002 ± 0.039
		$B^0 \to X_{sd}(\to K\pi)\gamma$		

pull distributions are gaussian. Figures 6.29 and 6.30 show the pull distributions for the floated yields in the fit model. Distributions of the shape parameter pulls can be found in Appendix E.3.

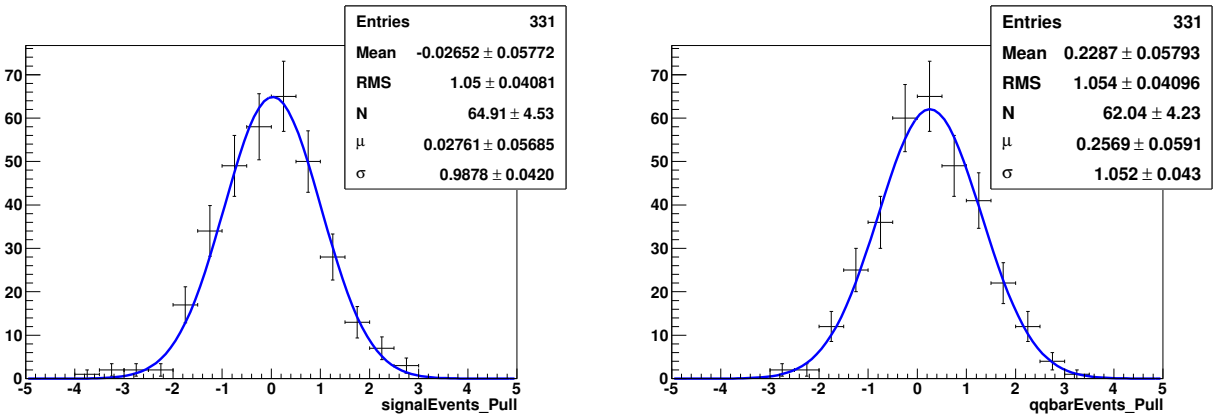

Figure 6.29: Signal-TM (left) and continuum *udsc* (right) yield pull distributions for the embedded toy studies with 331 toys, respectively.

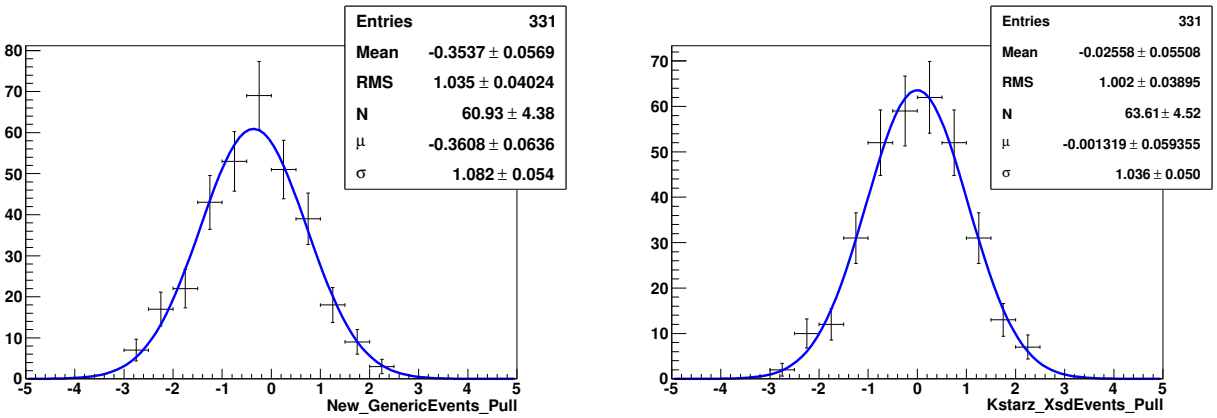

Figure 6.30: Generic B background (left) and $B^0 \to K^{*0}(\to K\pi)\gamma$ + $B^0 \to X_{sd}(\to K\pi)\gamma$ (right) yield pull distributions for the embedded toy studies with 331 toys, respectively.

6.5.4.3 Validation of the invariant mass spectra extraction method

In this section we present the validation tests, performed on MC, of the signal-TM invariant mass spectra extraction method. The tests consist in checking the ability of the fit model to discriminate signal-TM from other events in order to extract the $m_{K\pi\pi}$, $m_{K\pi}$ and $m_{\pi\pi}$ invariant mass distributions using the ${}_s\mathcal{P}lot$ technique[3]. To do so, we compare the ${}_s\mathcal{P}lot$

[3]The ${}_s\mathcal{P}lot$ technique, described in Sec. 5.4.4, allows to extract unknown distributions of one specific category, when the latter is well discriminated from other categories in the extended maximum likelihood fit. In the present analysis the relevant event category is the signal TM, whose yield appears unbiased (see the pull results in Sec. 6.5.4.2), which shows the model ability to discriminate this category.

distributions to the MC-truth ones. We first present the $K^+\pi^-\pi^+$ invariant mass extraction and then the "pseudo-Dalitz-plot" extraction. Indeed in the present analysis, the final state is composed of three charged particles ($K^+\pi^-\pi^+$) and a photon. We define the "pseudo-Dalitz-plot" as the $m^2_{K\pi} - m^2_{\pi\pi}$ plane. This implies that the pseudo-Dalitz-plot plane will not have properly defined phase-space boundaries. The photon is not contributing to any resonance, and its energy is only constrained by $m_{K\pi\pi}$; in the B meson rest frame, the photon recoils back to back with the $K^+\pi^-\pi^+$ system.

Invariant mass spectrum of the $K^+\pi^-\pi^+$ system

From the result of a fit performed on one MC pseudo experiment, we obtain the signal-TM ${}_s$Weights, and apply them to all $m_{K\pi\pi}$ values in the dataset.

Figure 6.31 compares the signal-TM $m_{K\pi\pi}$ distribution obtained using the ${}_s\mathcal{P}lot$ technique to the MC-truth information. There are no significant differences between the two distributions within statistical errors. From this we conclude that the model is able to extract the signal-TM $m_{K\pi\pi}$ spectrum.

Pseudo-Dalitz-plot distributions

We use the same procedure to reconstruct the pseudo-Dalitz-plot signal-TM distributions. Figure 6.32 shows the pseudo-Dalitz-plot distributions between the $K^+\pi^-$ and $\pi^+\pi^-$ invariant mass systems: the signal-TM ${}_s\mathcal{P}lot$, the MC-truth information and the residual distribution between them. Figure 6.33 shows a comparison between the MC truth and ${}_s\mathcal{P}lot$ distributions of the pseudo-Dalitz-plot projections on $m_{K\pi}$ and $m_{\pi\pi}$. As for the $m_{K\pi\pi}$

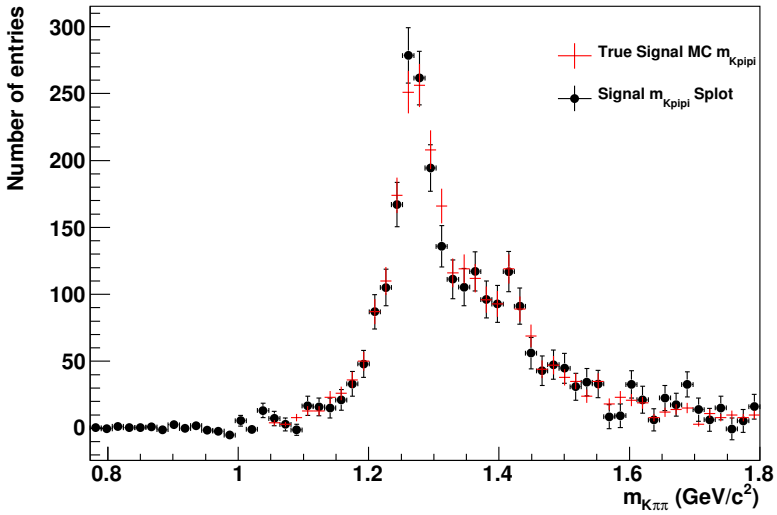

Figure 6.31: Background subtracted $m_{K\pi\pi}$ distribution (data expected statistic). The black points represent the background subtracted $m_{K\pi\pi}$ distribution, and the red points the MC-truth one.

spectrum, we do not observe significant differences between the MC truth and ${}_s\mathcal{P}lot$ distributions.

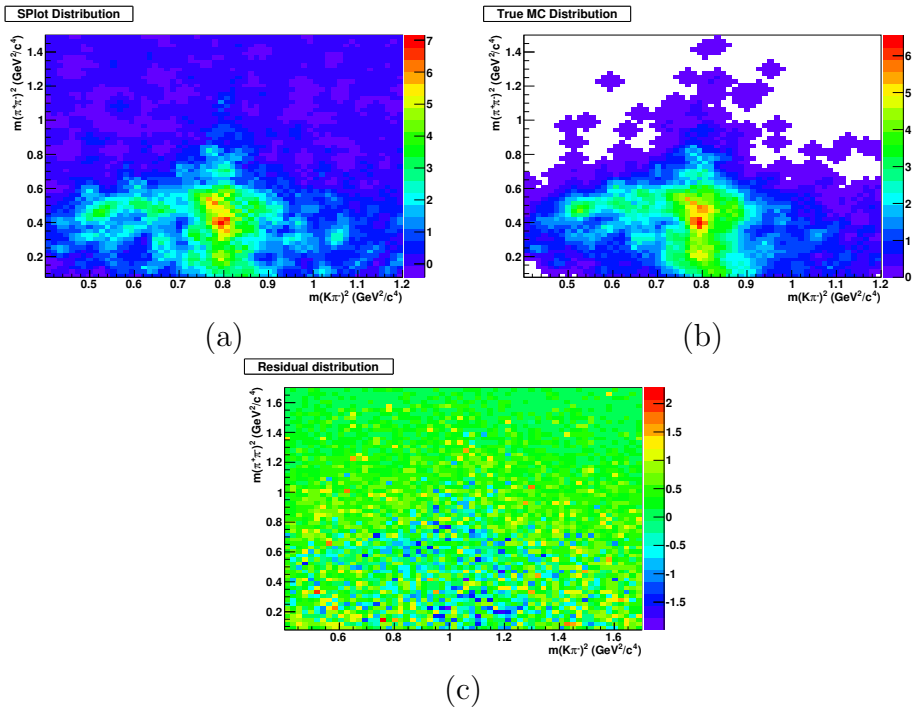

Figure 6.32: Background subtracted (a), MC truth (b) and residual (c) $K^+\pi^-\pi^+$ pseudo-Dalitz-plot distributions between $K^+\pi^-$ and $\pi^+\pi^-$ invariant mass system (data expected statistics). The residuals are obtained by dividing the difference between the histograms (a) and (b) by the square root of their sum. The unit in z corresponds to the number of events for (a) and (b).

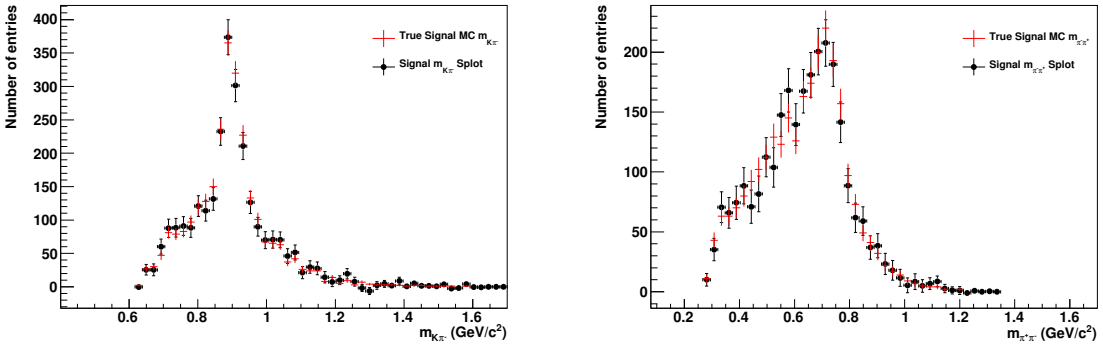

Figure 6.33: $K^+\pi^-$ (left) and $\pi^-\pi^+$ (right) invariant mass distributions (data expected statistic). The black points represent the background subtracted distributions, and the red points the MC-truth one.

6.5.5 Fit yields and projections

Here we present the results of the fit to $m_{\rm ES}$, ΔE and the Fisher discriminant. Table 6.17 gives the fitted yields and Figs. 6.34 to 6.35 show the fit variables projections (i.e. $m_{\rm ES}$, ΔE and the Fisher discriminant). We observe a good agreement between the model and the data in the signal region, within the statistical uncertainties. The model describes very well the $m_{\rm ES}$ and the Fisher discriminant data distributions, whereas the agreement is slightly worse for ΔE. The latter case was studied, and Figs. F.5 to F.15 in appendix F.2 indicate that these differences between the model and the data are probably due to some background fluctuations. Fit projections, enriched in signal events, for $m_{\rm ES}$ and the Fisher discriminant are also shown in App. F.1.

Table 6.17: $B^+ \to K^+\pi^-\pi^+\gamma$ fitted yields for the final *BABAR* Run1-6 dataset.

Category	Fitted yield	Fit error (stat.)
Signal TM	2441	91
Continuum $udsc$	70078	446
$B^0 \to K^{*0}(\to K\pi)\gamma$ + $B^0 \to X_{sd}(\to K\pi)\gamma$	1529	116
Generic B-background	3270	385

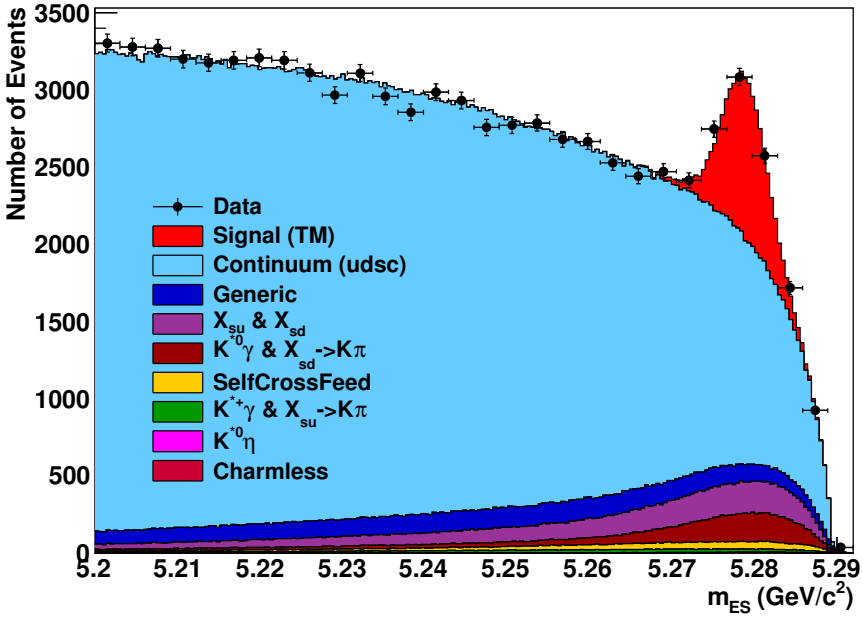

Figure 6.34: $m_{\rm ES}$ fit projection. Black points describe data events and the full colored histograms describe the contribution of each event species in the model.

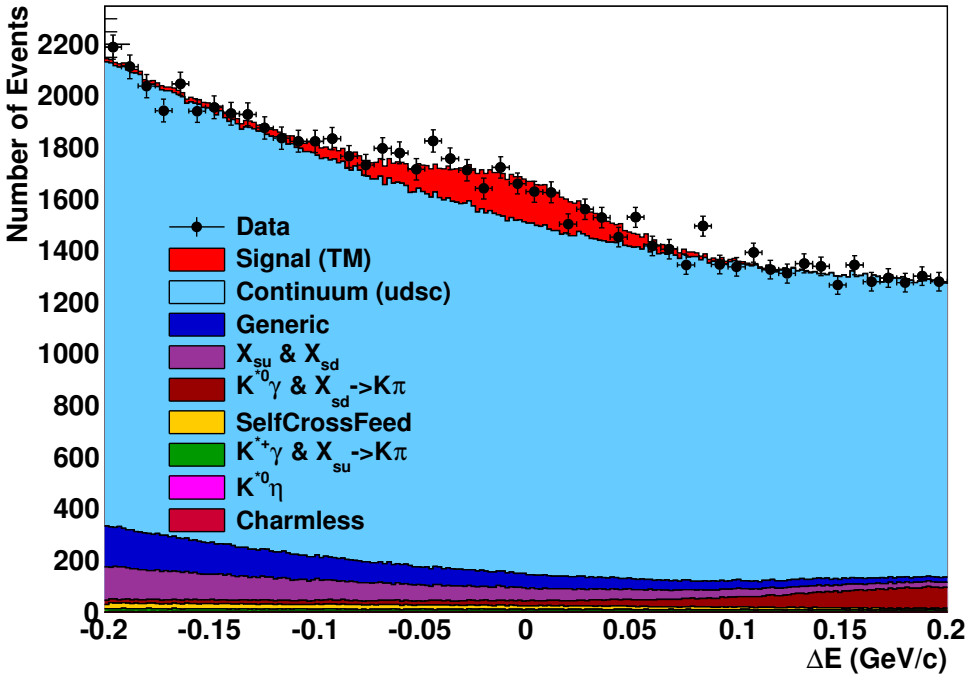

(a)

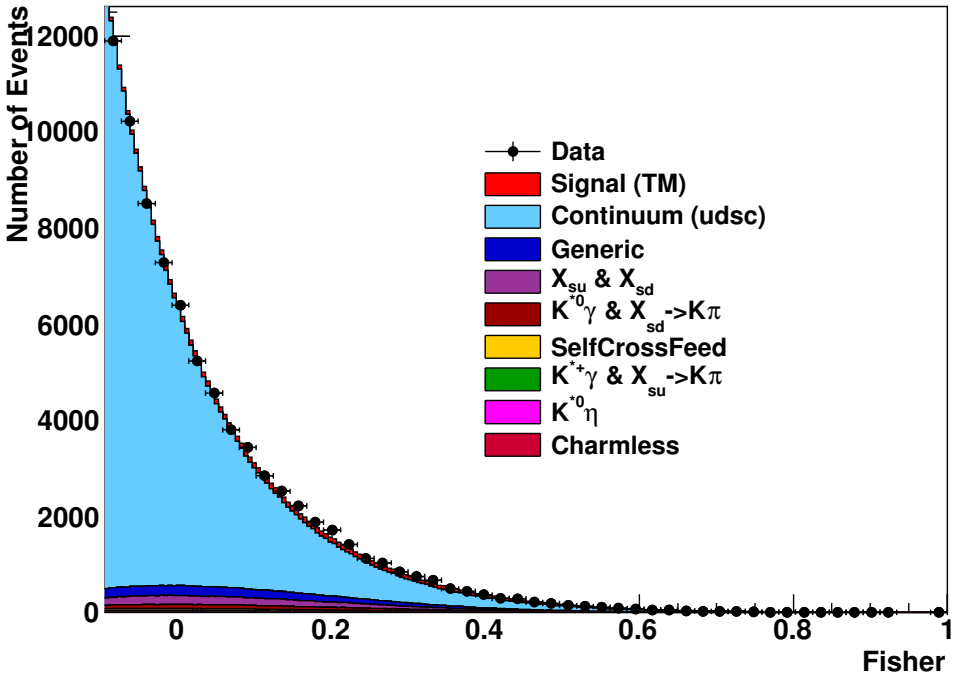

(b)

Figure 6.35: ΔE (a) and the Fisher discriminant (b) fit projections. Conventions are identical as in Fig. 6.34.

6.6 Fit to the $m_{K\pi\pi}$ spectrum

As already mentioned (see Sec. 6.3), not all the branching fractions of the contributions to the $m_{K\pi\pi}$ spectrum are known precisely. We perform a fit to the signal-TM ${}_s\mathcal{P}lot$ of $K^+\pi^-\pi^+$ invariant mass spectrum in order to extract their weights from data. The fit model[4] of the $m_{K\pi\pi}$ distribution is described in Sec. 6.6.1, and the fit results are given in Sec. 6.6.2.

6.6.1 Fit model

We model the $m_{K\pi\pi}$ distribution as a coherent sum of five resonances described by Relativistic Breit-Wigner (BW) line shapes, whose widths (Γ) are independent of the mass (m). The total PDF is then defined as:

$$|A(m;c_k)|^2 = \sum_J \left| \sum_k c_k \, \mathrm{BW}_k^J(m) \right|^2 \Bigg|_{m=m_{K\pi\pi}} , \tag{6.3}$$

with

$$\mathrm{BW}_k^J(m) = \frac{1}{(m_k^0)^2 - m^2 - i m_k^0 \Gamma_k^0} \Bigg|_{m=m_{K\pi\pi}} , \tag{6.4}$$

and

$$c_k = \alpha_k \, e^{i\phi_k} \ . \tag{6.5}$$

The values of m_k^0 and Γ_k^0 are listed in Tab. 6.18. In Eq. 6.3 the index J runs over the different spin parity (J^P) and the index k runs over the kaonic resonances of same J^P. In Eq. 6.5, the coefficients α_k and ϕ_k are the magnitude and phase of the complex coefficients, c_k, corresponding to a given resonance. Table 6.18 details the different resonances in the $m_{K\pi\pi}$ fit model. Six parameters of the complex coefficients vary in the fit: 4 magnitudes and 2 relative phases. The other parameters are fixed as references: 1 for the $K_1(1270)$ magnitude and 0 for the $K_1(1270)$, $K^*(1680)$ and $K_2^*(1430)$ phases. It has been checked that the choice of references does not affect the results. Note that we do not take phase-space effects into account here. However, distortions of line shapes of the kaonic resonances may occur from two sources: the available energy in the production process (i.e. $B \to K_{\mathrm{res.}}\gamma$), and the mass of particular intermediate-state particles being close to the threshold, for instance as in the case of $K_1(1270) \to K\rho^0(770)$. The first source of distortion was studied by comparing, for each kaonic resonance, the invariant-mass distribution generated by `EvtGen` to the BW that was used as an input to the generator. As shown in Figs. C.1 to C.5 of App. C, we do not observe any significant distortions. The second source of distortion would be complicated to estimate since it requires the knowledge of the proportions of each decaying process, which we want to extract next. This would require an complicated iterative procedure. Moreover, due to the relatively low available statistics (~ 2500 events in the whole $m_{K\pi\pi}$ mass range), we assume not to be sensitive to such effects. The model used here is effective; in the present analysis it describes the data rather well, but it may be improvable when larger data samples

[4] We implemented the $m_{K\pi\pi}$ fit model using the RooFit library [97] .

are analyzed.
The fit fractions FF(k) extracted for each kaonic resonance, as well as the interference fit fractions $FF(k,l)$ between same J^P resonances, are calculated as:

$$FF(k) = \frac{|c_k|^2 \langle \mathrm{BW}_k \mathrm{BW}_k^* \rangle}{\sum_{\mu\nu}(c_\mu c_\nu^*) \langle \mathrm{BW}_\mu \mathrm{BW}_\nu^* \rangle} \quad ; \quad FF(k,l) = \frac{2\,\mathcal{R}e\{(c_k c_l^*) \langle \mathrm{BW}_k \mathrm{BW}_l^* \rangle\}}{\sum_{\mu\nu}(c_\mu c_\nu^*) \langle \mathrm{BW}_\mu \mathrm{BW}_\nu^* \rangle} \ , \tag{6.6}$$

where the terms $\langle \mathrm{BW}_\mu \mathrm{BW}_\nu^* \rangle$ are:

$$\langle \mathrm{BW}_\mu \mathrm{BW}_\nu^* \rangle = \int \mathrm{BW}_\mu \mathrm{BW}_\nu^* dm \ . \tag{6.7}$$

In addition, we let free to vary two line-shape parameters in the fit: the widths of $K_1(1270)$ and $K^*(1680)$ resonances. This choice is motivated in the case of $K_1(1270)$ by the fact that the width quoted in Ref. [24] might be underestimated according to the measurements reported in Ref. [67]. In the case of $K^*(1680)$ the uncertainty on the width quoted in Ref. [24] being large and in order to minimize the systematic errors in the present analysis, we decided to let it free to vary. Finally eight parameters are free to vary in the fit.

Table 6.18: Resonances entering in the $m_{K\pi\pi}$ fit model. The pole mass m_k^0 and width Γ_k^0 are fixed to the values taken from Ref. [24].

J^P	K_{res}	Mass m_k^0 (MeV/c^2)	Width Γ_k^0 (MeV/c^2)
1^+	$K_1(1270)$	1272 ± 7	90 ± 20
	$K_1(1400)$	1403 ± 7	174 ± 13
1^-	$K^*(1410)$	1414 ± 15	232 ± 21
	$K^*(1680)$	1717 ± 27	322 ± 110
2^+	$K_2^*(1430)$	1425.6 ± 1.5	98.5 ± 2.7

6.6.2 Fit results

To extract the various K_{res} fit fractions we fit a binned distribution of signal-TM $K^+\pi^-\pi^+$ invariant mass, using the model described in Sec. 6.6.1. The choice of fitting a binned distribution comes from the fact that the ${}_s$Weights, used to retrieve the signal-TM $m_{K\pi\pi}$ distribution, can be negative, which introduces difficulties to perform an unbinned maximum likelihood fit. Figure 6.36 shows the fit projection as well as the residual distribution between the fitted PDF and the data points. Table 6.19 gives the fitted values of all free parameters as well as the extracted fit fractions FF(k). The statistical errors on the magnitudes and phases, as well as on the widths of $K_1(1270)$ and $K^*(1680)$ resonances come directly from the fit.

As the fit fractions are functions of the complex amplitudes c_k (Eq. 6.6), the statistical errors on the FF are estimated in a different way. Using the full information coming from

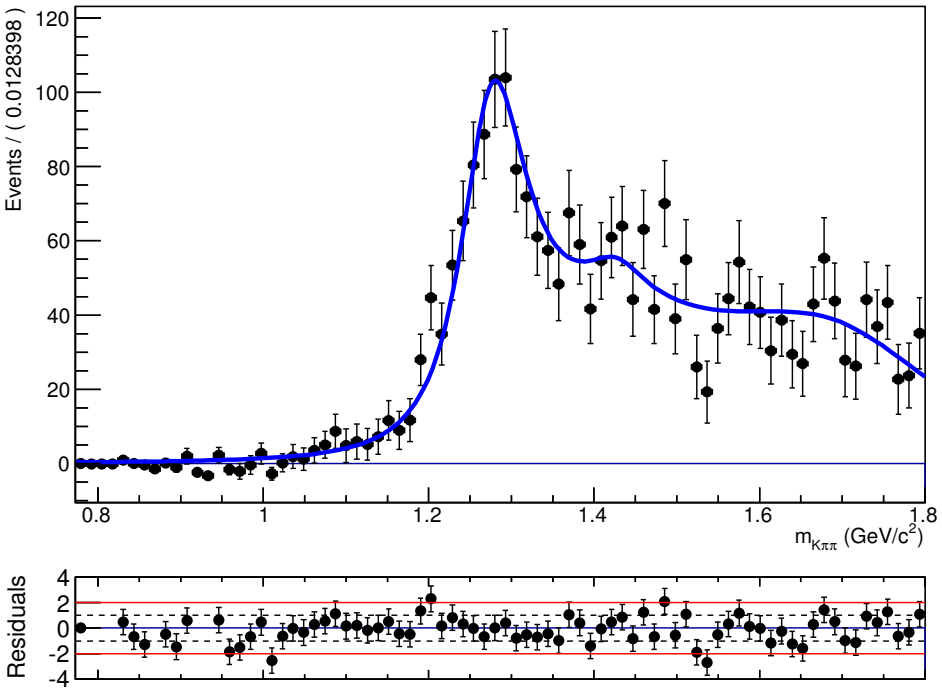

Figure 6.36: $m_{K\pi\pi}$ nominal fit projection (80 bins) and the residual distribution between the total PDF (blue solid curve) and the data points.

the nominal fit (including correlations between fitted parameters), approximately 10^5 sets of c_k values are randomly generated. Then, we calculate the corresponding fit fractions for each set and obtain the FF(k) distributions. The final fit fraction value of resonance k is calculated using the fitted c_k, while the $\pm 1\sigma$ statistical errors are taken as the values at $\pm 34\%$ of the FF distribution integral around the FF value extracted from the fit results.

We consider various sources of systematic uncertainties: the number of bins in the fitted dataset, the fixed parameters in the fit performed to $m_{\rm ES}$, ΔE and the Fisher discriminant from which we extract the signal TM ${}_s\mathcal{P}lot$ distributions and the fixed line-shape parameters. Details on the procedure to evaluate each source of systematic uncertainty as well as the corresponding values are given in Sec. 6.9.1. We add in quadrature the minus and plus signed uncertainties coming from the different sources in order to get the total minus and plus signed uncertainties, which correspond to the values reported in Tab. 6.19. It appears that dominant contribution to the total systematic uncertainties comes from the fixed parameters of the resonance line shapes in the $m_{K\pi\pi}$ fit model.

We also perform likelihood scans of the fitted parameters (Fig. 6.37), in order to check for the presence of multiple solutions. It appears that the fitted solution is unique. Each of these scans is obtained by fixing the corresponding parameter at several consecutive values. Each of the fits is repeated with random initial values of the varying parameters and

Table 6.19: Results of the $m_{K\pi\pi}$ fit. The nominal fit is performed with 80 bins. The quoted systematic errors take into account the uncertainties coming from various sources: the bin size of the dataset, the fixed parameters in the $m_{\rm ES}$-ΔE-Fisher fit model and the fixed parameters in the $m_{K\pi\pi}$ fit model. The individual systematic uncertainties are added in quadrature in order to obtain the total systematic errors. The dominant source of systematic uncertainty comes from the fixed parameters of the resonance line shapes in the $m_{K\pi\pi}$ fit (taken from Ref. [24]). Details on the values of the systematics errors from the various sources considered are given in Sec. 6.9.1.

J^P	$K_{\rm res}$	Magnitude α	Phase ϕ (rad.)	Fit fraction
1^+	$K_1(1270)$	1.0 (fixed)	0.0 (fixed)	$0.61^{+0.08}_{-0.05}(\text{stat.})^{+0.05}_{-0.05}(\text{syst.})$
	$K_1(1400)$	$0.71 \pm 0.10(\text{stat.})^{+0.12}_{-0.08}(\text{syst.})$	$2.97 \pm 0.17(\text{stat.})^{+0.11}_{-0.12}(\text{syst.})$	$0.17^{+0.08}_{-0.05}(\text{stat.})^{+0.05}_{-0.03}(\text{syst.})$
1^-	$K^*(1410)$	$1.25 \pm 0.16(\text{stat.})^{+0.18}_{-0.13}(\text{syst.})$	$3.15 \pm 0.12(\text{stat.})^{+0.03}_{-0.02}(\text{syst.})$	$0.37^{+0.08}_{-0.07}(\text{stat.})^{+0.06}_{-0.02}(\text{syst.})$
	$K^*(1680)$	$2.02 \pm 0.28(\text{stat.})^{+0.32}_{-0.21}(\text{syst.})$	0.0 (fixed)	$0.43^{+0.05}_{-0.04}(\text{stat.})^{+0.09}_{-0.06}(\text{syst.})$
2^+	$K_2^*(1430)$	$0.33 \pm 0.09(\text{stat.})^{+0.07}_{-0.14}(\text{syst.})$	0.0 (fixed)	$0.06^{+0.04}_{-0.03}(\text{stat.})^{+0.04}_{-0.05}(\text{syst.})$
Sum of fit fractions				$1.64^{+0.18}_{-0.14}(\text{stat.})^{+0.14}_{-0.07}(\text{syst.})$
Interferences		$J^P = 1^+ : \{K_1(1270) - K_1(1400)\}$		$-0.35^{+0.10}_{-0.16}(\text{stat.})^{+0.05}_{-0.06}(\text{syst.})$
		$J^P = 1^- : \{K^*(1410) - K^*(1680)\}$		$-0.29^{+0.08}_{-0.11}(\text{stat.})^{+0.06}_{-0.12}(\text{syst.})$

Line-shape parameters

$K_{\rm res}$	Mean (GeV/c^2)	Width (GeV/c^2)
$K_1(1270)$	1.272 (fixed)	$0.099 \pm 0.006(\text{stat.})^{+0.004}_{-0.006}(\text{syst.})$
$K^*(1680)$	1.717 (fixed)	$0.356 \pm 0.050(\text{stat.})^{+0.045}_{-0.026}(\text{syst.})$

always converge to the same likelihood solution. We further compare in Tab. 6.20 the ratio of the FFs extracted from the fit to the ratio of previously-used MC weights (mainly taken from theoretical estimations). The extracted FF ratio FF($K_2^*(1430)$)/FF($K_1(1270)$) is compatible with the unique MC weight ratio extracted from existing measurements (i.e. $\mathcal{B}(B^+ \to K_2^*(1430)^+\gamma)/\mathcal{B}(B^+ \to K_1(1270)^+\gamma)$, where the branching fractions are taken from Ref. [24]). The main difference concerns the $K^*(1680)$ FF for which the initially-estimated MC weight is widely underestimated. Nevertheless, the result obtained by the present analysis is compatible with existing measurements: from Ref. [24] we have $\mathcal{B}(B^+ \to K^*(1680)^+\gamma) < 1.9 \times 10^{-3}$ and $\mathcal{B}(B^+ \to K_1(1270)^+\gamma) = (4.3 \pm 1.3) \times 10^{-5}$.

Using efficiency-correction factors for each resonance, we calculate new MC weights (see column "Fit based MC weight" in Tab. 6.20) to be used to construct the appropriate signal-MC cocktail for the $m_{K\pi}$ fit (Sec. 6.7) and in the $B^0 \to K^0_S\rho^0\gamma$ analysis.

We also checked the dependance of these results in regard to the values of initial cocktail weights. Since the cocktail weights only affect the values of the signal PDFs parameters, we re-extract the values of these parameters for all the discriminating variables using the new cocktail weights from the results of the fit to $m_{K\pi\pi}$. Table 6.21 gives the values of

these parameters for the two cocktail weights: the initial one given in Tab. 6.3, which is based on existing measurements and theoretical predictions, and the one from the fit to $m_{K\pi\pi}$ given in Tab. 6.20. We observe that largest differences between the fitted values of the parameter, obtained with the two sets of signal weights, are comparable[5] to the fitted statistical uncertainty. Therefore, we consider that the impact of the difference in weights of signal cocktail is negligible for the rest of the analysis.

Table 6.20: Fit-based MC weights and fit-fraction ratios compared to the initially estimated MC weights and their ratios, respectively. The fit-based MC weights are defined as the fit fraction of the considered kaonic resonance divided by the sum of fit fractions, as given in Tab. 6.19, after correction for efficiency. The initially estimated MC weights are taken from Tab. 6.3. The "Fit fraction ratios" in the table are obtained by dividing the considered kaonic resonance fit fraction or initially estimated MC weight value by the one of the $K_1(1270)$ resonance. The uncertainties quoted in the columns "Fit fraction ratio" and "Fit based MC weight" correspond to the total uncertainties resulting from the quadratic sum of the statistical and total systematic uncertainties. The uncertainties quoted for the global efficiency reflect the limited size of the MC samples.

Resonance	Efficiency ratio	Fit fraction ratio	Initially estimated MC weight ratio	Fit based MC weight	Initially estimated MC weight
$K_1(1270)$	1.000	1.00	1.00	$0.309^{+0.083}_{-0.064}$	0.608 ± 0.145
$K_1(1400)$	0.991 ± 0.007	$0.28^{+0.17}_{-0.11}$	0.24	$0.086^{+0.055}_{-0.034}$	0.145
$K^*(1410)$	0.904 ± 0.007	$0.67^{+0.21}_{-0.15}$	0.23	$0.208^{+0.072}_{-0.054}$	0.140
$K_2^*(1430)$	0.982 ± 0.008	$0.11^{+0.09}_{-0.10}$	0.14 ± 0.04	$0.035^{+0.028}_{-0.031}$	0.087 ± 0.011
$K^*(1680)$	0.599 ± 0.009	$1.17^{+0.32}_{-0.23}$	0.03	$0.362^{+0.116}_{-0.084}$	0.020

[5] We observe for the parameter CB_μ(Coeff2) a difference of two time the size of the error. However, since this parameter is free to vary in the fit, it should have no impact on the further results.

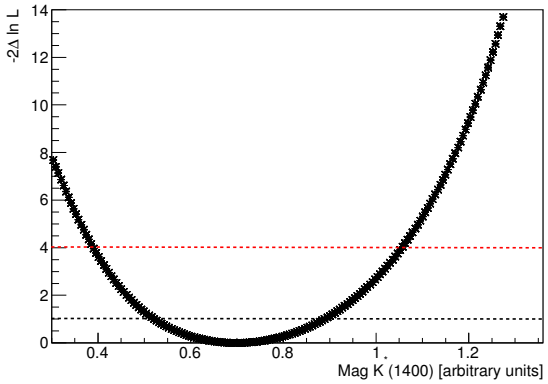

Mag. $K_1(1400)$

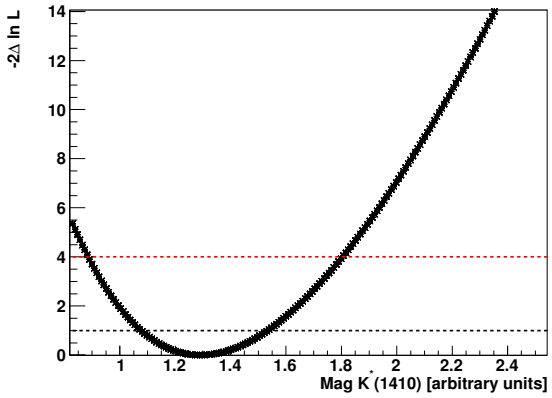

Mag. $K^*(1410)$

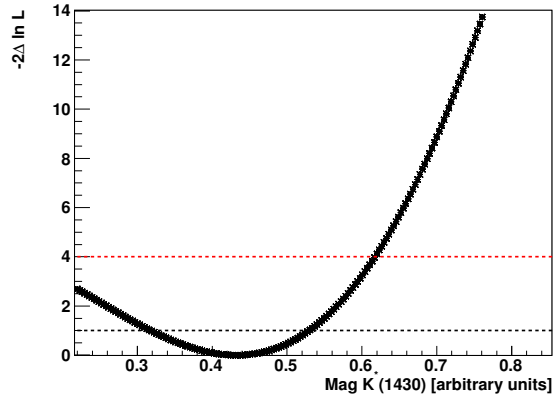

Mag. $K_2^*(1430)$

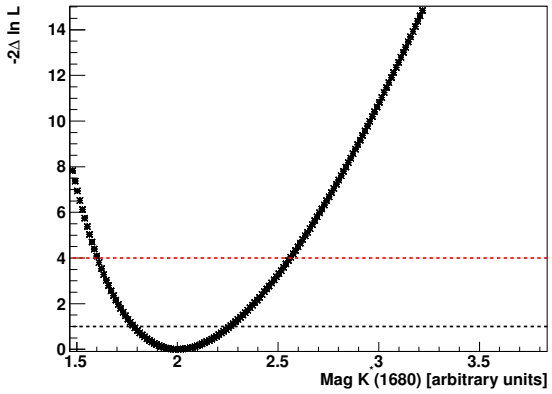

Mag. $K^*(1680)$

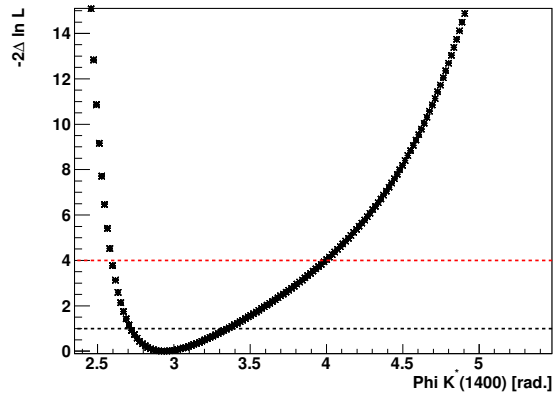

Phase. $K_1(1400)$

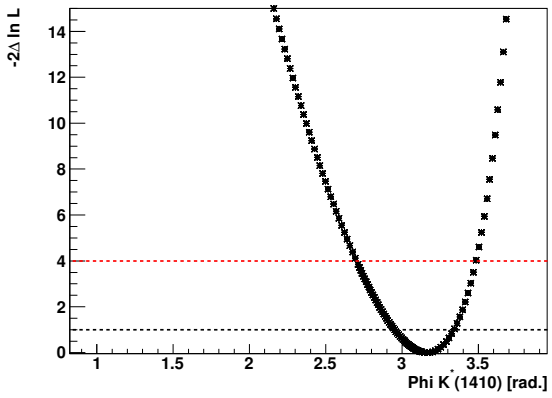

Phase $K^*(1410)$

Figure 6.37: One-dimensional scans of $-2\Delta\ln\mathcal{L}$ as a function of magnitudes (top and middle) and phases (bottom). The horizontal dashed lines mark the one- and two-standard deviation levels.

Table 6.21: Extracted values of the signal PDF parameters for the two sets of signal weights (the initial one based on existing measurements and theoretical predictions and the one from the fit to $m_{K\pi\pi}$). We also give the normalized difference, which corresponds to the absolute value of the difference between the two parameter values divided by the averaged error. When 0.0000 is quoted for the error value, it is less than 5×10^{-5}.

	Fit variable	Parameter	Initial cocktail weights	Fit based cocktail weights	Normalized difference
Signal TM	$m_{\rm ES}$	CB_{μ}(Coeff0)	5.2792 ± 0.0000	5.2792 ± 0.0000	0.7492
		CB_{μ}(Coeff1)	-0.0048 ± 0.0002	-0.0047 ± 0.0003	0.2769
		CB_{μ}(Coeff2)	-0.0994 ± 0.0026	-0.0917 ± 0.0036	2.0960
		CB_{σ}(Coeff0)	0.0025 ± 0.0000	0.0025 ± 0.0000	0.5359
		CB_{σ}(Coeff1)	0.0017 ± 0.0002	0.0011 ± 0.0003	0.1947
		CB_{σ}(Coeff2)	0.1568 ± 0.0044	0.1602 ± 0.0043	0.7851
		CB_{α}(Coeff0)	1.7802 ± 0.0923	1.6729 ± 0.0972	1.1978
		CB_{α}(Coeff1)	5.2342 ± 1.0052	4.3917 ± 0.8588	0.7758
		$\mathrm{CB}_{\rm order}$(Coeff0)	7.6280 ± 2.5806	10.258 ± 2.4375	1.0340
		$\mathrm{CB}_{\rm order}$(Coeff1)	-41.647 ± 37.350	-57.674 ± 34.158	0.4291
	ΔE	Cr_{μ}	-0.0021 ± 0.0054	-0.0022 ± 0.0053	0.0272
		Cr_{σ_L}	0.0592 ± 0.0076	0.0590 ± 0.0075	0.0220
		Cr_{σ_R}	0.0324 ± 0.0039	0.0322 ± 0.0038	0.0471
		Cr_{α_L}	0.2790 ± 0.0627	0.2788 ± 0.0622	0.0013
		Cr_{α_R}	0.1259 ± 0.0267	0.1237 ± 0.0264	0.0841
	Fisher	G_{μ}	0.1234 ± 0.0125	0.1248 ± 0.0124	0.1173
		G_{σ}	0.2310 ± 0.0085	0.2301 ± 0.0084	0.1113
Signal SCF	$m_{\rm ES}$	BG_{μ}	5.2757 ± 0.0404	5.2812 ± 0.0402	0.1368
		BG_{σ_L}	-0.0569 ± 0.0499	-0.0625 ± 0.0499	0.1129
		BG_{σ_R}	0.0041 ± 0.0022	0.0042 ± 0.0016	0.0566
		Arg $_{\rm end\ point}$	5.2892 ± 0.0004	5.2892 ± 0.0001	$< 10^{-5}$
		Arg $_{\rm slope}$	-149.53 ± 66.756	-145.15 ± 53.125	0.8232
		frac	0.3167 ± 0.6583	0.3520 ± 0.3828	0.9220
	ΔE	Lin_{c_1}	-3.0200 ± 0.4639	-3.2940 ± 0.3846	0.7126
	Fisher	G_{μ}	-0.0067 ± 0.0039	0.0078 ± 0.0316	0.4382
		G_{σ}	0.2315 ± 0.0201	0.2310 ± 0.0169	0.0322

6.7 Fit to the $m_{K\pi}$ spectrum

This section describes the fit performed on the efficiency-corrected $m_{K\pi}$ invariant mass spectrum in order to extract the efficiency-corrected dilution factor, to be used in the time dependent analysis of $B^0 \to K^0_S\rho^0\gamma$ decays. The efficiency correction is described in Sec. 6.7.1. Then the $m_{K\pi}$ fit model and the study of the parameters to vary in the fit are described in Sec. 6.7.2 and Sec. 6.7.4, respectively. Finally the fit results, as well as the extracted values of the FFs are given in Sec. 6.7.3.

6.7.1 Efficiency correction

In order to correct for efficiency effects, we construct efficiency maps in the ($m_{K\pi}$, $m_{\pi\pi}$) plane for each kaonic resonance in the fit model. Each efficiency map is constructed using an exclusive non resonant MC sample of the corresponding kaonic resonance (i.e. $B^+ \to K_{res}(K^+\pi^-\pi^+)\gamma$). The maps are shown in Fig. 6.38. Using the relative weights between each kaonic resonance extracted from the $m_{K\pi\pi}$ fit (see Tab. 6.20), we construct a combination of the individual maps. In order to get the $m_{K\pi}$ spectrum corrected for efficiency effects, we divide the ($m_{K\pi}$, $m_{\pi\pi}$) ${}_s\mathcal{P}lot$ distribution by the combined efficiency map. Then integrating over the $m_{\pi\pi}$ dimension, we construct the signal-TM $m_{K\pi}$ spectrum corrected for efficiency effects. Figure 6.39 shows the combined efficiency map, the ($m_{K\pi}$, $m_{\pi\pi}$) ${}_s\mathcal{P}lot$ distribution is given in Fig. 6.40 and Fig. 6.41 shows the signal-TM $m_{K\pi}$ spectrum before and after applying the efficiency corrections. The efficiency correction effects result in a global enhancement of the total number of events with a few small local effects.

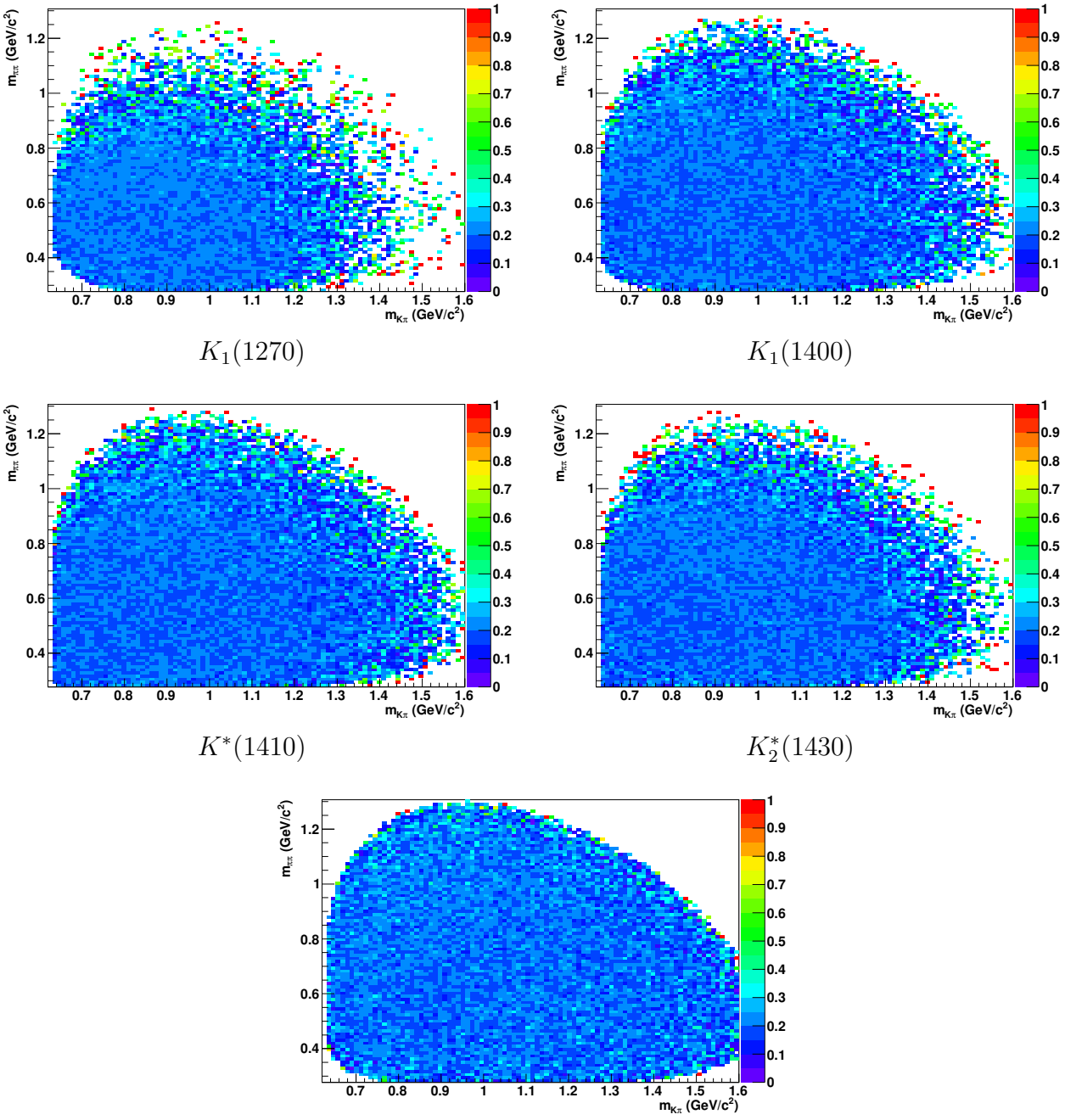

$K_1(1270)$ $K_1(1400)$

$K^*(1410)$ $K_2^*(1430)$

$K^*(1680)$

Figure 6.38: Two-dimensional ($m_{K\pi}$, $m_{\pi\pi}$) efficiency maps for each resonance contributing to the signal. In the upper right side of each map, some bins present efficiency close to one. This is due to the very low density of events in these bins, and to event migration.

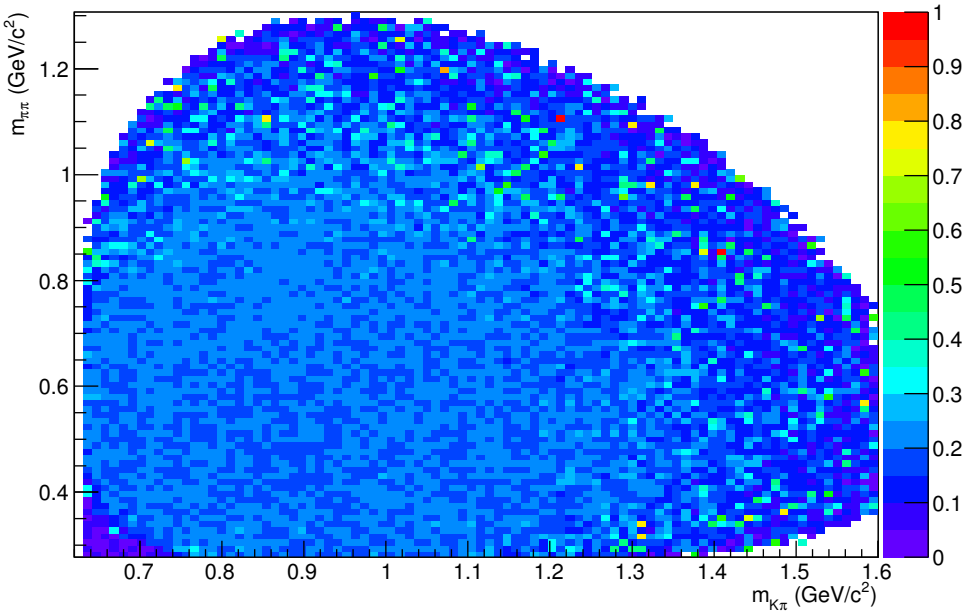

Figure 6.39: Result of the combination of the individual efficiency maps per kaonic resonance. The relative weights used for the combination are the ones extracted from the fit to the $m_{K\pi\pi}$ spectrum (Tab. 6.20).

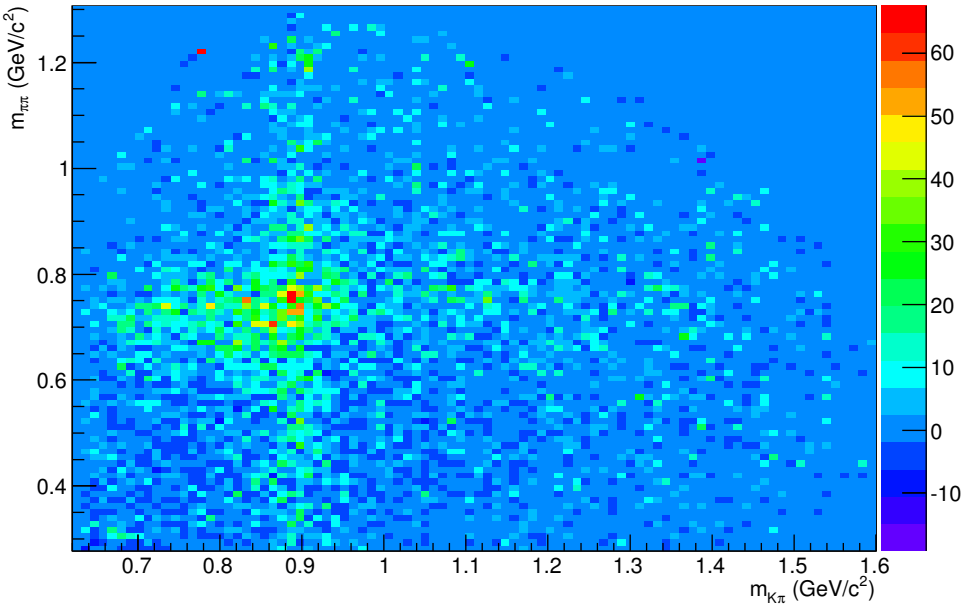

Figure 6.40: Signal-TM two-dimensional ($m_{K\pi}$, $m_{\pi\pi}$) ${}_s\mathcal{P}lot$ distribution, before application of the efficiency correction.

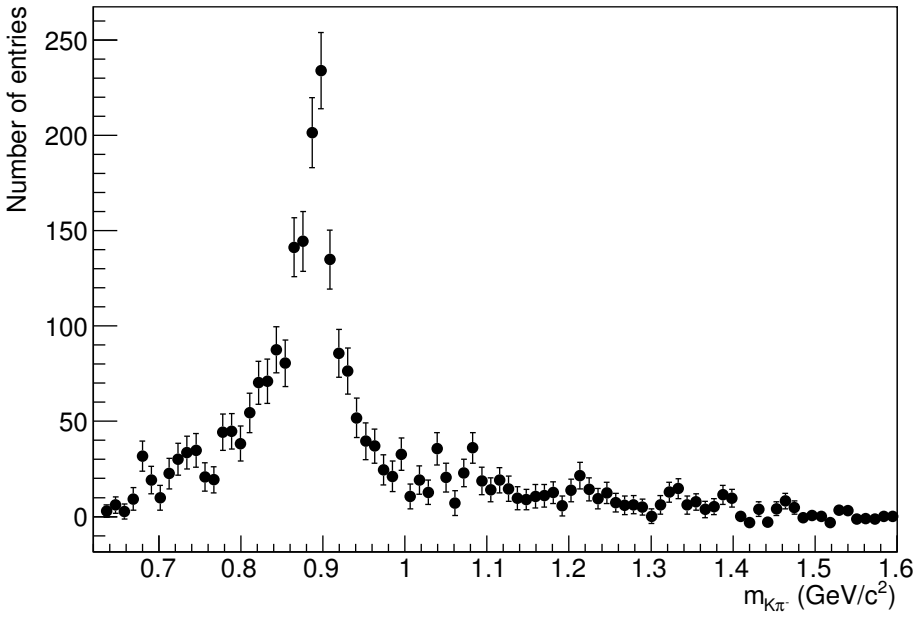

(a)

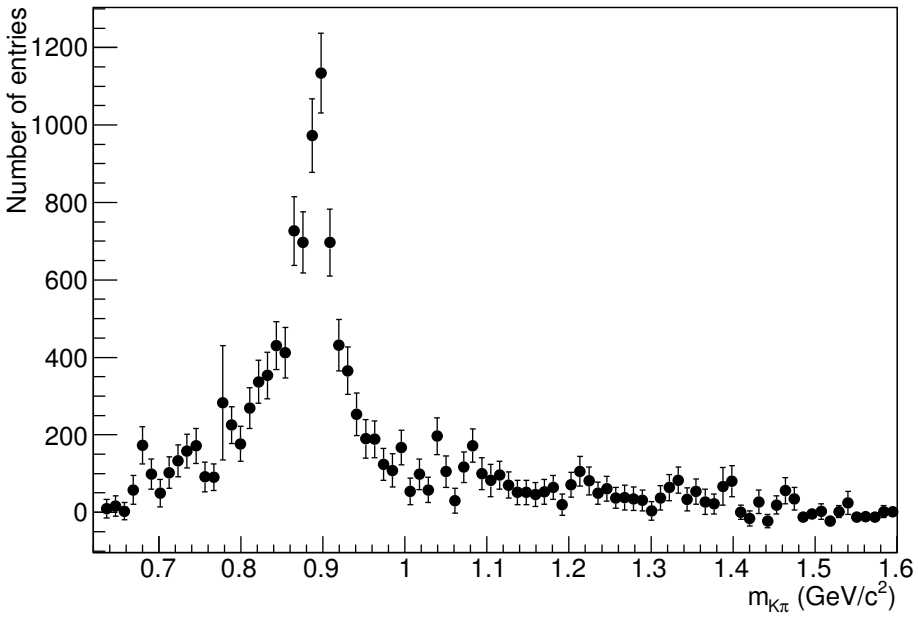

(b)

Figure 6.41: Signal-TM $m_{K\pi}$ spectrum before (a) and after (b) application of the efficiency correction.

6.7.2 Fit model

We model the $m_{K\pi}$ spectrum using the projections of two 1^- P-wave and one 0^+ S-wave components on the $m_{K\pi}$ dimension. The two P-wave components correspond to the $K^{*0}(892)$ and the $\rho^0(770)$ resonances, which can be described by the Relativistic Breit-Wigner (RBW) and Gounaris-Sakurai (GS) line-shapes, respectively. Their expressions are given in Eqs. 6.9 and 6.13. The 0^+ component of the $K\pi$ spectrum (referred to as $(K\pi)_0$, or $(K\pi)$ S-wave in this thesis) is poorly understood [111–113]; we use the LASS parameterization [111, 112], which is given in Eq. 6.18. It consists of the $K_0^*(1430)^0$ resonance together with an effective range non-resonant component.

Due to the relatively low mass of the kaonic resonances decaying to $K^+\pi^-\pi^+$, the line shapes are distorted[6]. In order to account for this effect, we model the invariant-mass-dependent magnitude of each resonance R_j by: $\sqrt{\mathrm{H}_{\mathrm{R}_j}(m_{K\pi}, m_{\pi\pi})}$, where H is a two-dimensional histogram. It is obtained from signal MC at the generator level using the `EvtGen` package [84].

In the event generator, the $K^{*0}(892)$ and the $\rho^0(770)$ are modeled by the RBW and GS line-shapes, respectively. The LASS parametrized S-wave component is obtained by applying weights to the MC sample, as will be described below. In order to take into account interferences between the components, the invariant-mass-dependent phases ($\Phi_{\mathrm{R}_j}(m)$) are required. The hypothesis made in the present analysis is that the phases can be directly taken from the analytical expression of the corresponding line shape:

$$\Phi_{\mathrm{R}_j}(m) = \arccos\left(\frac{\Re[\mathrm{R}_j(m)]}{|\mathrm{R}_j(m)|}\right) \Leftrightarrow \begin{cases} m = m_{K\pi} & \Rightarrow \begin{array}{l}\mathrm{R}_j(m_{K\pi}) \text{ is taken as} \\ \text{RBW for } K^{*0}(892) \text{ and} \\ \text{as LASS for S-wave ,}\end{array} \\ m = m_{\pi\pi} & \Rightarrow \begin{array}{l}\mathrm{R}_j(m_{\pi\pi}) \text{ is taken as a GS} \\ \text{line shape for } \rho^0(770) \text{ ,}\end{array} \end{cases} \tag{6.8}$$

where the different line-shapes are taken from the expressions below:

- The RBW parameterization [24] used to express the corresponding invariant-mass-dependent phase, $\Phi_{\mathrm{RBW}}(m_{K\pi})$, is defined as

$$\mathrm{R}_{\mathrm{RBW}}(m) = \left.\frac{1}{(m_0)^2 - m^2 - im^0\Gamma(m)}\right|_{m=m_{K\pi}} , \tag{6.9}$$

where m_0 is the nominal mass of the resonance and $\Gamma(m)$ is the mass-dependent width. For a spin-J resonance decaying into a pair of pseudo-scalar particles (i.e. $K\pi$), the latter can be expressed as

$$\Gamma(m) = \Gamma_0 \left(\frac{|\mathbf{q}|}{|\mathbf{q}|_0}\right)^{2J+1} \left(\frac{m_0}{m}\right) \left.\frac{X_J^2(|\mathbf{q}|r)}{X_J^2(|\mathbf{q}|_0 r)}\right|_{m=m_{K\pi}} . \tag{6.10}$$

[6]The phase space is noticeably different for events below or above the resonance pole mass

The symbol Γ_0 denotes the nominal width of the resonance. The values of m_0 and Γ_0 are listed in Tab. 6.22. The symbol $\mathbf{q}$ is the momenta of one of the resonance daughters, evaluated in the resonance rest frame. The modulus of $\mathbf{q}$ is a function of m and the resonance daughter masses, m_a and m_b, given by

$$|\mathbf{q}| = \frac{m}{2}\left(1 - \frac{(m_a+m_b)^2}{m^2}\right)^{1/2}\left(1 - \frac{(m_a-m_b)^2}{m^2}\right)^{1/2} . \tag{6.11}$$

The symbol $|\mathbf{q}|_0$ denotes the value of $|\mathbf{q}|$ when $m_{K\pi} = m_0$. The $X_J(|\mathbf{q}|r)$ function describes the Blatt-Weisskopf barrier factor [114] with barrier radius of r. Defining the quantity $z = |\mathbf{q}|r$, their expression, depending on the resonance spin-J value, are given by

$$\begin{aligned} X_{J=0}(z) &= 1 , \\ X_{J=1}(z) &= \sqrt{\frac{1+z_0^2}{1+z^2}} , \end{aligned} \tag{6.12}$$

where z_0 represents the value of z when the invariant mass is equal to the pole mass of the resonance. This factor only has an effect for $J > 0$.

- The Gounaris-Sakurai parameterization [115], used to express the corresponding invariant-mass-dependent phase, $\Phi_{\rm GS}(m_{\pi\pi})$, is given by:

$$\mathrm{R}_{\rm GS}(m) = \left.\frac{1 + d\cdot\Gamma_0/m_0}{((m_0)^2 - m^2) + f(m) - im_0\Gamma(m)}\right|_{m=m_{\pi\pi}} , \tag{6.13}$$

where

$$f(m) = \Gamma_0\frac{(m_0)^2}{|\mathbf{q}|_0^3}\left[|\mathbf{q}|^2(h(m) - h(m_0)) + ((m_0)^2 - m^2)|\mathbf{q}|_0^2\left.\frac{dh}{dm^2}\right|_{m=m_0}\right]\Bigg|_{m=m_{\pi\pi}} , \tag{6.14}$$

and the function $h(m)$ is defined as

$$h(m) = \frac{2}{\pi}\frac{|\mathbf{q}|}{m}\ln\left(\frac{m + 2|\mathbf{q}|}{2m_\pi}\right)\Bigg|_{m=m_{\pi\pi}} , \tag{6.15}$$

with

$$\left.\frac{dh}{dm^2}\right|_{m=m_0} = h(m_0)\left(\frac{1}{8|\mathbf{q}|_0^2} - \frac{1}{2(m_0)^2}\right) + \frac{1}{2\pi(m_0)^2} . \tag{6.16}$$

The normalization condition at $R_j(0)$ fixes the parameter $d = f(0)/(\Gamma_0 m_0)$. It is found to be:

$$d = \frac{3}{\pi}\frac{m_\pi^2}{|\mathbf{q}|_0^2}\ln\left(\frac{m_0 + 2|\mathbf{q}|_0}{2m_\pi}\right) + \frac{m_0}{2\pi|\mathbf{q}|_0} - \frac{m_\pi^2 m_0}{\pi|\mathbf{q}|_0^3} . \tag{6.17}$$

- The LASS parameterization, used to express the corresponding invariant-mass-dependent phase, $\Phi_{\rm LASS}(m_{K\pi})$, is given by:

$$\mathrm{R}_{\rm LASS}(m) = \frac{m}{|\mathbf{q}|\cot\delta_B - i|\mathbf{q}|} + e^{2i\delta_B}\left.\frac{m_0\Gamma_0\frac{m_0}{|\mathbf{q}|_0}}{(m_0^2-m^2) - im_0\Gamma_0\frac{|\mathbf{q}|}{m}\frac{m_0}{|\mathbf{q}|_0}}\right|_{m=m_{K\pi}}, \tag{6.18}$$

where

$$\cot\delta_B = \frac{1}{a|\mathbf{q}|} + \frac{1}{2}r|\mathbf{q}|. \tag{6.19}$$

Table 6.22 gives the parameters of the line shapes used to derive the invariant-mass-dependent phase of the components entering the fit model.

Finally, the total amplitude used to describe the $m_{K\pi}$ distribution can be written as:

$$|A(m_{K\pi};c_j)|^2 = \left|\int_{m_{\pi\pi}^{min}}^{m_{\pi\pi}^{max}}\left(\sum_j c_j\sqrt{\mathrm{H}_{\mathrm{R}_j}(m_{K\pi},m_{\pi\pi})}\,e^{i\Phi_{\mathrm{R}_j}(m)}\right)dm_{\pi\pi}\right|^2, \tag{6.20}$$

$$= |c_{K^*}|^2\,\mathcal{H}_{K^*} + |c_{\rho^0}|^2\,\mathcal{H}_{\rho^0} + \left|c_{(K\pi)_0}\right|^2\mathcal{H}_{(K\pi)_0} + I\ , \tag{6.21}$$

with

$$c_j = \alpha_j\,e^{i\phi_j}\ , \tag{6.22}$$

and

$$\mathcal{H}_{\mathrm{R}_j}(m_{K\pi}) = \int_{m_{\pi\pi}^{min}}^{m_{\pi\pi}^{max}}\mathrm{H}_{\mathrm{R}_j}(m_{K\pi},m_{\pi\pi})\,dm_{\pi\pi}. \tag{6.23}$$

Table 6.22: Parameters of the resonance line shapes used to express the corresponding invariant-mass-dependent phase (Φ_{R_j}) entering in the $m_{K\pi}$ fit model. For the fit the mean m_0 and width Γ_0 are fixed to the values taken from the corresponding references. The values of m_0 and Γ_0 are expressed in MeV/c^2. The parameters r and a correspond to the Blatt-Weisskopf barrier radius and the scattering length, respectively.

J^P	Resonance	Parameters	Analytical Expression	Ref. for Parameters
1^-	$K^{*0}(892)$	$m_0 = 895.94 \pm 0.22$ $\Gamma_0 = 50.8 \pm 0.9$ $r = 3.6 \pm 0.6$ (GeV/c)$^{-1}$	RBW	[24]
	$\rho^0(770)$	$m_0 = 775.49 \pm 0.34$ $\Gamma_0 = 149.1 \pm 0.8$ $r = 5.3^{+0.9}_{-0.7}$ (GeV/c)$^{-1}$	GS	[24]
0^+	$(K\pi)$ S-wave	$m_0 = 1425 \pm 50$ $\Gamma_0 = 270 \pm 80$ $a = 2.07 \pm 0.10$ (GeV/c)$^{-1}$ $r = 3.32 \pm 0.34$ (GeV/c)$^{-1}$	LASS	[24] [112]

The term I in Eq. 6.21 describes the interferences among the different components in the model. In the two-dimensional $m_{K\pi}$-$m_{\pi\pi}$ plane the interferences between the $(K\pi)$ S-wave and the $(K\pi)$ P-wave components are proportional to a cosine term. Therefore, when integrating over the $m_{\pi\pi}$ dimension, these interferences vanish. As the fit is to be performed to an efficiency-corrected $m_{K\pi}$ distribution, we do not allow for $(K\pi)$ S-wave and $(K\pi)$ P-wave interferences in the model. The remaining source of interferences comes from the $(K\pi)$ and $(\pi\pi)$ P-wave components (i.e. between the $K^{*0}(892)$ and the $\rho^0(770)$ resonances), as well as from the $(K\pi)$ S-wave and the $(\pi\pi)$ P-wave components, which is given by

$$
\begin{aligned}
I(m_{K\pi}; c_{\rho^0}, c_{(K\pi)_0}) \;=\; & 2\alpha_{\rho^0}\left[\cos(\phi_{\rho^0}-\Phi_{\mathrm{RBW}})\int_{m_{\pi\pi}^{min}}^{m_{\pi\pi}^{max}}\sqrt{\mathrm{H}_{\rho^0}\mathrm{H}_{K^*}}\cos(\Phi_{\mathrm{GS}})\,dm_{\pi\pi}\right. \\
& \left. -\sin(\phi_{\rho^0}-\Phi_{\mathrm{RBW}})\int_{m_{\pi\pi}^{min}}^{m_{\pi\pi}^{max}}\sqrt{\mathrm{H}_{\rho^0}\mathrm{H}_{K^*}}\sin(\Phi_{\mathrm{GS}})\,dm_{\pi\pi}\right] \\
& +2\alpha_{\rho^0}\alpha_{(K\pi)_0}\left[\cos(\phi_{\rho^0}-\phi_{(K\pi)_0}-\Phi_{\mathrm{LASS}})\int_{m_{\pi\pi}^{min}}^{m_{\pi\pi}^{max}}\sqrt{\mathrm{H}_{\rho^0}\mathrm{H}_{(K\pi)_0}}\cos(\Phi_{\mathrm{GS}})\,dm_{\pi\pi}\right. \\
& \left. -\sin(\phi_{\rho^0}-\phi_{(K\pi)_0}-\Phi_{\mathrm{LASS}})\int_{m_{\pi\pi}^{min}}^{m_{\pi\pi}^{max}}\sqrt{\mathrm{H}_{\rho^0}\mathrm{H}_{(K\pi)_0}}\sin(\Phi_{\mathrm{GS}})\,dm_{\pi\pi}\right] .
\end{aligned}
\tag{6.24}
$$

The $K^{*0}(892)$ coefficients, α_{K^*} and ϕ_{K^*} are set as references to 1 and 0, respectively. It has been checked that the choice of references does not affect the results. This leads to three four parameters in the fit (i.e. α_{ρ^0}, ϕ_{ρ^0}, $\alpha_{(K\pi)_0}$ and $\phi_{(K\pi)_0}$). The fit fractions FF(j) extracted for each component in the model, are defined as in the $m_{K\pi\pi}$ fit model by Eq. 6.6.

The two-dimensional projection histograms used to describe the $K^{*0}(892)$ and $\rho^0(770)$ resonance $m_{K\pi}$-dependent magnitudes are given in Fig. 6.42. They are obtained from a two-dimensional histogram, constructed as the combination of individual kaonic resonance

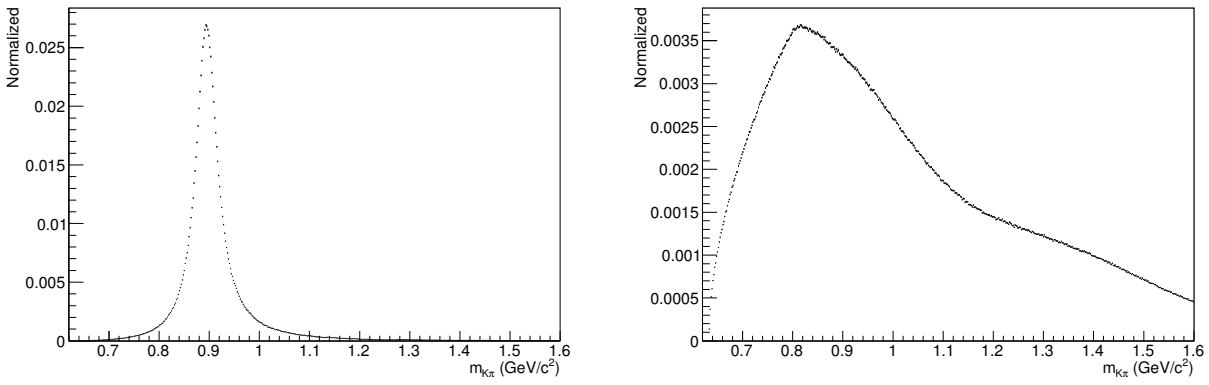

$K^{*0}(892)$ $\qquad$ $\rho^0(770)$

Figure 6.42: Two-dimensional histogram projections used to describe the $K^{*0}(892)$ and the $\rho^0(770)$ resonance modules in the $m_{K\pi}$ fit model. The histograms were generated using `EvtGen` [84] at the generator level.

contribution to the corresponding resonance (i.e. $K_{\rm res} \to K^{*0}(892)\pi$ or $K\rho^0(770)$). The combination is performed using the relative weights between each kaonic resonance extracted from the $m_{K\pi\pi}$ fit (see Tab. 6.20).

The `EvtGen` MC generator used to produce the two-dimensional distributions of the fit components do not allow a stand-alone use of the LASS parametrization in the present case. Therefore in order to obtain the S-wave distribution, we weighted a phase-space distribution of $B^+ \to K_1(1270)^+(\to K^\pm\pi^\mp\pi^+)\gamma$ processes generated from `EvtGen` using an accept-reject method based on the LASS expression given in Eq. 6.18. Figure 6.43 shows the distribution of the S-wave $m_{K\pi}$-dependent magnitude used in the model. The unusual shape of the S-wave distribution is due to phase-space effects. The LASS parametrization includes a effective range term, as well as a resonant term around $m_{K\pi} = 1425\,\text{MeV}/c^2$. Due to the fact that in the present analysis the $K^+\pi^-\pi^+$ system comes from the decay of the $K_1(1270)$ kaonic resonance, the resonant part of the LASS parametrization is very much suppressed, as observed in Fig. 6.43. The dominant contribution comes from the non-resonant term, which corresponds to the effective-range part.

For each histogram used to built the total PDF, the nominal numbers of the bins are 450 and 100 in the $m_{K\pi}$ and $m_{\pi\pi}$ dimensions, respectively.

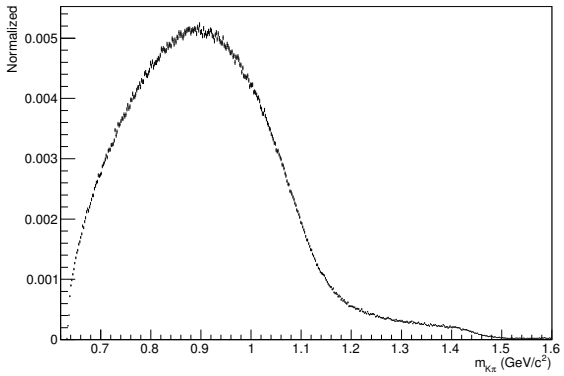

$(K\pi)$ S-wave

Figure 6.43: Two-dimensional histogram projection used to describe the 0^+ $(K\pi)$ S-wave component in the $m_{K\pi}$ fit model. The histogram was generated using an accept-reject method base on the LASS parametrization applied to a phase-space distribution generated using `EvtGen` [84] at the generator level.

6.7.3 Fit results

Figure 6.44 shows the fit projection and the residual distribution. The nominal fit is performed on a dataset of 90 bins. Table 6.23 gives the fitted values of the free parameters as well as the extracted FFs. The quoted errors on the magnitudes and the phase come directly from the fit. For the fit fractions, which are functions of the complex amplitudes c_j (Eq. 6.6), the errors were estimated in the same way as in the $m_{K\pi\pi}$ fit, as detailed in Sec. 6.6.2.

We consider various sources of systematic uncertainties: the number of bins in the fitted dataset, the number of bins in the PDF, the fixed parameters in the fit performed to $m_{\rm ES}$, ΔE and the Fisher discriminant, the fixed line-shape parameters of the resonances entering in the $m_{K\pi}$ fit model, the weights of the kaonic resonances used to construct the total PDF and the line-shape parameters of the kaonic resonances used in the MC generator. Details on the procedure to evaluate each source of systematic uncertainty as well as the corresponding values are given in Sec. 6.9.2. We add in quadrature the minus and plus signed uncertainties coming from the different sources in order to get the total minus and plus signed uncertainties, which correspond to the values reported in Tab. 6.23. It appears the dominant contribution to the total systematic uncertainties come from the weights of the kaonic resonances extracted from a fit to the $m_{K\pi\pi}$ spectrum.

We also perform likelihood scans of the fitted parameters, shown in Fig. 6.45, in order to check for multiple solutions. It appears that the fitted solution is unique. Each of these scans is obtained by fixing the corresponding parameter at several consecutive values, for each of which the fit is repeated with random initial values of the varying parameters and always converge to the same solution.

Table 6.23: Results of the $m_{K\pi}$ fit. The nominal fit is performed with 90 bins.

	Module α	Phase ϕ (rad.)	Fit Fraction	Measured Values [24]
$K^{*0}(892)$	1.0 (fixed)	0.0 (fixed)	$0.636^{+0.011}_{-0.009}(\text{stat.})^{+0.017}_{-0.012}(\text{syst.})$	0.576
$\rho^0(770)$	$0.725^{+0.015}_{-0.015}(\text{stat.})^{+0.013}_{-0.022}(\text{syst.})$	$3.110^{+0.036}_{-0.035}(\text{stat.})^{+0.060}_{-0.048}(\text{syst.})$	$0.335^{+0.015}_{-0.013}(\text{stat.})^{+0.033}_{-0.032}(\text{syst.})$	0.314
$(K\pi)$ S-wave	$0.808^{+0.044}_{-0.050}(\text{stat.})^{+0.044}_{-0.058}(\text{syst.})$	$3.197^{+0.132}_{-0.125}(\text{stat.})^{+0.126}_{-0.101}(\text{syst.})$	$0.416^{+0.039}_{-0.041}(\text{stat.})^{+0.056}_{-0.072}(\text{syst.})$	0.110
Sum of all fit fractions			$1.387^{+0.048}_{-0.042}(\text{stat.})^{+0.106}_{-0.088}(\text{syst.})$	1.000
Interferences				
$K^{*0}(892)$—$\rho^0(770)$			$-0.178^{+0.004}_{-0.006}(\text{stat.})^{+0.008}_{-0.010}(\text{syst.})$	$\emptyset$
$(K\pi)$ S-wave—$\rho^0(770)$			$-0.208^{+0.029}_{-0.044}(\text{stat.})^{+0.032}_{-0.049}(\text{syst.})$	$\emptyset$

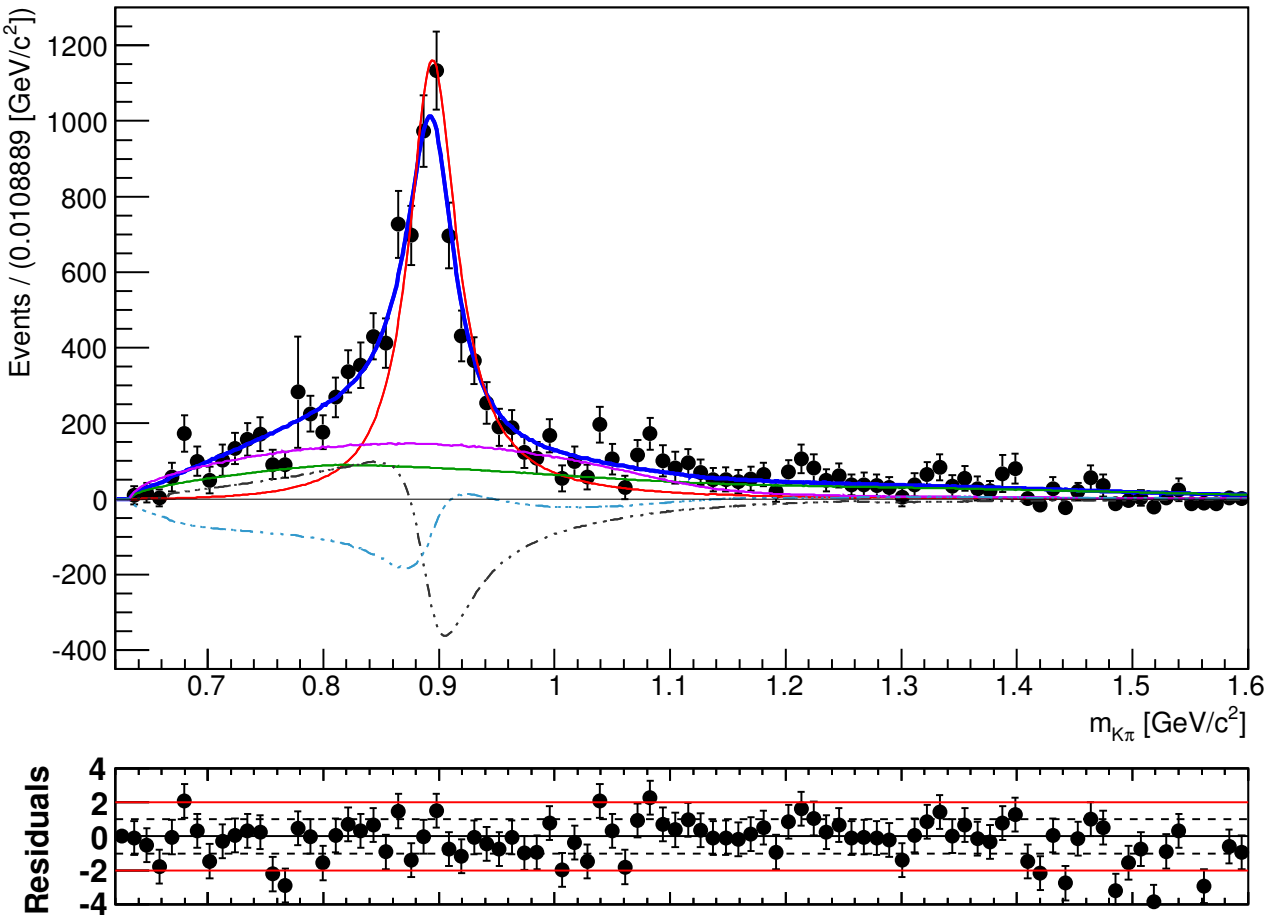

Figure 6.44: $m_{K\pi}$ nominal fit projection (90 bins) and the residual distribution between the total PDF (dark blue solid curve) and the data points. The solid red, green and magenta curves correspond to the $K^{*0}(892)$, $\rho^0(770)$ and $(K\pi)$ S-wave contributions, respectively. The dashed gray curve corresponds to the interferences between the two P-wave components, i.e. the $K^{*0}(892)$ and the $\rho^0(770)$ resonances, while the dashed light blue curve corresponds to the interferences between the $(K\pi)$ S-wave and $\rho^0(770)$ components.

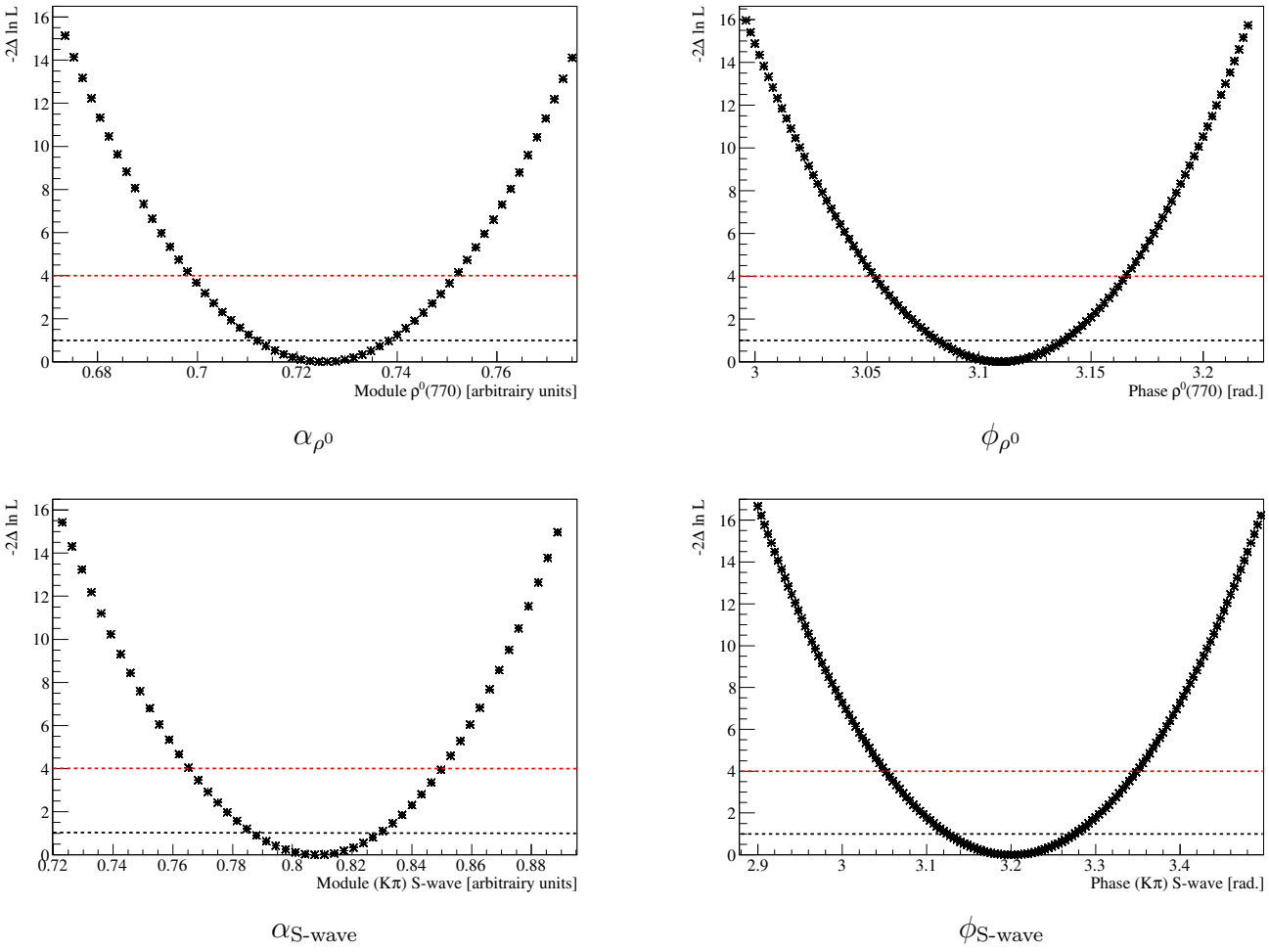

α_{ρ^0} ϕ_{ρ^0}

$\alpha_{\text{S-wave}}$ $\phi_{\text{S-wave}}$

Figure 6.45: One-dimensional scans of $-2\Delta\ln\mathcal{L}$ as a function of the magnitudes of $\rho^0(770)$ and $(K\pi)$ S-wave and the phase of $\rho^0(770)$. The horizontal dashed lines mark the one- and two-standard deviation levels.

6.7.4 Study of the model consistency

In order to check for possible biases, we perform pure toy studies of the model. From the parameters extracted from the nominal fit to the signal-TM $m_{K\pi}$ ${}_s\mathcal{P}lot$ we generated 1000 pseudo-experiments. These were then fitted in order to create the pull distributions of the fit fractions, which are functions of the fitted amplitudes. Figure 6.46 shows the pull distributions of each fit fraction. The pull means and widths, given in Tab. 6.24, are reasonably consistent, within the statistical uncertainties, with 0 and 1, respectively. We conclude that the model has no significant bias on the fit fractions.

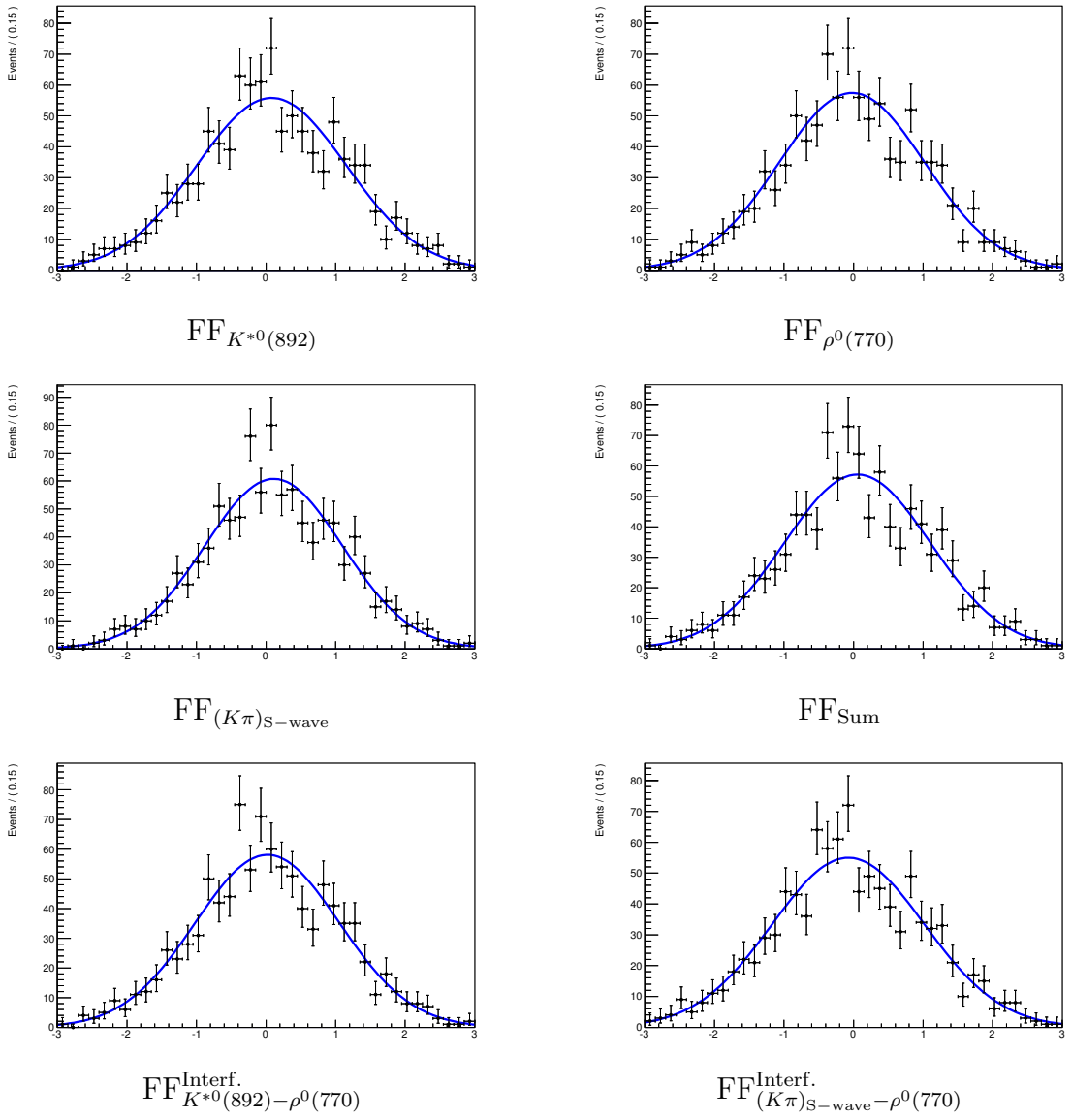

Figure 6.46: Pull distributions of the parameters in the $m_{K\pi}$ fit model.

Table 6.24: Pull means and widths of the parameters in the $m_{K\pi}$ fit model.

Fit fraction	Pull Mean	Pull Width
$\mathrm{FF}_{K^{*0}(892)}$	-0.027 ± 0.034	1.046 ± 0.026
$\mathrm{FF}_{\rho^0(770)}$	0.080 ± 0.035	1.077 ± 0.027
$\mathrm{FF}_{(K\pi)_{\mathrm{S-wave}}}$	0.109 ± 0.032	0.987 ± 0.024
$\mathrm{FF}_{\mathrm{Sum}}$	0.055 ± 0.034	1.050 ± 0.026
$\mathrm{FF}^{\mathrm{Interf.}}_{K^{*0}(892)-\rho^0(770)}$	0.018 ± 0.033	1.034 ± 0.025
$\mathrm{FF}^{\mathrm{Interf.}}_{(K\pi)_{\mathrm{S-wave}}-\rho^0(770)}$	-0.076 ± 0.036	1.095 ± 0.027

6.7.5 Angular moments and results interpretation

In order to add information for the interpretation of the fit results, we calculate the angular moments, defined as

$$\langle P_\ell\left(\cos\theta_{\mathrm{h}}\right)\rangle \equiv \int_{-1}^{1} d\Gamma P_\ell\left(\cos\theta_{\mathrm{h}}\right) d\cos\theta_{\mathrm{h}}\,, \tag{6.25}$$

where θ_{h} is the helicity angle between the K^+ and the π^+, measured in the rest frame of $K^+\pi^-$, P_ℓ is the ℓth Legendre polynomial, and $d\Gamma$ is the differential decay rate. For a three body decay $p \to ijk$ the helicity angle expression in the ij rest frame is given by

$$\cos\theta_{\mathrm{h}}^{ij} = \frac{m_{ij}^2 - m_i^2 - m_k^2 - 2E_i^* E_k^*}{2\sqrt{\left(\left(E_i^*\right)^2 - m_i^2\right)\left(\left(E_k^*\right)^2 - m_k^2\right)}}\,, \tag{6.26}$$

where E_i^* and E_k^* are the energy of particles i and k calculated in the ij rest frame, such as

$$E_i^* = \frac{m_{ij}^2 - m_j^2 + m_i^2}{2m_{ij}}\,, \tag{6.27}$$

$$E_k^* = \frac{m_{ijk}^2 - m_{ij}^2 - m_k^2}{2m_{ij}}\,. \tag{6.28}$$

Angular moments plotted as a function of $m_{K^+\pi^-}$ provide more information than the $m_{K\pi}$ invariant mass fit projections, in particular, spin information. However, in this case, as we are integrating over the whole $m_{K\pi\pi}$ dimension, some caution must be taken in the interpretation of results. We built the angular moments from the $m_{K\pi}$ data distribution, which is signal weighted using the ${}_s\mathcal{P}lot$ technique, using the Legendre polynomials from $\ell = 0$ up to the $\ell = 4$.

$$\begin{aligned} P_0\left(x\right) &= 1 & P_1\left(x\right) &= x \\ P_2\left(x\right) &= \frac{1}{2}\left(3x^2 - 1\right) & P_3\left(x\right) &= \frac{1}{2}\left(5x^3 - 3x\right) \\ P_4\left(x\right) &= \frac{1}{8}\left(35x^4 - 30x^2 + 3\right). \end{aligned} \tag{6.29}$$

The resulting $\langle P_\ell \rangle$ distributions are shown in Fig. 6.47.

• $\langle P_0 \rangle$ is simply the $m_{K\pi}$ invariant mass distribution. It indicates a large contribution from the $K^+\pi^-$ P-wave amplitude, as confirmed by the measured fit fractions (Tab. 6.23).

• $\langle P_1 \rangle$ can be interpreted as representing the projection of the P-wave $K^+\pi^-$ vector onto an effective S-wave vector. Then the fact that $\langle P_1 \rangle$ has a similar distribution to that of $\langle P_0 \rangle$, indicates that the effective S-wave vector lies along the imaginary axis in the complex plane. This appears to be quite different from what was observed in the $K\pi$ scattering experiment [66, 67], which indicates that the overlap with $K\rho^0$ is large.

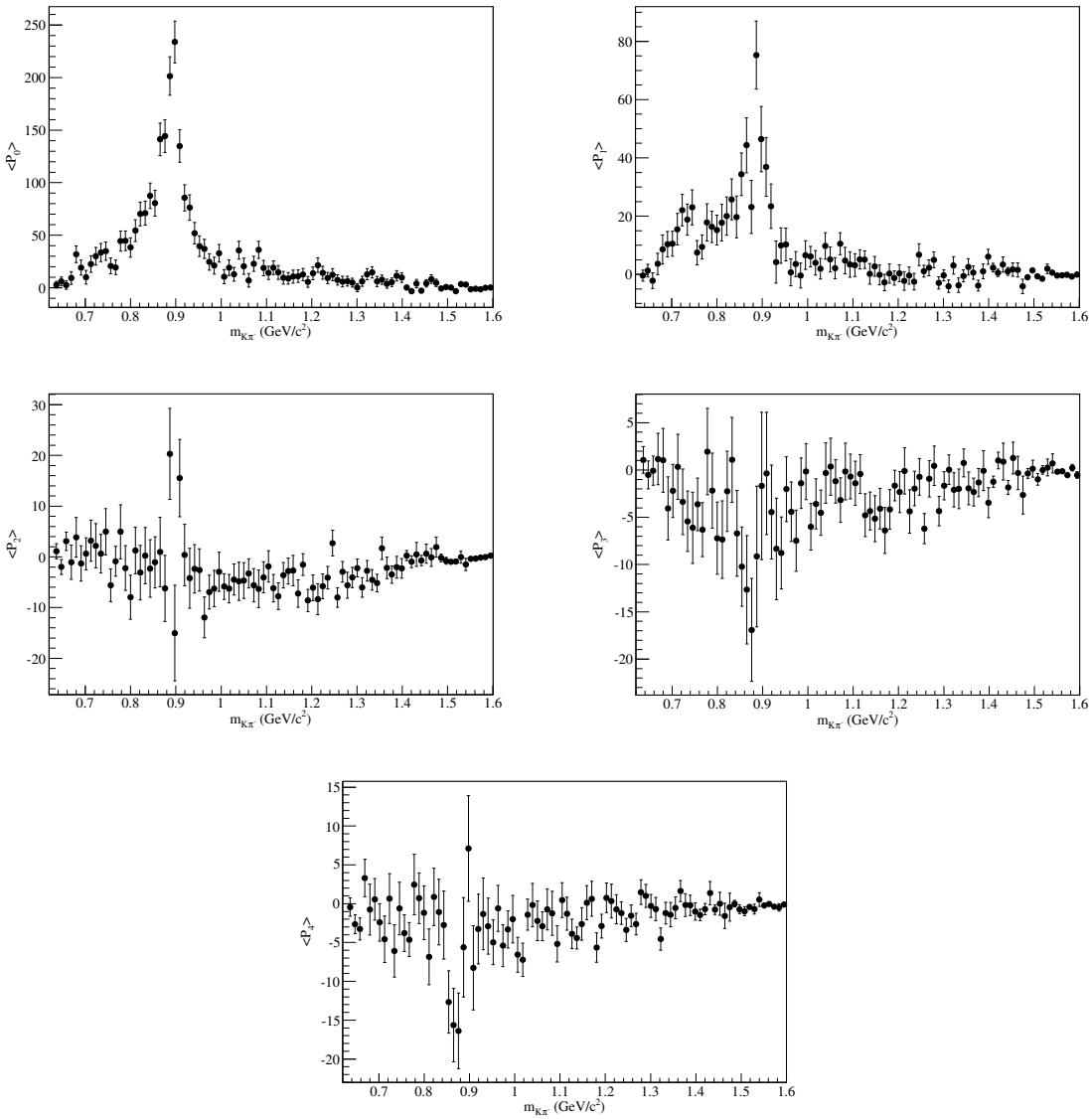

Figure 6.47: Angular moments computed as a function of $m_{K\pi}$ for signal-weighted data.

• $\langle P_2 \rangle$ gives information on the helicity state of the $K\pi$ P-wave amplitude with respect to the recoil pion. For a $K^+\pi^-$ P-wave amplitude produced with helicity-0, the $\langle P_2 \rangle$ distribution should be positive and for helicity either $+1$ or -1 it should be negative. Since we do not observe much of a signal at the $K^*(892)$ pole mass, and since the general trend is to be negative at higher mass values, it could be that there is significant production of helicity ± 1. However, this could also be due to $K\rho^0$ production, especially since the region above $1\,\mathrm{GeV}/c^2$ is probably correlated with the production of the $K_1(1270)$, which has a large expected branching fraction into the $K\rho^0$ mode.

• $\langle P_3 \rangle$ and $\langle P_4 \rangle$ are a good indicator for the presence of interferences with $K\rho^0$ mode. In the case where the interferences are zero or negligible, the $\langle P_3 \rangle$ and $\langle P_4 \rangle$ shapes should be flat along zero. Since we observe that these distributions are small, but non-zero, they cannot be explained by a simple S-P wave description of the $K^+\pi^-$ system, and presumably result from overlap with $K\rho^0$. This observation is in agreement with the fit results, which yields a rather larger contribution for the interference between the two P-wave resonant systems.

6.8 The dilution factor

6.8.1 Analytical expression of the dilution factor

Using the conventions from Ref. [50] we consider the time-dependence of the following exclusive decay processes

$$B^0(t) \to H_{\mathrm{res}} P_{\mathrm{scal}} \gamma \ , \tag{6.30}$$

where the B meson state is identified (tagged) as a B^0 (rather than a $\overline{B}^0$) at time $t = 0$, H_{res} represents a hadronic resonance and P_{scal} a pseudoscalar particle. In these processes, we specifically consider $H_{\mathrm{res}} P_{\mathrm{scal}}$ to represent the hadronic self-conjugate final state $K^0_S\pi^+\pi^-$. We assume that this state comes from a few resonant decay modes where H_{res} corresponds to ρ^0, K^{*+}, K^{*-}, $(K\pi)^+$ or $(K\pi)^-$ S-wave. P_{scal} corresponds to K^0_S or $\pi^\pm$. Note that here we implicitly integrate over the kaonic resonances contributing to the hadronic intermediate states. We can write the amplitudes for these transitions as

$$\begin{aligned}
A_R^{H_{\mathrm{res}}}(B^0 \to H_{\mathrm{res}} P_{\mathrm{scal}} \gamma_L) &= \xi_1 A_{H_{\mathrm{res}}} \sin\psi e^{-i\phi_R^{H_{\mathrm{res}}}} e^{i\delta^{H_{\mathrm{res}}}} \ , \\
A_L^{H_{\mathrm{res}}}(B^0 \to H_{\mathrm{res}} P_{\mathrm{scal}} \gamma_R) &= \xi_2 A_{H_{\mathrm{res}}} \cos\psi e^{-i\phi_L^{H_{\mathrm{res}}}} e^{i\delta^{H_{\mathrm{res}}}} \ , \\
\overline{A}_L^{H_{\mathrm{res}}}(\overline{B}^0 \to H_{\mathrm{res}} P_{\mathrm{scal}} \gamma_L) &= \xi_3 A_{H_{\mathrm{res}}} \cos\psi e^{i\phi_L^{H_{\mathrm{res}}}} e^{i\delta^{H_{\mathrm{res}}}} \ , \\
\overline{A}_R^{H_{\mathrm{res}}}(\overline{B}^0 \to H_{\mathrm{res}} P_{\mathrm{scal}} \gamma_R) &= \xi_4 A_{H_{\mathrm{res}}} \sin\psi e^{i\phi_R^{H_{\mathrm{res}}}} e^{i\delta^{H_{\mathrm{res}}}} \ ,
\end{aligned} \tag{6.31}$$

where $A_{H_{\mathrm{res}}}$ is the (complex) amplitude of the resonance H_{res}, ξ_i are the CP eigenvalues, $\xi_i \equiv CP(H_{\mathrm{res}} P_{\mathrm{scal}}) = \pm 1$, ψ is related to the short-distance Wilson coefficients C_{7_γ} and C'_{7_γ} by $\tan\psi = C'_{7_\gamma}/C_{7_\gamma}$, $\phi_{L/R}^{H_{\mathrm{res}}}$ are the CP-odd weak phases, and $\delta^{H_{\mathrm{res}}}$ corresponds to the strong phases and is related to the corresponding hadronic matrix elements. $\tan\psi$ gives the relative

amount of left-polarized photons and right-polarized photons in $\overline{B}^0$ decays and the sign ξ_i are:

$$\begin{aligned}(\xi_1,\xi_2,\xi_3,\xi_4) &= (+,-,+,-) \quad \text{for } \rho \text{ and } K^{*\pm} \ , \\ (\xi_1,\xi_2,\xi_3,\xi_4) &= (+,+,+,+) \quad \text{for } (K\pi)^{\pm} \text{ S-wave} \ .\end{aligned}$$

The time-evolution of a state $B^0(t=0)$, which oscillates into a mixture of B^0 and $\overline{B}^0$ and decays at time t to $H_{\rm res}P_{\rm scal}\gamma$, can be written as

$$\mathrm{f}_{\pm}(t) \equiv \frac{1}{2}\left(e^{-i\mathrm{M}_L t}e^{-\frac{1}{2}\Gamma_L t} \pm e^{-i\mathrm{M}_H t}e^{-\frac{1}{2}\Gamma_H t}\right) \ . \tag{6.32}$$

We can then define $\Delta\mathrm{M} = \mathrm{M}_H - \mathrm{M}_L$ and $\Delta\Gamma = \Gamma_H - \Gamma_L$, where M_L and M_H are the masses of the mass eigenstates in the $B^0\overline{B}^0$ mixture, B_L and B_H, and Γ_L and Γ_H are their widths. In the case of $B_{\rm d}$ mesons, we have $\Delta\Gamma \ll \Delta\mathrm{M}$, which allows to consider only the leading term in the expansion of the exponential terms in Eq. 6.32. We can then define the time-dependent CP asymmetry as

$$A_{CP}(t) = \frac{\Gamma_{\overline{B}^0}(t) - \Gamma_{B^0}(t)}{\Gamma_{\overline{B}^0}(t) + \Gamma_{B^0}(t)} \equiv \mathcal{C}\cos(\Delta\mathrm{M}t) + \mathcal{S}\sin(\Delta\mathrm{M}t) \ , \tag{6.33}$$

where

$$\begin{aligned}\Gamma_{B^0}(t) &= |\mathcal{M}_L(t)|^2 + |\mathcal{M}_R(t)|^2 \ , \\ \Gamma_{\overline{B}^0}(t) &= \left|\overline{\mathcal{M}}_L(t)\right|^2 + \left|\overline{\mathcal{M}}_R(t)\right|^2 \ ,\end{aligned} \tag{6.34}$$

with $\mathcal{M}$ corresponding to the total amplitudes defined as

$$\begin{aligned}\mathcal{M}_L(t) &= \sum_{H_{\rm res}}\left(A_L^{H_{\rm res}}\mathrm{f}_+(t) + \overline{A}_L^{H_{\rm res}}\frac{q}{p}\mathrm{f}_-(t)\right) \ , \\ \mathcal{M}_R(t) &= \sum_{H_{\rm res}}\left(A_R^{H_{\rm res}}\mathrm{f}_+(t) + \overline{A}_R^{H_{\rm res}}\frac{q}{p}\mathrm{f}_-(t)\right) \ , \\ \overline{\mathcal{M}}_L(t) &= \sum_{H_{\rm res}}\left(\overline{A}_L^{H_{\rm res}}\mathrm{f}_+(t) + A_L^{H_{\rm res}}\frac{q}{p}\mathrm{f}_-(t)\right) \ , \\ \overline{\mathcal{M}}_R(t) &= \sum_{H_{\rm res}}\left(\overline{A}_R^{H_{\rm res}}\mathrm{f}_+(t) + A_R^{H_{\rm res}}\frac{q}{p}\mathrm{f}_-(t)\right) \ ,\end{aligned} \tag{6.35}$$

with

$$\frac{q}{p} = e^{-i\phi} \ , \tag{6.36}$$

where ϕ is the phase in the box diagram such as $\phi \simeq 2\beta$.

We can now consider the time-dependent CP asymmetry for two cases: when we only consider the presence of the ρ^0 resonance ($A_{CP}^{K^0_S\rho\gamma}(t)$), and when the sums in the total amplitudes run over all the hadronic resonances $H_{\rm res}$ ($A_{CP}^{K^0_S\pi^+\pi^-\gamma}(t)$). The former writes

$$A_{CP}^{K^0_S\rho\gamma}(t) = 2\cos\psi\sin\psi\sin(\phi - \phi_L - \phi_R)\sin(\Delta\mathrm{M}t) \ , \tag{6.37}$$

and the latter:

$$
\begin{aligned}
A_{CP}^{K^0_S\pi^+\pi^-\gamma}(t) \;=\; & \frac{1}{\int\left[|A_\rho|^2+\Re\left(A_\rho^* A_{K^{*+}}\right)+\Re\left(A_\rho^* A_{K^{*-}}\right)+\frac{\left|A_{K^{*+}}\right|^2+\left|A_{K^{*-}}\right|^2}{2}+\frac{\left|A_{(K\pi)^+}\right|^2+\left|A_{(K\pi)^-}\right|^2}{2}\right]} \\
& \times\Bigg\{+2\cos\psi\sin\psi\sin(\phi-\phi_L-\phi_R)\sin(\Delta\mathrm{M}t) \\
& \quad\times\int\left[|A_\rho|^2+\Re\left(A_\rho^* A_{K^{*+}}\right)+\Re\left(A_\rho^* A_{K^{*-}}\right)+\Re(A_{K^{*+}}^* A_{K^{*-}})+\Re(A_{(K\pi)^+}^* A_{(K\pi)^-})\right] \\
& \quad-4(\cos^2\psi-\sin^2\psi)\cos(\Delta\mathrm{M}t) \\
& \quad\times\int\left[\frac{\Re(A_{(K\pi)^+}^* A_\rho)+\Re(A_{(K\pi)^-}^* A_\rho)}{2}\right]\Bigg\}\,. \qquad (6.38)
\end{aligned}
$$

Note that the amplitudes $A_{H_{\rm res}}$ correspond to the decay of either a B or a $\overline{B}$ meson. The dilution factor $\mathcal{D}_{K^0_S\rho\gamma}$ is then defined as the ratio between the coefficients multiplying the $\sin(\Delta\mathrm{M}t)$ terms in Eqs. 6.37 and 6.38

$$
\begin{aligned}
\mathcal{D}_{K^0_S\rho\gamma} \;\equiv\; & \frac{\mathcal{S}_{K^0_S\pi^+\pi^-\gamma}}{\mathcal{S}_{K^0_S\rho\gamma}} \qquad (6.39)\\
=\; & \frac{\int\left[|A_\rho|^2+\Re\left(A_\rho^* A_{K^{*+}}\right)+\Re\left(A_\rho^* A_{K^{*-}}\right)+\Re\left(A_{K^{*+}}^* A_{K^{*-}}\right)+\Re(A_{(K\pi)^+}^* A_{(K\pi)^-})\right]}{\int\left[|A_\rho|^2+\Re\left(A_\rho^* A_{K^{*+}}\right)+\Re\left(A_\rho^* A_{K^{*-}}\right)+\frac{\left|A_{K^{*+}}\right|^2+\left|A_{K^{*-}}\right|^2}{2}+\frac{\left|A_{(K\pi)^+}\right|^2+\left|A_{(K\pi)^-}\right|^2}{2}\right]}\,,
\end{aligned}
$$

where the amplitudes $A_{H_{\rm res}}$ depend on the invariant masses $m_{\pi\pi}$ or $m_{K\pi}$ through the corresponding line-shape expressions, and $A^*_{H_{\rm res}}$ are simply the complex conjugates of $A_{H_{\rm res}}$. In both Eqs. 6.39 and 6.38, phase-space integrals are performed over a given region, which is detailed in Sec. 6.8.2. Here we impose the same value of ϕ_L, as well as the same value of ϕ_R for all the hadronic resonances. Moreover, as discussed in Sec. 6.7.2, we do not take into account the interferences between the $K\pi$ P- and S-wave components. Due to opposite *CP* final states the interference terms between the $\pi\pi$ P-wave and the $(K\pi)$ S-wave components cancel and, therefore, do not appear in the dilution factor expression.

6.8.2 Extraction of the dilution factor

Using the hypothesis of Isospin conservation, we assume that B^0 decays have the same amplitudes, $A_{H_{\rm res}}$, as B^+ decays. This allows to use the results extracted from the fit to the $m_{K\pi}$ spectrum in $B^+ \to K^+\pi^+\pi^-\gamma$ decays from the measured amplitudes to obtain the dilution factor for the time dependent analysis.

In the charged-mode analysis, the amplitude of a resonance is modeled in m_{12} as

$$F_{\rm res} = c_{\rm res}\sqrt{{\rm H}_{\rm res}(m_{12},m_{23})}e^{i\Phi(m_{12})} \ , \tag{6.40}$$

where $c_{\rm res}$ is a complex constant, and $\rm H_{res}$ is a real distribution, $\sqrt{{\rm H}_{\rm res}(m_{12},m_{23})}e^{i\Phi(m_{12})}$ being the line shape. The total event rate (given here without the $(K\pi)$ S-wave for simplicity) is written as

$$|F|^2 = |F_\rho + F_{K^*}|^2 \ . \tag{6.41}$$

In the analysis, we consider the total event rate from B^+ and B^- in the $m_{K\pi}$ ($K\pi^+$ or $K\pi^-$)–$m_{\pi\pi}$ plane. If the charge specific amplitudes are noted $F^+_{\rm res}$ and $F^-_{\rm res}$, this implies the underlying assumption

$$|F_\rho + F_{K^*}|^2 = |F^+_\rho + F^+_{K^*}|^2 + |F^-_\rho + F^-_{K^*}|^2 \tag{6.42}$$

or

$$\begin{aligned} |F_\rho|^2 + |F_{K^*}|^2 + 2\Re(F_\rho F^*_{K^*}) \ &= \ |F^+_\rho|^2 + |F^-_\rho|^2 + |F^+_{K^{*+}}|^2 + |F^-_{K^{*-}}|^2 \\ &\quad +2\Re(F^+_\rho F^{+*}_{K^{*+}}) + 2\Re(F^-_\rho F^{-*}_{K^{*-}}) \ . \end{aligned} \tag{6.43}$$

Assuming no direct CP violation in the considered transition:

$$F_\rho \ = \ \sqrt{2}F^+_\rho = \sqrt{2}F^-_\rho \ , \tag{6.44}$$

$$F_{K^*} \ = \ e^{i\delta_{\rm rescat.}}\sqrt{2}F^+_{K^{*+}} = \sqrt{2}F^-_{K^{*-}} \ , \tag{6.45}$$

with $\delta = \delta_{\rm rescat.} = 0$ or π. Given that we measure a sizable interference between the ρ and the K^* (see Tab. 6.23), we keep $\delta_{\rm rescat.} = 0$. Indeed, $\delta_{\rm rescat.} = \pi$ would result in zero interference, as can be deduced from Eq. 6.43. Identical expressions are obtained for the $(K\pi)$ S-wave terms.

Using these conventions, the term $|A_\rho|^2$ in Eq. 6.39 can be written as

$$|A_\rho|^2 = \frac{|F^+_\rho|^2 + |F^-_\rho|^2}{2} = \frac{|F_\rho|^2}{2} \ , \tag{6.46}$$

which contribution to the dilution factor is

$$\begin{aligned} \frac{1}{2}\int |F_\rho|^2 \ &= \ \frac{1}{2}|c_\rho|^2 \int_{m_{12}}\int_{m_{23}} |{\rm H}_\rho(m_{12},m_{23})|^2 dm_{12}dm_{23} \\ &= \ \frac{1}{2}{\rm FF}_\rho \ , \end{aligned} \tag{6.47}$$

where $\rm FF_\rho$ is the measured fit fraction of the ρ resonance in the considered $m_{K\pi}$-$m_{\pi\pi}$ domain, with $m_{12} = m_{K\pi}$ and $m_{23} = m_{\pi\pi}$.

The term

$$\frac{|A_{K^{*+}}|^2 + |A_{K^{*-}}|^2}{2} \tag{6.48}$$

in Eq. 6.39 is written as

$$\frac{|F^{+}_{K^{*+}}|^2 + |F^{-}_{K^{*-}}|^2}{2} = \frac{|F_{K^*}|^2}{2} \tag{6.49}$$

and its contribution to the dilution factor is

$$\begin{aligned} \frac{1}{2}\int |F_{K^*}|^2 &= \frac{1}{2}|c_{K^*}|^2 \int_{m_{12}}\int_{m_{23}} |\mathrm{H_{K^*}}(m_{12}, m_{23})|^2 dm_{12} dm_{23} \\ &= \frac{1}{2}\mathrm{FF_{K^*}} \ , \end{aligned} \tag{6.50}$$

where FF_{K^*} is the measured fit fraction of the K^* resonance in the considered $m_{K\pi}$-$m_{\pi\pi}$ domain.

Identically, the term

$$\frac{|A_{(K\pi)^+}|^2 + |A_{(K\pi)^-}|^2}{2} \tag{6.51}$$

is written as

$$\frac{|F^{+}_{(K\pi)^+}|^2 + |F^{-}_{(K\pi)^-}|^2}{2} = \frac{|F_{(K\pi)}|^2}{2} \tag{6.52}$$

and its contribution to the dilution factor is

$$\begin{aligned} \frac{1}{2}\int |F_{(K\pi)}|^2 &= \frac{1}{2}|c_{(K\pi)}|^2 \int_{m_{12}}\int_{m_{23}} |\mathrm{H}_{(K\pi)}(m_{12}, m_{23})|^2 dm_{12} dm_{23} \\ &= \frac{1}{2}\mathrm{FF}_{(K\pi)} \ , \end{aligned} \tag{6.53}$$

where $\mathrm{FF}_{(K\pi)}$ is the measured fit fraction of the $(K\pi)$ S-wave component in the considered $m_{K\pi}$-$m_{\pi\pi}$ domain.

The terms $\Re(A^*_\rho A_{K^{*+}}) + \Re(A^*_\rho A_{K^{*-}})$ are written as

$$\begin{aligned} \Re(F^{+*}_\rho + F^{+}_{K^{*+}}) + \Re(F^{-*}_\rho + F^{-}_{K^{*-}}) &= 2\Re\left(\frac{1}{\sqrt{2}}F^*_\rho \frac{1}{\sqrt{2}}F_{K^*}\right) \\ &= \Re\left(F^*_\rho F_{K^*}\right) \\ &= \Re\left(c^*_\rho c_{K^*}\sqrt{\mathrm{H}_\rho(m_{12}, m_{23})\mathrm{H_{K^*}}(m_{12}, m_{23})}e^{i(\Phi_{\mathrm{RBW}}(m_{12}) - \Phi_{\mathrm{GS}}(m_{23}))}\right) \ . \end{aligned} \tag{6.54}$$

Then, with the notation $c_{\rm res} = \alpha_{\rm res} e^{i\phi_{\rm res}}$, the contribution of the terms in Eq. 6.54 to the dilution factor is

$$\begin{aligned}
&\alpha_\rho \alpha_{K^*} \int_{m_{12}} dm_{12} \int_{m_{23}} dm_{23} \sqrt{\mathrm{H}_\rho(m_{12},m_{23})\mathrm{H}_{\mathrm{K}^*}(m_{12},m_{23})}\cos\left(\phi_\rho - \phi_{K^*} + \Phi_{\rm GS}(m_{23}) - \Phi_{\rm RWB}(m_{12})\right) \\
&= \alpha_\rho \left[\int_{m_{12}} dm_{12} \cos\left(\phi_\rho - \phi_{\rm RWB}(m_{12})\right) \int_{m_{23}} dm_{23} \sqrt{\mathrm{H}_\rho(m_{12},m_{23})\mathrm{H}_{\mathrm{K}^*}(m_{12},m_{23})}\cos\left(\Phi_{\rm GS}(m_{23})\right) \right. \\
&\qquad \left. - \int_{m_{12}} dm_{12} \sin\left(\phi_\rho - \Phi_{\rm RWB}(m_{12})\right) \int_{m_{23}} dm_{23} \sqrt{\mathrm{H}_\rho(m_{12},m_{23})\mathrm{H}_{\mathrm{K}^*}(m_{12},m_{23})}\sin\left(\Phi_{\rm GS}(m_{23})\right) \right] \\
&= \frac{1}{2}\mathrm{FF}^{\rm interf.}_{K^*-\rho} \ ,
\end{aligned}$$

where $\mathrm{FF}^{\rm interf.}_{K^*-\rho}$ is the measured fit fraction of the interference between the K^* and the ρ resonances in the considered $m_{K\pi}$-$m_{\pi\pi}$ domain. By convention $\alpha_{K^*} = 1$ and $\phi_{K^*} = 0$.

The term $\Re(A^*_{K^{*+}} A_{K^{*-}})$ in Eq. 6.39 is written as

$$\Re(F^{+*}_{K^{*+}} F^{-}_{K^{*-}}) = \frac{1}{2}\Re\left(e^{i\delta}|c_{K^*}|^2 \sqrt{\mathrm{H}_{\mathrm{K}^*}(m_{12},m_{13})\mathrm{H}_{\mathrm{K}^*}(m_{13},m_{12})} e^{i(\Phi_{\rm RBW}(m_{12}) - \Phi_{\rm RBW}(m_{13}))}\right) \ .$$

Note that here $m_{12} = m_{K\pi^+}$ and $m_{23} = m_{K\pi^-}$. This term's contribution to the dilution factor is

$$\begin{aligned}
&\frac{|c_{K^*}|^2}{2} \int_{m_{12}} dm_{12} \int_{m_{13}} dm_{13} \sqrt{\mathrm{H}_{\mathrm{K}^*}(m_{12},m_{13})\mathrm{H}_{\mathrm{K}^*}(m_{13},m_{12})}\cos\left(\delta + \Phi_{\rm RBW}(m_{12}) - \Phi_{\rm RBW}(m_{13})\right) \\
&= \frac{1}{2}\left[\int_{m_{12}} dm_{12} \cos\left(\delta + \Phi_{\rm RBW}(m_{12})\right) \int_{m_{13}} dm_{13} \sqrt{\mathrm{H}_{\mathrm{K}^*}(m_{12},m_{13})\mathrm{H}_{\mathrm{K}^*}(m_{13},m_{12})}\cos\left(\Phi_{\rm RBW}(m_{13})\right) \right. \\
&\qquad \left. + \int_{m_{12}} dm_{12} \sin\left(\delta + \Phi_{\rm RBW}(m_{12})\right) \int_{m_{13}} dm_{13} \sqrt{\mathrm{H}_{\mathrm{K}^*}(m_{12},m_{13})\mathrm{H}_{\mathrm{K}^*}(m_{13},m_{12})}\sin\left(\Phi_{\rm RBW}(m_{13})\right) \right] ,
\end{aligned}$$

where the constant factor $|c_{K^*}|^2$ has been removed since $|c_{K^*}|^2 = 1$ by convention. The contribution of the term $\Re(A^*_{(K\pi)^+} A_{(K\pi)^-})$ is obtained in a similar way and is:

$$\begin{aligned}
&\frac{|c_{(K\pi)}|^2}{2}\left[\int_{m_{12}} dm_{12} \cos\left(\delta + \Phi_{\rm RBW}(m_{12})\right) \int_{m_{13}} dm_{13} \sqrt{\mathrm{H}_{(K\pi)}(m_{12},m_{13})\mathrm{H}_{(K\pi)}(m_{13},m_{12})}\cos\left(\Phi_{\rm RBW}(m_{13})\right) \right. \\
&\quad \left. + \int_{m_{12}} dm_{12} \sin\left(\delta + \Phi_{\rm RBW}(m_{12})\right) \int_{m_{13}} dm_{13} \sqrt{\mathrm{H}_{(K\pi)}(m_{12},m_{13})\mathrm{H}_{(K\pi)}(m_{13},m_{12})}\sin\left(\Phi_{\rm RBW}(m_{13})\right) \right] .
\end{aligned}$$

Since the dilution factor is defined as the ratio between the effective value of $\mathcal{S}\ \mathcal{S}_{K^0_S\pi^+\pi^-\gamma}$ and the target value $\mathcal{S}_{K^0_S\rho\gamma}$, the error on $\mathcal{S}_{K^0_S\rho\gamma}$ is expected to be greater than the one on $\mathcal{S}_{K^0_S\pi^+\pi^-\gamma}$. A large value of the dilution factor is thus preferential. From Eq. 6.39, it is clear that to obtain a large value for $\mathcal{D}_{K^0_S\rho\gamma}$, the proportion of the $\rho^0(770)$ component needs to be

maximized while minimizing the proportions of the $K^*(892)$ and $(K\pi)$ S-wave components. Moreover, since the value of the interference term between the $K^*(892)$ and the $\rho^0(770)$, $\Re(F_\rho^{+*}+F_{K^{*+}}^{+})+\Re(F_\rho^{-*}+F_{K^{*-}}^{-})$, as extracted from a fit to the $m_{K\pi}$ spectrum (Tab. 6.23), is negative, its contribution also needs to be minimized. For this reason, we apply selection cuts in the $m_{\pi\pi}$ dimension around the $\rho^0(770)$ mass as well as a veto on the $K^*(892)$ resonance in the $m_{K\pi}$ dimension. These criteria are optimized taking into account the estimated error on $\mathcal{S}_{K^0_S\pi^+\pi^-\gamma}$, which is more or less proportional to the estimated number of signal events in the dataset after applying these cuts. We found that the best estimated value of the error on $\mathcal{S}_{K^0_S\rho\gamma}$ was obtained for:

- $m_{\pi\pi} \in [0.600, 0.900]$ (GeV/c^2) ;
- $m_{K\pi} \in [m_{K\pi}^{\min}, 0.845] \cup [0.945, m_{K\pi}^{\max}]$ (GeV/c^2) ;

where $m_{K\pi}^{\min}$ and $m_{K\pi}^{\max}$ denote the allowed phase-space boundaries in the $m_{K\pi}$ dimension. This set of cut gives an estimated value of the error on $\mathcal{S}_{K^0_S\rho\gamma}$ of ~ 0.5. Note that the cuts on $m_{\pi\pi}$ take into account the fact that the $\rho^0(770)$ is mainly distorted in the small invariant mass region due to phase space effects. The K^* veto in the $m_{K\pi}$ dimensions roughly corresponds to $(m_{K^*} \pm \Gamma_{K^*})$, where m_{K^*} and Γ_{K^*} are the mass and width of the $K^*(892)$ resonance.

Using the integration region defined above in the $m_{\pi\pi}$ and $m_{K\pi}$ dimensions, each term that appears in the dilution factor expression given in Eq. 6.39 can now be calculated. The corresponding values are:

- $|A_\rho|^2 = 0.270^{+0.030}_{-0.028}$;
- $\frac{|A_{K^{*+}}|^2+|A_{K^{*-}}|^2}{2} = 0.078^{+0.002}_{-0.001}$;
- $\frac{|A_{(K\pi)^+}|^2+|A_{(K\pi)^-}|^2}{2} = 0.139^{+0.023}_{-0.027}$;
- $\Re\big(A_\rho^* A_{K^{*+}}\big) + \Re\big(A_\rho^* A_{K^{*-}}\big) = -0.092^{+0.005}_{-0.006}$;
- $\Re\big(A_{K^{*+}}^* A_{K^{*-}}\big) = 0.002^{+0.001}_{-0.000}$;
- $\Re\Big(A_{(K\pi)^+}^* A_{(K\pi)^-}\Big) = 0.037^{+0.008}_{-0.010}$.

The quoted uncertainties account for both statistical and systematical uncertainties, which were summed up in quadrature.

We finally obtain for the dilution factor:

$$\mathcal{D}_{K^0_S\rho\gamma} = 0.549^{+0.096}_{-0.094} \ . \tag{6.55}$$

6.9 Systematics

As the main purpose of the charged channel is to extract the dilution factor $\mathcal{D}_{K^0_S\rho\gamma}$, we study effects that may influence its extracted value. As described in the previous section, the latter depends on the resonance amplitudes extracted from a fit to the $m_{K\pi}$ spectrum. Therefore in Sec. 6.9.2, we studied various sources of systematic uncertainties on the parameters of the fit to the $m_{K\pi}$ spectrum. Since the $m_{K\pi}$ model depends on the kaonic-resonance amplitudes extracted from a fit to the $m_{K\pi\pi}$ spectrum, we also studied various sources of systematic uncertainties on the parameters of the fit to the $m_{K\pi\pi}$ spectrum, as detailed in Sec. 6.9.1.

6.9.1 Fit to the $m_{K\pi\pi}$ spectrum

Here we give the systematic uncertainties on the parameters of the fit to the $m_{K\pi\pi}$ spectrum (Sec. 6.6.2) originating from: the number of bins in the fitted dataset (Sec. 6.9.1.1), the fixed parameters in the fit performed to $m_{\rm ES}$, ΔE and the Fisher discriminant (Sec. 6.9.1.2) and the fixed line-shape parameters of the kaonic resonances entering in the $m_{K\pi\pi}$ fit model (Sec. 6.9.1.3). We also checked the effects of modifying the procedure of the signal-TM $m_{K\pi\pi}$ ${}_s\mathcal{P}lot$ extraction (Sec. 6.9.1.4). Finally, we studied the effects of some minor model corrections, such as the parametrization of the ΔE distribution for the SCF event category (Sec. 6.9.1.5) and the criteria of assigning events to the SCF category (Sec. 6.9.1.6).

The dominant source of systematic uncertainty n this category is the fixed parameters of the resonance line shapes in the $m_{K\pi\pi}$ fit model.

6.9.1.1 Number of bins in the fitted dataset

To assign systematic uncertainties to the choice of bin size, we perform new fits using either 60 or 100 bins, instead of 80 in the nominal fit. We take the lower and upper deviations from the nominal value of each free parameter as minus- and plus-signed uncertainties, respectively. The corresponding values are given in Tab. 6.25.

6.9.1.2 Fixed parameters in the fit to $m_{\rm ES}$-ΔE-Fisher

To assign systematic uncertainties due to the fixed parameters in the fit to $m_{\rm ES}$, ΔE and the Fisher discriminant, we vary each of the 109 fixed parameters within its uncertainties[7] and redo the fit. Since the $m_{\rm ES}$-ΔE distribution of $B^0 \to K^{*0}(\to K\pi)\gamma + B^0 \to X_{sd}(\to K\pi)\gamma$ background is described by a two-dimensional histogram, we fluctuate the bins and redo the fit. The fixed yields are varied according to the corresponding branching fraction uncertainties taken from [24]. For the categories describing a sum of modes, the fraction of each mode is varied according to the relative branching fraction uncertainties taken from [24]. The SCF yield is varied according to the uncertainties due to MC statistics[8] and the total signal branching fraction uncertainties in Ref. [24] are also taken into account. The fixed yield of the Generic B-background category, describing a sum of several small contributions from

[7] e.g. in the fit to the MC sample from which it is extracted.

[8] All the uncertainties due to MC statistics are scaled to the size of the expected data sample.

Table 6.25: Systematic uncertainties on the parameters of the fit to the $m_{K\pi\pi}$ spectrum due to number of bins in the fitted dataset.

Parameter	+ signed deviation	− signed deviation
Magnitude $K_1(1400)$	0.003	0.001
Magnitude $K^*(1410)$	0.005	0.002
Magnitude $K_2^*(1430)$	0.002	0.006
Magnitude $K^*(1680)$	0.008	0.005
Phase $K_1(1400)$	0.002	0.002
Phase $K^*(1410)$	0.002	0.001
Width $K_1(1270)$	0.001	0.003
Width $K^*(1680)$	0.005	0.001
FF $K_1(1270)$	0.001	0.009
FF $K_1(1400)$	0.007	0.001
FF $K^*(1410)$	0.005	0.005
FF $K_2^*(1430)$	0.003	0.002
FF $K^*(1680)$	0.006	0.001
FF $\{K_1(1270) - K_1(1400)\}$	0.002	0.001
FF $\{K^*(1410) - K^*(1680)\}$	0.001	0.001
FF Sum	0.002	0.002

Table 6.26: Systematic uncertainties on the parameters of the fit to the $m_{K\pi\pi}$ spectrum due to fixed parameters in the fit performed to $m_{\rm ES}$, ΔE and the Fisher discriminant.

Parameter	+ signed deviation	− signed deviation
Magnitude $K_1(1400)$	0.027	0.014
Magnitude $K^*(1410)$	0.060	0.025
Magnitude $K_2^*(1430)$	0.015	0.026
Magnitude $K^*(1680)$	0.108	0.047
Phase $K_1(1400)$	0.018	0.022
Phase $K^*(1410)$	0.013	0.005
Width $K_1(1270)$	0.002	0.004
Width $K^*(1680)$	0.012	0.004
FF $K_1(1270)$	0.010	0.009
FF $K_1(1400)$	0.009	0.003
FF $K^*(1410)$	0.019	0.005
FF $K_2^*(1430)$	0.008	0.012
FF $K^*(1680)$	0.010	0.005
FF $\{K_1(1270) - K_1(1400)\}$	0.011	0.013
FF $\{K^*(1410) - K^*(1680)\}$	0.004	0.020
FF Sum	0.023	0.001

various B-background modes, is varied according to the uncertainties due to MC statistics. For each new fit performed this way, we generate a $m_{K\pi\pi}$ ${}_s\mathcal{P}lot$ distribution that we then fit using the nominal $m_{K\pi\pi}$ model. Assuming no correlations between the fixed parameters, we sum up in quadrature each of the lower and upper deviations from the nominal value of each free parameter, and take the resulting values as minus- and plus-signed uncertainties, respectively. The corresponding values are given in Tab. 6.26.

6.9.1.3 Fixed parameters of the kaonic-resonance line shapes

For the systematic uncertainties due to the fixed parameters of the line-shape resonances in the $m_{K\pi\pi}$ fit model, we vary each of the 8 fixed parameters according to its uncertainties, taken from [24], and redo the fit to the nominal signal-TM $m_{K\pi\pi}$ ${}_s\mathcal{P}lot$ distribution. We sum up in quadrature each of the lower and upper deviations from the nominal value of each free parameter, and take the results as minus- and plus-signed uncertainties, respectively. The corresponding values are given in Tab. 6.27.

Table 6.27: Systematic uncertainties on the parameters of the fit to the $m_{K\pi\pi}$ spectrum due to fixed line-shape parameters of the kaonic resonances entering in the $m_{K\pi\pi}$ fit model.

Parameter	+ signed deviation	− signed deviation
Magnitude $K_1(1400)$	0.117	0.075
Magnitude $K^*(1410)$	0.174	0.127
Magnitude $K_2^*(1430)$	0.073	0.135
Magnitude $K^*(1680)$	0.303	0.202
Phase $K_1(1400)$	0.104	0.118
Phase $K^*(1410)$	0.024	0.022
Width $K_1(1270)$	0.004	0.003
Width $K^*(1680)$	0.043	0.025
FF $K_1(1270)$	0.050	0.050
FF $K_1(1400)$	0.052	0.030
FF $K^*(1410)$	0.053	0.023
FF $K_2^*(1430)$	0.035	0.049
FF $K^*(1680)$	0.089	0.056
FF $\{K_1(1270) - K_1(1400)\}$	0.050	0.060
FF $\{K^*(1410) - K^*(1680)\}$	0.057	0.115
FF Sum	0.140	0.072

6.9.1.4 The ${}_s\mathcal{P}lot$ extraction procedure

As described in Ref. [101], when using the ${}_s\mathcal{P}lot$ technique in the case where one or more event categories have their yields fixed in the maximum likelihood fit, the estimate of the x-distribution considered ${}_s\tilde{\mathrm{M}}_\mathrm{n}$, which is obtained as the sum of the ${}_s$Weights in each bin, needs to be corrected. The correction consists in adding to the ${}_s\tilde{\mathrm{M}}_\mathrm{n}$ histogram the normalized

distributions of each fixed category scaled by the factor $c_{\rm n} = N_{\rm n} - \sum_j {\rm V}_{{\rm n}j}$, where V is the covariance matrix resulting from the fit and N the expected yield of category n. This procedure, which is used in the present analysis to extract the signal-TM ${}_s\mathcal{P}lot$, implies that the x-distributions of the fixed categories are well known. Here the $m_{K\pi\pi}$ distributions are taken from MC, are cannot be considered to fulfill this criterium. Therefore, in order to check for possible effects on the parameters of the fit to the $m_{K\pi\pi}$ spectrum, we performed a new fit to $m_{\rm ES}$, ΔE and the Fisher discriminant, where we merged all the previously fixed-yield categories. Since the shape of PDFs for the Generic B background and of the merged category are very similar, we add the former to the latter and consider them as a single "large background" category. This way we were able to perform a fit with four event categories

Table 6.28: $B^+ \to K^+\pi^-\pi^+\gamma$ fitted yields for the final *BABAR* Run1-6 dataset where all the backgrounds with fixed yields and Generic B background are merged into a single large background category, whose yield is free to vary in the fit.

Category	Fitted yield	Fit error (stat.)
Signal TM	2418	95
Continuum $udsc$	71086	418
$B^0 \to K^{*0}(\to K\pi)\gamma$ + $B^0 \to X_{sd}(\to K\pi)\gamma$	1555	119
Large background	6298	375

Table 6.29: Systematic uncertainties on the parameters of the fit to the $m_{K\pi\pi}$ spectrum due to ${}_s\mathcal{P}lot$ extraction procedure.

Parameter	+ signed deviation	− signed deviation
Magnitude $K_1(1400)$	0.003	$\emptyset$
Magnitude $K^*(1410)$	$\emptyset$	0.016
Magnitude $K_2^*(1430)$	$\emptyset$	0.007
Magnitude $K^*(1680)$	$\emptyset$	0.051
Phase $K_1(1400)$	0.004	$\emptyset$
Phase $K^*(1410)$	$\emptyset$	0,000
Width $K_1(1270)$	0.001	$\emptyset$
Width $K^*(1680)$	$\emptyset$	0.002
FF $K_1(1270)$	0.009	$\emptyset$
FF $K_1(1400)$	0.005	$\emptyset$
FF $K^*(1410)$	$\emptyset$	0.001
FF $K_2^*(1430)$	$\emptyset$	0.001
FF $K^*(1680)$	$\emptyset$	0.009
FF $\{K_1(1270) - K_1(1400)\}$	$\emptyset$	0.009
FF $\{K^*(1410) - K^*(1680)\}$	0.005	$\emptyset$
FF Sum	$\emptyset$	0.004

(i.e. signal-TM, continuum, $B^0 \to K^{*0}(\to K\pi)\gamma$ + $B^0 \to X_{sd}(\to K\pi)\gamma$ and the new large background) where all the yields are free to vary in the fit. We observe a good agreement, within statistical uncertainties, between the fitted yields in the present and the nominal fit configurations; the yields in the two cases are given in Tab. 6.28 and 6.17, respectively. Thus we further extracted the signal-TM ${}_s\mathcal{P}lot$ distributions, where no corrections are to be applied since no event category is fixed in this configuration. We performed a fit to the new $m_{K\pi\pi}$ ${}_s\mathcal{P}lot$ distribution, using the nominal $m_{K\pi\pi}$ fit model. Table 6.29 gives the deviations from the nominal value of each free parameter. In this case, since only one fit is performed, only one deviation is reported (lower or upper) for each free parameter.

6.9.1.5 Parametrization of the SCF ΔE distribution

As described in Sec. 6.5.1, the ΔE distribution of the SCF event category is parametrized using a linear function. In Fig. 6.11, we observe a small disagreement between this parametrization and the MC distribution. In order to study its effect, we modified the parametrization from a linear function to a 4-th order chebychev polynomial. The latter is shown in Fig. 6.48. Using this parametrization, we performed a new fit to $m_{\rm ES}$, ΔE and the Fisher discriminant, from which we generated a new $m_{K\pi\pi}$ ${}_s\mathcal{P}lot$ distribution that we fit using the nominal $m_{K\pi\pi}$ model. The deviations from the nominal value of each free parameter appear to be non significant ($\mathcal{O}(10^{-4})$) compared to the other sources of systematic uncertaintiy, and thus we do not take them into account

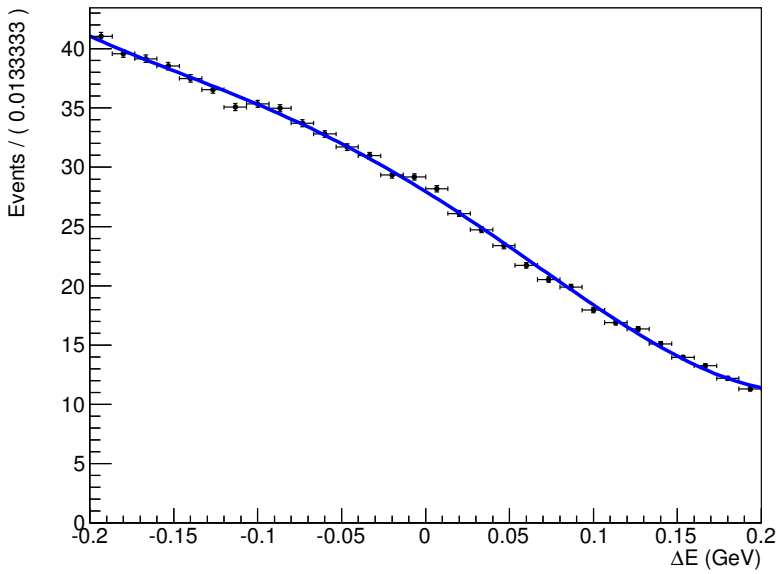

Figure 6.48: Alternative ΔE parametrization of signal SCF category for the systematic uncertainty study. Here the ΔE distribution is parametrized by a 4-th order chebychev polynomial function. Convention are similar to those of Fig. 6.11.

6.9.1.6 Characterization of the signal event category

As described in Sec. 6.3.1, it has been realized at an advanced stage of the analysis that the case of Kaon/Pion swap was in fact corresponding to true SCF. Therefore, we studied the effect of considering these events to be a part of the TM category. Since the fraction of such events (given in Tab. 6.8) is small compared to the estimated number of signal events, the effect of this correction is small. However, we check for possible deviations of the parameters of the fit to the $m_{K\pi\pi}$ spectrum. Since the considered correction only affects the initial values

Table 6.30: Extracted values of the signal PDF parameters before and after correcting for Kaon/Pion swap. We also give the normalized difference, which corresponds to the absolute value of the difference between the two parameter values divided by the averaged error. When 0.0000 is quoted for the error value, it is less than 5×10^{-5}.

	Fit variable	Parameter	Before Kaon/Pion swap correction	After Kaon/Pion swap correction	Normalized difference
Signal TM	m_{ES}	CB_{μ}(Coeff0)	5.2792 ± 0.0000	5.2792 ± 0.0000	0.0558
		CB_{μ}(Coeff1)	-0.0048 ± 0.0002	-0.0048 ± 0.0003	0.0967
		CB_{μ}(Coeff2)	-0.0994 ± 0.0026	-0.0989 ± 0.0020	0.2248
		CB_{σ}(Coeff0)	0.0025 ± 0.0000	0.0025 ± 0.0000	0.3381
		CB_{σ}(Coeff1)	0.0017 ± 0.0002	0.0017 ± 0.0001	0.0651
		CB_{σ}(Coeff2)	0.1568 ± 0.0044	0.1549 ± 0.0052	0.3987
		CB_{α}(Coeff0)	1.7802 ± 0.0923	1.7794 ± 0.0638	0.0107
		CB_{α}(Coeff1)	5.2342 ± 1.0052	5.8407 ± 1.3813	0.5083
		$\mathrm{CB}_{\mathrm{order}}$(Coeff0)	7.6280 ± 2.5806	6.3329 ± 3.0377	0.4610
		$\mathrm{CB}_{\mathrm{order}}$(Coeff1)	-41.647 ± 37.350	-36.239 ± 48.101	0.1266
	ΔE	Cr_{μ}	-0.0021 ± 0.0054	-0.0017 ± 0.0032	0.0922
		Cr_{σ_L}	0.0592 ± 0.0076	0.0563 ± 0.0079	0.3755
		Cr_{σ_R}	0.0324 ± 0.0039	0.0331 ± 0.0050	0.1636
		Cr_{α_L}	0.2790 ± 0.0627	0.2491 ± 0.0818	0.4142
		Cr_{α_R}	0.1259 ± 0.0267	0.1295 ± 0.0233	0.1427
	Fisher	G_{μ}	0.1234 ± 0.0125	0.1222 ± 0.0102	0.1060
		G_{σ}	0.2310 ± 0.0085	0.2320 ± 0.0108	0.1009
Signal SCF	m_{ES}	BG_{μ}	5.2757 ± 0.0404	5.2600 ± 0.0326	0.4292
		BG_{σ_L}	-0.0569 ± 0.0499	-0.0759 ± 0.0603	0.3455
		BG_{σ_R}	0.0041 ± 0.0022	0.0055 ± 0.0028	0.5468
		$\mathrm{Arg}_{\mathrm{endpoint}}$	5.2892 ± 0.0004	5.2892 ± 0.0004	0.0730
		$\mathrm{Arg}_{\mathrm{slope}}$	-149.530 ± 66.756	-136.010 ± 98.144	0.1640
		frac	0.3167 ± 0.6583	0.4025 ± 0.9044	0.1098
	ΔE	Lin_{c_1}	-3.0200 ± 0.4639	-3.0653 ± 0.2673	0.1238
	Fisher	G_{μ}	-0.0067 ± 0.0039	-0.0059 ± 0.0022	0.2766
		G_{σ}	0.2315 ± 0.0201	0.2378 ± 0.0232	0.2908

of PDF parameters for TM and SCF events, we re-extract these parameters from a fit to the (initial) cocktail of signal MC sample and compare the obtained values to the original ones. Table 6.30 gives the two sets of parameters values. We observe that the largest differences are comparable to the statistical uncertainty corresponding to the extraction of the parameters from MC. Therefore, we do not take these effects into account as a systematic uncertainty.

6.9.2 Fit to the $m_{K\pi}$ spectrum

Here we give the systematic uncertainties on the parameters of the fit to the $m_{K\pi}$ spectrum (Sec. 6.7.3) originating from: the number of bins in the fitted dataset as well as the number of bins in the PDF (Sec. 6.9.2.1), the fixed parameters in the fit performed to $m_{\rm ES}$, ΔE and the Fisher discriminant (Sec. 6.9.2.2), the fixed line-shape parameters of the resonances entering in the $m_{K\pi}$ fit model (Sec. 6.9.2.3), the weights of the kaonic resonances used to construct the total PDF (Sec. 6.9.2.4) and the line-shape parameters of the kaonic resonances used in the MC generator (Sec. 6.9.2.5). The dominant source of systematic uncertainty in this category is due to the weights of the kaonic resonances extracted from a fit to the $m_{K\pi\pi}$ spectrum. We also checked the effects of modifying the procedure of the signal-TM $m_{K\pi}$ ${}_s\mathcal{P}lot$ extraction (Sec. 6.9.2.6). Finally, we studied the effects of some minor model corrections, such as the parametrization of the ΔE distribution for the SCF event category (Sec. 6.9.2.7) and the criteria of assigning events to the SCF category (Sec. 6.9.2.8).

6.9.2.1 Number of bins in the fitted dataset and in the PDF

We account for two sources of systematic uncertainties from the number of bins: in the fitted ${}_s\mathcal{P}lot$ (90 bins in the nominal fit) and in the two-dimensional histograms used to create the total PDF (450×100 bins in the nominal fit for $m_{K\pi} \times m_{\pi\pi}$, respectively). We estimate the effect of the bin size of the ${}_s\mathcal{P}lot$ from fits performed with 75 and 105 bins, while the bin size of the PDF is fixed to its nominal value. The corresponding results are given in Tab. 6.31. We associate one systematic uncertainty to the bin size in $m_{K\pi}$ and another to the one in $m_{\pi\pi}$. We estimate the effect of the bin sizes of the PDF, in the $m_{K\pi}(m_{\pi\pi})$ dimension, from fits performed with alternative PDFs with 270(50) and 630(150) bins in $m_{K\pi}(m_{\pi\pi})$, and the nominal number of bins in the other dimension. For each of these sources we take the lower and upper deviations from the nominal value of each FF as the corresponding uncertainty. We add the uncertainties coming from the bin size in $m_{K\pi}(m_{\pi\pi})$ in quadrature assuming no correlations between them. The corresponding values are given in Tab. 6.32.

6.9.2.2 Fixed parameters in the fit to $m_{\rm ES}$-ΔE-Fisher

Using the procedure described in Sec. 6.9.1.2, we generate a set of new $m_{K\pi}$ ${}_s\mathcal{P}lot$ distributions that we fit using the nominal model. We sum up in quadrature each of the lower and upper deviations from the nominal result of each free parameter, and take the resulting values as minus and plus signed uncertainties, respectively. The corresponding values are given in Tab. 6.33.

6.9.2.3 Parameters of the resonances in the $m_{K\pi}$ fit model

To account for systematic effects due to the fixed parameters of the resonances in the $m_{K\pi}$ fit model, we vary each of them according to the uncertainties given in Tab. 6.22. These parameters appear both in the line shapes used to generate the histograms of the resonances as well as in the corresponding analytical phase expression. Therefore, for each parameter variation in a given line shape, we apply the accept-reject method to a non-resonant phase

Table 6.31: Systematic uncertainties on the parameters of the fit to the $m_{K\pi}$ spectrum due to the number of bins in the ${}_s\mathcal{P}lot$.

Parameter	+ signed deviation	− signed deviation
Magnitude $\rho^0(770)$	0.006	0.000
Magnitude $(K\pi)$ S-wave	0.000	0.035
Phase $\rho^0(770)$	0.000	0.009
Phase $(K\pi)$ S-wave	0.000	0.016
FF $K^{*0}(892)$	0.011	0.000
FF $\rho^0(770)$	0.014	0.000
FF $(K\pi)$ S-wave	0.000	0.029
FF $\{K^{*0}(892) - \rho^0(770)\}$	0.000	0.006
FF $\{(K\pi)$ S-wave $- \rho^0(770)\}$	0.000	0.020
FF Sum	0.053	0.000

Table 6.32: Systematic uncertainties on the parameters of the fit to the $m_{K\pi}$ spectrum due to the number of bins in the PDF.

Parameter	+ signed deviation	− signed deviation
Magnitude $\rho^0(770)$	0.000	0.004
Magnitude $(K\pi)$ S-wave	0.020	0.000
Phase $\rho^0(770)$	0.012	0.000
Phase $(K\pi)$ S-wave	0.013	0.000
FF $K^{*0}(892)$	0.000	0.006
FF $\rho^0(770)$	0.000	0.003
FF $(K\pi)$ S-wave	0.015	0.000
FF $\{K^{*0}(892) - \rho^0(770)\}$	0.001	0.000
FF $\{(K\pi)$ S-wave $- \rho^0(770)\}$	0.007	0.000
FF Sum	0.000	0.022

space MC distribution as described in Sec. 6.22 to generate a new distribution of the corresponding resonance, and use the same parameter value in the analytical phase expression. For each variation we perform a new fit to the nominal $m_{K\pi}$ ${}_s\mathcal{P}lot$ distribution. We sum up in quadrature each of the lower and upper deviations from the nominal result of each free parameter, and take the resulting values as minus and plus signed uncertainties, respectively. The corresponding values are given in Tab. 6.34. The dominant effect here is due to the line-shape parameters of the $K_0^*(1430)$ corresponding to the resonant part of the LASS parametrization. The effects coming from the $\rho^0(770)$ and $K^{*0}(892)$ line-shape parameters are negligible.

Table 6.33: Systematic uncertainties on the parameters of the fit to the $m_{K\pi}$ spectrum due to the fixed parameters in the fit performed to $m_{\rm ES}$, ΔE and the Fisher discriminant.

Parameter	+ signed deviation	− signed deviation
Magnitude $\rho^0(770)$	0.005	0.009
Magnitude $(K\pi)$ S-wave	0.018	0.005
Phase $\rho^0(770)$	0.045	0.003
Phase $(K\pi)$ S-wave	0.073	0.006
FF $K^{*0}(892)$	0.002	0.003
FF $\rho^0(770)$	0.011	0.009
FF $(K\pi)$ S-wave	0.020	0.013
FF $\{K^{*0}(892) - \rho^0(770)\}$	0.003	0.001
FF $\{(K\pi)$ S-wave $- \rho^0(770)\}$	0.013	0.007
FF Sum	0.024	0.045

Table 6.34: Systematic uncertainties on the parameters of the fit to the $m_{K\pi}$ spectrum due to the line-shape parameters of the resonances used in the $m_{K\pi}$ fit model.

Parameter	+ signed deviation	− signed deviation
Magnitude $\rho^0(770)$	0.002	0.001
Magnitude $(K\pi)$ S-wave	0.007	0.001
Phase $\rho^0(770)$	0.012	0.017
Phase $(K\pi)$ S-wave	0.018	0.042
FF $K^{*0}(892)$	0.000	0.004
FF $\rho^0(770)$	0.003	0.011
FF $(K\pi)$ S-wave	0.021	0.001
FF $\{K^{*0}(892) - \rho^0(770)\}$	0.002	0.001
FF $\{(K\pi)$ S-wave $- \rho^0(770)\}$	0.014	0.004
FF Sum	0.007	0.039

6.9.2.4 Weights of the kaonic resonances used to construct the total PDF

To account for systematic effects due to the weights of kaonic resonances used to construct the total PDF, we first generated a large number of sets of weights (10000) from the $m_{K\pi\pi}$ fit-fractions correlation matrix (taking into account the corresponding statistical and systematical uncertainties). In a second step, we performed a fit to the $m_{K\pi}$ spectrum using each of these sets of weight as a new parametrization of the total PDF. From the results of these fits we obtained a distribution for each free parameter and for each of the fit fractions. Finally we took the values at plus and minus 34.1% of the integral of the corresponding distribution from the nominal fit value as the plus or minus signed uncertainties, respectively. The corresponding values are given in Tab. 6.35.

6.9.2.5 Parameters of the kaonic-resonances used in the MC generator

The distortions of the $\rho^0(770)$ and $K^{*0}(892)$ resonances, taken into account in the fit model by histograms generated using MC distributions from exclusive kaonic resonance decays, are correlated to the parameters of the kaonic-resonance line shapes in the MC generator. In order to study systematic effects from the fixed values of these parameters, we generated new MC distributions of the $\rho^0(770)$ and $K^{*0}(892)$ for each kaonic resonance. We checked that the only significant effect arrises for the $\rho^0(770)$ distribution in the $K_1(1270) \to K\rho^0(770)$ decay channel. Therefore, in order to estimate the systematic uncertainties coming from the $K_1(1270)$ resonance parameters, we varied its mean and its width, taken from Ref. [24],

Table 6.35: Systematic uncertainties on the parameters of the fit to the $m_{K\pi}$ spectrum due to the weights of the kaonic resonances used to construct the total PDF.

Parameter	+ signed deviation	− signed deviation
Magnitude $\rho^0(770)$	0.011	0.003
Magnitude $(K\pi)$ S-wave	0.009	0.046
Phase $\rho^0(770)$	0.030	0.030
Phase $(K\pi)$ S-wave	0.077	0.042
FF $K^{*0}(892)$	0.013	0.007
FF $\rho^0(770)$	0.027	0.006
FF $(K\pi)$ S-wave	0.012	0.065
FF $\{K^{*0}(892) - \rho^0(770)\}$	0.005	0.008
FF $\{(K\pi)$ S-wave $- \rho^0(770)\}$	0.020	0.038
FF Sum	0.087	0.030

Table 6.36: Systematic uncertainties on the parameters of the fit to the $m_{K\pi}$ spectrum due to the line-shape parameters of the kaonic resonances used in the MC generator.

Parameter	+ signed deviation	− signed deviation
Magnitude $\rho^0(770)$	0.000	0.003
Magnitude $(K\pi)$ S-wave	0.014	0.001
Phase $\rho^0(770)$	0.021	0.030
Phase $(K\pi)$ S-wave	0.025	0.063
FF $K^{*0}(892)$	0.000	0.005
FF $\rho^0(770)$	0.000	0.005
FF $(K\pi)$ S-wave	0.006	0.001
FF $\{K^{*0}(892) - \rho^0(770)\}$	0.002	0.001
FF $\{(K\pi)$ S-wave $- \rho^0(770)\}$	0.008	0.003
FF Sum	0.011	0.021

according to the corresponding uncertainty in our fit on the $m_{K\pi\pi}$ spectrum. For each variation we generated a new PDF, that we used to perform a fit to the nominal $m_{K\pi}$ ${}_s\mathcal{P}lot$ distribution. We sum up in quadrature each of the lower and upper deviations from the nominal result of each free parameter, and take the resulting values as minus and plus signed uncertainties, respectively. The corresponding values are given in Tab. 6.36.

6.9.2.6 The ${}_s\mathcal{P}lot$ extraction procedure

To account for systematic effects coming from the ${}_s\mathcal{P}lot$ extraction procedure on the parameters of the fit to the $m_{K\pi}$ spectrum, we performed a fit to the $m_{K\pi}$ ${}_s\mathcal{P}lot$ distribution, obtained from the procedure described in Sec. 6.9.1.4, using the nominal $m_{K\pi}$ fit model. Table 6.37 gives the deviations from the nominal value of each free parameter. Again in this case, since only one fit is performed, only one deviation is reported (lower or upper) for each free parameter.

6.9.2.7 Parametrization of the SCF ΔE distribution

As in the case of the $m_{K\pi\pi}$ spectrum (see Sec. 6.9.1.5, we studied the effects of changing the parametrization of the ΔE distribution for the SCF event category (initially a linear function, changed for a 4-th order chebychev polynomial function, the latter shown in Fig. 6.11) on the parameters of the fit to the $m_{K\pi}$ spectrum. As previously, the deviations from the nominal value of each free parameter appear to be non significant (< 0.001) compared to other sources of systematic uncertainties. Therefore we do not take into account these deviations as a systematic uncertainty.

Table 6.37: Systematic uncertainties on the parameters of the fit to the $m_{K\pi}$ spectrum due to the ${}_s\mathcal{P}lot$ extraction procedure.

Parameter	+ signed deviation	− signed deviation
Magnitude $\rho^0(770)$	$\emptyset$	0.019
Magnitude $(K\pi)$ S-wave	0.030	$\emptyset$
Phase $\rho^0(770)$	$\emptyset$	0.014
Phase $(K\pi)$ S-wave	$\emptyset$	0.042
FF $K^{*0}(892)$	0.001	$\emptyset$
FF $\rho^0(770)$	$\emptyset$	0.027
FF $(K\pi)$ S-wave	0.043	$\emptyset$
FF $\{K^{*0}(892) - \rho^0(770)\}$	0.004	$\emptyset$
FF $\{(K\pi)$ S-wave $- \rho^0(770)\}$	0.014	$\emptyset$
FF Sum	$\emptyset$	0.048

6.9.2.8 Characterization of the signal event category

From the conclusion of the study of the change in the initial PDFs parameters of signal TM and SCF given in Sec. 6.9.1.6, we conclude that, as in the case of the $m_{K\pi\pi}$ spectrum, the effects of moving the Kaon-Pion swap events from the TM into the SCF category are not significant and therefore, we do not take these effects into account as a systematic uncertainty.

Chapter 7

Time Dependent Analysis of $B^0 \to K^0_S\pi^+\pi^-\gamma$ decays: probing the photon helicity

Contents

Before presenting the analysis, whose purpose is to extract the CP violation parameters, we introduce, in Sec. 7.1, some additional analysis techniques that are particular to time-dependent analyses in B-meson decays, such as tagging (Section 7.1.1), the measurement of Δt between the decay of the two B mesons in the event modeling the Δt resolution (Section 7.1.2) and finaly the Δt PDFs for each event species considered in the present analysis (Secs. 7.1.3 and 7.1.4).

7.1 Time-dependent model

7.1.1 Flavor tagging

As discussed at the beginning of Part II, in order to perform the measurement of time-dependent *CP* asymmetries it is essential to determine the flavor of one of the two neutral B mesons in the event, referred to as $B_{\rm tag}$. This is achieved by looking at the decay products of the B meson when it decays into a flavor-specific state. Among these, semileptonic decays, in which the charge of the lepton ℓ unambiguously identifies that of the b quark and hence the B-meson flavor, represent one of the best example.

Since the statistical error (σ) on measurements of time-dependent parameters (such as *CP* asymmetry parameters in the present study or sin2β and Δm_d or, in other *BABAR* analyses) strongly depends on the tagging algorithm, it is primordial to maximize the tagging efficiency ϵ_{tag} while minimizing the probability of assigning a wrong flavor to $B_{\rm tag}$, also called *mistag rate* or ω. Indeed, σ is inversely proportional to the square-root of the "effective tagging efficiency", Q [25]:

$$\sigma \propto \frac{1}{\sqrt{Q}}, \qquad \text{with} \qquad Q = \epsilon_{tag}\,(1-2\omega)^2\,. \tag{7.1}$$

The efficiency ϵ_{tag}, which is defined as the fraction of events that are assigned a tag, is calculated with respect to the sample of events that satisfy the requirements for the tag-side vertexing (see Section 7.1.2) and that have at least one fully reconstructed candidate. In order to improve the tagging algorithm, various tagging categories "c" (detailed in Sec. 7.1.1.1) are defined. To each one are assigned a tagging efficiency and a mistag rate (ϵ^c_{tag} and ω^c), in which case the effective tagging efficiency can be written as $Q = \sum_c \epsilon^c_{tag}(1-2\omega^c)^2$. With the latest version of the *BABAR* tagging protocol, `Tag08` [116], which is used in the present analysis and described later in this section, a value of $Q = 32.7 \pm 0.3\%$ is achieved.

Using the probability ω ($\bar{\omega}$) of incorrectly reporting a $B_{tag} = B^0$ as $\overline{B}^0$ ($B_{tag} = \overline{B}^0$ as B^0), we can define quantities that are more convenient from the experimental point of view, in each of the tagging category c:

$$\langle\omega\rangle^c = \tfrac{1}{2}(\omega^c + \bar{\omega}^c) \quad , \qquad \Delta\omega^c = (\omega^c - \bar{\omega}^c) \tag{7.2}$$

$$\mathcal{D}^c = 1 - 2\omega^c \quad , \qquad \overline{\mathcal{D}}^c = 1 - 2\bar{\omega}^c \tag{7.3}$$

$$\langle\mathcal{D}\rangle^c = \tfrac{1}{2}(\mathcal{D}^c + \overline{\mathcal{D}}^c) = 1 - (\omega^c + \bar{\omega}^c) \quad , \qquad \Delta\mathcal{D}^c = (\mathcal{D}^c - \overline{\mathcal{D}}^c) = -2(\omega^c - \bar{\omega}^c), \tag{7.4}$$

where $\mathcal{D}$ is referred to as the "dilution factor" and $\Delta\mathcal{D}^c$ parameterize a possible difference in performance of the tagging procedure for the two tags, B^0 and $\overline{B}^0$.

7.1.1.1 The *BABAR* flavor tagging algorithm

In order to achieve an optimal separation between B^0 and $\overline{B}^0$ events, the *BABAR* tagging algorithm [117] is based on multivariate techniques, that combine several different signatures. In a first step, tracks from the fully reconstructed B meson ($B_{\rm rec}$) are removed, the rest of the event being assigned to the $B_{\rm tag}$. Tracks from the $B_{\rm tag}$ are then analyzed by a Neural

Network (NN), referred to as `Tag08`, whose output values range from -1 to $+1$, where the absolute value represents the confidence in the estimation, and the sign indicates the flavor of the meson:

- NN $> 0 \to B_{\text{tag}} = B^0$
- NN $< 0 \to B_{\text{tag}} = \overline{B}^0$

The output value of `Tag08`, and hence the B_{tag} flavor, is calculated from the combination of nine other NNs, referred to as "sub-taggers", each of which being optimized to identify specific signatures such as the charge, momentum or decay angles of charged leptons, kaons and pions. The sub-taggers are called `Electron, Muon, Kinematical Lepton, Kaon, slow pion, Kaon-slow pion, maximum-momentum, fast-slow particles correlation` and `Lambda`. As an illustration of the procedure used to identify the B_{tag} flavor, a detailed description of some of the sub-taggers contributing the most to the value of Q in *BABAR*, is given below:

- **Lepton sub-taggers**

  In order to fully exploit the semileptonic decays of the B meson (with $\mathcal{B} = 10.4\%$ [24]), these sub-taggers focuse on electrons and muons, which provide excellent tagging information. Indeed in $b \to c\ell^-\bar{\nu}$ processes, where a virtual $W^-(W^+)$ boson, emitted by the $b(\bar{b})$ quark, decays to an electron or a muon and an (anti)neutrino, the charge of the *primary lepton* is unambiguously linked to the flavor of the B meson. Other processes occur, containing *secondary leptons* such as in cascade decays, where the lepton comes from the decay of a daughter D^0 meson. The issue, then, is to isolate the primary leptons from secondary leptons, since the latter carries opposite tagging information: their charge is opposite to that of the primary lepton.

  For this purpose, several discriminating variables are used. Since the secondary leptons are characterized by a softer momentum spectrum, the CM momentum of the track, p^* is used. In addition, due to directions of the primary $\ell\nu$ pair that are expected to be anticorrelated in the CM frame, the cosine of the angle between the missing momentum (which approximates that of the neutrino) and the lepton's momentum, $\cos\theta_{miss}$, is also used. Finally, the energy contained in the hemisphere defined by the direction of the virtual $W^\pm$, is also used. Indeed the primary leptons, unlike secondary ones, are likely to be isolated from the rest of the charged tracks involved as illustrated in Fig. 7.1.

  The flavor tagging algorithm uses three different sub-taggers trained independently, which exploit the discriminating variables described above:

  - the electron sub-tagger, with tracks that satisfy the `VeryTight` (see Section 5.2.3) electron ID criteria
  - the muon sub-tagger, with tracks that satisfy the `Tight` muon candidates
  - the kinematical lepton sub-tagger, based only on kinematics in order to recover the primary leptons that where not selected by the two previous PID criteria

- **Kaon sub-tagger**

  This sub-tagger uses signatures from charged kaons, formed mainly in cascade decays, $B^0 \to \bar{D}\,(\to K^+ Y)\,X$, as input to the tagging algorithm. As in the case of leptons, a clear distinction much be achieved between kaons whose charges correlate differently with the flavor of $B_{\rm tag}$. The dominant source of charged kaons comes from $b \to c \to s$ processes, which gives rise to *right-sign* kaons (e.g. in the $b \to W^- c(\to s \to K^-)$ transition), whereas the *wrong sign* kaons come from the decay products of the W^-, for instance in $b \to XW^-$ transitions with $W^- \to \overline{c}q, (\overline{c} \to \overline{s} \to K^+)$. This is illustrated in Figure 7.1. Due to the high branching fraction for inclusive $B^0 \to K^{\pm}X$ decays (78(8)% [24]) and the good signal-to-background ratio, the kaon sub-tagger is the most powerful source of tagging information in *BABAR*.

  The NN input variables are here: the charge and PID likelihood of the best three kaon candidates of the event; the number of K^0_S candidates; the sum of transverse momentum squared on the tag side, Σp_t^2. The higher is Σp_t^2 the better is the discrimination of kaons originating from a W rather than from a charmed object. On the contrary, a non-zero number of K^0_S will decrease the tag power, since they are likely to come from the strange quark in the cascade $b \to c \to s$, providing no information on the $B_{\rm tag}$ flavor.

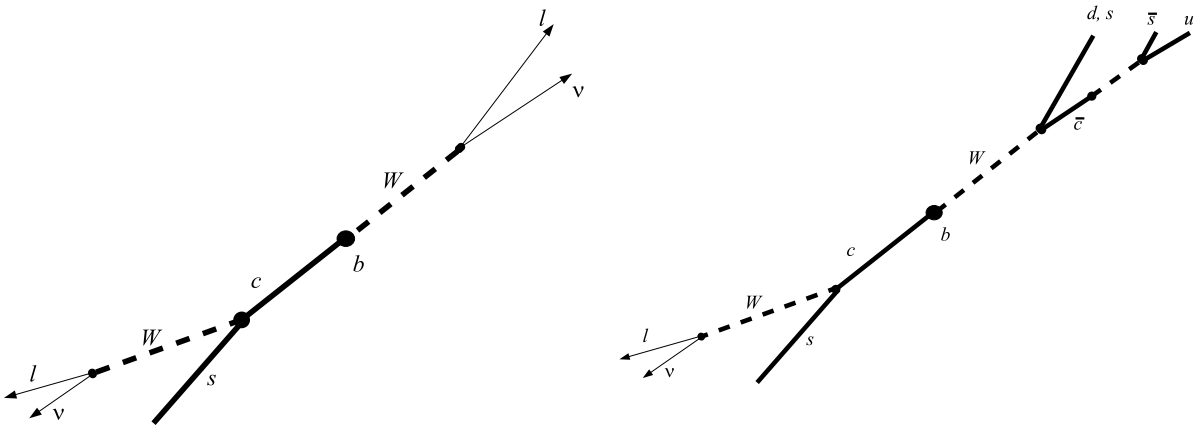

Figure 7.1: Diagrams representing b decays likely to produce a `Lepton` tag (left) and a `Kaon` tag (right). The right-hand diagram demonstrates how right- and wrong-sign kaons may appear in a b decay.

A further classification of the events into tagging categories is performed according to their overall numerical value of the NN, to which all nine sub-taggers contribute. In order of increasing mistag rate, these categories are: `Lepton, KaonI, KaonII, Kaon-Pion, Pion, Other` and `Untagged`, where the last one is a category where no reliable tagging information is provided (i.e. $\mathcal{D}_{\texttt{untagged}} = 0$). The name given to each category are related to the sub-tagger with the largest contribution in the flavor identification.

To ensure the good behavior of the algorithm, it is trained and checked using MC. It is further validated on data using a large sample of fully reconstructed flavor-specific decays: $B^0 \to D^{(*)\pm}\pi^{\mp}$, $B^0 \to D^{(*)\pm}\rho^{\mp}$ and $B^0 \to D^{(*)\pm}a_1^{\mp}$. A fit to the data Δt distribution allows the extraction of the mistag rates (see Table 7.1).

Table 7.1: Performance of *BABAR*'s `Tag08` tagging algorithm in terms of efficiency and mistag probabilities, as measured on a large sample of fully reconstructed flavor-specific decays. The definition for $\Delta\epsilon^c_{tag}$ and ΔQ^c is analogous to the one of $\Delta\omega^c$. The algorithm is described in detail in [118] and references therein.

Category	$\epsilon^c_{tag}(\%)$	$\Delta\epsilon^c_{tag}(\%)$	$\omega^c(\%)$	$\Delta\omega^c(\%)$	$Q^c(\%)$	$\Delta Q^c(\%)$
`Lepton`	9.70 ± 0.07	-0.0 ± 0.2	2.0 ± 0.2	0.6 ± 0.5	8.95 ± 0.11	-0.28 ± 0.37
`KaonI`	11.38 ± 0.08	-0.2 ± 0.2	4.9 ± 0.3	0.6 ± 0.6	9.27 ± 0.14	-0.44 ± 0.46
`KaonII`	15.71 ± 0.09	0.4 ± 0.3	13.5 ± 0.3	-1.0 ± 0.6	8.36 ± 0.16	0.68 ± 0.49
`Kaon-Pion`	13.39 ± 0.08	0.2 ± 0.2	23.0 ± 0.4	-0.9 ± 0.7	3.90 ± 0.12	0.33 ± 0.34
`Pion`	17.20 ± 0.09	-0.1 ± 0.3	33.6 ± 0.4	0.2 ± 0.6	1.85 ± 0.09	-0.07 ± 0.24
`Other`	10.19 ± 0.07	-0.2 ± 0.2	41.1 ± 0.5	4.8 ± 0.8	0.32 ± 0.04	-0.35 ± 0.10
Total	77.59 ± 0.10	0.0 ± 0.6			32.7 ± 0.3	-0.1 ± 0.9

7.1.2 Δt measurement and resolution

7.1.2.1 Δz measurement

In order to be able to determine the time difference between the decays of the two B mesons, the distance along the z-axis between the two corresponding vertexes must be measured first. For this purpose, the $B_{\rm rec}$ vertex is reconstructed using all the daughter tracks as described in Sec. 5.2.4. In the case of charmonium sin2β analyses [119], the resolution in z is about $65\,\mu$m for more than 99% of the B meson candidates ($\sim 45\mu m$ for more than 80%). The resolution is evaluated by subtracting the true value from the reconstructed one, and the uncertainty corresponds to the RMS of this residual distribution. In contrast, the $B_{\rm tag}$ meson is reconstructed inclusively, using all the other tracks in the event, in order to keep a reasonably high level of efficiency. This leads to a total uncertainty on the Δz measurement of $\sim 190\,\mu$m ($\sim 150\mu m$ for 99% of the events), which dominates the overall resolution in Δz. To avoid too large biases and tails in the reconstruction algorithm of the $B_{\rm tag}$ vertex, the daughters of long-lived particles, such as K^0_S and Λ, are replaced by the trajectories of the composite particles. Additionally, the tracks consistent with photon conversions are removed. Since the lifetimes of D mesons and other charmed particles are comparable to those of the B mesons, their daughters can still introduce the undesired effects described above. In order to reduce these contributions, an iterative fit procedure is used, in which the track with the largest vertex χ^2 contribution (i.e. greater than 6 units) is removed and the fit is redone. This procedure is repeated until no track fails the criterion.

In modes where the $B_{\rm rec}$ is fully reconstructed, like in both analyses presented in this thesis, the measurement of Δz can be further improved be means of the quantities extracted

from the $B_{\rm rec}$ vertex fit. In particular, its three-momentum, its decay vertex, the beam spot position and the $\Upsilon(4S)$ average boost can be used as input to a geometrical fit to the tagging candidate daughters into a common vertex. This is illustrated in Figure 2.3 giving a representation of the tagging process.

7.1.2.2 Δt determination

To determine Δt from the Δz measurement, the *BABAR* reconstruction code uses the boost $\beta\gamma$ of the $\Upsilon(4S)$ resonance in the laboratory frame

$$\Delta t = \frac{\Delta z}{\beta\gamma c} \ , \tag{7.5}$$

the average separation between the two vertices due to the boosted $\Upsilon(4S)$ rest frame being given by

$$\beta\gamma c\tau_{B^0} = 257\,\mu\text{m} \ , \tag{7.6}$$

where $\beta\gamma$ is known to high precision from the beam energies, which are monitored every 5 s with an accuracy of 0.1%, and corresponds to $\beta\gamma = 0.56$.

The previous expression given for Δt is only accurate in the case of negligible B momenta in the $\Upsilon(4S)$ rest frame. Since the B mesons do have a small momentum in the $\Upsilon(4S)$ rest frame, $p^*_B = 340\,\text{MeV}/c$,Eq. 7.5 needs to be corrected accordingly. In the case of fully reconstructed $B_{\rm rec}$ mesons, their momentum can be measured and Δz can then be written as

$$\Delta z = \beta\gamma\gamma^*_{rec}c\,(t_{rec} - t_{tag}) + \gamma\beta^*_{rec}\gamma^*_{rec}\cos\theta^*_{rec}c\,(t_{rec} + t_{tag}) \ , \tag{7.7}$$

where $t_{rec}(t_{tag})$ is the instant when the $B_{\rm rec}$ ($B_{\rm tag}$) meson decayed, and $\gamma^*_{rec} = 1.002$, $\beta^*_{rec} = 0.064$ and θ^*_{rec} are, respectively, the boost factor of the reconstructed B meson in the center-of-mass frame, its speed, and its angle with respect to the z axis. However, the correction depends on the quantity $t_{rec}+t_{tag}$, which is not directly measured. Instead its average value, $\langle t_{rec} + t_{tag}\rangle = \tau_B + |\Delta t|$, is used to correct for the measured $B_{\rm rec}$ momentum direction and extract Δt from the following expression:

$$\Delta z = \beta\gamma\gamma^*_{rec}c\,(t_{rec} - t_{tag}) + \gamma\beta^*_{rec}\gamma^*_{rec}\cos\theta^*_{rec}c\,(\tau_B + |\Delta t|) \ . \tag{7.8}$$

The use of Eq. 7.8 improves the Δt resolution by about 5%, and the value of Δt is only corrected by about 0.02 ps relative to the expression used in Eq. 7.5. It also removes a correlation between the true value of Δt and its resolution.

7.1.2.3 Δt resolution model

The imperfect measurement of Δt is taken into account through a function describing the resolution on the Δt measurement, which is convoluted with the Δt PDFs as described below.

The resolution function has different parametrization depending on the event category (signal, various backgrounds). For the signal the resolution in Δt is modeled as the sum

of three gaussians, consisting of a "core" and a "tail" each of whose mean (width) is given by the event-by-event uncertainty on Δt, $\sigma_{\Delta t}$, scaled by an independent bias (scale factor) parameter. The third "outlier" Gaussian is broad and is not scaled by the event-by-event uncertainty: the $b^c_{\rm out}$ and $s^c_{\rm out}$ parameters correspond to the mean and width of the outlier Gaussian. The parameters of the resolution function can, in general, vary with the tagging category "c" as:

$$\begin{aligned}\mathcal{R}^c_{sig}(\Delta t, \sigma_{\Delta t}) &= (1 - f_{\rm tail} - f_{\rm out})\, G\left(\Delta t; b^c_{\rm core}\sigma_{\Delta t}, s^c_{\rm core}\sigma_{\Delta t}\right) \\ &\quad + f_{\rm tail}\, G\left(\Delta t; b^c_{\rm tail}\sigma_{\Delta t}, s^c_{\rm tail}\sigma_{\Delta t}\right) \\ &\quad + f_{\rm out}\, G\left(\Delta t; b^c_{\rm out}, s^c_{\rm out}\right),\end{aligned} \tag{7.9}$$

where the G functions are normalized Gaussians:

$$G(\Delta t, \mu, \sigma) = \frac{1}{\sigma\sqrt{2\pi}} \exp\left(-\frac{(\Delta t - \mu)^2}{2\sigma^2}\right). \tag{7.10}$$

The introduction of the means and widths dependence on the error $\sigma_{\Delta t}$, is due to the presence of correlations between event-by-event uncertainty and the means and RMS of the Δt residual distributions. These effects are caused by the decay products of charmed resonances. In the case where the charmed meson flies along the z direction, rather than in the xy plane, it leads to even larger effects. Indeed, the determination of the z component of the $B_{\rm tag}$ vertex is impacted by particles coming from a secondary displaced vertex. Therefore, a bias in Δz is produced, due to the correlation between larger values of $\sigma_{\Delta z}$ that appears. A smaller correlation was observed in events tagged by a lepton, which explains why the b and s parameters are defined as tagging-category-dependent quantities in Eq. 7.9. Figure 7.2 illustrates the effects that a typical resolution model has on the Δt distribution.

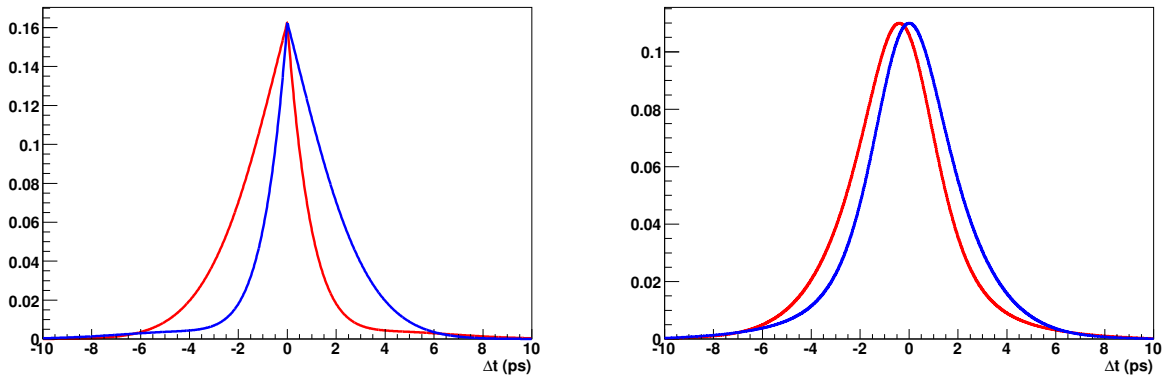

Figure 7.2: Δt distributions for B^0 (red) and $\overline{B}^0$ (blue) tagged events with perfect tagging and resolution (left), and with typical *BABAR* mistag rates and resolution effects incorporated (right). A simple single gaussian model has been used in the demonstration of the resolution effects.

The parameters used in the present analysis, given in Table 7.2, are taken from comprehensive studies for the charmonium sin2β. Indeed, since the dominant factor in the Δt error

comes from the $B_{\rm tag}$ vertex resolution, and hence is generally independent of the channel into which the $B_{\rm rec}$ decays, the resolution in Δt can be assumed to be the same for most channels.

The implementation of the convolution between the expected PDFs and the resolution to obtain the *observed* Δt distributions are described elsewhere [96].

Table 7.2: Parameters describing the resolution in Δt for signal events, as extracted from a large sample of fully reconstructed flavor-specific decays for the charmonium sin2β analyses [119], and used in the present analysis.

Parameters	Core Gaussian		Tail Gaussian	Outlier Gaussian
	lepton-tagged	non-lepton-tagged		
mean	-0.0789 ± 0.0304	-0.1850 ± 0.0138	-1.1186 ± 0.1354	0
sigma	1.0610 ± 0.0459	1.1059 ± 0.0223	3	8
fraction	$1 - f_{\rm tail} - f_{\rm outlier}$	$1 - f_{\rm tail} - f_{\rm outlier}$	0.1050 ± 0.0094	0.0034 ± 0.0006

7.1.3 Signal Δt PDF

The signal Δt PDF accounting for $B^0\overline{B}^0$ mixing and decay effects is defined as:

$$\mathcal{P}_{\rm sig}(\Delta t, \sigma_{\Delta t}) = \frac{e^{-|\Delta t|/\tau_{B^0}}}{4\tau_{B^0}} \times \left[1 + q_{\rm tag}\frac{\Delta D^c}{2} - q_{\rm tag}\left\langle D\right\rangle^c \mathcal{C}\cos\left(\Delta m_d \Delta t\right)\right. \quad (7.11)$$

$$\left. + q_{\rm tag}\left\langle D\right\rangle^c \mathcal{S}\sin\left(\Delta m_d \Delta t\right)\right] \otimes \mathcal{R}^c_{sig}(\Delta t, \sigma_{\Delta t}),$$

where $q_{\rm tag}$ is the flavor-tag of the event: $q_{\rm tag} = -1$ for B^0 mesons (i.e. $B_{\rm rec} = B^0$ and $B_{\rm tag} = \overline{B}^0$) and $q_{\rm tag} = +1$ for $\overline{B}^0$ mesons (i.e. $B_{\rm rec} = \overline{B}^0$ and $B_{\rm tag} = B^0$), τ_{B^0} is the B^0 lifetime and Δm_d is the $B^0\overline{B}^0$ oscillation frequency. The coefficients $\mathcal{S}$ and $\mathcal{C}$ are the parameters associated with mixing-induced *CP* violation and direct *CP* violation, respectively.

7.1.4 Background Δt PDFs

The Δt resolution function for each B-background category j described below is in general the same as for signal, except in a few selected modes, in which a few parameters are changed.

7.1.4.1 Charged B-background Δt PDF

For backgrounds from charged B mesons decays, Δt is modeled as an exponential decay with an effective lifetime, with a value very close to τ_{B^+}, convoluted with the usual resolution

function:

$$\mathcal{P}_{B^\pm}(\Delta t, \sigma_{\Delta t}) = \frac{e^{-|\Delta t'|/\tau_j}}{4\tau_j} \times \left[\left(\frac{1 - q_{\rm tag} A_j}{2} \right) \omega^c + \left(\frac{1 + q_{\rm tag} A_j}{2} \right) (1 - \omega^c) \right] \otimes \mathcal{R}^c_{B^\pm}(\Delta t' - \Delta t, \sigma_{\Delta t}), \tag{7.12}$$

where the index j refers to the background category. The A_j parameter is the asymmetry taking into account for possible differences between B^0 and $\overline{B}^0$ tags, and the τ_j parameter is the effective lifetime. In cases where secondary vertices occur, the effective lifetime and/or resolution can be significantly altered.

7.1.4.2 Flavor eigenstates neutral B-background Δt PDF

For backgrounds from neutral B mesons decays to flavor eigenstates, a similar treatment to that of charged B backgrounds is used, differing only in the mixing term that now appears in the Δt PDF:

$$\mathcal{P}_{B^0_{\rm Flv}}(\Delta t, \sigma_{\Delta t}) = \frac{e^{-|\Delta t'|/\tau_j}}{4\tau_j} \times \left[\left(\frac{1 - q_{\rm tag} A_j}{2} \right) \omega^c \left(1 - \cos(\Delta m_d \Delta t')\right) + \left(\frac{1 + q_{\rm tag} A_j}{2} \right) (1 - \omega^c) \left(1 + \cos(\Delta m_d \Delta t')\right) \right] \otimes \mathcal{R}^c_{B^0_{\rm Flv}}(\Delta t' - \Delta t, \sigma_{\Delta t}). \tag{7.13}$$

7.1.4.3 CP eigenstates neutral B-background Δt PDF

For backgrounds from neutral B mesons decays to CP eigenstates, we account for possible CP violation effects using a similar Δt PDF as for signal:

$$\mathcal{P}_{B^0_{CP}}(\Delta t', \sigma_{\Delta t}) = \frac{e^{-|\Delta t'|/\tau_j}}{4\tau_j} \times \left[1 + q_{\rm tag} \frac{\Delta D^c}{2} - q_{\rm tag} \langle D \rangle^c \mathcal{C} \cos\left(\Delta m_d \Delta t'\right) + q_{\rm tag} \langle D \rangle^c \mathcal{S} \sin\left(\Delta m_d \Delta t'\right) \right] \otimes \mathcal{R}^c_{B^0_{CP}}(\Delta t' - \Delta t, \sigma_{\Delta t}), \tag{7.14}$$

where τ_j are effective lifetimes.

7.1.4.4 Continuum background Δt PDF

We describe the Δt PDF for the continuum background as a combination of "prompt" decays and "lifetime" decays coming from charmed mesons:

$$\mathcal{P}_{\rm bg}(\Delta t, \sigma_{\Delta t}) = \left[f_{\rm prompt}\delta(\Delta t' - \Delta t) + (1 - f_{\rm prompt}) \exp\left(-\frac{|\Delta t|}{\tau_{\rm bg}}\right)\right] \otimes \mathcal{R}_{\rm bg}, \tag{7.15}$$

where $\mathcal{R}_{\rm bg}$ is the resolution function defined as a sum of a "core" and an "outlier" Gaussian:

$$\mathcal{R}_{\rm bg} = (1 - f_{\rm out})\, G\left(\Delta t; b_{\rm core}\sigma_{\Delta t}, s_{\rm core}\sigma_{\Delta t}\right) + f_{\rm out}\, G\left(\Delta t; b_{\rm out}, s_{\rm out}\right). \tag{7.16}$$

The outlier Gaussian has the bias fixed to $b_{\rm out} = 0$, while the core Gausian's width and bias are scaled with the event-by-event uncertainty on Δt. All the continuum background Δt PDF parameters (except for $b_{\rm out}$) were extracted from a fit to the *Off-Peak* data sample (see Sec. 7.6.4.2). The "lifetime" parameter $\tau_{\rm bg}$ in Eq. 7.15 corresponds to an effective lifetime.

7.2 Signal Monte Carlo cocktail

As detailed in Sec. 6.1, the branching fractions of the various resonances that may contribute to the signal are not well measured. Using isospin symmetry, we assume that the fraction and phase of each kaonic resonance channel in the B^0 decay is the same as that in the B^+ decay. Therefore, using the relative weights of each kaonic resonance channel extracted from a fit to the $m_{K\pi\pi}$ spectrum (Tab. 6.20) and the branching fractions of the corresponding kaonic resonance in the $K^+\pi^-\pi^+$ final state from Ref. [24] we estimate the branching fractions of $B \to K_{\rm res}\gamma$ using as a reference the value of $\mathcal{B}(B \to K_1(1270)) = 4.3 \times 10^{-5}$, taken from Ref. [23]. This allows to estimate the branching fractions of the $B^0 \to K^0_{\rm res}(K^0_S\pi^+\pi^-)\gamma$ processes, using the corresponding values of $\mathcal{B}(K_{\rm res} \to K^0_S\pi^+\pi^-)$ reported in Ref. [24].

Table 7.3: Estimated branching fractions of decays of B^0 mesons to $K^0_S\pi^-\pi^+\gamma$ (using different intermediate kaonic resonances) and their relatives weights. Since we reconstruct the K^0_S in two charged pions, here the estimated branching fractions take into account the value of $\mathcal{B}(K^0_S \to \pi^+\pi^-)$.

Signal mode	Estimated $\mathcal{B}$ (10^{-6})	Relative Weights
$B^0 \to K_1(1270)^0(K^0_S\pi^+\pi^-)\gamma$	6.47	0.305
$B^0 \to K_1(1400)^0(K^0_S\pi^+\pi^-)\gamma$	2.64	0.097
$B^0 \to K^*(1410)^0(K^0_S\pi^+\pi^-)\gamma$	5.98	0.219
$B^0 \to K^*_2(1430)^0(K^0_S\pi^+\pi^-)\gamma$	0.32	0.036
$B^0 \to K^*(1680)^0(K^0_S\pi^+\pi^-)\gamma$	5.29	0.344
$B^0 \to K^0_S\pi^+\pi^-\gamma$	20.70	$\emptyset$

Table 7.3 summarizes the weights that are used to create the signal cocktail. Finally, we apply a global scale to the entire cocktail to make it equivalent to the integrated luminosity of our On-Resonance data sample.

7.3 Event selection

At first order, the candidate selection for the present analysis relies on the selection criteria from the charged channel analysis, described in Sec. 6.2.2. Additional selection criteria are applied, as described in Sec. 7.3.1 below. We determine optimal cut values following the procedure described in Sec. 7.3.2.

In signal events containing more than one candidate after event selection, we use the same technique for multiple candidate selection as in the charged channel analysis, described in Sec. 6.2.4.

7.3.1 Selection cuts

This Section gives the selection cuts applied to MC and data samples. Only the new selection criteria, with respect to the charged channel analysis, are detailed here: Secs. 7.3.1.1 and 7.3.1.2 present the K^0_S selection and the cuts applied to the time variables Δt and $\sigma_{\Delta t}$, respectively. The values of the other selection cuts are reported in Tab. 7.5.

We found that the set of variables used to build the Fisher discriminant in the charged mode (Sec. 6.2.2.8) is still optimal. Therefore, we only updated the coefficients in the linear combination to optimize the separation between signal and continuum background events.

7.3.1.1 K^0_S selection

As described in Sec. 5.2.4, we select K^0_S candidates from the `KsDefault` list. The geometric fit performed by `TreeFitter` that determines the K^0_S decay vertex, allows to evaluate the K^0_S candidate four momentum and trajectory. Its mass is also computed using $\pi^\pm$ track momenta evaluated at the vertex. In order to determine the trajectory, the K^0_S production vertex (i.e. the B decay vertex) is also required.

The displaced decay of the K^0_S is useful for rejecting background, especially $q\overline{q}$ events. Thus, we compute the decay length significance, $d_{K^0_S}/\sigma(d_{K^0_S})$, defined as the ratio of the three-dimensional length of the K^0_S trajectory divided by the error on that quantity obtained from the vertex fit. We also compute θ_{flight} corresponding to the angle between the K^0_S trajectory and its momentum vector. The following cuts are applied on K^0_S candidates:

- $|m_{\pi^+\pi^-} - m_{K^0_S}| < 11\,\text{MeV}/c^2$
- $cos\theta_{\text{flight}} > 0.995$
- $d_{K^0_S} > 5\sigma(d_{K^0_S})$

These selection criteria corresponds to standard requirements in *BABAR* analyses. Their values are taken from Ref. [120], and not re-optimized for the present analysis.

7.3.1.2 Δt and $\sigma_{\Delta t}$

Very loose cuts are also applied to the variables Δt and $\sigma_{\Delta t}$. These cuts are the same as those applied in the *BABAR* charmonium sin2β analyses [119], from which we take the parameters of the signal Δt resolution function (see Tab. 7.2). We apply the following cuts:

- $|\Delta t| \leq 20\,\text{ps}$
- $\sigma_{\Delta t} \leq 2.5\,\text{ps}$

7.3.1.3 $m_{\pi\pi}$ and $m_{K\pi}$

As described in Sec. 6.8.2, in order to increase the dilution factor value (i.e. increase the proportion of $B^0 \to K^0_S\rho^0\gamma$ events), we apply cuts on the $m_{\pi\pi}$ and $m_{K\pi}$ dimensions:

- $0.6\,\text{GeV}/c^2 \leq m_{\pi\pi} \leq 0.9\,\text{GeV}/c^2$,
- $m_{K\pi} \leq 0.845\,\text{GeV}/c^2$ or $0.945\,\text{GeV}/c^2 \leq m_{K\pi}$,

where in the latter case the cut is applied in both $K^+\pi^-$ and $K^-\pi^+$ dimensions. These sets of cut are optimized to minimize the final error on the indirect *CP* asymmetry parameter.

7.3.2 Cut Optimization

The cuts were optimized in order to maximize the sensitivity on the *CP* asymmetry parameters $\mathcal{S}$ and $\mathcal{C}$. We first use the `BumpHunter` algorithm in order to maximize the FOM $S/\sqrt{S+B}$, where S is the yield of TM-signal MC and B is the total yield of backgrounds. Both S and B are normalized to the luminosity in the data, as in the control channel analysis. This first step of the optimization procedure was done inside the signal region (*i.e.* for $m_{\text{ES}} > 5.26\,\text{GeV}/c^2$), using a set of 6 variables:

- PhotonMergedPi0Consistency
- Pi0VetoLikelihoodRatio
- EtaVetoLikelihoodRatio
- Daug2TrackPID_PiSelectorKM
- Daug3TrackPID_PiSelectorKM
- BvtxProbChi2

`BumpHunter` was able to find an optimum for these variables. The correlations between them were found to be non significant.

In a second step, using the full fit region in m_{ES} ($m_{\text{ES}} > 5.20\,\text{GeV}/c^2$), we built 25 sets of cuts with different ranges in ΔE and the Fisher discriminant given in Tab. 7.4. Each set is assigned a unique "selection-cut code" that is given in the table.

For each set we generated and fitted a pseudo experiment composed of embedded signal events (drawn from MC sample) as well as two B-background categories (from the B^+B^- and $B^0\overline{B}^0$ generic MC, respectively) and a continuum category (generated from the PDFs). Since the aim is to select a set of cut which minimize the errors on $\mathcal{S}$ and $\mathcal{C}$, we use the total available MC statistics in order to minimize the uncertainty on the fitted errors. Since the generic MC samples correspond to about 3 times the luminosity in the data, we generate the pseudo experiment using the estimated yields of each event category scaled by a factor three. Figure 7.3 shows the fitted errors on the *CP*-asymmetry parameters: $\mathcal{S}$ and $\mathcal{C}$. The selected set of cuts corresponds to a value of the Fisher discriminant ≥ 0.0 and $\Delta E \in [-0.200; 0.200]\,\mathrm{GeV}/c^2$ (i.e. cut code = 79). This choice appears to be a good compromise between *CP*-asymmetry parameters sensitivity and continuum background suppression with the tighter cut on the Fisher Discriminant.

With this set of cuts on the Fisher Discriminant and ΔE, the optimization of the figure of merit $S/\sqrt{S+B}$ was done again. The changes in the optimized cuts appeared to be non significant. The value of the FOM is $S/\sqrt{S+B} \simeq 6.7$ in the signal region (i.e. $m_{\mathrm{ES}} \geq 5.26\,\mathrm{GeV}/c^2$) and $S/\sqrt{S+B} \simeq 3.6$ in the fit region (i.e. $m_{\mathrm{ES}} \geq 5.20\,\mathrm{GeV}/c^2$) .

7.3.3 Efficiency

Table 7.5 details, for each of the final cuts, the selection efficiency of TM candidates in signal MC. The reconstruction efficiency is also indicated. Tab. 7.6 gives the total efficiency once multiple-candidate selection is applied (same procedure as described in Sec. 6.2.4). Tab. 7.7 shows the overall efficiencies for the different kaonic resonances. The observed differences in the efficiencies among these, are mainly due to the cut on the $m_{\pi\pi}$ and $m_{K\pi}$ dimensions, since each kaonic resonance have different branching fractions in $\rho^0 K^0_S$ and $K^{*\pm}\pi^{\mp}$ channels.

Table 7.4: The sets of cuts on the Fisher Discriminant and ΔE used for the optimization on the *CP*-asymmetry parameters sensitivity. The selection-cut codes are defined as $\alpha \times 10 + \beta$, where the values of α and β correspond to given ranges of the Fisher Discriminant (labelled $\mathcal{F}$ in this table) and ΔE, respectively.

Cut code	$\mathcal{F} \geq 0.3$ $\alpha = 1$	$\mathcal{F} \geq 0.2$ $\alpha = 3$	$\mathcal{F} \geq 0.1$ $\alpha = 5$	$\mathcal{F} \geq 0.0$ $\alpha = 7$	$\mathcal{F} \geq -0.1$ $\alpha = 9$
$\Delta E \in [-0.100; 0.100]$ $\beta = 1$	11	31	51	71	91
$\Delta E \in [-0.125; 0.125]$ $\beta = 3$	13	33	53	73	93
$\Delta E \in [-0.150; 0.150]$ $\beta = 5$	15	35	55	75	95
$\Delta E \in [-0.175; 0.175]$ $\beta = 7$	17	37	57	77	97
$\Delta E \in [-0.200; 0.200]$ $\beta = 9$	19	39	59	79	99

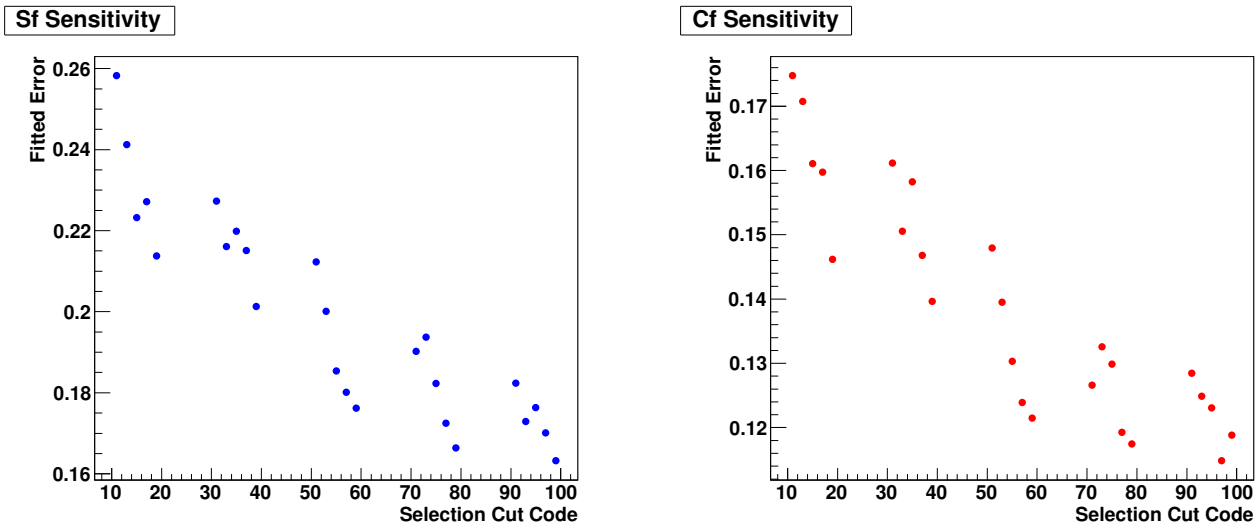

(a) (b)

Figure 7.3: Fitted error on the *CP* asymmetry parameter $\mathcal{S}$ (a) and $\mathcal{C}$ (b). The selection cut codes on the x-axis are related to the corresponding cuts in Tab. 7.4. Note that the origin of the y-axis have been set to entry with the lower value in both graphs.

Note that the overall efficiency is smaller than that of the charged channel analysis. This is mainly due to the cut applied on the $m_{\pi\pi}$ and $m_{K\pi}$ dimensions, to the tighter cut applied on the Fisher discriminant and also to the reconstruction of the K^0_S candidate, which is slightly less efficient than charged tracks.

Table 7.5: Absolute, last- and first-cut efficiencies of candidate selection cuts in TM signal MC. The absolute efficiency is obtained from the product of all the preceding cut efficiencies in the table, including the corresponding one. The reconstruction efficiency is obtained from the ratio between the numbers of generated events and of reconstructed events, before any of the cuts is applied. The last- (first-)cut efficiency is the efficiency of the corresponding cut when applied after (before) all the other cuts. Events that satisfy the condition on the cut value are selected. Mass and time cuts are expressed in GeV/c^2 and ps, respectively.

Cut	Value	Absolute efficiency	Last-cut efficiency	First-cut efficiency
Reconstruction	$\emptyset$	0.497	$\emptyset$	$\emptyset$
$m_{K\pi\pi}$	$x < 1.8$	0.399	0.548	0.768
$\mathcal{LR}_{\pi^0}$	$x < 0.838$	0.369	0.893	0.925
$\mathcal{LR}_{\eta}$	$x < 0.975$	0.361	0.969	0.977
B vertex probability	$0.00351 < x$	0.327	0.758	0.905
ΔE	$-0.2 \leq x \leq 0.2$	0.304	0.891	0.929
m_{ES}	$5.2 < x$	0.301	0.887	0.992
Fisher	$x > 0.0$	0.239	0.743	0.794
$\mathrm{B}_{\Delta t}$	$-20 \leq x \leq 20$	0.238	0.954	0.998
$\mathrm{B}_{\sigma_{\Delta t}}$	$x < 2.5$	0.232	0.929	0.974
B vertex status	$x = 0$	0.232	0.921	0.999
B tag vertex status	$x = 0$	0.232	0.965	0.999
$\cos\theta_\gamma$	$-0.74 \leq x \leq 0.93$	0.231	0.999	0.999
Photon bump distance	$25 < x$	0.223	0.917	0.964
Photon track distance	$25 < x$	0.207	0.892	0.925
Photon merged π^0 consistency	$x < 0.00087$	0.204	0.980	0.985
$\lvert m_{\pi^+\pi^-} - m_{K^0_S}\rvert$	$x < 0.011$	0.200	0.707	0.984
$\cos\theta_{\mathrm{flight}}$	$0.995 < x$	0.195	0.445	0.975
$d_{K^0_S}/\sigma(d_{K^0_S})$	$5 < x$	0.188	0.545	0.962
π_1 PID	`SuperLooseKMPion`	0.180	0.843	0.959
π_2 PID	`SuperLooseKMPion`	0.173	0.839	0.956
$m_{\pi^+\pi^-}$ ($\rho^0(770)$ selection)	$0.6 \leq x \leq 0.9$	0.107	0.651	0.675
$m_{K\pi}$ ($K^*(892)$ veto)	$[x \leq 0.845] \cup [0.945 \leq x]$	0.052	0.537	0.893

Table 7.6: Individual and absolute efficiency (product of all the preceding cut efficiencies in the table, including the corresponding one) of candidate selection cuts in TM signal MC.

Cut	Relative efficiency	Cumulative efficiency
Reconstruction	0.497	0.497
Candidate selection	0.105	0.052
MCS	0.903	0.047

Table 7.7: Overall efficiency of $m_{K\pi\pi}$ TM candidates in signal MC by kaonic resonance. The observed differences in the resonance efficiencies, are mainly due to the cut on the $m_{\pi\pi}$ and $m_{K\pi}$ dimensions. Uncertainties come from MC statistics.

Resonance	$K_1(1270)$	$K_1(1400)$	$K^*(1410)$	$K_2^*(1430)$	$K^*(1680)$
Overal efficiency	0.0563 ± 0.0004	0.0287 ± 0.0009	0.0264 ± 0.0010	0.0409 ± 0.0011	0.0420 ± 0.0002

7.4 Classification of signal events

Signal events are separated in two categories: TM and self-cross-feed (SCF) by the same criteria as in the charged channel analysis (see Sec. 6.3.1). The corresponding PDFs are presented in Sec. 7.6.1.

The total signal yield, is estimated by multiplying the total number of B mesons expected in the final *BABAR* dataset by the estimated branching fractions of each mode given in Tab. 7.3, and then by summing up the resulting products. The TM and SCF yields are estimated using the fraction of each category in the MC.

Since the SCF contributes to the time-dependent *CP* violation, the SCF is not considered as a background in the present analysis, contrarily to the charged-mode analysis.

Table 7.8: $B^0 \to K_S^0\pi^+\pi^-\gamma$ signal estimated yields for the final *BABAR* Run1-6 dataset.

Category	Estimated yield	Fraction
Signal TM	153 ± 26	0.728 ± 0.002
Signal SCF	57 ± 10	0.272 ± 0.003
Total Signal	210 ± 36	$\emptyset$

7.5 Background study

This section describes the study of the B backgrounds (discussed in Sec. 7.5.1) as well as the continuum background (discussed in Sec. 7.5.2). The same background identification procedure as in the charged channel analysis (Sec. 6.4) is applied here. Again the main background comes from continuum events, and the dominant source of B background arises from radiative $b \to s\gamma$ transitions. For the time-dependent analysis we further classify the different identified B backgrounds into three categories: charged, *CP* eigenstates and flavor eigenstates. As shown in Sec. 7.1, different time-dependent PDF are applied to each of these categories. Table 7.10 gives the yields of the different background categories defined in the $B^0 \to K_S^0\pi^+\pi^-\gamma$ analysis. The resulting PDFs are presented in Sec. 7.6.2.

7.5.1 B backgrounds

7.5.1.1 Radiative $b \to s\gamma$ B backgrounds

From the generic MC, we isolate six dominant radiative B backgrounds, listed in Tab. 7.9. As in the case of the charged channel, the size of the generic MC sample does not allow to perform an accurate study of these radiative B backgrounds. Therefore, we use exclusive MC datasets, as described in Sec. 5.1.1.

We first separate these six dominant radiative B backgrounds in the same two groups than in the charged channel analysis: the "low multiplicity" decays (i.e. the $B \to K\pi\gamma$ decays), as detailed in Tab. 7.9, and the "Higher multiplicity" decays where one particle or more has been missed in the reconstruction.

We further classify these backgrounds according to their time-dependent properties. We divide the neutral $B \to K\pi\gamma$ radiative B backgrounds in two categories, depending on the K^{*0} or the X_{sd} final states: $K^{*0}(X_{sd}) \to K^0_S\pi^0$ and $K^{*0}(X_{sd}) \to K^\pm\pi^\mp$ correspond to the neutral CP and neutral flavor eigenstates, respectively. Charged $B^+ \to K\pi\gamma$ decays form another B-background category. For the second group of radiative B backgrounds, the "Higher multiplicity decays" of Tab. 7.9, we separate the charged and the neutral contributions. Many of the X_{su} or X_{sd} decays contribute to these backgrounds. Therefore in the case of the neutral category, we account for a possible CP asymmetry coming from specific decay modes using the neutral CP eigenstate time-dependent model. The contributions to $\mathcal{S}$ are diluted by non CP eigenstates, which are also included in this category. As for the charged channel (see Sec. 6.4.1.2), corrective weights, obtained in Ref. [107], are applied separately to each X_s decay mode.

Table 7.9: Radiative backgrounds contributing to $B^0 \to K^0_S\rho^0\gamma$, observed in the generic MC.

Specificity	Decay mode
$B \to K\pi\gamma$	$B^0 \to K^{*0}(\to K^0_S\pi^0)\gamma$
	$B^0 \to X_{sd}(\to K^0_S\pi^0)\gamma$
	$B^0 \to K^{*0}(\to K^\pm\pi^\mp)\gamma$
	$B^0 \to X_{sd}(\to K^\pm\pi^\mp)\gamma$
	$B^+ \to K^{*+}(\to K^0_S\pi^+)\gamma$
	$B^+ \to X_{su}(\to K^0_S\pi^+)\gamma$
Higher multiplicity decays	$B^0 \to X_{sd}(\nrightarrow K\pi)\gamma$
	$B^+ \to X_{su}(\nrightarrow K\pi)\gamma$

7.5.1.2 Other B backgrounds

All the other B-background contributions, which do not exceed one expected event in the data, are grouped in two categories labelled "B^+B^- generic B background" and "$B^0\overline{B}^0$

generic B background". As for the neutral $B^0 \to X_{sd}(\nrightarrow K\pi)\gamma$ category, we use the neutral CP eigenstate time-dependent model to describe the $B^0\overline{B}^0$ generic Δt PDF.

7.5.2 Continuum background

To model the continuum background, we use the complete Off-Peak dataset of 44.81 fb^{-1} collected by *BABAR*. The continuum yield is estimated using the same normalization procedure as in the charged channel (see Sec. 6.4.2).

Table 7.10: Estimated yields for backgrounds to $B^0 \to K^0_S\pi^+\pi^-\gamma$ decays for the final *BABAR* Run1-6 dataset.

Background category	Time-dependent model	Estimated yield
Continuum ($udsc$)	Continuum	2236
$B^+ \to X_{su}(\nrightarrow K\pi)\gamma$	Charged	94
$B^+ \to K^{*+}(\to K^0_S\pi^+)\gamma$ $B^+ \to X_{su}(\to K^0_S\pi^+)\gamma$	Charged	54
$B^0 \to X_{sd}(\nrightarrow K\pi)\gamma$	Neutral CP	51
$B^0\overline{B}^0$ generic B background	Neutral CP	35
B^+B^- generic B background	Charged	34
$B^0 \to K^{*0}(\to K^0_S\pi^0)\gamma$ $B^0 \to X_{sd}(\to K^0_S\pi^0)\gamma$	Neutral CP	30
$B^0 \to K^{*0}(\to K^\pm\pi^\mp)\gamma$ $B^0 \to X_{sd}(\to K^\pm\pi^\mp)\gamma$	Neutral flavor	4
Total Bkg		2538

7.6 Fit to $m_{\rm ES}$, ΔE, the Fisher discriminant and Δt

Here we present the fit performed on $m_{\rm ES}$, ΔE, the Fisher discriminant and Δt in order to extract the CP asymmetry parameters of the signal. Sections 7.6.1 and 7.6.2 detail the PDFs used in the fit model and the correlations between the fit variables for the signal and the backgrounds categories, respectively. Then Sec. 7.6.3 summarizes the fitting functions. Section 7.6.5 presents the validation tests of the fit model. Finally, Sec. 7.6.6.1 gives the projections, the yields and the CP asymmetries extracted by the fit.

7.6.1 Signal PDFs

PDFs for the TM and SCF signal events are constructed using the cocktail of signal MC samples (Tab. 7.3). The TM and SCF PDFs for each discriminating variable entering the fit model are shown in Figs. 7.4 and 7.5, respectively. The total number of events shown in these figures is normalized to the expected yield, given in Tab. 7.8. Formulas of the functional forms used to describe the PDFs presented below are available in Appendix A.

The ΔE distribution of the SCF category, which is expected to be described by a linear function, appears to be better described by a higher order polynomial. This feature was investigated and is not due to TM contamination. Splitting the SCF into sub-categories, depending on which particle (i.e. the K^0_S, one of the π or the γ) is taken from the other side

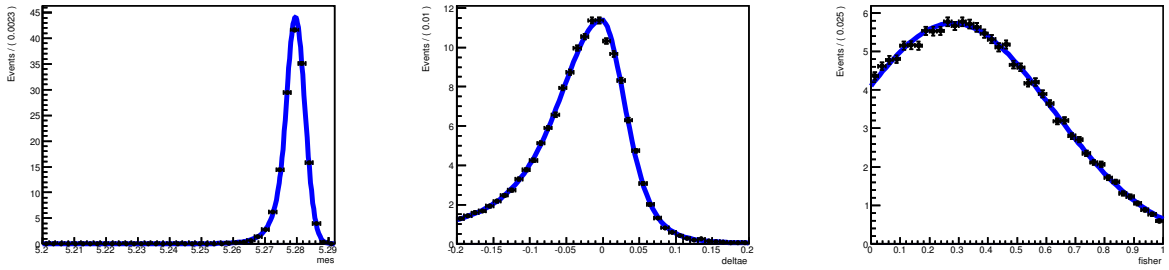

Figure 7.4: Probability density functions for the fit variables $m_{\rm ES}$ (left), ΔE (center) and the Fisher discriminant (right) of signal-TM events. Here the $m_{\rm ES}$ PDF is described by a Crystal Ball function, the ΔE PDF by a Cruijff function and the Fisher discriminant PDF by a Gaussian. The blue curves represent the PDF distributions, and the black points correspond to MC events.

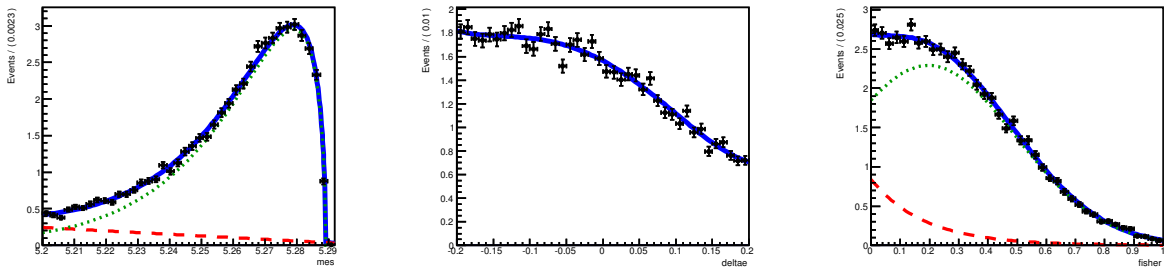

Figure 7.5: Probability density functions for the fit variables $m_{\rm ES}$ (left), ΔE (center) and the Fisher discriminant (right) of signal SCF events. Here the $m_{\rm ES}$ PDF is described by the sum of a first order Chebychev polynomial (red dashed line) and an Argus function (green dotted line), the ΔE PDF by a forth order Chebychev polynomial and the Fisher discriminant PDF by the sum of a Gaussian (green dotted line) and an exponential (red dashed line). The blue curves represent the PDF distributions, and the black points correspond to MC events.

of the event, it clearly appears that each sub-category has a different distribution in ΔE. When either the K^0_S or the γ are taken from the other B, the corresponding ΔE distributions are linear. When it is one of the pions that is taken from the other side, the ΔE shape is better described by a second order polynomial. The combination of these different shapes yields a complex shape described by a non-linear function. In the fit to data, we do not split anymore the SCF into sub-categories, and as shown later (see Sec. 7.6.5), the coefficients of the 4th order chebychev polynomial function used to describe SCF ΔE distribution have to be fixed.

7.6.1.1 Correlations among the fit variables for signal events

We checked for possible correlations among our fit variables. No significant correlations were found between the Fisher discriminant and both $m_{\rm ES}$ and ΔE. As in the charged channel analysis, the correlations between $m_{\rm ES}$ and ΔE are not significant for the signal SCF category. Again, it is in the signal-TM component that the stronger correlations appear.

Following the same procedure (see Sec. 6.5.1) we found that the $m_{\rm ES}$-ΔE correlations for the signal-TM category can be parametrized using a two-dimensional PDF. As previously, it is constructed as the product of a conditional PDF (Crystal Ball for $m_{\rm ES}$) by a marginal PDF (Cruijff for ΔE). The $m_{\rm ES}$ Crystal Ball parameters dependence in ΔE was studied using the same set of ΔE subsets as listed in Tab. 6.13. For each of the ten subsets, we perform an unbinned maximum likelihood fit to extract the Crystal Ball parameters.

The following polynomial functions are used to describe the evolution of the Crystal-Ball parameters between ΔE bins:

- μ and σ: second order polynomial [Fig. 7.6];
- α and n: first and second order polynomial, respectively [Fig. 7.7].

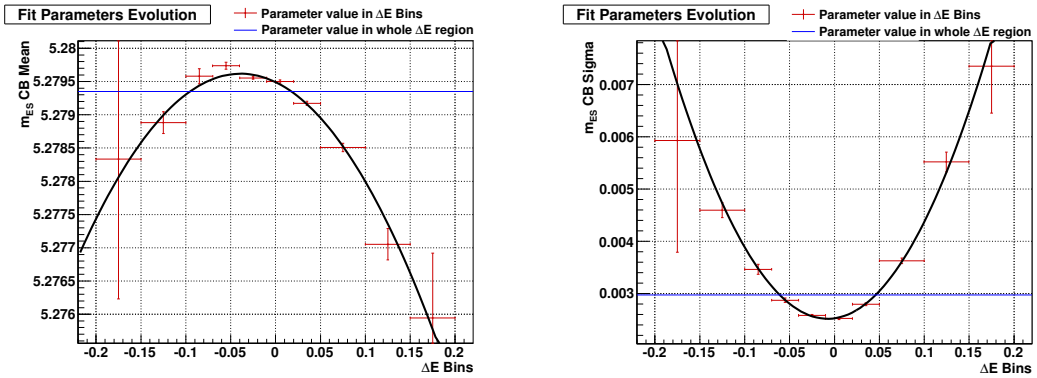

Figure 7.6: Evolution of the parameters μ (left) and σ (right) of the $m_{\rm ES}$ PDF in bins of ΔE. The central value of each point is the fitted value of the corresponding Crystal Ball parameter, the vertical error bars correspond to the parameter fit error and the horizontal error bars to the size of each ΔE bin. The blue horizontal line corresponds to a 1-dimensional Crystal-Ball PDF without $m_{\rm ES}$-ΔE correlations. The black curve correspond to the fitted polynomial function describing the evolution of the corresponding Crystal Ball parameter as a function of ΔE.

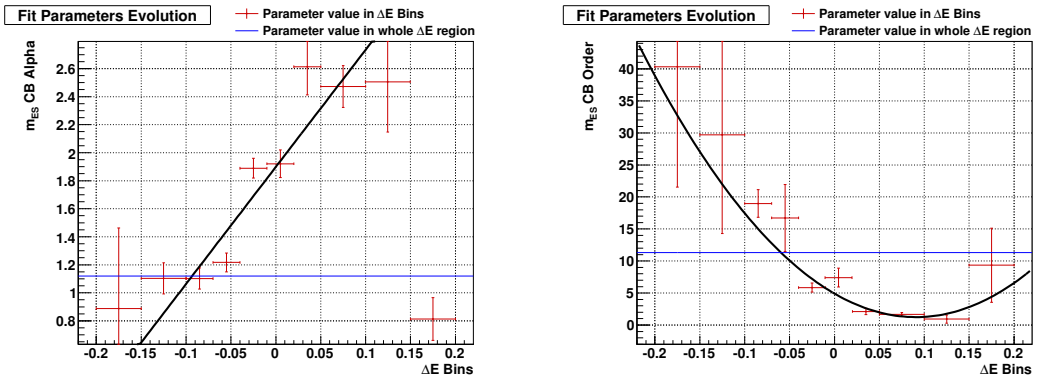

Figure 7.7: Evolution of the parameters α (left) and n (right) of the $m_{\rm ES}$ PDF in bins of ΔE. Conventions are identical as those of Fig. 7.6.

7.6.2 Background PDFs

Here we present the probability density functions of all the background categories previously defined. They are presented in Figs. 7.8 to 7.14 in a decreasing order of expected yields. The total number of events is always normalized to the expected yield for each category. Details on the function used to describe the PDFs presented below are available in Appendix A. Note that when constructing the PDFs for a particular B-background mode, we ensure, using MC truth information, that none of the other identified background modes appear in the other side of the event. This procedure ensures that the PDFs corresponding to a given mode are not contaminated by contributions from the other identified background modes.

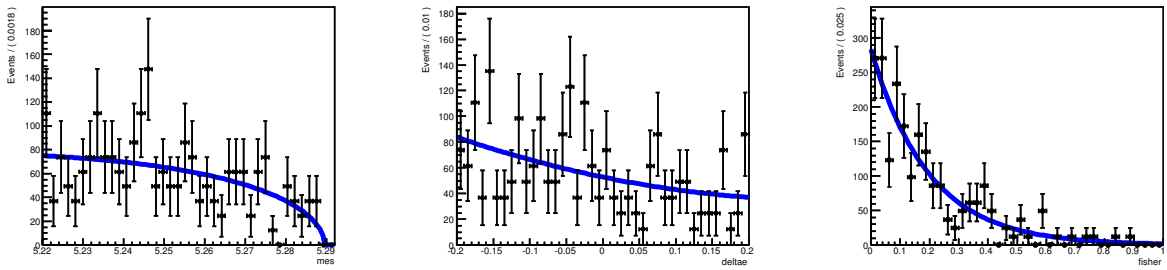

Figure 7.8: Probability density functions for the fit variables $m_{\rm ES}$ (left), ΔE (center) and the Fisher discriminant (right) of continuum ($udsc$) background category. The blue curves represent the PDF distributions, and the black points correspond to MC events. Here the $m_{\rm ES}$ PDF is described by an Argus, the ΔE PDF by a second order Chebychev polynomial and the Fisher discriminant by an exponential.

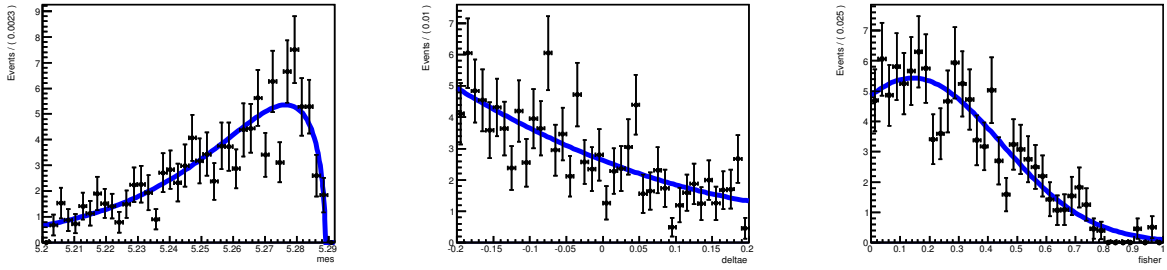

Figure 7.9: PDFs of $B^+ \to X_{su}(\nrightarrow K\pi)\gamma$ B-background category. Conventions are similar to those of Fig. 7.8. Here the $m_{\rm ES}$ PDF is described by an Argus, the ΔE PDF by a second order Chebychev polynomial and the Fisher discriminant by a Gaussian function.

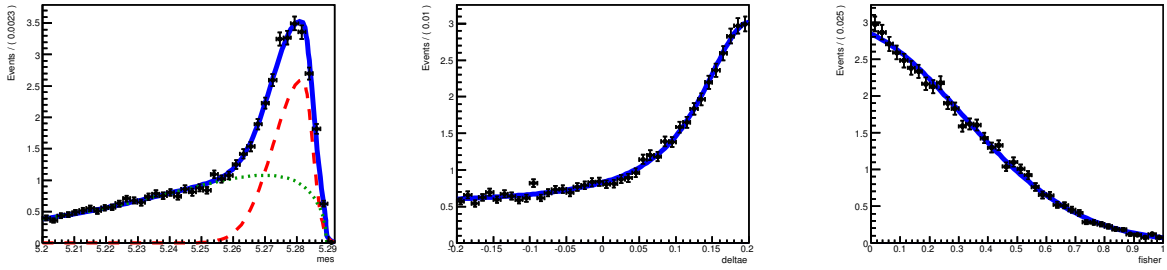

Figure 7.10: PDFs of $B^+ \to K^{*+}(\to K^0_S\pi^+)\gamma$ + $B^+ \to X_{su}(\to K^0_S\pi^+)\gamma$ background category. Conventions are similar to those of Fig. 7.8. Here the $m_{\rm ES}$ PDF is described by the sum of a Cruijff (red dotted line) and an Argus (green dashed line), the ΔE PDF by a second order Chebychev polynomial and the Fisher discriminant PDF by a Gaussian function.

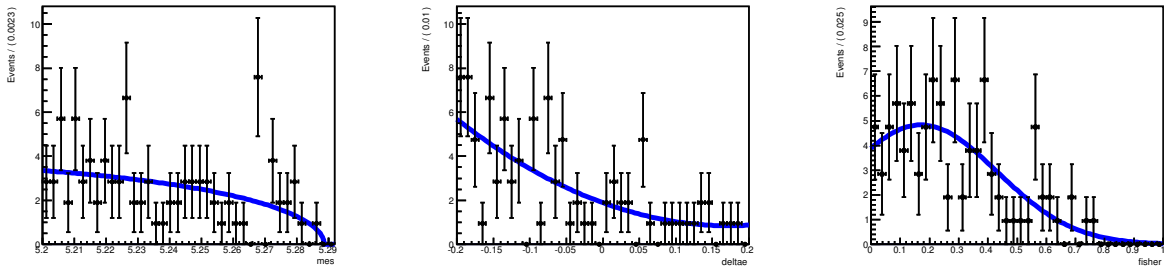

Figure 7.11: PDFs of B^+B^- generic B-background category. Conventions are similar to those of Fig. 7.8. Here the $m_{\rm ES}$ PDF is described by an Argus, the ΔE PDF by a second order Chebychev polynomial function and the Fisher discriminant by a Gaussian function.

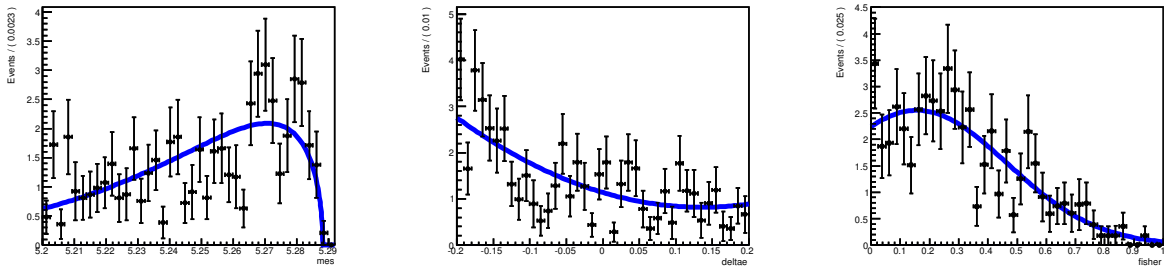

Figure 7.12: PDFs of $B^0 \to X_{sd}(\nrightarrow K\pi)\gamma + B^+ \to X_{su}(\nrightarrow K\pi)\gamma$ background category. Conventions are similar to those of Fig. 7.8. Here the $m_{\rm ES}$ PDF is described by a Crystal Ball function, the ΔE PDF by a Cruijff function and the Fisher discriminant PDF is described by a Gaussian function.

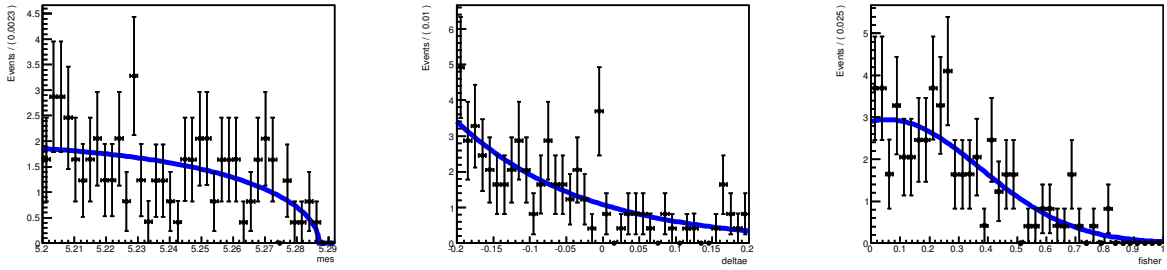

Figure 7.13: PDFs of $B^0\overline{B}^0$ generic background category. Conventions are similar to those of Fig. 7.8. Here the $m_{\rm ES}$ PDF is described by an Argus, the ΔE PDF by a second order Chebychev polynomial function and the Fisher discriminant PDF is described by a Gaussian function.

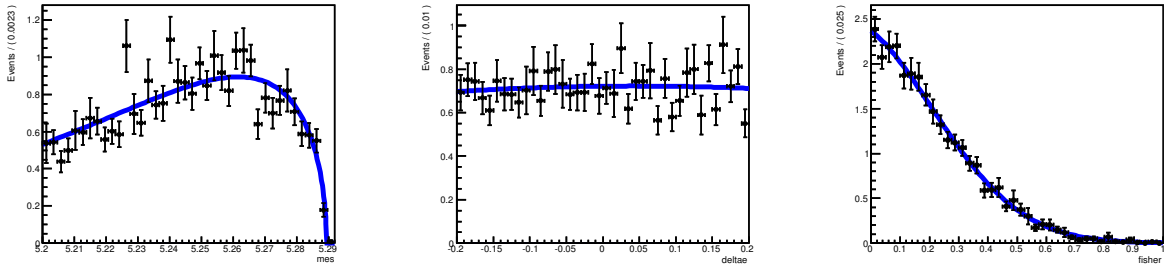

Figure 7.14: PDFs of $B^0 \to K^{*0}(\to K^0_S\pi^0)\gamma + B^0 \to X_{sd}(\to K^0_S\pi^0)\gamma$ background category. Conventions are similar to those of Fig. 7.8. Here the $m_{\rm ES}$ PDF is described by an Argus, the ΔE PDF is described by a second order Chebychev polynomial function and the Fisher discriminant PDF is described by a Gaussian function.

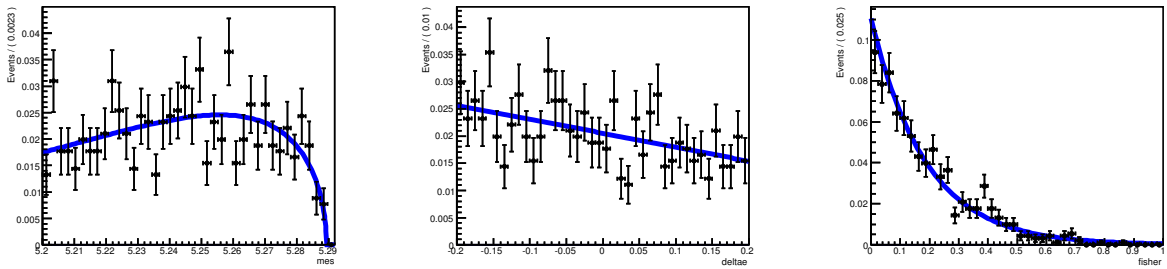

Figure 7.15: PDFs of $B^0 \to K^{*0}(\to K^{\pm}\pi^{\mp})\gamma + B^0 \to X_{sd}(\to K^{\pm}\pi^{\mp})\gamma$ background category. Conventions are similar to those of Fig. 7.8. Here the $m_{\rm ES}$ PDF is described by an Argus, the ΔE PDF is described by a first order Chebychev polynomial function and the Fisher discriminant PDF is described by an exponential.

7.6.2.1 Correlations among the fit variables in background events

We checked for possible correlations between the fit variables, in background events. No significant correlations were found between the Fisher discriminant and both $m_{\rm ES}$ and ΔE. We only observed significant correlations between $m_{\rm ES}$ and ΔE in two B-background categories, namely $B^+ \to K^{*+}(\to K^0_S\pi^+)\gamma$ + $B^+ \to X_{su}(\to K^0_S\pi^+)\gamma$ and $B^+ \to K^{*+}(\to K^0_S\pi^+)\eta(\to \gamma\gamma)$, as shown in Figs. 7.16 and 7.17, respectively. Since the expected yield of the $B^+ \to K^{*+}(\to K^0_S\pi^+)\eta(\to \gamma\gamma)$ background is very small compared to the other ones, we decided to neglect the correlations between $m_{\rm ES}$ and ΔE in this category. In the case of $B^+ \to K^{*+}(\to K^0_S\pi^+)\gamma$ + $B^+ \to X_{su}(\to K^0_S\pi^+)\gamma$, we take the correlations into account using a non parametric two-dimensional PDF for $m_{\rm ES}$-ΔE. The histogram is taken from a cocktail of MC events.

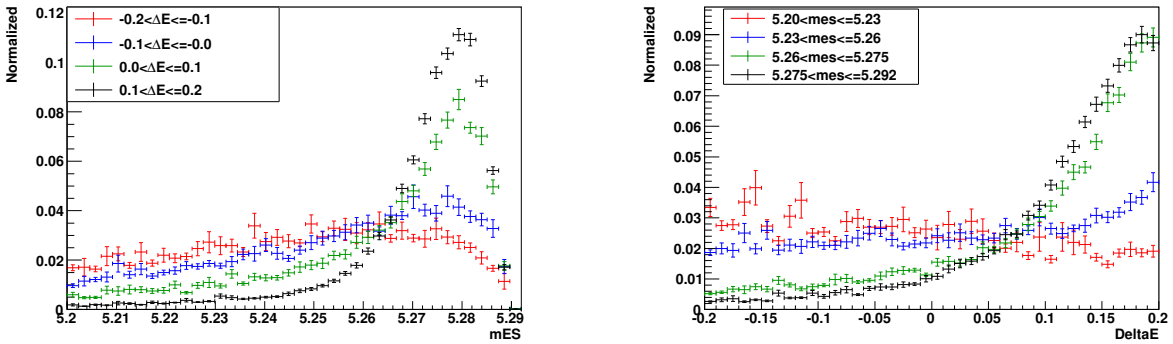

Figure 7.16: $m_{\rm ES}$ (left) and ΔE (right) distributions of $B^+ \to K^{*+}(\to K^0_S\pi^+)\gamma$ + $B^+ \to X_{su}(\to K^0_S\pi^+)\gamma$ events in ΔE and $m_{\rm ES}$ bins, respectively

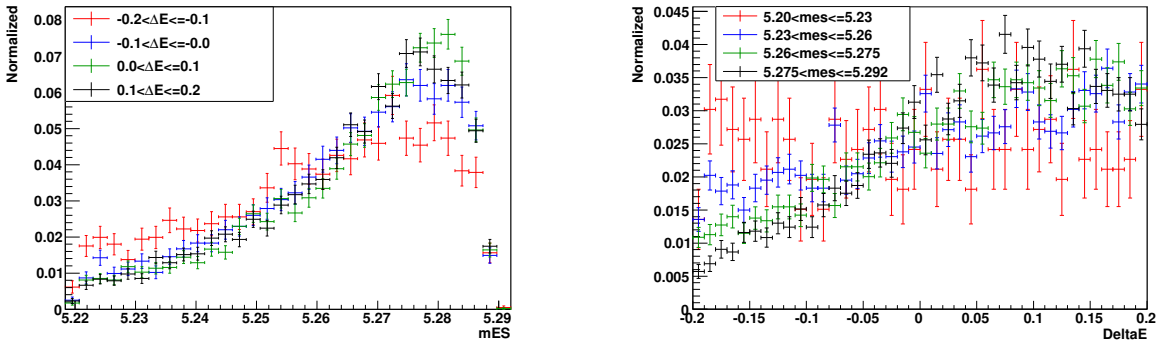

Figure 7.17: $m_{\rm ES}$ (left) and ΔE (right) distributions of $B^+ \to K^{*+}(\to K^0_S\pi^+)\eta(\to \gamma\gamma)$ events in ΔE and $m_{\rm ES}$ bins, respectively

7.6.3 Fitting functions

Table 7.11 summarizes the choice of functions used to parametrize the different fit components. Note that for both signal-TM and $B^0 \to K^{*0}(\to K\pi)\gamma$ + $B^0 \to X_{sd}(\to K\pi)\gamma$ categories, the PDF functions are two-dimensional. This is motivated by the correlations that arise between $m_{\rm ES}$ and ΔE, as shown in Secs. 7.6.1 and 7.6.2, respectively.

Table 7.11: Summary of all the fit components and the functions used to parametrize their PDFs.

Fit component	PDF parametrization		
	$m_{\rm ES}$	ΔE	Fisher
Signal TM	Two-dimensional parametric (Crystal Ball – Cruijff)		Gaussian
Signal SCF	Argus + Chebychev ($1^{\rm st}$ order)	Chebychev ($4^{\rm th}$ order)	Gaussian + Exponential
Continuum $udsc$	Argus	Chebychev ($2^{\rm nd}$ order)	Exponential
$B^+ \to X_{su}(\nrightarrow K\pi)\gamma$	Argus	Chebychev ($2^{\rm nd}$ order)	Gaussian
$B^+ \to K^{*+}(\to K^0_S\pi^+)\gamma$ $B^+ \to X_{su}(\to K^0_S\pi^+)\gamma$	Two-dimensional non parametric		Gaussian
B^+B^- generic	Argus	Chebychev ($2^{\rm nd}$ order)	Gaussian
$B^0 \to X_{sd}(\nrightarrow K\pi)\gamma$	Argus	Chebychev ($2^{\rm nd}$ order)	Gaussian
$B^0\overline{B}^0$ generic	Argus	Exponential	Gaussian
$B^0 \to K^{*0}(\to K^0_S\pi^0)\gamma$ $B^0 \to X_{sd}(\to K^0_S\pi^0)\gamma$	Argus	Chebychev ($2^{\rm nd}$ order)	Gaussian
$B^0 \to K^{*0}(\to K^\pm\pi^\mp)\gamma$ $B^0 \to X_{sd}(\to K^\pm\pi^\mp)\gamma$	Argus	Chebychev ($1^{\rm st}$ order)	Exponential

7.6.4 Parameters of the Δt PDFs

7.6.4.1 Signal

The parameters of the resolution function as well as the dilutions, dilution differences and tagging-category fractions are taken from the *BABAR* charmonium sin2β analyses [119], and are detailed in Tab. 7.2 and Tab 7.1, respectively.

The signal events are separated in two categories (i.e. TM and SCF); the total number of signal events is free to vary in the fit, while we fix the fraction of SCF events. As we split signal according to the tagging categories, we assign a fraction of SCF events for each of those. The SCF fractions, given in Tab. 7.12, are obtained from true MC information in signal MC samples and are fixed in the fit. In each tagging category, we use the same resolution function parameters, dilutions and dilution differences for both TM and SCF events.

The error functions ($\sigma_{\Delta t}$) for both TM and SCF are separated in tagging category and parametrized using a Landau distribution, where the "mean" and "width" are extracted from MC. They are given in Tab. 7.13.

Table 7.12: Signal SCF fractions separated in tagging category (extracted using true MC information).

Tagging category	SCF fraction
`Lepton`	0.168 ± 0.004
`KaonI`	0.245 ± 0.005
`KaonII`	0.276 ± 0.004
`Kaon-Pion`	0.265 ± 0.005
`Pion`	0.289 ± 0.004
`Other`	0.298 ± 0.006
`Untagged`	0.307 ± 0.004

Table 7.13: Signal TM and SCF error function parameters, extracted from fits to MC using a Landau distribution.

Tagging category	Signal TM		Signal SCF	
	μ	σ	μ	σ
`Lepton`	0.505 ± 0.000	0.083 ± 0.000	0.551 ± 0.024	0.124 ± 0.013
`KaonI`	0.502 ± 0.006	0.071 ± 0.004	0.550 ± 0.019	0.109 ± 0.009
`KaonII`	0.572 ± 0.005	0.088 ± 0.004	0.618 ± 0.018	0.105 ± 0.007
`Kaon-Pion`	0.601 ± 0.006	0.114 ± 0.003	0.668 ± 0.026	0.147 ± 0.012
`Pion`	0.635 ± 0.007	0.116 ± 0.003	0.688 ± 0.020	0.150 ± 0.012
`Other`	0.637 ± 0.011	0.126 ± 0.005	0.678 ± 0.022	0.129 ± 0.011
`Untagged`	0.663 ± 0.006	0.127 ± 0.003	0.737 ± 0.019	0.153 ± 0.012

7.6.4.2 Continuum

The parameters of the resolution function are extracted from a fit to the Off-Peak data. In order to maximize the sensitivity, we enlarged the Fisher discriminant range from its nominal lower value (i.e. 0.0) to -0.4. This allows to obtain 3.6 times more events. It was checked that this procedure does not affect the PDF parameters of the other variables in the fit (i.e. $m_{\rm ES}$, ΔE and the Fisher discriminant). Table 7.14 gives the values of the fitted resolution function parameters and Fig. 7.18 shows a comparison between the Δt distribution in the Off-Peak data and in a sample generated from the results of the fit performed to extract the continuum Δt parameters. The tagging-category fractions, given in Tab. 7.15, are extracted from Off-Peak data using the `Tag08` algorithm. The error functions ($\sigma_{\Delta t}$) are separated in tagging category and parametrized using a Landau distribution, where the "mean" and "width" are extracted from fits to Off-Peak data. They are given in Tab. 7.16.

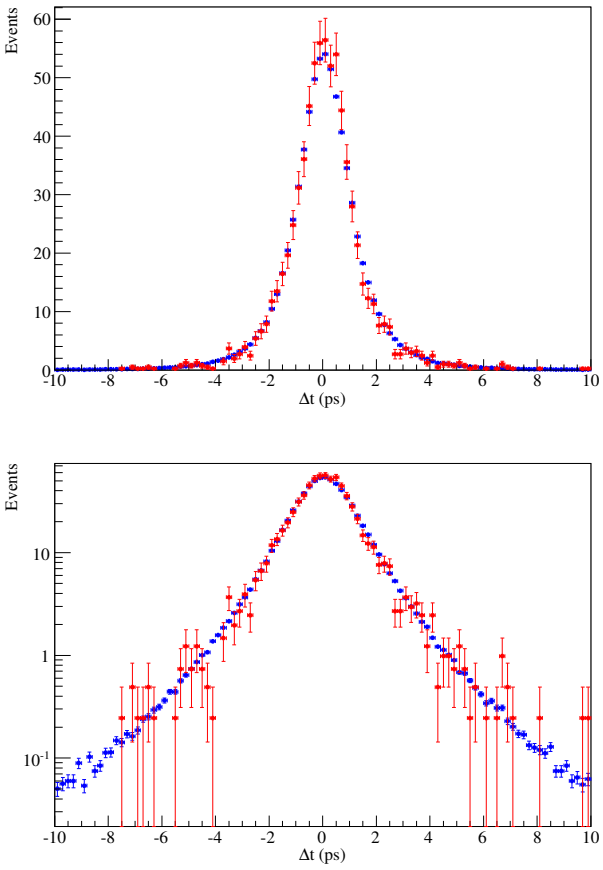

Figure 7.18: Compared Off-Peak data and fitted Δt distributions with normal-scale y axis (top) and log-scale y axis (bottom). Blue points correspond to event generated using the fit results and the red points correspond to Off-Peak data. The generated distribution is normalized to the Off-Peak integral.

Table 7.14: Continuum Δt resolution function parameters extracted from a fit to Off-Peak data.

Parameters	Core Gaussian	Outlier Gaussian
mean	0.0690 ± 0.0314	0.0
sigma	1.2503 ± 0.0327	0.8521 ± 0.4349
fraction	$1 - f_{\text{outlier}}$	0.0456 ± 0.0317
"lifetime" τ	2.3703 ± 0.3353	
prompt fraction	0.9206 ± 0.0223	

Table 7.15: Continuum tagging-category fractions (ϵ^c) extracted from Off-Peak data using `Tag08` algorithm.

Tagging category	ϵ
`Lepton`	0.010 ± 0.002
`KaonI`	0.063 ± 0.005
`KaonII`	0.147 ± 0.007
`Kaon-Pion`	0.112 ± 0.005
`Pion`	0.187 ± 0.008
`Other`	0.119 ± 0.006
`Untagged`	0.363 ± 0.011

Table 7.16: Continuum error function parameters, extracted from fits to Off-Peak data using a Landau distribution.

Tagging category	μ	σ
`Lepton`	0.686 ± 0.184	0.037 ± 0.121
`KaonI`	0.539 ± 0.058	0.117 ± 0.033
`KaonII`	0.614 ± 0.047	0.132 ± 0.029
`Kaon-Pion`	0.713 ± 0.057	0.145 ± 0.029
`Pion`	0.756 ± 0.066	0.180 ± 0.028
`Other`	0.779 ± 0.070	0.164 ± 0.035
`Untagged`	0.769 ± 0.041	0.191 ± 0.022

7.6.4.3 B backgrounds

The parameters of the resolution function are taken from the `BReco` fit to data, except for two B-background categories, for which the parameters are extracted from fits to MC distributions. Tables 7.17 and 7.18 give the fitted values of the resolution function parameters for $B^+ \to K^{*+}(\to K^0_S\pi^+)\gamma$ + $B^+ \to X_{su}(\to K^0_S\pi^+)\gamma$ and $B^0 \to K^{*0}(\to K^0_S\pi^0)\gamma$ + $B^0 \to X_{sd}(\to K^0_S\pi^0)\gamma$ B-backgrounds, respectively.

The tagging-category fractions (ϵ^c), mis-tag fractions (ω^c) and dilution differences (ΔD^c) are extracted from MC using true information and are given in Tabs. 7.19 and 7.20 for charged and neutral B backgrounds, respectively.

The error functions ($\sigma_{\Delta t}$) are separated in tagging category for each B background. We use a Landau parametrization, where the "mean" and "width" are extracted from fits to MC, except for $B^+ \to K^{*+}(\to K^0_S\pi^+)\gamma$ + $B^+ \to X_{su}(\to K^0_S\pi^+)\gamma$ and $B^0 \to K^{*0}(\to K^0_S\pi^0)\gamma$ + $B^0 \to X_{sd}(\to K^0_S\pi^0)\gamma$, for which the Landau parametrization did not fit well the MC distributions. For these two B-background categories, we use the histograms obtained from the MC. The fitted parameters for the other B backgrounds are given in Tabs. 7.22 and 7.23.

Table 7.21 gives the values extracted from a fit to MC of the $\mathcal{S}$ and $\mathcal{C}$ parameters for the radiative CP-eigenstate neutral B backgrounds. These values are compatible with zero, therefore in the fit to the data we fix the $\mathcal{S}$ and $\mathcal{C}$ parameters for radiative CP-eigenstate neutral B backgrounds to 0. The non radiative CP-eigenstate neutral B background (i.e. $B^0\overline{B}^0$ generic event category) contains both CP-eigenstates and flavor-eigenstates. As the contribution of the latter is expected to be dominant, the $\mathcal{S}$ and $\mathcal{C}$ parameters are both fixed to 0. It was checked that the effect on the signal CP parameters was negligible compared

Table 7.17: $B^+ \to K^{*+}(\to K^0_S\pi^+)\gamma$ + $B^+ \to X_{su}(\to K^0_S\pi^+)\gamma$ B-background Δt resolution function parameters extracted from a fit to MC.

B-background Category	Parameters	Core Gaussian	Tail Gaussian	Outlier Gaussian
$B^+ \to K^{*+}(\to K^0_S\pi^+)\gamma$ $B^+ \to X_{su}(\to K^0_S\pi^+)\gamma$	mean	-0.081 ± 0.012	0.383 ± 0.539	0.0
	sigma	0.892 ± 0.020	1.210 ± 0.776	8.0
	fraction	$1 - f_{\rm tail} - f_{\rm outlier}$	0.019 ± 0.002	$< 5 \times 10^{-3}$ ± 0.002
	"lifetime" τ	1.464 ± 0.018		

Table 7.18: $B^0 \to K^{*0}(\to K^0_S\pi^0)\gamma$ + $B^0 \to X_{sd}(\to K^0_S\pi^0)\gamma$ B-background Δt resolution function parameters extracted from a fit to MC.

B-background Category	Parameters	Core Gaussian	Tail Gaussian	Outlier Gaussian
$B^0 \to K^{*0}(\to K^\pm\pi^\mp)\gamma$ $B^0 \to X_{sd}(\to K^\pm\pi^\mp)\gamma$	mean	−0.038 ± 0.021	−0.367 ± 0.306	0.0
	sigma	0.986 ± 0.029	3.936 ± 0.609	8.0
	fraction	$1 - f_{\rm tail} - f_{\rm outlier}$	0.047 ± 0.012	0.009 ± 0.004
	"lifetime" τ	1.018 ± 0.028		
	"oscillation" Δm	0.502		

to the statistical errors. We generated a pseudo-experiment with $\mathcal{S} = 0$ and performed a fit with $\mathcal{S} = \sin(2\beta)$ and found that the deviation on the signal *CP* parameter was not significant compared to the statistical error. Finally, the direct *CP* asymmetry between the number of events with a B or a $\overline{B}$ meson, for the charged and the flavor-eigenstate neutral B backgrounds, are given in Tab. 7.24. These parameters are not separated into tagging categories.

Table 7.19: Charged B-backgrounds tagging-category fractions (ϵ^c), mis-tag fractions (ω^c) and dilution differences (ΔD^c) extracted using true MC information.

B-background category	Tagging category	ϵ	ω	ΔD
$B^+ \to K^{*+}(\to K^0_S\pi^+)\gamma$ $B^+ \to X_{su}(\to K^0_S\pi^+)\gamma$	`Lepton`	0.043 ± 0.018	0.018 ± 0.012	-0.059 ± 0.054
	`KaonI`	0.129 ± 0.033	0.067 ± 0.010	-0.011 ± 0.043
	`KaonII`	0.165 ± 0.046	0.130 ± 0.013	0.003 ± 0.059
	`Kaon-Pion`	0.148 ± 0.032	0.228 ± 0.020	0.048 ± 0.096
	`Pion`	0.153 ± 0.038	0.376 ± 0.021	-0.017 ± 0.096
	`Other`	0.095 ± 0.033	0.377 ± 0.027	-0.050 ± 0.114
	`Untagged`	0.242 ± 0.047	0.5	0.0
$B^+ \to X_{su}(\nrightarrow K\pi)\gamma$	`Lepton`	0.062 ± 0.014	0.028 ± 0.047	0.048 ± 0.339
	`KaonI`	0.091 ± 0.023	0.151 ± 0.071	0.032 ± 0.265
	`KaonII`	0.191 ± 0.029	0.262 ± 0.075	-0.175 ± 0.304
	`Kaon-Pion`	0.167 ± 0.027	0.314 ± 0.108	-0.001 ± 0.416
	`Pion`	0.181 ± 0.028	0.329 ± 0.125	-0.152 ± 0.427
	`Other`	0.119 ± 0.021	0.393 ± 0.126	0.216 ± 0.563
	`Untagged`	0.285 ± 0.042	0.5	0.0
B^+B^- generic	`Lepton`	0.009 ± 0.031	0.651 ± 0.408	$0.859 \pm 1,852$
	`KaonI`	0.049 ± 0.056	0.394 ± 0.294	$-0.215 \pm 1,041$
	`KaonII`	0.246 ± 0.076	0.383 ± 0.262	0.286 ± 0.892
	`Kaon-Pion`	0.066 ± 0.063	0.612 ± 0.299	0.248 ± 0.958
	`Pion`	0.180 ± 0.073	0.577 ± 0.324	$-0.763 \pm 1,302$
	`Other`	0.091 ± 0.059	0.304 ± 0.406	$-0.635 \pm 1,878$
	`Untagged`	0.246 ± 0.104	0.5	0.0

Table 7.20: Neutral B-backgrounds tagging-category fractions (ϵ^c), mis-tag fractions (ω^c) and dilution differences (ΔD^c) extracted using true MC information.

B-background category	Tagging category	ϵ	ω	ΔD
$B^0 \to K^{*0}(\to K^0_S\pi^0)\gamma$ $B^0 \to X_{sd}(\to K^0_S\pi^0)\gamma$	`Lepton`	0.051 ± 0.027	0.187 ± 0.034	$-0.120 \pm 1,537$
	`KaonI`	0.099 ± 0.037	0.192 ± 0.030	$-0.316 \pm 1,261$
	`KaonII`	0.157 ± 0.048	0.291 ± 0.026	0.026 ± 0.349
	`Kaon-Pion`	0.163 ± 0.043	0.343 ± 0.035	-0.301 ± 0.515
	`Pion`	0.233 ± 0.052	0.440 ± 0.033	0.112 ± 0.546
	`Other`	0.163 ± 0.043	0.449 ± 0.038	0.239 ± 0.687
	`Untagged`	0.307 ± 0.075	0.0	0.0
$B^0 \to X_{sd}(\nrightarrow K\pi)\gamma$	`Lepton`	0.059 ± 0.031	0.065 ± 0.033	-0.010 ± 0.109
	`KaonI`	0.098 ± 0.036	0.107 ± 0.030	-0.032 ± 0.092
	`KaonII`	0.237 ± 0.054	0.219 ± 0.037	-0.067 ± 0.152
	`Kaon-Pion`	0.193 ± 0.047	0.280 ± 0.058	0.069 ± 0.191
	`Pion`	0.186 ± 0.055	0.389 ± 0.053	-0.029 ± 0.192
	`Other`	0.116 ± 0.048	0.399 ± 0.062	-0.180 ± 0.201
	`Untagged`	0.267 ± 0.074	0.5	0.0
$B^0\overline{B}^0$ generic	`Lepton`	0.052 ± 0.024	0.603 ± 0.303	$0.942 \pm 1,286$
	`KaonI`	0.072 ± 0.034	$1,015 \pm 0.300$	$0.017 \pm 1,179$
	`KaonII`	0.178 ± 0.054	0.757 ± 0.164	0.298 ± 0.722
	`Kaon-Pion`	0.183 ± 0.052	0.840 ± 0.158	-0.064 ± 0.785
	`Pion`	0.257 ± 0.069	0.758 ± 0.201	0.184 ± 0.647
	`Other`	0.118 ± 0.042	0.570 ± 0.181	0.231 ± 0.726
	`Untagged`	0.282 ± 0.066	0.5	0.0
$B^0 \to K^{*0}(\to K^\pm\pi^\mp)\gamma$ $B^0 \to X_{sd}(\to K^\pm\pi^\mp)\gamma$	`Lepton`	0.025 ± 0.056	0.249 ± 0.134	0.373 ± 0.742
	`KaonI`	0.082 ± 0.112	0.965 ± 0.176	-0.072 ± 0.799
	`KaonII`	0.419 ± 0.324	0.792 ± 0.124	0.055 ± 0.559
	`Kaon-Pion`	0.202 ± 0.213	0.775 ± 0.146	0.084 ± 0.588
	`Pion`	0.398 ± 0.284	0.571 ± 0.107	-0.299 ± 0.445
	`Other`	0.147 ± 0.143	0.552 ± 0.138	-0.321 ± 0.677
	`Untagged`	0.375 ± 0.221	0.5	0.0

Table 7.21: $\mathcal{S}$ and $\mathcal{C}$ values for radiative *CP*-eigenstate neutral B backgrounds extracted from a fit to MC.

B-background category	$\mathcal{S}$	$\mathcal{C}$
$B^0 \to K^{*0}(\to K^0_S\pi^0)\gamma$ $B^0 \to X_{sd}(\to K^0_S\pi^0)\gamma$	$(0.936 \pm 9.237) \times 10^{-2}$	$(3.298 \pm 5.935) \times 10^{-2}$
$B^0 \to X_{sd}(\nrightarrow K\pi)\gamma$	$(2.213 \pm 19.64) \times 10^{-2}$	$(-4.733 \pm 11.91) \times 10^{-2}$

Table 7.22: Charged B-backgrounds error function parameters, extracted from fits to MC using a Landau distribution.

B-background category	Tagging category	μ	σ
$B^+ \to X_{su}(\nrightarrow K\pi)\gamma$	`Lepton`	0.557 ± 0.048	0.117 ± 0.033
	`KaonI`	0.531 ± 0.031	0.082 ± 0.022
	`KaonII`	0.602 ± 0.026	0.103 ± 0.014
	`Kaon-Pion`	0.698 ± 0.045	0.143 ± 0.021
	`Pion`	0.699 ± 0.036	0.146 ± 0.023
	`Other`	0.702 ± 0.050	0.137 ± 0.028
	`Untagged`	0.757 ± 0.038	0.177 ± 0.020
B^+B^- generic	`Lepton`	0.513 ± 0.100	0.056 ± 0.041
	`KaonI`	0.608 ± 0.087	0.125 ± 0.041
	`KaonII`	0.712 ± 0.092	0.170 ± 0.049
	`Kaon-Pion`	0.665 ± 0.145	0.204 ± 0.055
	`Pion`	0.701 ± 0.092	0.146 ± 0.061
	`Other`	0.678 ± 0.102	0.164 ± 0.055
	`Untagged`	0.699 ± 0.055	0.140 ± 0.029

Table 7.23: Neutral B-backgrounds error function parameters, extracted from fits to MC using a Landau distribution.

B-background category	Tagging category	μ	σ
$B^0 \to X_{sd}(\nrightarrow K\pi)\gamma$	`Lepton`	0.586 ± 0.079	0.121 ± 0.043
	`KaonI`	0.579 ± 0.035	0.063 ± 0.019
	`KaonII`	0.671 ± 0.043	0.082 ± 0.028
	`Kaon-Pion`	0.702 ± 0.056	0.144 ± 0.029
	`Pion`	0.679 ± 0.051	0.140 ± 0.033
	`Other`	0.816 ± 0.081	0.192 ± 0.048
	`Untagged`	0.635 ± 0.036	0.120 ± 0.020
$B^0\overline{B}^0$ generic	`Lepton`	0.616 ± 0.069	0.049 ± 0.047
	`KaonI`	0.680 ± 0.082	0.177 ± 0.056
	`KaonII`	0.588 ± 0.064	0.117 ± 0.030
	`Kaon-Pion`	0.722 ± 0.079	0.186 ± 0.044
	`Pion`	0.703 ± 0.059	0.136 ± 0.035
	`Other`	0.748 ± 0.085	0.132 ± 0.044
	`Untagged`	0.816 ± 0.083	0.213 ± 0.041
$B^0 \to K^{*0}(\to K^{\pm}\pi^{\mp})\gamma$ $B^0 \to X_{sd}(\to K^{\pm}\pi^{\mp})\gamma$	`Lepton`	0.562 ± 0.037	0.102 ± 0.023
	`KaonI`	0.483 ± 0.014	0.064 ± 0.008
	`KaonII`	0.524 ± 0.018	0.095 ± 0.008
	`Kaon-Pion`	0.524 ± 0.024	0.100 ± 0.011
	`Pion`	0.540 ± 0.024	0.124 ± 0.011
	`Other`	0.622 ± 0.036	0.109 ± 0.020
	`Untagged`	0.549 ± 0.026	0.122 ± 0.012

Table 7.24: Direct CP asymmetry, between B and $\overline{B}$ events, for the charged and the flavor-eigenstate neutral B backgrounds.

B-background category	Asymmetry
$B^+ \to X_{su}(\nrightarrow K\pi)\gamma$	-0.029 ± 0.057
$B^+ \to K^{*+}(\to K^0_S\pi^+)\gamma$ $B^+ \to X_{su}(\to K^0_S\pi^+)\gamma$	-0.098 ± 0.074
B^+B^- generic	0.028 ± 0.178
$B^0 \to K^{*0}(\to K^{\pm}\pi^{\mp})\gamma$ $B^0 \to X_{sd}(\to K^{\pm}\pi^{\mp})\gamma$	0.421 ± 0.830

7.6.5 Validation tests

We first tested the ability of the fitter to yield unbiassed measurements of the *CP* asymmetry parameters $\mathcal{S}$ and $\mathcal{C}$ in signal regardless to their values. The results of these validation tests are given in Sec. 7.6.5.1. In order to test the robustness of our model before fitting the data, we perform validation tests by means of the toy MC studies, using the procedure previously described in Sec. 6.5.4. Again, two types of toy studies are used: pure (Sec. 7.6.5.2) and embedded (Sec. 7.6.5.3). The different parameters entering the Δt PDFs (dilutions, dilution differences, asymmetries, resolution function parameters) as well as the tagging-category fractions are discussed in Sec. 7.6.4.

7.6.5.1 Validation of $\mathcal{S}$ and $\mathcal{C}$ extraction

In order to test the ability of the maximum likelihood fit to yield unbiassed results of the signal $\mathcal{S}$ and $\mathcal{C}$ parameters, we use simplified toy studies with only signal and continuum. Signal events are drawn from the fully reconstructed MC samples, whereas events for continuum are generated out of the corresponding PDFs. The available MC for signal was generated with zero $\mathcal{S}$ and $\mathcal{C}$ values. Therefore, using the full MC statistics, we created by rejecting events several sets of samples (not statistically independent) with different non-zero values of $\mathcal{S}$ and $\mathcal{C}$, within the constraint $\mathcal{S}^2 + \mathcal{C}^2 \leq 1$. Each sample was obtained by weighting the number of B^0 and $\overline{B}^0$ events from MC true information using an accept-reject method based on the fraction f:

$$f = \frac{1 - (\mathcal{S}\sin(\Delta m \Delta t) - \mathcal{C}\cos(\Delta m \Delta t))}{1 + (\mathcal{S}\sin(\Delta m \Delta t) - \mathcal{C}\cos(\Delta m \Delta t))}. \tag{7.17}$$

From a random number (x_1) drawn uniformly between 0 and 1, we accept an event from a B^0 meson if:

$$x_1 \leq \frac{1}{1+f}, \tag{7.18}$$

and reject it otherwise. From another random number (x_2) drawn uniformly between 0 and 1, we accept an event from a $\overline{B}^0$ meson if:

$$x_2 \leq \frac{f}{1+f}, \tag{7.19}$$

and reject it otherwise.

We then performed a fit to each pseudo experiment obtained this way with a simplified model containing signal and continuum only, where the initial values for $\mathcal{S}$ and $\mathcal{C}$ are set to zero. All the other parameters are fixed in the fit, except for the signal and continuum yields. Note that the yields are not realistic, since the aim of the test is to validate the ability to correctly extract non-zero values of $\mathcal{S}$ and $\mathcal{C}$. Therefore full signal MC statistics is used and the continuum background yield is scaled to the obtained signal one, given the ratio of their expected yields in the data.

Tables 7.25 and 7.26 give the fitted values of $\mathcal{S}$ and $\mathcal{C}$, respectively. We observe that within the statistical uncertainties, the fitted values of $\mathcal{S}$ and $\mathcal{C}$ are in good agreement with the true generated values. From these results, we conclude that the fitter is able to correctly extract non-zero values of $\mathcal{S}$ and $\mathcal{C}$.

Table 7.25: Fitted values of $\mathcal{S}$ for each of the signal weighted MC samples. Cells with the symbol $\varnothing$ designate non-allowed values given the constraint $\mathcal{S}^2 + \mathcal{C}^2 \leq 1$.

$\mathcal{C}$ \ $\mathcal{S}$	-0.9	-0.7	-0.5	-0.3	-0.1
-0.9	$\varnothing$	$\varnothing$	$\varnothing$	-0.317 ± 0.048	-0.159 ± 0.048
-0.7	$\varnothing$	-0.664 ± 0.044	-0.473 ± 0.046	-0.307 ± 0.049	-0.091 ± 0.050
-0.5	$\varnothing$	-0.621 ± 0.046	-0.529 ± 0.048	-0.275 ± 0.052	-0.061 ± 0.051
-0.3	-0.850 ± 0.046	-0.630 ± 0.048	-0.505 ± 0.050	-0.197 ± 0.052	-0.025 ± 0.051
-0.1	-0.899 ± 0.044	-0.658 ± 0.048	-0.470 ± 0.050	-0.268 ± 0.051	-0.104 ± 0.051
$+0.1$	-0.836 ± 0.045	-0.639 ± 0.050	-0.479 ± 0.050	-0.287 ± 0.052	-0.068 ± 0.052
$+0.3$	-0.895 ± 0.043	-0.666 ± 0.048	-0.448 ± 0.050	-0.225 ± 0.051	-0.101 ± 0.051
$+0.5$	$\varnothing$	-0.709 ± 0.046	-0.468 ± 0.048	-0.282 ± 0.051	-0.175 ± 0.050
$+0.7$	$\varnothing$	-0.717 ± 0.044	-0.475 ± 0.047	-0.301 ± 0.049	-0.067 ± 0.050
$+0.9$	$\varnothing$	$\varnothing$	$\varnothing$	-0.240 ± 0.047	-0.131 ± 0.048

$\mathcal{C}$ \ $\mathcal{S}$	$+0.1$	$+0.3$	$+0.5$	$+0.7$	$+0.9$
-0.9	0.109 ± 0.047	0.346 ± 0.046	$\varnothing$	$\varnothing$	$\varnothing$
-0.7	0.135 ± 0.048	0.296 ± 0.049	0.456 ± 0.048	0.685 ± 0.044	$\varnothing$
-0.5	0.042 ± 0.050	0.237 ± 0.050	0.478 ± 0.049	0.724 ± 0.046	$\varnothing$
-0.3	0.110 ± 0.052	0.333 ± 0.050	0.490 ± 0.050	0.677 ± 0.048	0.844 ± 0.045
-0.1	0.080 ± 0.053	0.356 ± 0.051	0.449 ± 0.051	0.622 ± 0.049	0.789 ± 0.045
$+0.1$	0.106 ± 0.052	0.327 ± 0.050	0.372 ± 0.051	0.667 ± 0.048	0.802 ± 0.046
$+0.3$	0.115 ± 0.052	0.286 ± 0.050	0.410 ± 0.050	0.636 ± 0.049	0.915 ± 0.042
$+0.5$	0.060 ± 0.051	0.298 ± 0.050	0.380 ± 0.051	0.622 ± 0.047	$\varnothing$
$+0.7$	0.070 ± 0.049	0.254 ± 0.049	0.442 ± 0.049	0.609 ± 0.046	$\varnothing$
$+0.9$	0.102 ± 0.048	0.266 ± 0.048	$\varnothing$	$\varnothing$	$\varnothing$

Table 7.26: Fitted values of $\mathcal{C}$ for each of the signal weighted MC samples. Cells with the symbol $\varnothing$ designate non-allowed values given the constraint $\mathcal{S}^2 + \mathcal{C}^2 \leq 1$.

$\mathcal{S}$ \ $\mathcal{C}$	-0.9	-0.7	-0.5	-0.3	-0.1
-0.9	$\varnothing$	$\varnothing$	$\varnothing$	-0.340 ± 0.032	-0.160 ± 0.033
-0.7	$\varnothing$	-0.716 ± 0.029	-0.531 ± 0.032	-0.274 ± 0.033	-0.125 ± 0.034
-0.5	$\varnothing$	-0.716 ± 0.030	-0.510 ± 0.033	-0.278 ± 0.033	-0.071 ± 0.034
-0.3	-0.908 ± 0.026	-0.703 ± 0.030	-0.481 ± 0.032	-0.255 ± 0.034	-0.041 ± 0.034
-0.1	-0.878 ± 0.027	-0.715 ± 0.030	-0.509 ± 0.033	-0.321 ± 0.034	-0.107 ± 0.034
$+0.1$	-0.878 ± 0.028	-0.700 ± 0.031	-0.461 ± 0.033	-0.323 ± 0.034	-0.116 ± 0.034
$+0.3$	-0.879 ± 0.027	-0.726 ± 0.030	-0.555 ± 0.033	-0.350 ± 0.034	-0.117 ± 0.034
$+0.5$	$\varnothing$	-0.680 ± 0.031	-0.507 ± 0.032	-0.285 ± 0.034	-0.115 ± 0.034
$+0.7$	$\varnothing$	-0.716 ± 0.029	-0.509 ± 0.032	-0.259 ± 0.033	-0.159 ± 0.034
$+0.9$	$\varnothing$	$\varnothing$	$\varnothing$	-0.301 ± 0.033	-0.086 ± 0.034

$\mathcal{S}$ \ $\mathcal{C}$	$+0.1$	$+0.3$	$+0.5$	$+0.7$	$+0.9$
-0.9	0.043 ± 0.033	0.262 ± 0.033	$\varnothing$	$\varnothing$	$\varnothing$
-0.7	0.078 ± 0.034	0.282 ± 0.033	0.500 ± 0.031	0.683 ± 0.028	$\varnothing$
-0.5	0.083 ± 0.034	0.303 ± 0.033	0.447 ± 0.033	0.670 ± 0.030	$\varnothing$
-0.3	0.061 ± 0.034	0.262 ± 0.034	0.493 ± 0.033	0.656 ± 0.031	0.874 ± 0.027
-0.1	0.061 ± 0.034	0.311 ± 0.034	0.484 ± 0.033	0.683 ± 0.031	0.832 ± 0.028
$+0.1$	0.065 ± 0.034	0.259 ± 0.034	0.484 ± 0.033	0.687 ± 0.031	0.913 ± 0.026
$+0.3$	0.101 ± 0.035	0.307 ± 0.034	0.505 ± 0.032	0.700 ± 0.030	0.825 ± 0.028
$+0.5$	0.090 ± 0.034	0.319 ± 0.033	0.483 ± 0.032	0.696 ± 0.030	$\varnothing$
$+0.7$	0.055 ± 0.034	0.317 ± 0.033	0.495 ± 0.032	0.659 ± 0.030	$\varnothing$
$+0.9$	0.100 ± 0.034	0.330 ± 0.032	$\varnothing$	$\varnothing$	$\varnothing$

7.6.5.2 Pure toy studies

We generate with our fitter an ensemble of 500 pseudo experiments using the PDFs listed in Tab. 7.11. In each pseudo experiment, the yield of each category is randomly generated from a Poisson distribution (aka "poissonized") corresponding to its expected value (Tabs. 7.8 and 7.10 for signal and background yields, respectively). The values of shape parameters are extracted from all the MC information available for signal and B background. For continuum background the shape parameters are extracted from Run1-6 Off-Peak data sample.

We use the nominal PDF to fit each of the 500 pseudo-experiments, and we set the values of $\mathcal{S}$ and $\mathcal{C}$ parameters for the signal event category both to zero. Due to the large number of shape parameters (more than 100) we fix many of them, mainly in the background PDFs. Several combinations were tested in order to maximize the number of varied parameters in order to reduce systematic uncertainties without impairing on the fit ability to discriminate the different components. As a result, we fix all the B-background shape parameters, as well as all their yields, except for the $B^+ \to K^{*+}(\to K^0_S\pi^+)\gamma$ + $B^+ \to X_{su}(\to K^0_S\pi^+)\gamma$ one. Indeed, as some of them have similar PDF shapes, the fitter has difficulties to discriminate them. Furthermore, we fix all the SCF shape parameters as well as the Argus and Exponential parameters of the $m_{\rm ES}$ and the Fisher discriminant PDFs for the continuum background, respectively. For the signal TM, we found that it is possible to vary the Gaussian parameter μ of the Fisher discriminant, the Cruijff parameters σ_L and σ_R and all the evolution coefficients of Crystal Ball parameters μ and σ describing the ΔE polynomial dependence of $m_{\rm ES}$ in the two-dimensional PDF.

Concerning the Δt PDFs parameters, we fix all the dilutions, dilution differences, tagging category fractions and asymmetries as well as all the $\sigma_{\Delta t}$ parameters. We fix the resolution function parameters of all the categories in the model, except for the continuum background, for which the mean and sigma of the core gaussian as well as the width and the fraction of the outlier gaussian are free to vary in the fit. The $\mathcal{S}$ and $\mathcal{C}$ parameters for signal are free to vary in the fit, while the ones for the CP-eigenstate neutral B backgrounds are fixed.

Table 7.27 gives the results of the pure toy studies, showing the mean and width of the pull distributions of each floated parameter in our model. We conclude from these results that the model has no intrinsic dysfunction. Note that the fit convergence rate is 100%, and that all the pull distributions are gaussian of means and widths that are compatible, within the statistical uncertainties, with 0 and 1, respectively. Figure 7.19 shows the pull distributions of the signal $\mathcal{S}$ and $\mathcal{C}$ parameters. Pull distributions of the yields, the shape parameters and the continuum background resolution function parameters can be found in Appendix G.1.

7.6.5.3 Embedded toy studies

For the embedded toy studies, we produced pseudo experiments by generating events out of the PDFs for the simpler species (background categories with no significant correlation among the fit variables), whereas events for signal (TM and SCF) and the B-background $B^0 \to K^{*0}(\to K^0_S\pi^0)\gamma$ + $B^0 \to X_{sd}(\to K^0_S\pi^0)\gamma$ are drawn from the fully reconstructed MC samples. In the signal MC sample the values of the $\mathcal{S}$ and $\mathcal{C}$ parameters for the signal event

Table 7.27: Means and widths of pull distributions of all the floated parameters entering the time-dependent model from the pure toy studies.

	Fit variable	Fit Parameter	Pull Mean	Pull Width
Signal TM	$m_{\rm ES}$	CB_μ(Coeff0)	0.071 ± 0.049	1.059 ± 0.037
		CB_μ(Coeff1)	-0.078 ± 0.050	1.062 ± 0.038
		CB_μ(Coeff2)	-0.187 ± 0.055	1.103 ± 0.046
		CB_σ(Coeff0)	-0.095 ± 0.054	1.053 ± 0.035
		CB_σ(Coeff1)	0.064 ± 0.044	0.898 ± 0.041
		CB_σ(Coeff2)	-0.002 ± 0.045	0.960 ± 0.038
	ΔE	Cr_{σ_R}	0.025 ± 0.044	0.941 ± 0.031
		Cr_{σ_L}	0.038 ± 0.046	0.826 ± 0.038
	Fisher	G_μ	0.027 ± 0.045	0.996 ± 0.037
udsc	ΔE	Chebychev(Coeff0)	-0.003 ± 0.045	0.976 ± 0.038
		Chebychev(Coeff1)	0.001 ± 0.045	0.987 ± 0.031
	$\mathcal{R}_{\rm bg}$	$b_{\rm core}$	0.043 ± 0.044	0.964 ± 0.032
		$s_{\rm core}$	-0.104 ± 0.046	0.997 ± 0.037
		$s_{\rm outlier}$	0.166 ± 0.061	1.247 ± 0.056
		$f_{\rm outlier}$	0.086 ± 0.045	0.961 ± 0.045
Yields		Signal	0.084 ± 0.049	0.977 ± 0.034
		Continuum *udsc*	0.032 ± 0.046	0.985 ± 0.036
		$B^+ \to K^{*+}(\to K^0_S\pi^+)\gamma$	-0.049 ± 0.046	1.003 ± 0.041
		$B^+ \to X_{su}(\to K^0_S\pi^+)\gamma$		
		$\mathcal{S}$	0.082 ± 0.048	1.053 ± 0.037
		$\mathcal{C}$	-0.020 ± 0.046	1.001 ± 0.035

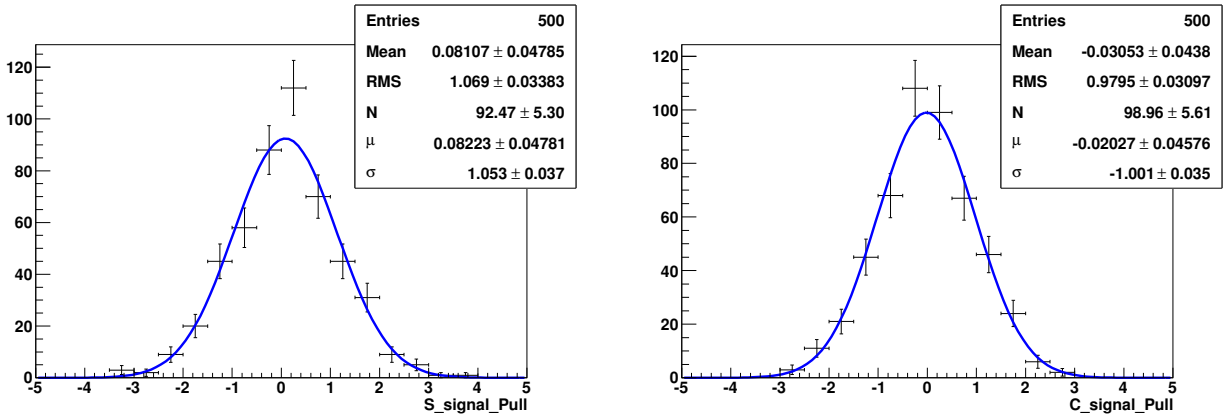

Figure 7.19: Signal $\mathcal{S}$ (left) and $\mathcal{C}$ (right) pull distributions for the pure toy studies with 500 toys.

category are both equal to zero. 351 of such pseudo experiments are generated, which are then fitted using the same PDFs as in the pure toy studies. The yield of each event category is poissonized around their expected value. Table 7.28 gives the results of the embedded toy studies, showing the means and widths of the pull distributions of each floated parameter in the model. The fit convergence is 100%. Figure 7.20 shows the pull distributions of the signal $\mathcal{S}$ and $\mathcal{C}$ parameters. We observe that our model has no significant bias on the yield and on the *CP* asymmetry parameters for signal, when both $\mathcal{S}$ and $\mathcal{C}$ are generated in MC as equal to zero. Pull distributions of the shape parameters can be found in Appendix G.2.

In addition, to check for possible biases in the whole range of the *CP* asymmetry parameter space, we performed several embedded-toy studies where only signal events were embedded (i.e. continuum and B-background events are generated from the corresponding PDFs). These events were drawn from weighted MC samples, which were created using the same method as in the validation test of the time-dependent fitter (see Sec. 7.6.5.1). We generated and fitted 20 sets of 300 embedded pseudo experiments with different $\mathcal{S}$ and $\mathcal{C}$ values such as $\mathcal{S} = 0.4i$ and $\mathcal{C} = 0.4j$ with $(i, j) \in [-2, -1, 0, +1, +2]$ and with the constraint $\mathcal{S}^2 + \mathcal{C}^2 \leq 1$. In each toy study (i.e. for each set of embedded pseudo experiments), the same parameters, as in the nominal embedded toy study presented above, are free to vary in the fit. The results of the $\mathcal{S}$ and $\mathcal{C}$ pull means and widths are given in Tabs. 7.29 and 7.30. We observe a good behavior of the pull means and widths for values of $\mathcal{S}$ and $\mathcal{C}$ close to the SM expected values (i.e. zero for both). For some combination of large $\mathcal{S}$ and $\mathcal{C}$ values (i.e. one at 0.8 and the other at 0.4), some small biases appear. Since it is very unlikely that such values of $\mathcal{S}$ and $\mathcal{C}$ arise from the fit to the data, we conclude that the model is robust for any combination of $\mathcal{S}$ and $\mathcal{C}$, with values taken in the range $[-0.4; 0.4]$. Note that the fit convergence is in all cases 100%.

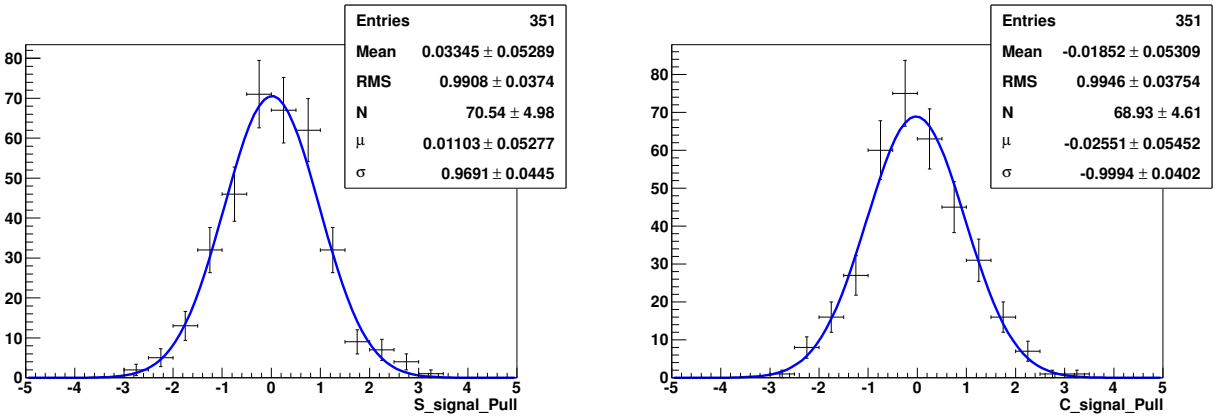

Figure 7.20: Signal $\mathcal{S}$ (left) and $\mathcal{C}$ (right) pull distributions for the embedded toy studies with 259 toys, respectively.

Table 7.28: Means and widths of pull distributions of all the floated parameters entering the time-dependent model from the embedded toy studies.

	Fit variable	Fit Parameter	Pull Mean	Pull Width
Signal TM	$m_{\rm ES}$	CB_μ(Coeff0)	0.118 ± 0.059	1.085 ± 0.046
		CB_μ(Coeff1)	-0.156 ± 0.064	1.155 ± 0.048
		CB_μ(Coeff2)	-0.188 ± 0.066	1.171 ± 0.051
		CB_σ(Coeff0)	-0.153 ± 0.062	1.085 ± 0.060
		CB_σ(Coeff1)	0.052 ± 0.054	0.969 ± 0.044
		CB_σ(Coeff2)	-0.062 ± 0.057	0.992 ± 0.048
	ΔE	Cr_{σ_R}	0.012 ± 0.053	0.955 ± 0.039
		Cr_{σ_L}	0.057 ± 0.055	0.821 ± 0.040
	Fisher	G_μ	0.164 ± 0.054	0.991 ± 0.043
udsc	ΔE	Chebychev(Coeff0)	-0.047 ± 0.054	0.983 ± 0.035
		Chebychev(Coeff1)	0.055 ± 0.053	0.952 ± 0.040
	$\mathcal{R}_{\rm bg}$	$b_{\rm core}$	0.020 ± 0.052	0.962 ± 0.038
		$s_{\rm core}$	-0.157 ± 0.054	0.995 ± 0.039
		$s_{\rm outlier}$	0.123 ± 0.068	1.186 ± 0.053
		$f_{\rm outlier}$	0.148 ± 0.054	0.923 ± 0.043
Yields		Signal	-0.001 ± 0.054	0.967 ± 0.042
		Continuum *udsc*	0.050 ± 0.055	1.010 ± 0.044
		$B^+ \to K^{*+}(\to K^0_S\pi^+)\gamma$	-0.151 ± 0.054	0.990 ± 0.040
		$B^+ \to X_{su}(\to K^0_S\pi^+)\gamma$		
		$\mathcal{S}$	0.011 ± 0.053	0.969 ± 0.044
		$\mathcal{C}$	-0.026 ± 0.055	0.999 ± 0.040

Table 7.29: Means and widths of pull distributions of all the *CP* asymmetry parameters for a few selected points in the parameter space for $\mathcal{S} \leq -0.4$.

Generated value in MC		Fit Parameter	Pull Mean	Pull Width
$\mathcal{S} = -0.8$	$\mathcal{C} = -0.8$	$\mathcal{S}$	$\varnothing$	$\varnothing$
		$\mathcal{C}$	$\varnothing$	$\varnothing$
	$\mathcal{C} = -0.4$	$\mathcal{S}$	0.067 ± 0.050	0.882 ± 0.035
		$\mathcal{C}$	0.030 ± 0.058	1.020 ± 0.041
	$\mathcal{C} = \ \ 0.0$	$\mathcal{S}$	-0.031 ± 0.057	0.977 ± 0.040
		$\mathcal{C}$	-0.023 ± 0.062	1.070 ± 0.044
	$\mathcal{C} = +0.4$	$\mathcal{S}$	-0.007 ± 0.056	0.989 ± 0.040
		$\mathcal{C}$	0.069 ± 0.055	0.978 ± 0.039
	$\mathcal{C} = +0.8$	$\mathcal{S}$	$\varnothing$	$\varnothing$
		$\mathcal{C}$	$\varnothing$	$\varnothing$
$\mathcal{S} = -0.4$	$\mathcal{C} = -0.8$	$\mathcal{S}$	-0.032 ± 0.063	1.110 ± 0.044
		$\mathcal{C}$	-0.135 ± 0.060	1.060 ± 0.042
	$\mathcal{C} = -0.4$	$\mathcal{S}$	0.021 ± 0.059	1.040 ± 0.041
		$\mathcal{C}$	0.006 ± 0.058	1.028 ± 0.041
	$\mathcal{C} = \ \ 0.0$	$\mathcal{S}$	0.011 ± 0.057	1.024 ± 0.040
		$\mathcal{C}$	0.062 ± 0.060	1.067 ± 0.042
	$\mathcal{C} = +0.4$	$\mathcal{S}$	0.061 ± 0.063	1.101 ± 0.045
		$\mathcal{C}$	0.081 ± 0.061	1.062 ± 0.043
	$\mathcal{C} = +0.8$	$\mathcal{S}$	-0.146 ± 0.060	1.047 ± 0.043
		$\mathcal{C}$	0.161 ± 0.062	1.076 ± 0.044

Table 7.30: Means and widths of pull distributions of all the *CP* asymmetry parameters for a few selected points in the parameter space for $\mathcal{S} > -0.4$.

Generated value in MC		Fit Parameter	Pull Mean	Pull Width
$\mathcal{S} = 0.0$	$\mathcal{C} = -0.8$	$\mathcal{S}$	-0.091 ± 0.059	1.097 ± 0.046
		$\mathcal{C}$	-0.116 ± 0.057	1.041 ± 0.044
	$\mathcal{C} = -0.4$	$\mathcal{S}$	-0.058 ± 0.060	1.048 ± 0.042
		$\mathcal{C}$	-0.001 ± 0.059	1.039 ± 0.042
	$\mathcal{C} = 0.0$	$\mathcal{S}$	0.011 ± 0.053	0.969 ± 0.044
		$\mathcal{C}$	-0.026 ± 0.055	0.999 ± 0.040
	$\mathcal{C} = +0.4$	$\mathcal{S}$	0.006 ± 0.058	1.02 ± 0.041
		$\mathcal{C}$	0.074 ± 0.059	1.041 ± 0.042
	$\mathcal{C} = +0.8$	$\mathcal{S}$	0.104 ± 0.058	1.025 ± 0.041
		$\mathcal{C}$	-0.060 ± 0.057	1.008 ± 0.040
$\mathcal{S} = 0.4$	$\mathcal{C} = -0.8$	$\mathcal{S}$	0.077 ± 0.062	1.086 ± 0.044
		$\mathcal{C}$	-0.074 ± 0.057	1.004 ± 0.041
	$\mathcal{C} = -0.4$	$\mathcal{S}$	0.005 ± 0.061	1.058 ± 0.043
		$\mathcal{C}$	0.012 ± 0.060	1.045 ± 0.043
	$\mathcal{C} = 0.0$	$\mathcal{S}$	0.066 ± 0.063	1.113 ± 0.045
		$\mathcal{C}$	0.114 ± 0.056	0.976 ± 0.039
	$\mathcal{C} = +0.4$	$\mathcal{S}$	0.066 ± 0.063	1.097 ± 0.045
		$\mathcal{C}$	0.081 ± 0.057	0.986 ± 0.040
	$\mathcal{C} = +0.8$	$\mathcal{S}$	0.052 ± 0.062	1.083 ± 0.044
		$\mathcal{C}$	0.105 ± 0.065	1.163 ± 0.046
$\mathcal{S} = 0.8$	$\mathcal{C} = -0.8$	$\mathcal{S}$	$\varnothing$	$\varnothing$
		$\mathcal{C}$	$\varnothing$	$\varnothing$
	$\mathcal{C} = -0.4$	$\mathcal{S}$	-0.062 ± 0.058	0.992 ± 0.041
		$\mathcal{C}$	-0.102 ± 0.060	1.024 ± 0.042
	$\mathcal{C} = 0.0$	$\mathcal{S}$	-0.014 ± 0.058	1.013 ± 0.041
		$\mathcal{C}$	0.028 ± 0.064	1.095 ± 0.045
	$\mathcal{C} = +0.4$	$\mathcal{S}$	-0.141 ± 0.056	0.994 ± 0.039
		$\mathcal{C}$	0.036 ± 0.058	1.039 ± 0.041
	$\mathcal{C} = +0.8$	$\mathcal{S}$	$\varnothing$	$\varnothing$
		$\mathcal{C}$	$\varnothing$	$\varnothing$

7.6.6 Results

7.6.6.1 Yields and projections

Here we present the results of the fit to $m_{\rm ES}$, ΔE, the Fisher discriminant and Δt. Table 7.31 gives the yields and Figures 7.21, 7.22 and 7.23 show the projections of $m_{\rm ES}$, ΔE, the Fisher discriminant and Δt. We observe some non negligible fluctuations of the data distributions in these projections. We therefore study these effects by examining the behavior of signal-enriched projections. These are shown in Figs 7.24 to 7.27. They were obtained by applying cuts around the signal region in the other dimensions of the fit (e.g. in ΔE for the $m_{\rm ES}$ enriched fit projection). In the enriched projections, we observe a good agreement between the model and the data points, within the statistical uncertainties, which indicates that the differences between the model and the data, in the whole fit region, are probably due to background fluctuations.

Table 7.31: $B^0 \to K^0_S\pi^+\pi^-\gamma$ fitted yields for the final *BABAR* Run1-6 dataset.

Category	Fitted yield	Fit error (stat.)
Signal (TM+SCF)	245.0	24.3
Continuum *udsc*	2446.4	56.8
$B^+ \to K^{*+}(\to K^0_S\pi^+)\gamma$ $B^+ \to X_{su}(\to K^0_S\pi^+)\gamma$	41.7	21.8

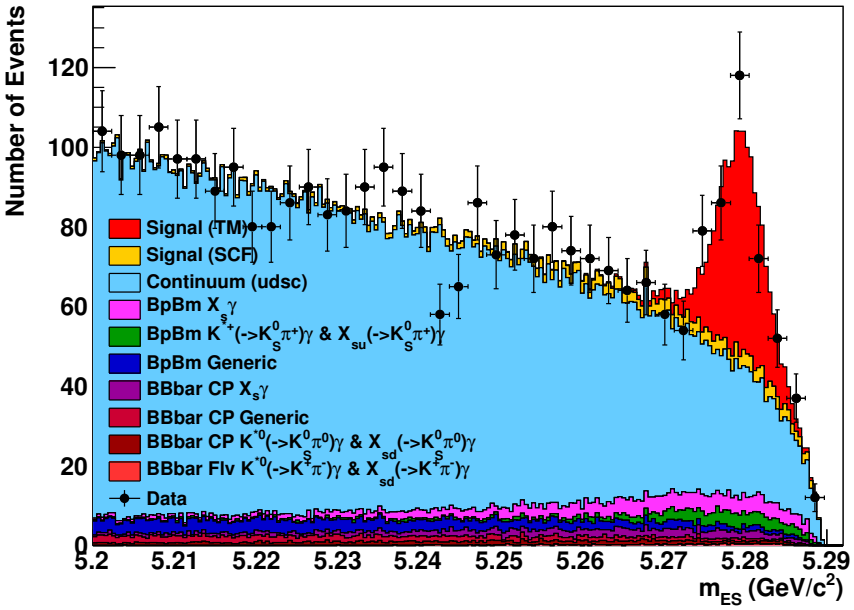

Figure 7.21: $m_{\rm ES}$ fit projection. Black points describe data events and the full colored histograms describe the contribution of each event species in the model.

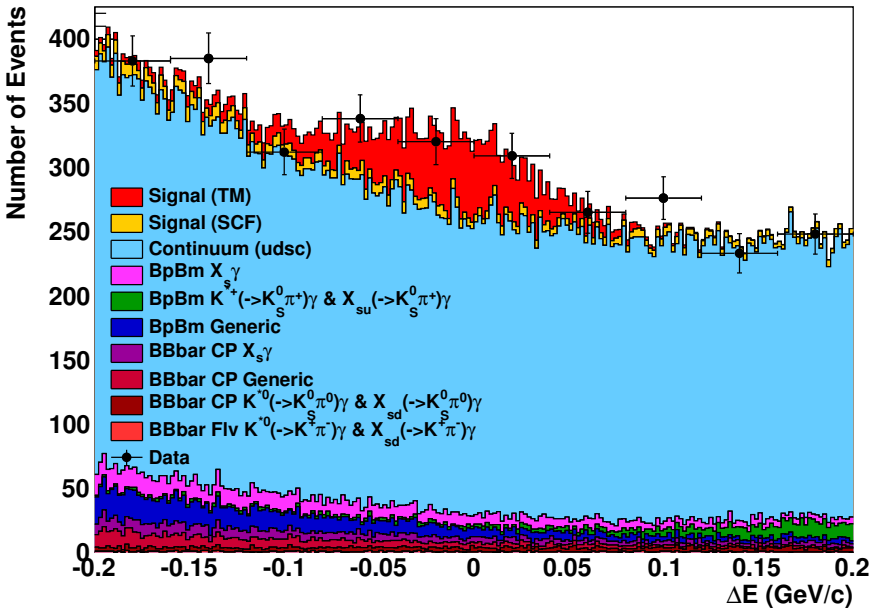

(a)

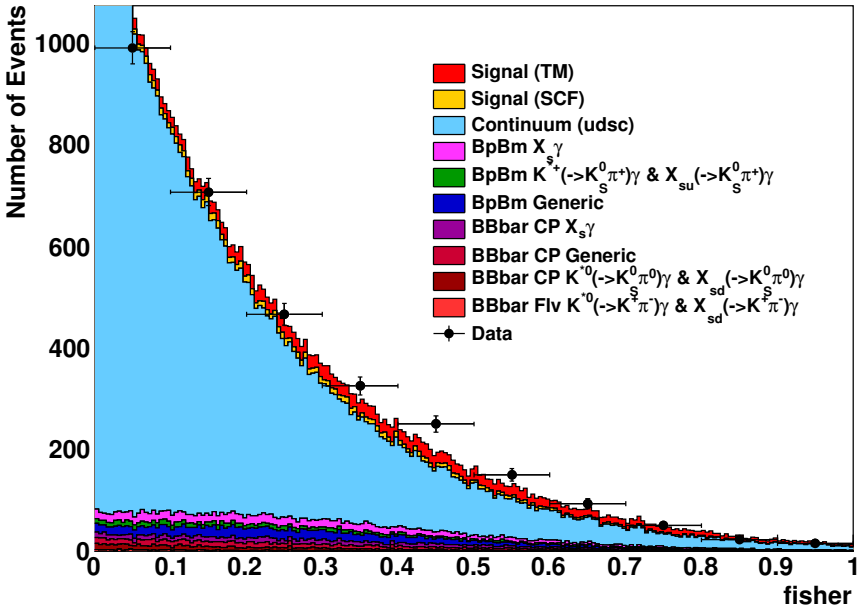

(b)

Figure 7.22: ΔE (a) and the Fisher discriminant (b) fit projections. Conventions are identical as in Fig. 7.21.

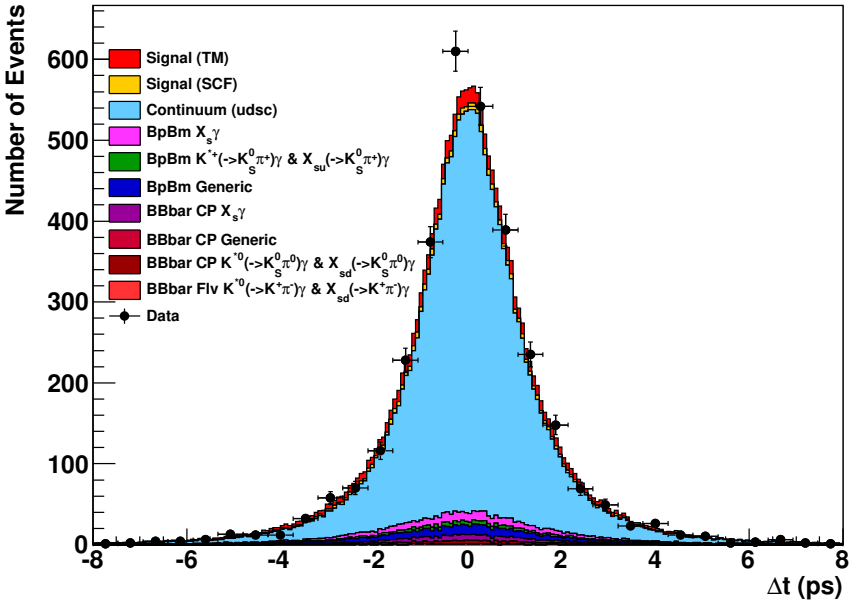

Figure 7.23: Δt fit projection. Black points describe data events and the full colored histograms describe the contribution of each event species in the model.

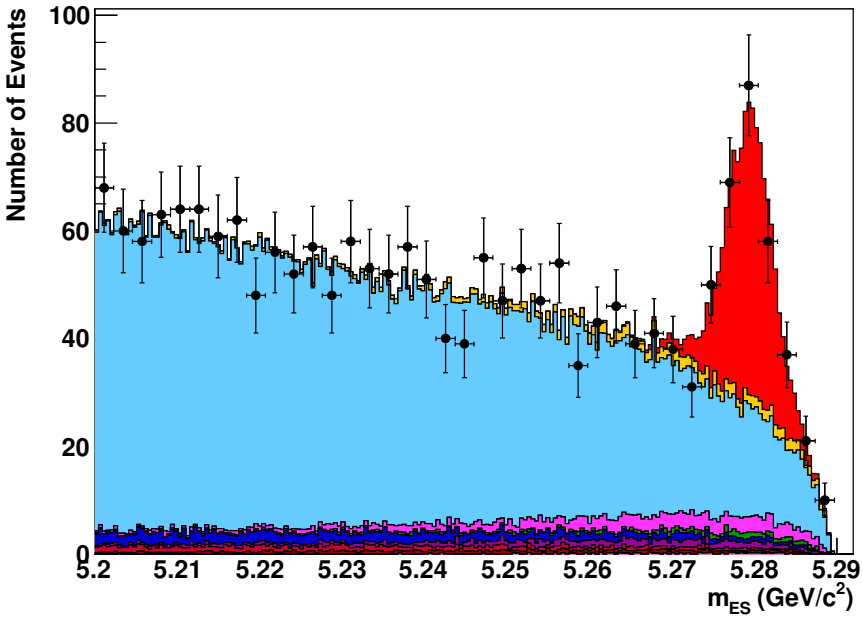

(a)

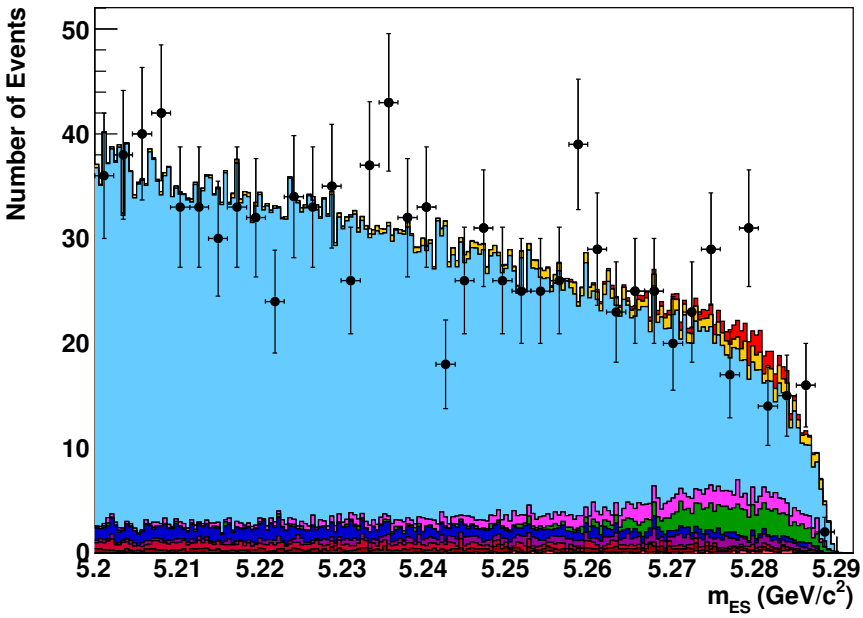

(b)

Figure 7.24: $m_{\rm ES}$ fit projections in the signal region ($-0.15 \leq \Delta E \leq 0.10\,{\rm GeV}/c$) (a) and in the background region ($\Delta E \leq -0.15\,{\rm GeV}/c$ or $\Delta E \geq 0.10\,{\rm GeV}/c$) (b). Conventions are identical as in Fig. 7.21.

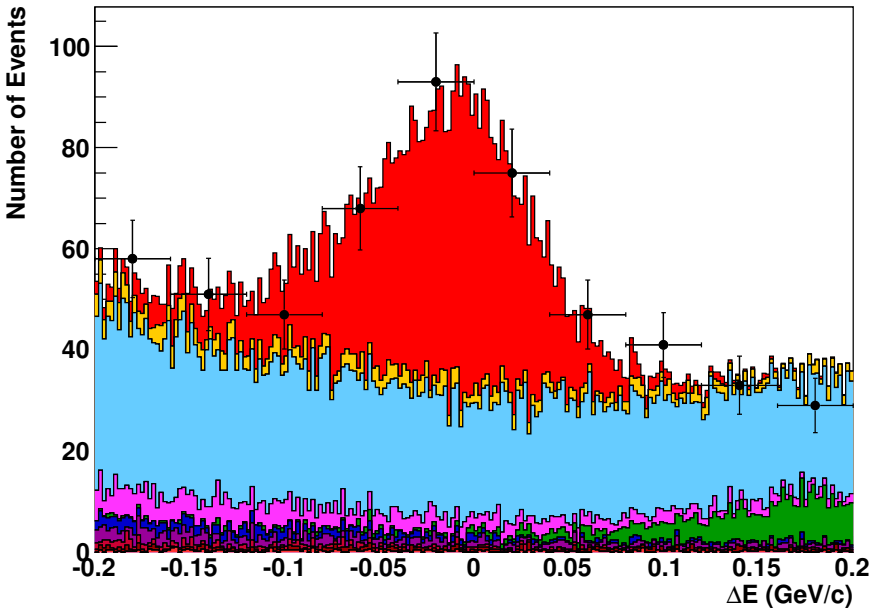

(a)

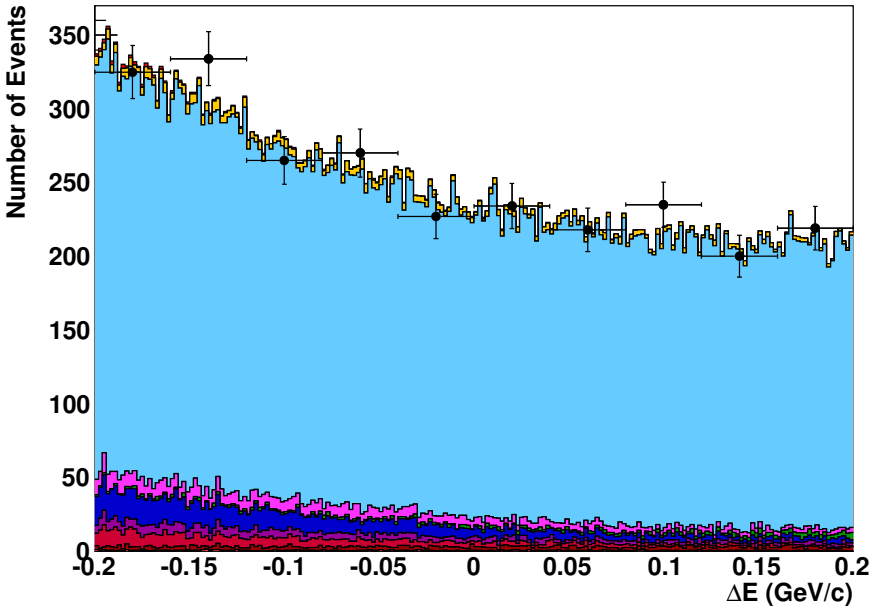

(b)

Figure 7.25: ΔE fit projections in the signal region ($m_{\rm ES} > 5.27\,{\rm GeV}/c^2$) (a) and in the background region ($m_{\rm ES} < 5.27\,{\rm GeV}/c^2$) (b). Conventions are identical as in Fig. 7.21.

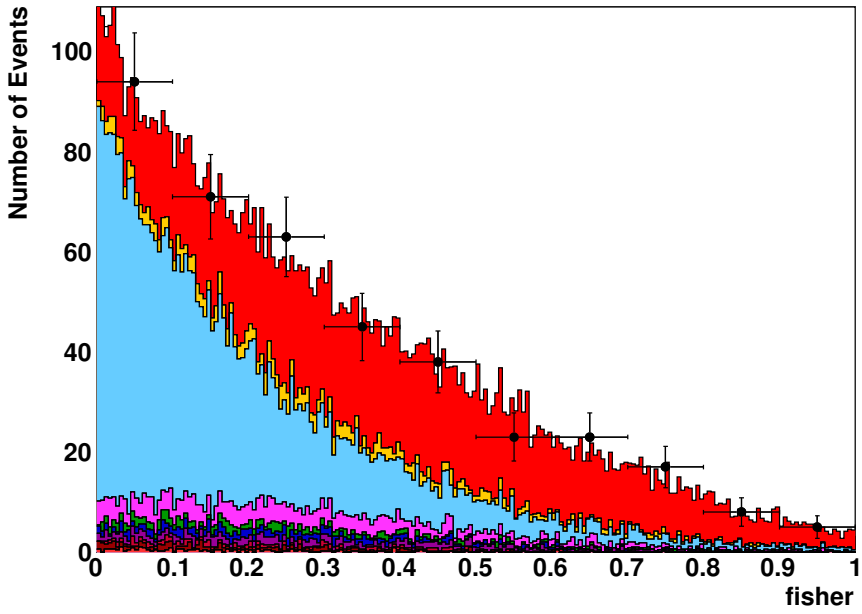

(a)

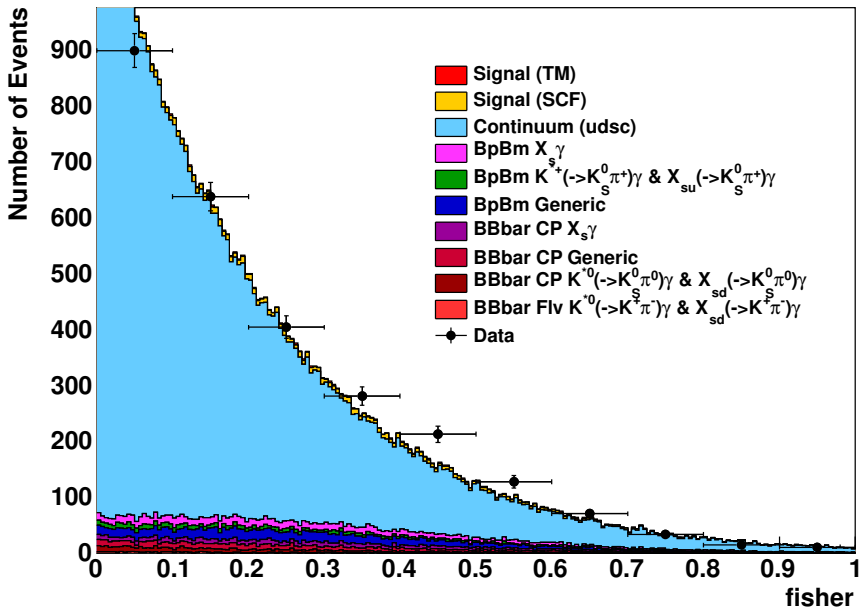

(b)

Figure 7.26: Fisher discriminant fit projections in the signal region ($m_{\rm ES} > 5.27\,{\rm GeV}/c^2$ and $-0.15 \leq \Delta E \leq 0.10\,{\rm GeV}/c$) (a) and in the background region ($m_{\rm ES} < 5.27\,{\rm GeV}/c^2$ and $\Delta E \leq -0.15$ or $\Delta E \geq 0.10\,{\rm GeV}/c$) (b). Conventions are identical as in Fig. 7.21.

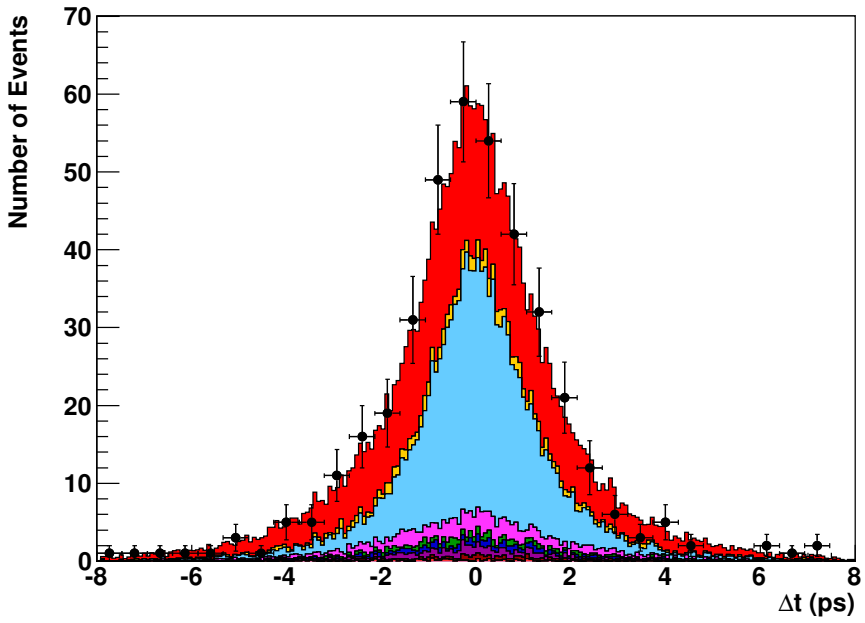

(a)

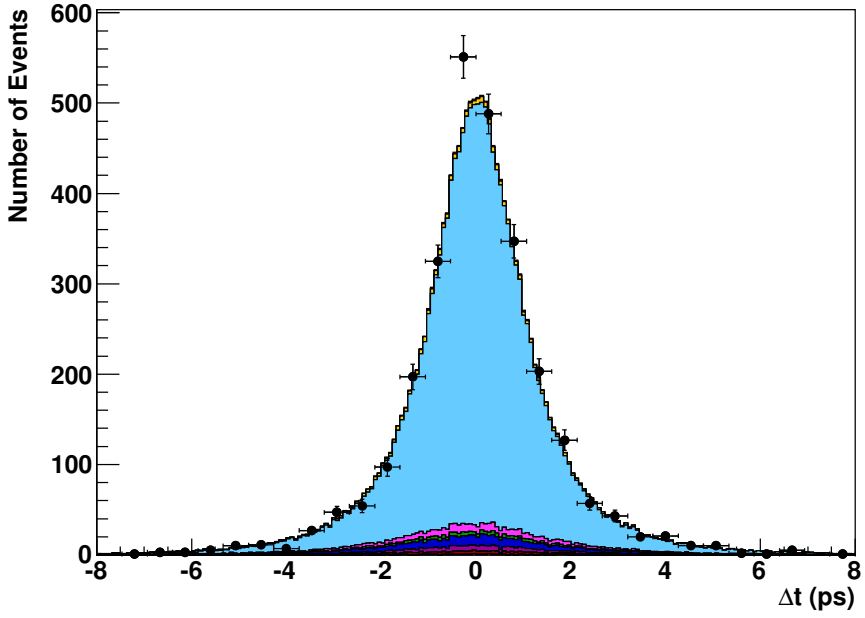

(b)

Figure 7.27: Δt fit projections in the signal region ($m_{\rm ES} > 5.27\,{\rm GeV}/c^2$ and $-0.15 \leq \Delta E \leq 0.10\,{\rm GeV}/c$) (a) and in the background region ($m_{\rm ES} < 5.27\,{\rm GeV}/c^2$ and $\Delta E \leq -0.15$ or $\Delta E \geq 0.10\,{\rm GeV}/c$) (b). Conventions are identical as in Fig. 7.21.

7.6.6.2 Extraction of the *CP* asymmetry parameters

The result of the fit to data for the time-dependent *CP* violation parameters in signal events is

$$\begin{aligned} \mathcal{S}_{K^0_S\pi^+\pi^-\gamma} &= 0.137 \pm 0.249(\text{stat.})^{+0.042}_{-0.033}(\text{syst.}) \ , \\ \mathcal{C}_{K^0_S\pi^+\pi^-\gamma} &= -0.390 \pm 0.204(\text{stat.})^{+0.045}_{-0.050}(\text{syst.}) \ , \end{aligned}$$

where the first quoted uncertainties are statistical and the second are systematic. Details on the procedure to extract the latter are given in Sec. 7.7.

In order to obtain the value of $\mathcal{S}_{K^0_S\rho\gamma}$, we divide $\mathcal{S}_{K^0_S\pi^+\pi^-\gamma}$ by the dilution factor given in Sec. 6.8.2, which gives:

$$\mathcal{S}_{K^0_S\rho\gamma} = 0.249 \pm 0.455(\text{stat.})^{+0.076}_{-0.060}(\text{syst.}) \ . \tag{7.20}$$

7.6.6.3 Comparison with the Belle results

The results we obtain for the time-dependent *CP* violation parameters directly from the fit are compatible with the ones Belle previously published [3]:

$$\begin{aligned} \mathcal{S}^{\text{Belle}}_{K^0_S\pi^+\pi^-\gamma} &= 0.09 \pm 0.27(\text{stat.})^{+0.04}_{-0.07}(\text{syst.}) \ , \\ \mathcal{C}^{\text{Belle}}_{K^0_S\pi^+\pi^-\gamma} &= -0.05 \pm 0.18(\text{stat.}) \pm 0.06(\text{syst.}) \ . \end{aligned}$$

However, some noticeable differences appear in the computation of the dilution factor. Indeed, in the expression of the amplitudes contributing to the $B^0 \to K^0_S\pi^+\pi^-\gamma$ decay amplitude (see Eq. 6.31), the signs of the *CP* eigenvalues ξ_i for $K\rho$ and $K^*\pi$ are different between the Belle analysis and the present one[1] [121]:

$$\begin{aligned} (\xi_1,\xi_2,\xi_3,\xi_4)_{(K\rho),(K^*\pi)} &= (+,-,+,-) \quad \text{in the present analysis,} \\ (\xi_1,\xi_2,\xi_3,\xi_4)_{(K\rho),(K^*\pi)} &= (-,+,+.-) \quad \text{in Belle's analysis.} \end{aligned}$$

As a consequence, the expression for the time-dependent *CP* asymmetry for $B^0 \to K^0_S\pi^+\pi^-\gamma$ decays given in Eq. 6.38 is modified, and the term related to $\cos(\Delta \text{M}t)$ does not appear when using Belle's definition for ξ_i. Note that in the present case, this have no impact on the expression of the dilution factor, since it is defined as the ratio between the $\sin(\Delta \text{M}t)$ terms in $A_{CP}^{K^0_S\pi^+\pi^-\gamma}(t)$ and $A_{CP}^{K^0_S\rho\gamma}(t)$.

Another difference with Belle is the fact that in the present analysis we account for the presence of a $(K\pi)$ S-wave component in the nominal expression of the dilution factor, whereas in the Belle paper, the $(K\pi)$ S-wave component is only taken into account for the estimation of systematic uncertainties on the value of the dilution factor. In addition, the

[1] Note that the signs of ξ_i for the $(K\pi)\pi$ S-wave component in Ref. [50] are different from the ones used here and by Belle: $(\xi_1,\xi_2,\xi_3,\xi_4)_{(K\pi)_{\text{S-wave}}} = (-,-,+.+)$. This results in a different expression of the dilution factor for $\mathcal{S}$.

($K\pi$) S-wave parametrization differ between the two analyses: Belle uses a the $K^{*0}(1430)$ resonance, while in the present analysis, the use a LASS parametrization consisting of a non resonant part and a resonant part that describes the $K^{*0}(1430)$.

When looking at the results obtained from the fit to the charged $B^+ \to K^+\pi^-\pi^+\gamma$ mode, it appears that the contribution of the interference term between the $K\rho$ and $K^*\pi$ channels are different. Indeed, in the present analysis, the interferences are found to be destructive, while in the Belle paper they are constructive. The value of the dilution factor, and thus the final value and errors on $\mathcal{S}_{K^0_S\rho\gamma}$ strongly depend on this term. From the dilution factor expression (Eq. 6.39), one can easily see that a negative interference term decreases the value of the dilution factor. This explains why in the present analysis we veto the K^*, while Belle does not[2].

However, the result on $\mathcal{S}_{K^0_S\rho\gamma}$ obtained in the present analysis is compatible with the one reported by Belle [3]:

$$\mathcal{S}^{\rm Belle}_{K^0_S\rho\gamma} = 0.11 \pm 0.33({\rm stat.})^{+0.05}_{-0.09}({\rm syst.}) \ . \tag{7.21}$$

[2]Since the intensity of the interference is proportional to the amount of K^* and ρ, a veto on the K^* significantly decreases the contribution of the interference term.

7.7 Time-dependent analysis systematics

The aim of the neutral channel analysis is to extract the values of the time-dependent *CP*-asymmetry parameters from a fit to $m_{\rm ES}$, ΔE, the Fisher discriminant and Δt. In order to assign systematic uncertainties due to the fixed parameters in the fit, we vary each of the fixed parameters within its uncertainties, which are taken from different sources that are detailed below, and redo the fit. The fixed shape parameters of $m_{\rm ES}$, ΔE and the Fisher discriminant PDFs are varied according to the errors obtained in the fit to the MC samples from which they are extracted. Since the $m_{\rm ES}$-ΔE distribution of $B^+ \to K^{*+}(\to K^0_S\pi^+)\gamma$ + $B^+ \to X_{su}(\to K^0_S\pi^+)\gamma$ background events is described by a two-dimensional histogram, we use several histograms with fluctuated bin contents. The fixed yields are varied according to the corresponding branching fraction uncertainties taken from [24]. For the categories describing a sum of modes, the fraction of each mode is varied according to the relative branching fraction uncertainties taken from [24]. The SCF fractions are varied according to the uncertainties due to MC statistics[3] and the total signal branching fraction uncertainties in Ref. [24] are also taken into account. The fixed yields of $B^0\overline{B}^0$ and B^+B^- generic B backgrounds, describing a sum of several small contributions from various B-background modes, are varied according to the uncertainties due to MC statistics. The fixed parameters of the Δt PDFs are varied according to the errors that are either taken from other *BABAR* measurements or extracted from individual fits to MC. The parameters of the Δt PDFs, as well as their corresponding uncertainties, are given in Secs. 7.1 and 7.6.4.

Assuming no correlations between the fixed parameters, we sum up in quadrature each of the lower and upper deviations from the nominal value of each of the time-dependent *CP*-asymmetry parameters, and take the resulting values as minus- and plus-signed uncertainties, respectively. The corresponding values are given in Tab. 7.32. Note that these uncertainties are small compared to the statistical uncertainties.

Table 7.32: Systematic uncertainties on the time-dependent *CP*-asymmetry parameters due to the fixed parameters in the fit to $m_{\rm ES}$, ΔE, the Fisher discriminant and Δt.

Parameter	+ signed deviation	− signed deviation
$\mathcal{S}_{K^0_S\pi^+\pi^-\gamma}$	0.042	0.033
$\mathcal{C}_{K^0_S\pi^+\pi^-\gamma}$	0.045	0.050

[3] All the uncertainties due to MC statistics are scaled to the size of the expected data sample.

Summary, conclusion and perspectives

We have measured the time-dependent *CP* asymmetry in the decay $B^0 \to K^0_S\pi^+\pi^-\gamma$, with the full *BABAR* dataset of 470.9 million $B\overline{B}$ pairs (429.0 fb^{-1}) at the $\Upsilon(4S)$, using events with $m_{K\pi\pi} < 1.8\,\mathrm{GeV}/c^2$, $0.6 < m_{\pi\pi} < 0.9\,\mathrm{GeV}/c^2$ and with $m_{K\pi} < 0.845\,\mathrm{GeV}/c^2$ and $m_{K\pi} > 0.945\,\mathrm{GeV}/c^2$. We obtain the *CP*-violating parameters $\mathcal{S}_{K^0_S\pi^+\pi^-\gamma} = 0.137 \pm 0.249^{+0.042}_{-0.033}$ and $\mathcal{C}_{K^0_S\pi^+\pi^-\gamma} = -0.390 \pm 0.204^{+0.045}_{-0.050}$, where the first quoted errors are statistical and the second are systematic. To probe the photon polarization in the underlying $b \to s\gamma$ transition, the time-dependent *CP* asymmetry related to the hadronic *CP* eigenstate $\rho^0 K^0_S$ in the final state needs to be extracted. Given that the sample size is not sufficient to perform an angular- or an amplitude-analysis of $B^0 \to K^0_S\pi^+\pi^-\gamma$ decays, we extract resonant amplitudes in the mode $B^+ \to K^+\pi^+\pi^-\gamma$, and, assuming isospin symmetry, use them to compute a dilution factor $\mathcal{D}_{K^0_S\rho\gamma}$ such that $\mathcal{S}_{K^0_S\rho\gamma} = \mathcal{S}_{K^0_S\pi^+\pi^-\gamma}/\mathcal{D}_{K^0_S\rho\gamma}$. We measure

$$\mathcal{D}_{K^0_S\rho\gamma} = 0.549^{+0.096}_{-0.094}\ ,$$

which yields

$$\mathcal{S}_{K^0_S\rho\gamma} = 0.249 \pm 0.455^{+0.076}_{-0.060}\ .$$

The quoted errors on $\mathcal{D}_{K^0_S\rho\gamma}$ account for both statistical and systematic uncertainties, while the first quoted errors on $\mathcal{S}_{K^0_S\rho\gamma}$ are statistical and the second are systematic. These results are consistent with those from Belle [3], and with the standard model expectation of $\mathcal{S} \approx 0.03, \mathcal{C} \approx 0$ [53]. It is also consistent with the similar measurements in $B^0 \to K^0_S\pi^0\gamma$ decays from *BABAR* [4] and Belle [5].

The measurement of amplitudes in $B^+ \to K^+\pi^+\pi^-\gamma$ decays provides several observables of interest, beyond the purpose of extracting the dilution factor. We have measured the fractions of the different $K_{\mathrm{res}} \to K\pi\pi$ states, and found[4]:

$$\begin{aligned}
\mathrm{FF}_{K_1(1270)^+} &= 0.61^{+0.09}_{-0.07}\ ; & \epsilon_{\mathrm{rel.}} &= 1.000\ ,\\
\mathrm{FF}_{K_1(1400)^+} &= 0.17^{+0.10}_{-0.06}\ ; & \epsilon_{\mathrm{rel.}} &= 0.991 \pm 0.007\ ,\\
\mathrm{FF}_{K^*(1410)^+} &= 0.37^{+0.10}_{-0.07}\ ; & \epsilon_{\mathrm{rel.}} &= 0.904 \pm 0.007\ ,\\
\mathrm{FF}_{K^*_2(1340)^+} &= 0.06^{+0.05}_{-0.06}\ ; & \epsilon_{\mathrm{rel.}} &= 0.982 \pm 0.008\ ,\\
\mathrm{FF}_{K^*(1680)^+} &= 0.43^{+0.10}_{-0.07}\ ; & \epsilon_{\mathrm{rel.}} &= 0.599 \pm 0.009\ ,
\end{aligned}$$

with $\epsilon_{\mathrm{rel.}}$ the relative efficiencies with respect to that of $K_1(1270)^+$. The quoted errors on the fit fractions account for both statistical and systematic uncertainties. In addition, the

[4] Before the publication of this work, it is planned to extract from these observables the branching fractions.

overall fractions of the $\rho^0 K^+$, $K^{*0}\pi^+$ and $(K\pi)_{\mathrm{S-wave}}\pi^+$ components are measured to be:

$$\begin{aligned} \mathrm{FF}_{\rho^0 K^+} &= 0.335^{+0.036}_{-0.035}\ , \\ \mathrm{FF}_{K^{*0}\pi^+} &= 0.636^{+0.020}_{-0.015}\ , \\ \mathrm{FF}_{(K\pi)_{\mathrm{S-wave}}\pi^+} &= 0.416^{+0.068}_{-0.083}\ , \end{aligned}$$

where the quoted errors account for both statistical and systematic uncertainties.

The measurement of the time-dependent *CP* asymmetry in $B^0 \to K^0_S\pi^0\gamma$ and $B^0 \to K^0_S\rho^0\gamma$ decays is at reach of e^+e^- *B* Factories rather than hadronic colliders. The state-of-the-art of time-dependent *CP* asymmetry measurements in radiative decays after the era of *B* Factories shows an overall consistency with the standard model but the obtained precision does not allow to draw clear conclusions about possible contribution of NP processes.

However, probing the photon helicity in radiative $b \to s\gamma$ decays by other methods is one of the hot topics of LHCb. Until the end of the year 2012, the experiment has recorded roughly $3\,\mathrm{fb}^{-1}$ of data, and has already obtained several results providing information on the observable of interest. For instance, an angular analyses of $B^0 \to K^{*0}\mu^+\mu^-$ decays has been performed using $1\,\mathrm{fb}^{-1}$ of data [64, 122]. Ref. [64] presents, among other observables, a measurement of S_3 that is proportional to the ratio of processes involving left- and right-handed photons. The result is consistent with the standard model prediction. Ref. [122] presents the measurement of form-factor independent observables, and reports a tantalizing tension at the level of 3.7 standard deviations for one of these observables at a certain region of the dimuon invariant mass. Another key channels of LHCb towards a measurement of the photon polarization, this time from *CP* asymmetry observables, is the $B^0_S \to \phi\gamma$ decay. This mode is rather in the LHCb ball park, since B_s decays are generally not accessible at the *B* Factories[5]. Yet, such an analysis is challenging in LHCb due to the low tagging efficiency in hadronic colliders. A first step was recently completed through the measurement of the ratio of branching fractions $\mathcal{B}(B^0 \to K^{*0}\gamma)/\mathcal{B}(B^0_S \to \phi\gamma)$ [52, 123].

LHCb is expected to collect at least $7\,\mathrm{fb}^{-1}$ of data by the end of 2017. In addition, two major projects in flavor physics are being developed. An upgrade of the LHCb experiment is planned in 2018, and the super flavor factory Belle-II in KEK is expected to start collecting data in 2015. The LHCb upgrade consists in adapting the trigger system and the detector, to enable them to operate in a higher instantaneous luminosity. The upgraded detector will collect 5 to $10\,\mathrm{fb}^{-1}$ per year, resulting in a sample of $50\,\mathrm{fb}^{-1}$. Belle-II is a second-generation high-luminosity flavor factory, which is expected to accumulate, over a period of five-years, a sample of $50\,\mathrm{ab}^{-1}$. The analysis presented in this thesis could be much improved, possibly by means of a more sophisticated method, in Belle-II. The ensemble of future measurements in the different decay modes that are sensitive to the photon helicity will hopefully shed light on the open issues in the domain.

[5] Apart from a data sample of $124.4\,\mathrm{fb}^{-1}$ collected at the $\Upsilon(5S)$ by Belle.

Appendix A

Probability Density Function Definitions

In this section, we give the definitions of PDFs used in the fit.

A.1 Gaussian function

The expression for the standard Gaussian function is given below.

$$\mathrm{G}(x;\mu,\sigma) = \frac{1}{a}\exp\left[\frac{1}{2}\left(\frac{x-\mu}{\sigma}\right)^2\right]$$

The parameters μ and σ are the mean and the width of the Gaussian; $1/a$ is a normalization constant.

A.2 Bifurcated Gaussian function

The expression for the standard Bifurcated Gaussian function is given below.

$$\mathrm{BG}(x;\mu,\sigma_l,\sigma_r) = \frac{1}{a}\exp\left[\frac{1}{2}\left(\frac{x-\mu}{\sigma_i}\right)^2\right]\begin{cases} i=l & (x-\mu)<0 \\ i=r & (x-\mu)>0 \end{cases}$$

The parameters μ and σ_i describe a Gaussian; $1/a$ is a normalization constant.

A.3 Cruijff function

The expression for the standard Cruijff function is given below.

$$\mathrm{Cruijff}(x;\mu,\sigma_l,\sigma_r,\alpha_l,\alpha_l) = \frac{1}{a}\exp\left[-\frac{(x-\mu)^2}{2\sigma_i^2+\alpha_i(x-\mu)^2}\right]\begin{cases} i=l & (x-\mu)<0 \\ i=r & (x-\mu)>0 \end{cases}$$

The parameters μ and σ_i describe a Gaussian, while the α_i parameters describe the curvature of the slope; $1/a$ is a normalization constant.

A.4 Crystal Ball function

The expression for the standard Crystal Ball function is given below.

$$\mathrm{CB}(x;\mu,\sigma,\alpha,n) = \frac{1}{a}\begin{cases} \left(\frac{n}{\alpha}\right)^n \frac{\exp(-\alpha^2/2)}{((\mu-x)/\sigma+n/\alpha-\alpha)^n} & x \leq \mu-\alpha\sigma \\ \exp\left[\frac{1}{2}\left(\frac{x-\mu}{\sigma}\right)^2\right] & x > \mu-\alpha\sigma \end{cases}$$

The parameters μ and σ describe a Gaussian, which is truncated on the low side at $\mu-\alpha\sigma$ and joined continuously to a power function with an exponent n; $1/a$ is a normalization constant.

A.5 Argus function

The Argus function [124], is given by

$$\mathrm{Argus}(x;\xi,E_b) = \frac{1}{a}x\sqrt{1-x^2/E_b^2}\,e^{-\xi\sqrt{1-x^2/E_b^2}}$$

The parameter ξ is the Argus shape parameter, the cutoff E_b is at the nominal beam energy, and $1/a$ is a normalization constant.

A.6 Exponential function

The Exponential function, is given by

$$\mathrm{Ex}(x;s) = \frac{1}{a}\,e^{sx}$$

$1/a$ is a normalization constant.

A.7 Linear function

The Linear function, is given by

$$\mathrm{Lin}(x) = \frac{1}{a}\,(1+c_1x)$$

$1/a$ a normalization constant.

Appendix B

Fragmentation corrective weights

Here we give the fragmentation corrective weights (as reported in [107]) applied to the different X_s decay modes in order to build the radiative B background PDFs, as described in Sec. 6.4.1.2.

The X_s events are separated in several modes depending on the particle contents of the final states. Moreover, the X_s events are splitted in four mass ranges. Tables B.1- B.4, give the applied weight for each mode, as their definition in term of final state particle content, each table for one specific X_s mass range. In this analysis, we use true MC information in order to separate the X_s events in the different modes and mass ranges.

Table B.1: The reweighing factors in mass region m_{X_s}=1.1-1.5 GeV, as reported in [107].

Modes definition	Frag. Weight Found in m_{X_s}=1.1-1.5 GeV
2 bodies without π^0	0.650 ± 0.027
2 bodies with 1 π^0	0.533 ± 0.051
3 bodies without π^0	1.195 ± 0.025
3 bodies with 1 π^0	1.701 ± 0.047
4 bodies without π^0	0.337 ± 0.079
4 bodies with 1 π^0	1.242 ± 0.125
3/4 bodies with 2 π^0s	0.563 ± 0.186
5 bodies with 0-2 π^0s	$1.000^{+1.048}_{-1.000}$
$\eta \to \gamma\gamma$	0.938 ± 0.145
3K modes	0.000 ± 0.000

Table B.2: The reweighing factors found in mass region m_{X_s}=1.5-2.0 GeV, as reported in [107].

Modes definition	Frag. Weight Found in m_{X_s}=1.5-2.0 GeV
2 bodies without π^0	0.376 ± 0.033
2 bodies with 1 π^0	0.276 ± 0.060
3 bodies without π^0	1.008 ± 0.037
3 bodies with 1 π^0	1.026 ± 0.060
4 bodies without π^0	1.339 ± 0.101
4 bodies with 1 π^0	1.156 ± 0.108
3/4 bodies with 2 π^0s	1.365 ± 0.298
5 bodies with 0-2 π^0s	0.573 ± 0.159
$\eta \to \gamma\gamma$	1.719 ± 0.200
3K modes	0.621 ± 0.109

Table B.3: The reweighing factors found in mass region m_{X_s}=2.0-2.4 GeV, as reported in [107].

Modes definition	Frag. Weight Found in m_{X_s}=2.0-2.4 GeV
2 bodies without π^0	$0.047^{+0.052}_{-0.047}$
2 bodies with 1 π^0	0.323 ± 0.119
3 bodies without π^0	0.723 ± 0.105
3 bodies with 1 π^0	0.334 ± 0.125
4 bodies without π^0	1.115 ± 0.229
4 bodies with 1 π^0	1.279 ± 0.268
3/4 bodies with 2 π^0s	0.828 ± 0.533
5 bodies with 0-2 π^0s	0.743 ± 0.284
$\eta \to \gamma\gamma$	2.470 ± 0.502
13K modes	0.744 ± 0.307

Table B.4: The reweighing factors found in mass region m_{X_s}=2.4-2.8 GeV, as reported in [107].

Modes definition	Frag. Weight Found in m_{X_s}=2.4-2.8 GeV
2 bodies without π^0	0.175 ± 0.134
2 bodies with 1 π^0	$0.145\ ^{+0.246}_{-0.145}$
3 bodies without π^0	$0.250^{+0.252}_{-0.250}$
3 bodies with 1 π^0	$1.000^{+0.465}_{-1.000}$
4 bodies without π^0	2.294 ± 0.740
4 bodies with 1 π^0	$0.102^{+0.387}_{-0.102}$
3/4 bodies with 2 π^0s	2.064 ± 1.643
5 bodies with 0-2 π^0s	$0.294^{+1.270}_{-0.294}$
$\eta \to \gamma\gamma$	$1.085^{+1.033}_{-1.085}$
3K modes	$0.825^{+1.107}_{-0.825}$

Appendix C

Kaonic resonances distortion

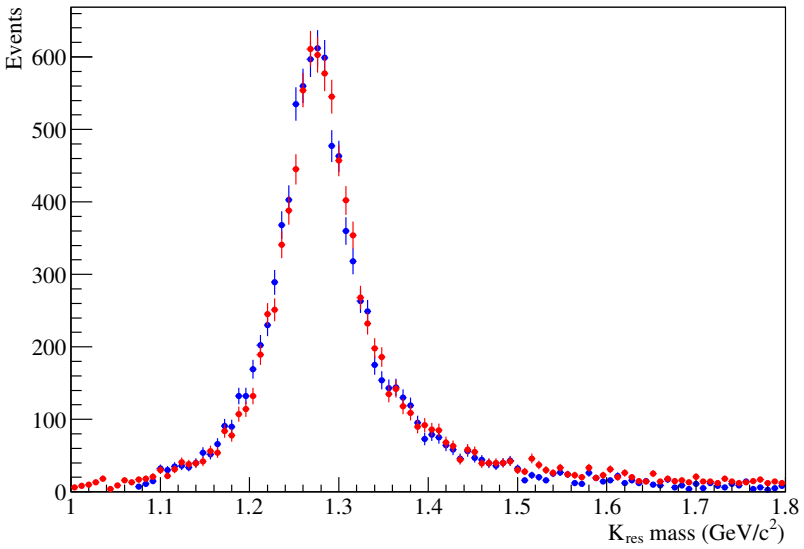

Figure C.1: Compared $K_1(1270)$ distributions generated from `EvtGen` (blue points) and the RBW expression (red points).

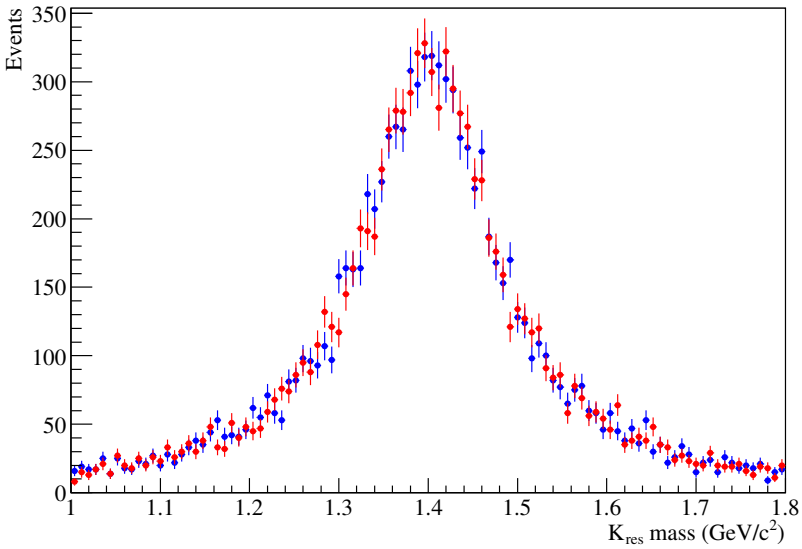

Figure C.2: Compared $K_1(1400)$ distributions generated from `EvtGen` (blue points) and the RBW expression (red points).

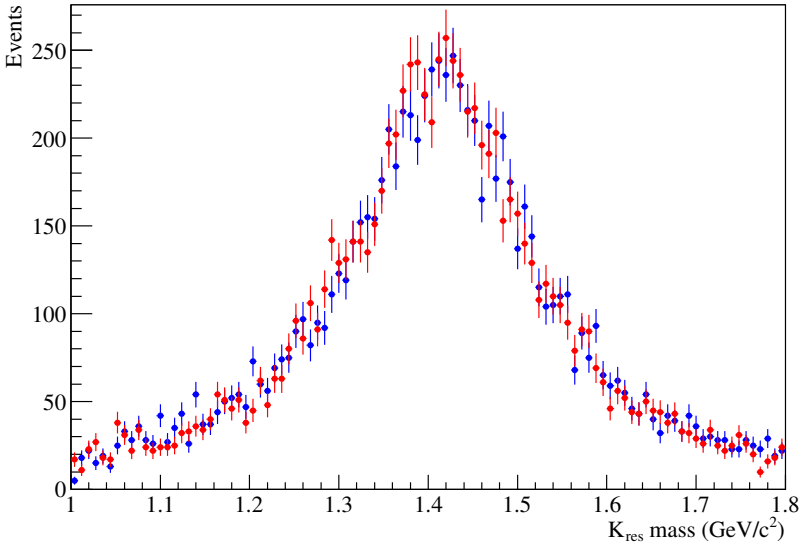

Figure C.3: Compared $K^*(1410)$ distributions generated from `EvtGen` (blue points) and the RBW expression (red points).

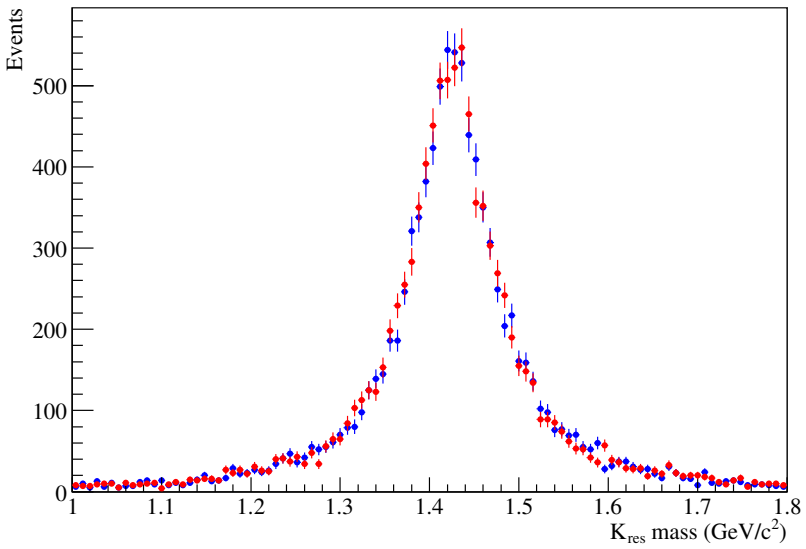

Figure C.4: Compared $K_2^*(1430)$ distributions generated from `EvtGen` (blue points) and the RBW expression (red points).

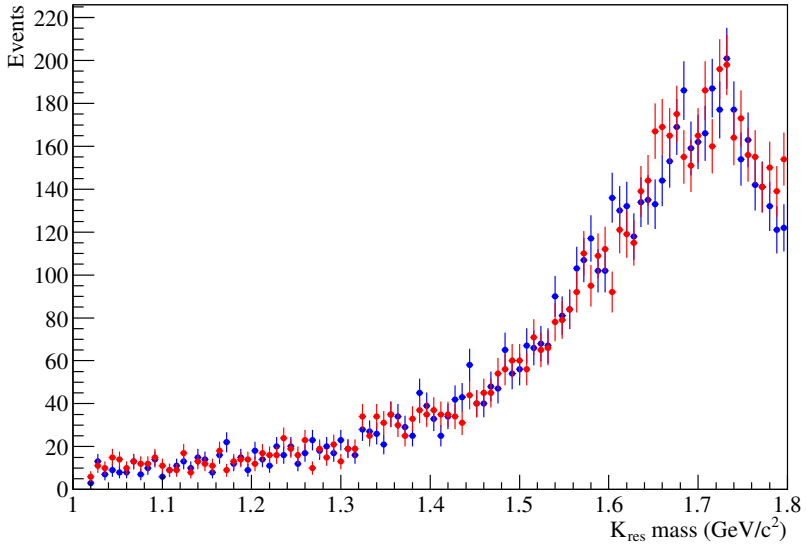

Figure C.5: Compared $K^*(1680)$ distributions generated from `EvtGen` (blue points) and the RBW expression (red points).

Appendix D

Parametrization of TM m_{ES}-ΔE correlations

Here we present the results of the signal-TM m_{ES}-ΔE correlations study.

D.1 Study of ΔE Cruijff parameters dependence in m_{ES} bins

$B^+ \to K^+\pi^-\pi^+\gamma$ signal-TM case

The study of ΔE Cruijff parameters dependence in m_{ES} study was done using a set of ten bins in m_{ES} as listed in Tab. D.1.

Table D.1: ΔE bins definition for the m_{ES} Crystal Ball parameters dependence in ΔE.

m_{ES} bin number	m_{ES} range (GeV/c^2)
0	[5.200 ; 5.270[
1	[5.270 ; 5.272[
2	[5.272 ; 5.274[
3	[5.274 ; 5.275[
4	[5.275 ; 5.276[
5	[5.276 ; 5.278[
6	[5.278 ; 5.280[
7	[5.280 ; 5.282[
8	[5.282 ; 5.284[
9	[5.284 ; 5.292]

Figures D.1 to D.5 show the implicit dependence of the Cruijff parameters in m_{ES} bins. The first bin in m_{ES} (m_{ES} bin0) having a large range compared to others, we present for

each Cruijff parameter distributions two plots: the first one in the whole $m_{\rm ES}$ range, the second in a tighter region excluding the $m_{\rm ES}$ bin0.

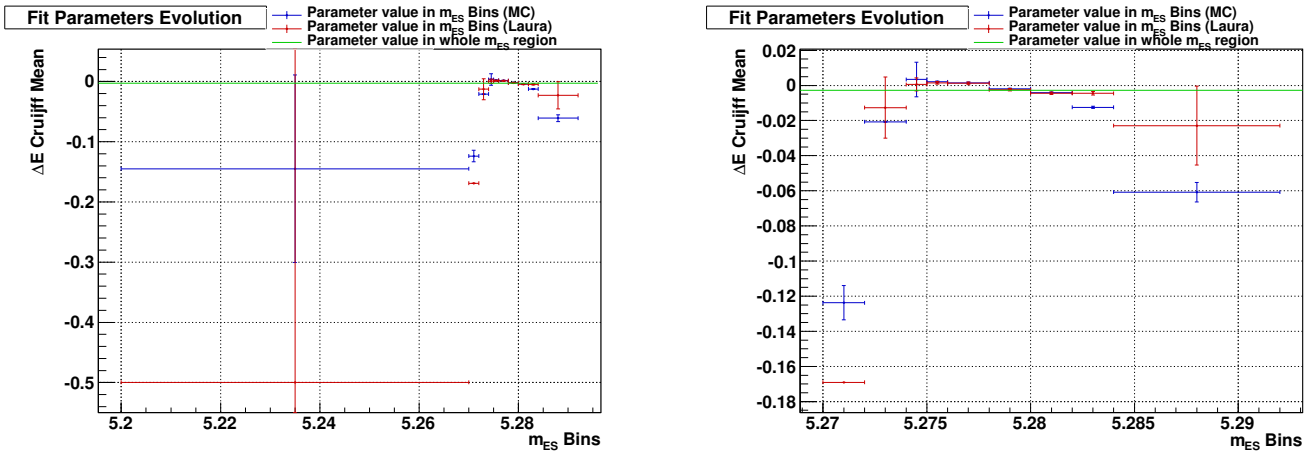

Figure D.1: ΔE Cruijff μ parameter evolution in $m_{\rm ES}$ bins, in the whole $m_{\rm ES}$ range (left) and excluding $m_{\rm ES}$ bin0 (right). Blue points correspond to MC sample, red points correspond to generated sample using our two-dimensional conditional PDF, and the green horizontal line corresponds to the uni-dimensional Cruijff initial PDF. The central value of each point corresponds to the fitted value of the Cruijff parameter, the vertical error bars correspond to the parameter fit error given by `MINUIT` and the horizontal error bars define the size of each ΔE bin.

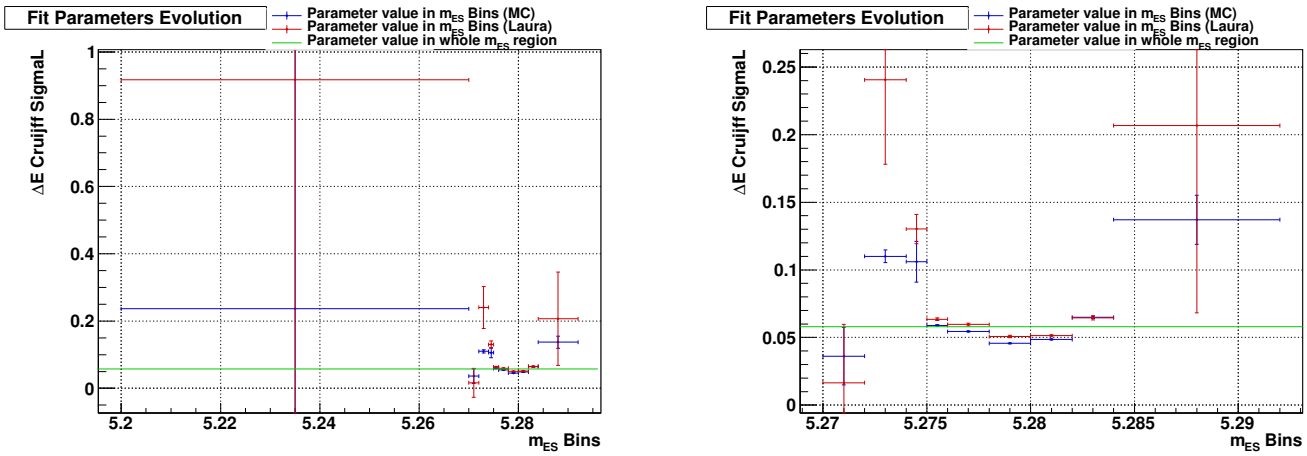

Figure D.2: ΔE Cruijff σ_l parameter evolution in $m_{\rm ES}$ bins, in the whole $m_{\rm ES}$ range (left) and excluding $m_{\rm ES}$ bin0 (right). Conventions are identical as those used in Fig. D.1.

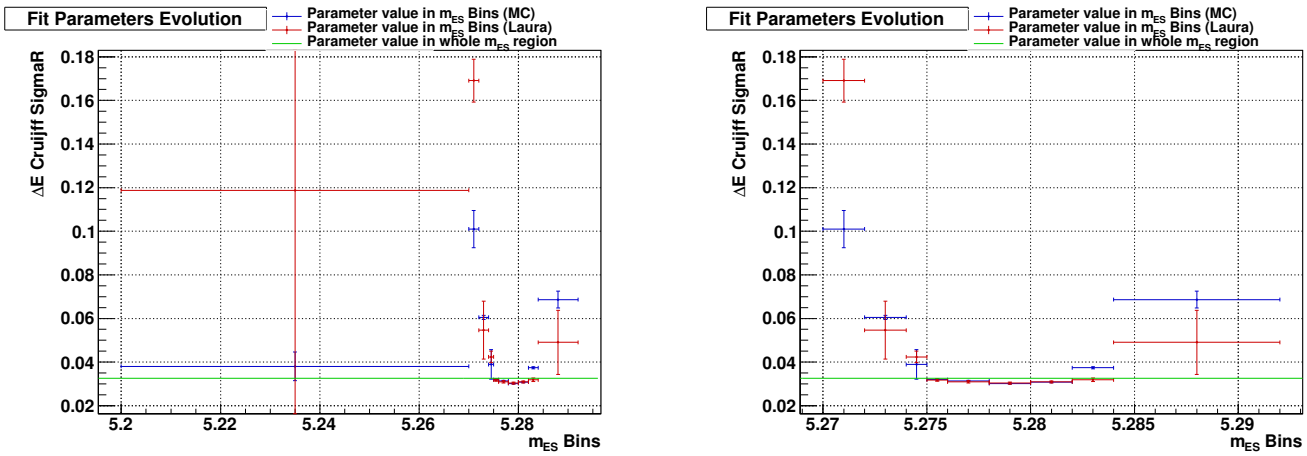

Figure D.3: ΔE Cruijff σ_r parameter evolution in $m_{\rm ES}$ bins, in the whole $m_{\rm ES}$ range (left) and excluding $m_{\rm ES}$ bin0 (right). Conventions are identical as those used in Fig. D.1.

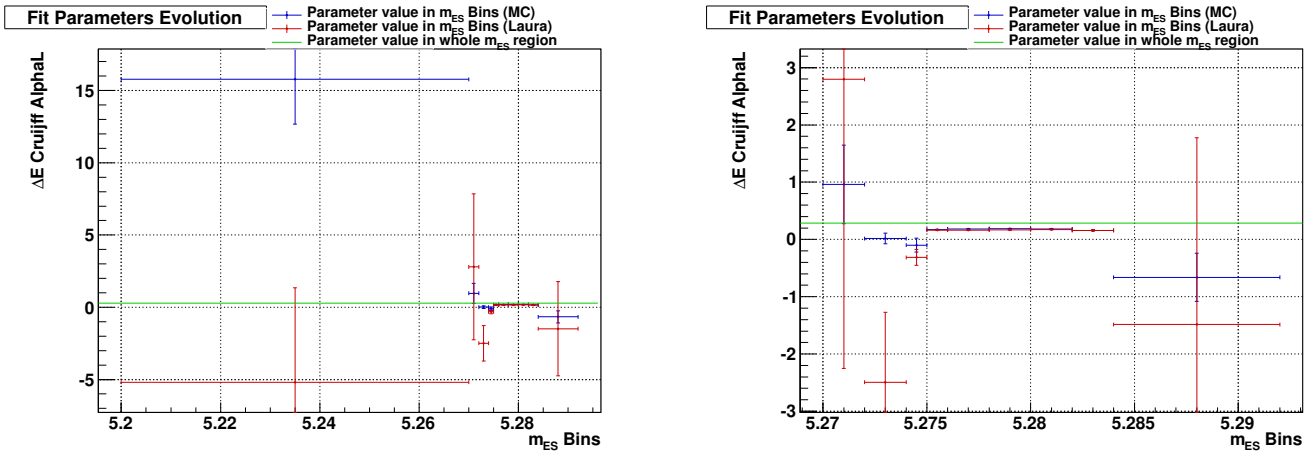

Figure D.4: ΔE Cruijff α_l parameter evolution in $m_{\rm ES}$ bins, in the whole $m_{\rm ES}$ range (left) and excluding $m_{\rm ES}$ bin0 (right). Conventions are identical as those used in Fig. D.1.

D.2 Fit projections

Here we present the study of the two-dimensional PDF implemented in Laura++. The PDF is the product of a conditional PDF (Crystal Ball for $m_{\rm ES}$) and a marginal PDF (Cruijff for ΔE), where the Crystal Ball parameters are functions of ΔE. This two-dimensional PDF is used to describe the correlations between $m_{\rm ES}$ and ΔE of signal-TM events. The aim of this study is to check the behavior of the two-dimensional PDF comparing the distributions of events taken from MC to the one generated using the PDF. Section D.2.1 presents the projections on the $m_{\rm ES}$ dimension for several bins in ΔE, defined in Tab. 6.13, while Sec. D.2.2 presents the projections on the ΔE dimension for several bins in $m_{\rm ES}$, defined in Tab. F.1. In each plot, we compare the MC-truth signal-TM distribution (blue points) to the distribution generated using the two-dimensional PDF (red points). In addition, the curves (corresponding colors), represent the fit result using the corresponding one-dimensional PDF

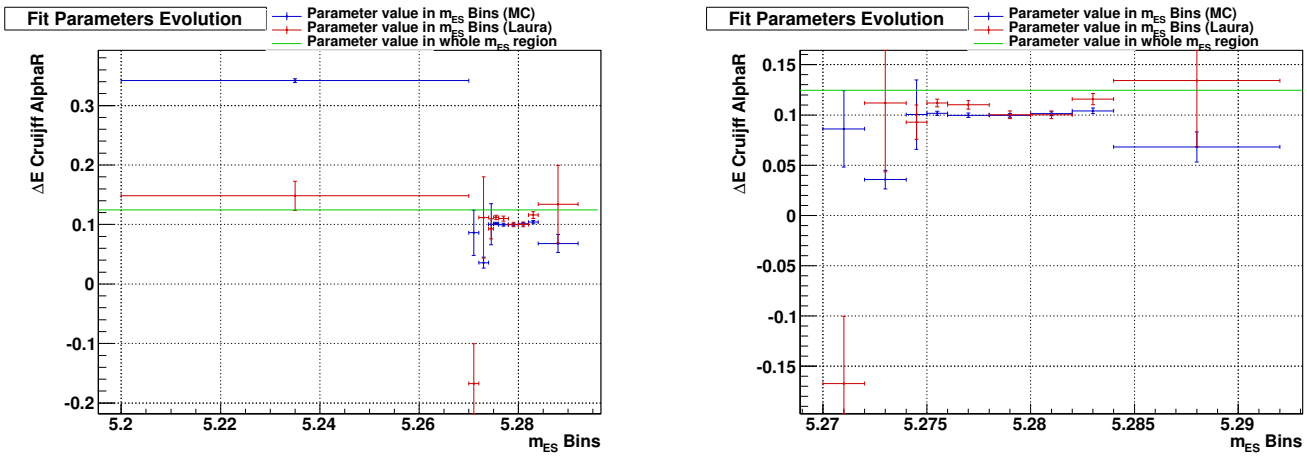

Figure D.5: ΔE Cruijff α_r parameter evolution in $m_{\rm ES}$ bins, in the whole $m_{\rm ES}$ range (left) and excluding $m_{\rm ES}$ bin0 (right). Conventions are identical as those used in Fig. D.1.

(either a Crystal Ball for $m_{\rm ES}$ or a Cruijff for ΔE).

In a few bins, significative differences appear between the MC-truth and the generated distributions. However, these differences concerns only low-statistics bins, where the parameters describing the correlations have large uncertainties. Moreover, from the embedded toy studies, no significant bias appeared corresponding these parameters. Therefore, we conclude that the two-dimensional PDF is reliable.

D.2.1 $m_{\rm ES}$ projections in ΔE bins

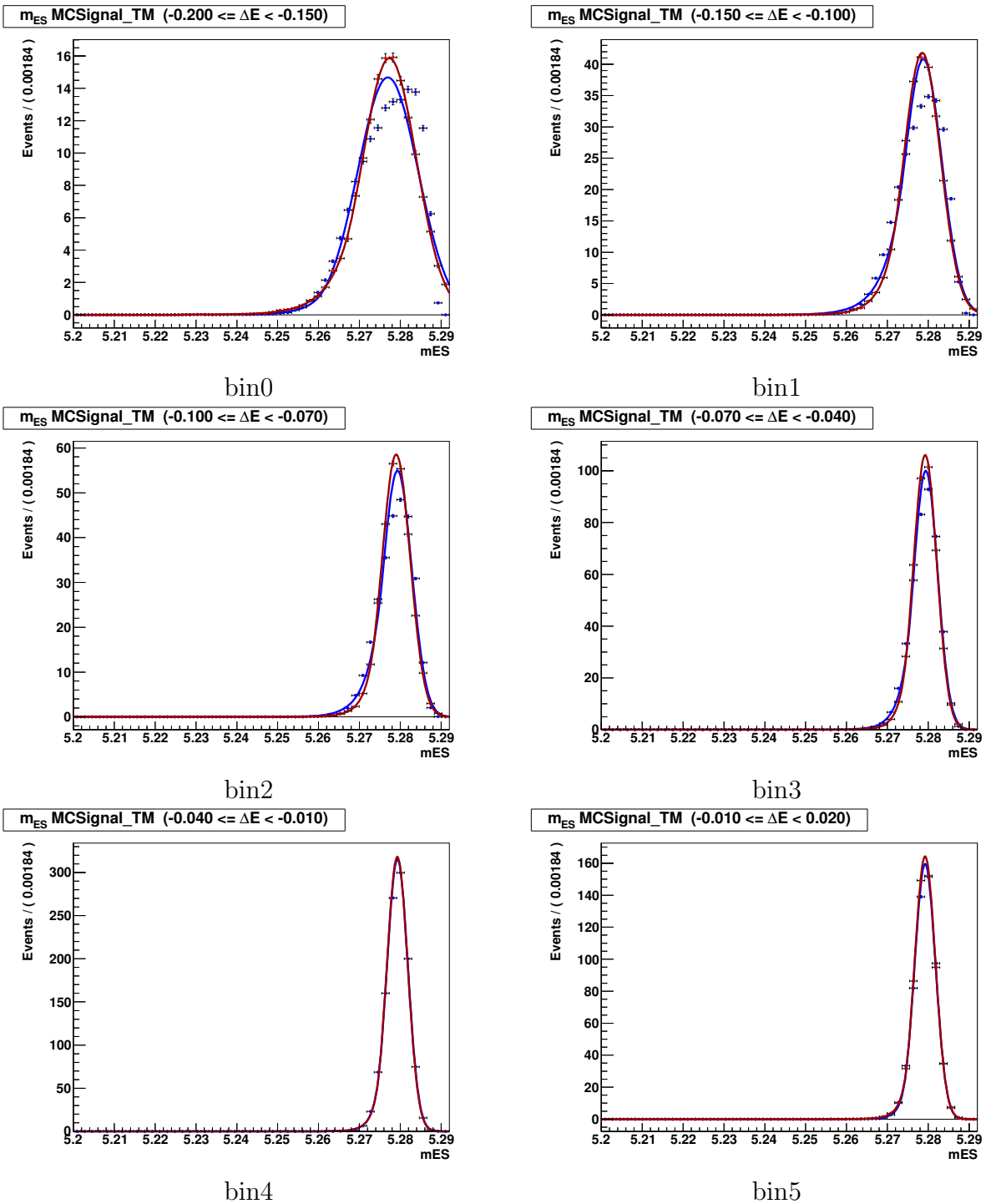

bin0 bin1 bin2 bin3 bin4 bin5

Figure D.6: $m_{\rm ES}$ Crystal Ball fit projection in ΔE bins 0 to 5. Blue curve correspond to MC sample, red curve correspond to generated sample using our two-dimensional conditional PDF.

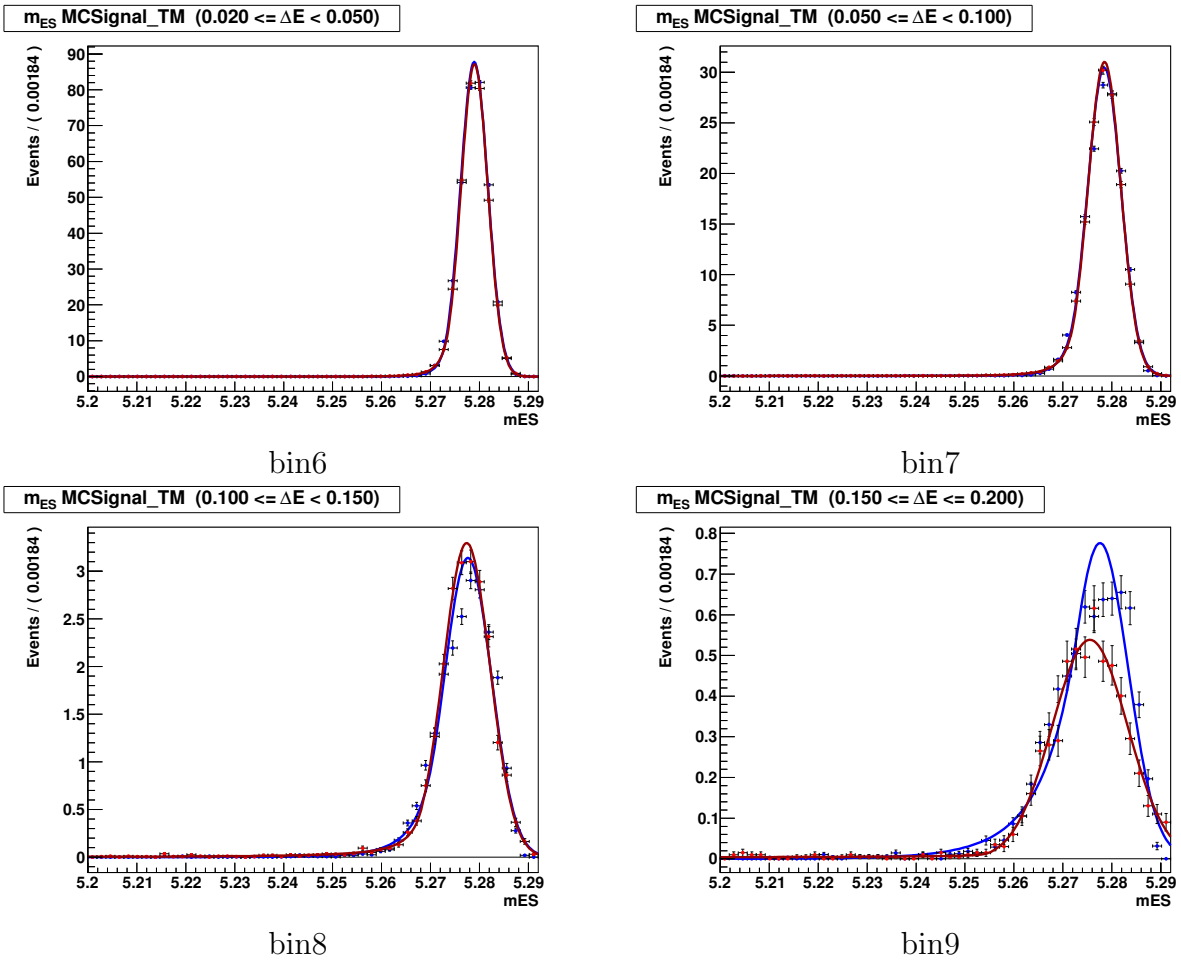

Figure D.7: m_{ES} Crystal Ball fit projection in ΔE bins 6 to 9. Blue curve correspond to MC sample, red curve correspond to generated sample using our two-dimensional conditional PDF.

D.2.2 ΔE projections in $m_{\rm ES}$ bins

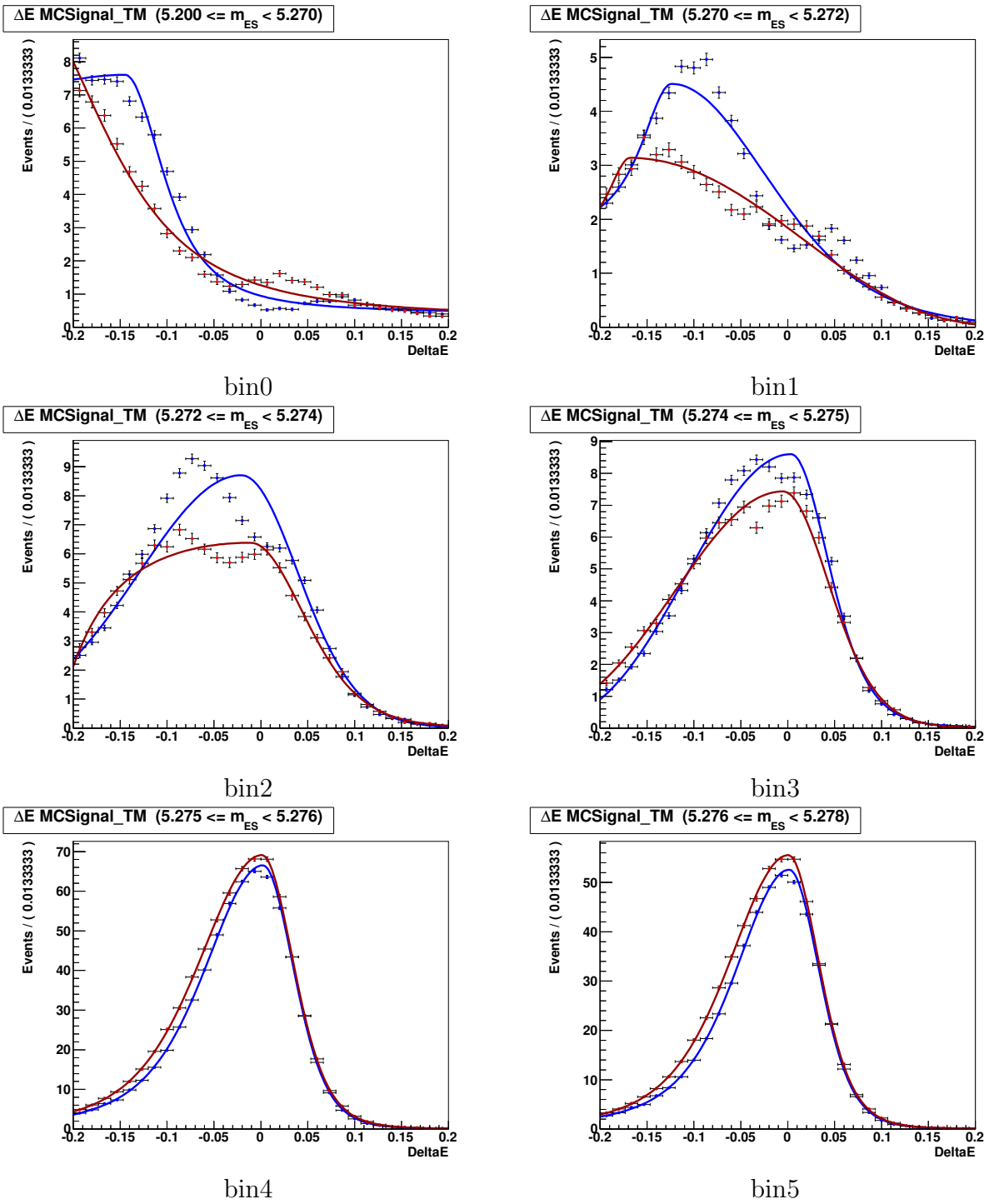

bin0 bin1 bin2 bin3 bin4 bin5

Figure D.8: ΔE Cruijff fit projection in $m_{\rm ES}$ bins 0 to 5. Blue curve correspond to MC sample, red curve correspond to generated sample using our two-dimensional conditional PDF.

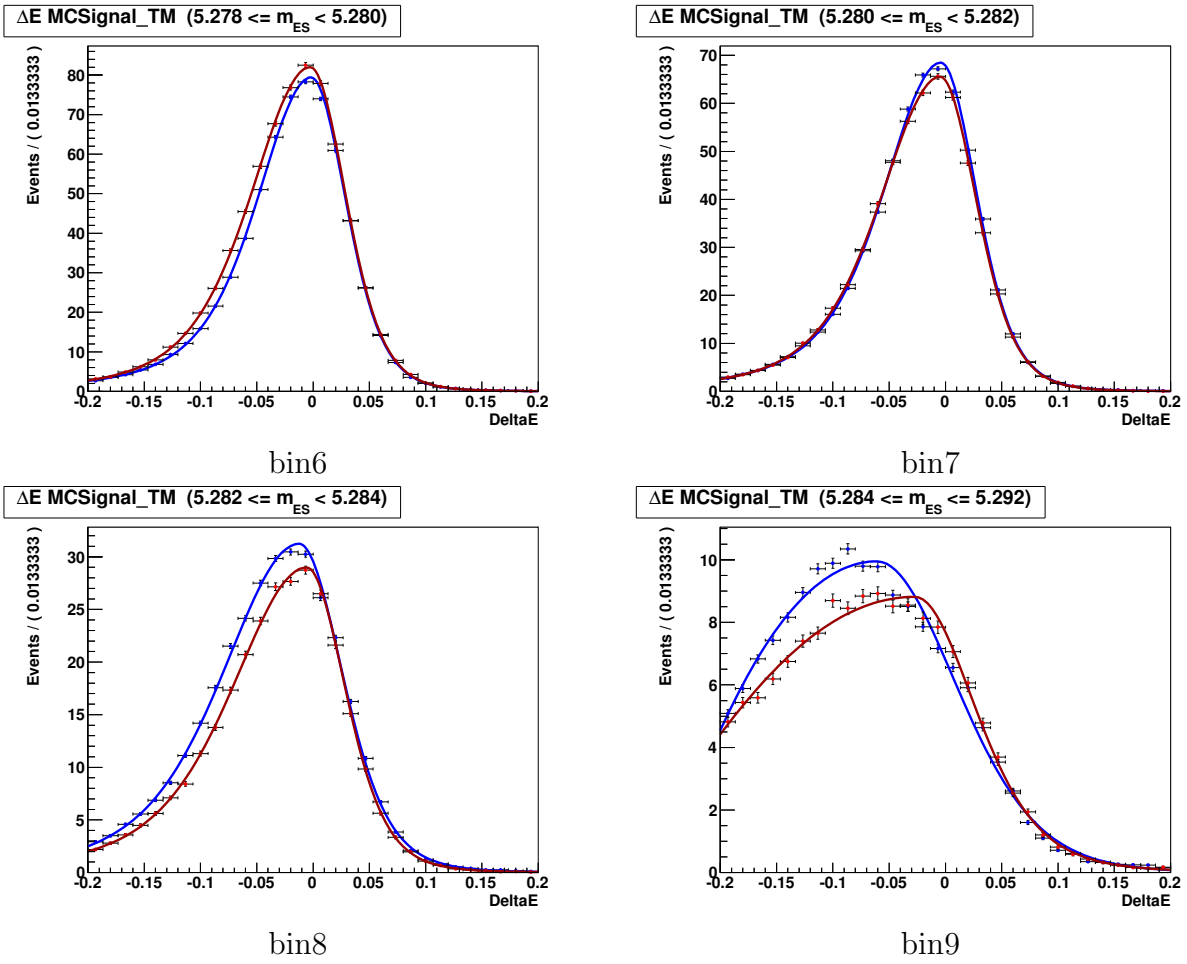

Figure D.9: ΔE Cruijff fit projection in m_{ES} bins 6 to 9. Blue curve correspond to MC sample, red curve correspond to generated sample using our two-dimensional conditional PDF.

Appendix E

Toy studies for the charged channel analysis

E.1 Self-cross-feed fraction

In this Section we present the different results that lead us to separate the SCF and signal-TM categories in our fit model. This conclusion was made after testing our model in a very simple case, with only the SCF, signal-TM and continuum *udsc* categories. We tested two configurations:

1. the SCF is described as a fraction of the signal yield;
2. the SCF is described as a separated category.

We performed pure toys studies based on 4000 toys and 2000 toys for the two configurations listed above, respectively.

From this study, we observed that the second configuration gave better results on the pulls. Figures E.1 and E.2 show the pull distributions for the SCF fraction and the SCF yield parameters for configurations (1) and (2), respectively. Figures E.3 and E.4 show the pull distributions for the total signal yield and the signal-TM yield for configurations (1) and (2), respectively.

Furthermore, we found that when describing the SCF component as a fraction of the total signal yield, significant correlations ($\rho = 0.86$) appeared between the signal yield and the SCF fraction. When using configuration (2), the correlation between the SCF fraction that became the SCF yield and the signal yield that became the signal-TM yield almost disappeared ($\rho = -0.36$). Figures E.5 and E.6 show the linear correlations between the floated parameters entering in the fit when the SCF component is described as a fraction of the total signal events or as a separated category, respectively.

From these results we decided to separate explicitly the SCF contribution from the signal TM in a different category.

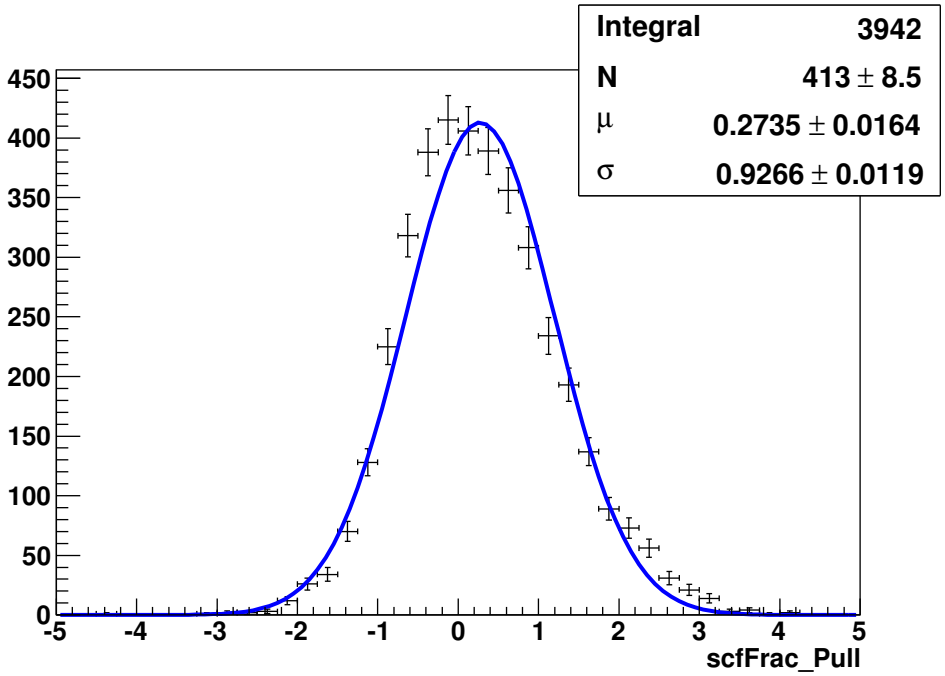

Figure E.1: SCF fraction pull distribution, when the SCF component is described as a fraction of the total signal.

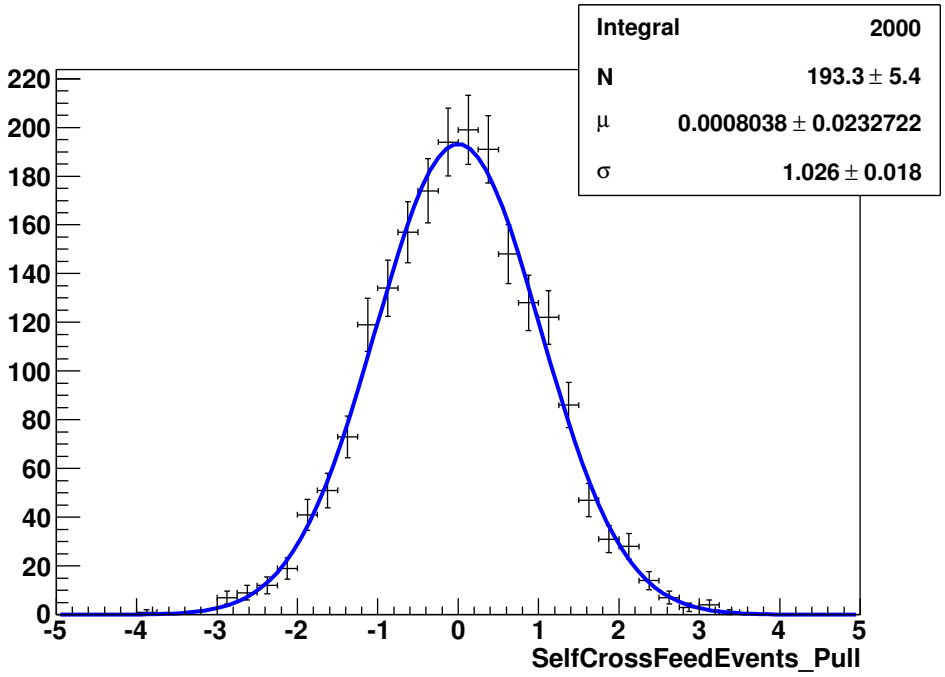

Figure E.2: SCF yield pull distribution, when the SCF component is described as a separated category.

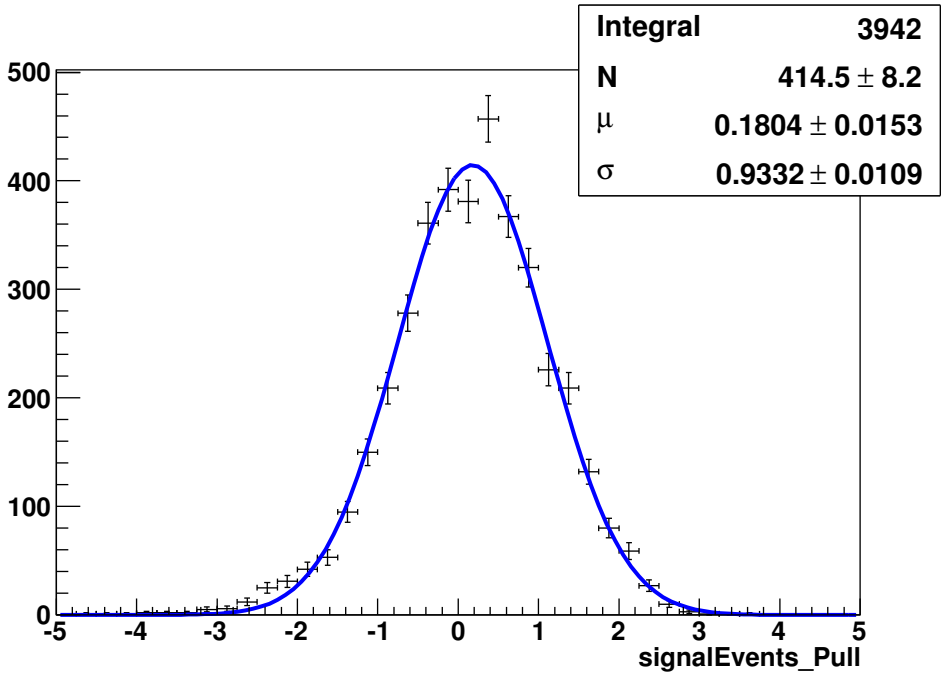

Figure E.3: Total signal yield pull distribution, when the SCF component is described as a fraction of the total signal.

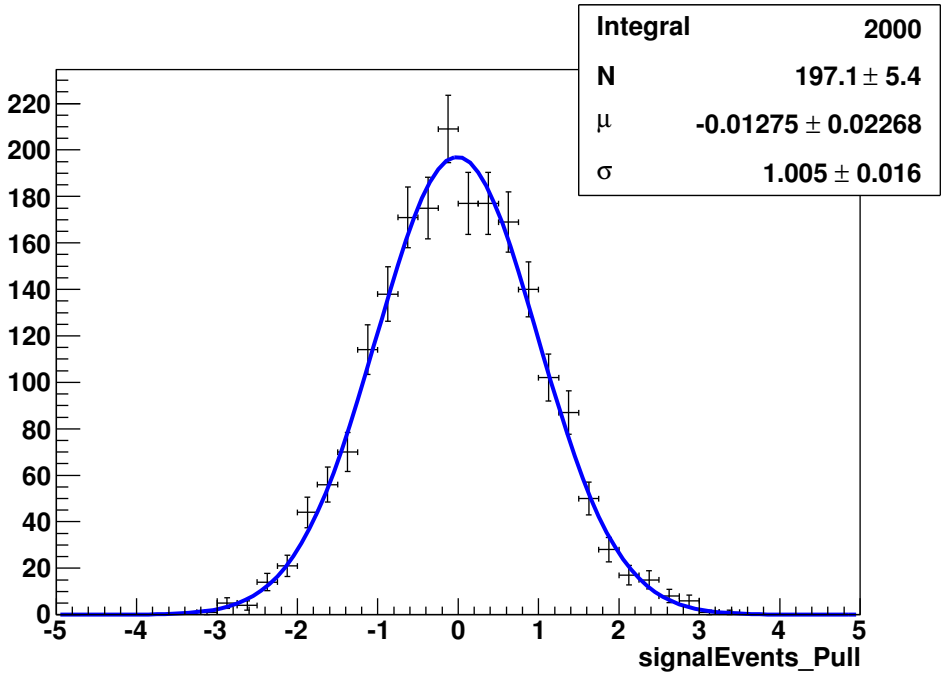

Figure E.4: Signal-TM yield pull distribution, when the SCF component is described as a separated category.

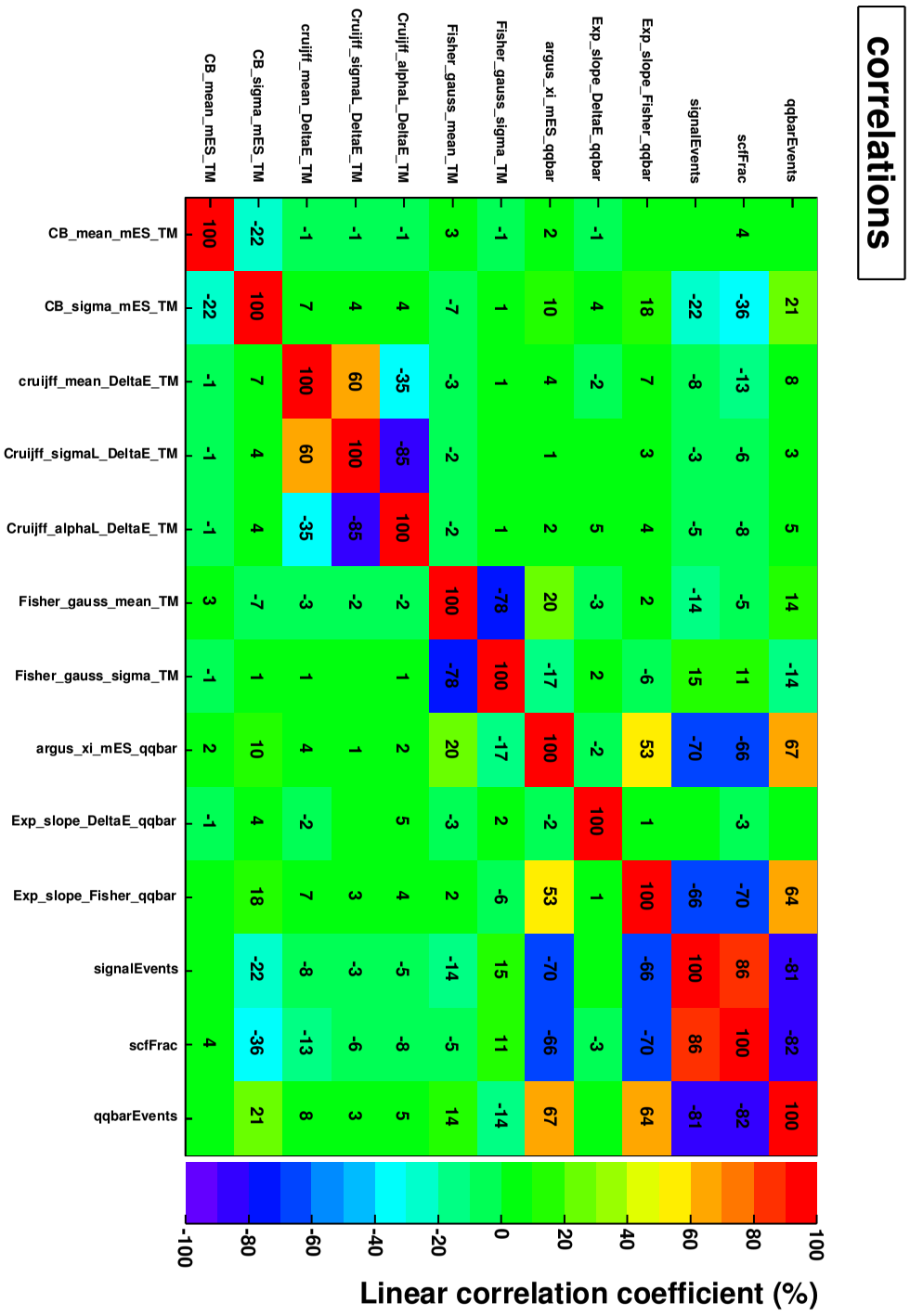

Figure E.5: Linear correlations between all floated parameters. Here the fitted components are the signal TM, the SCF and the continuum *udsc*. The SCF component is described as a fraction of the total signal.

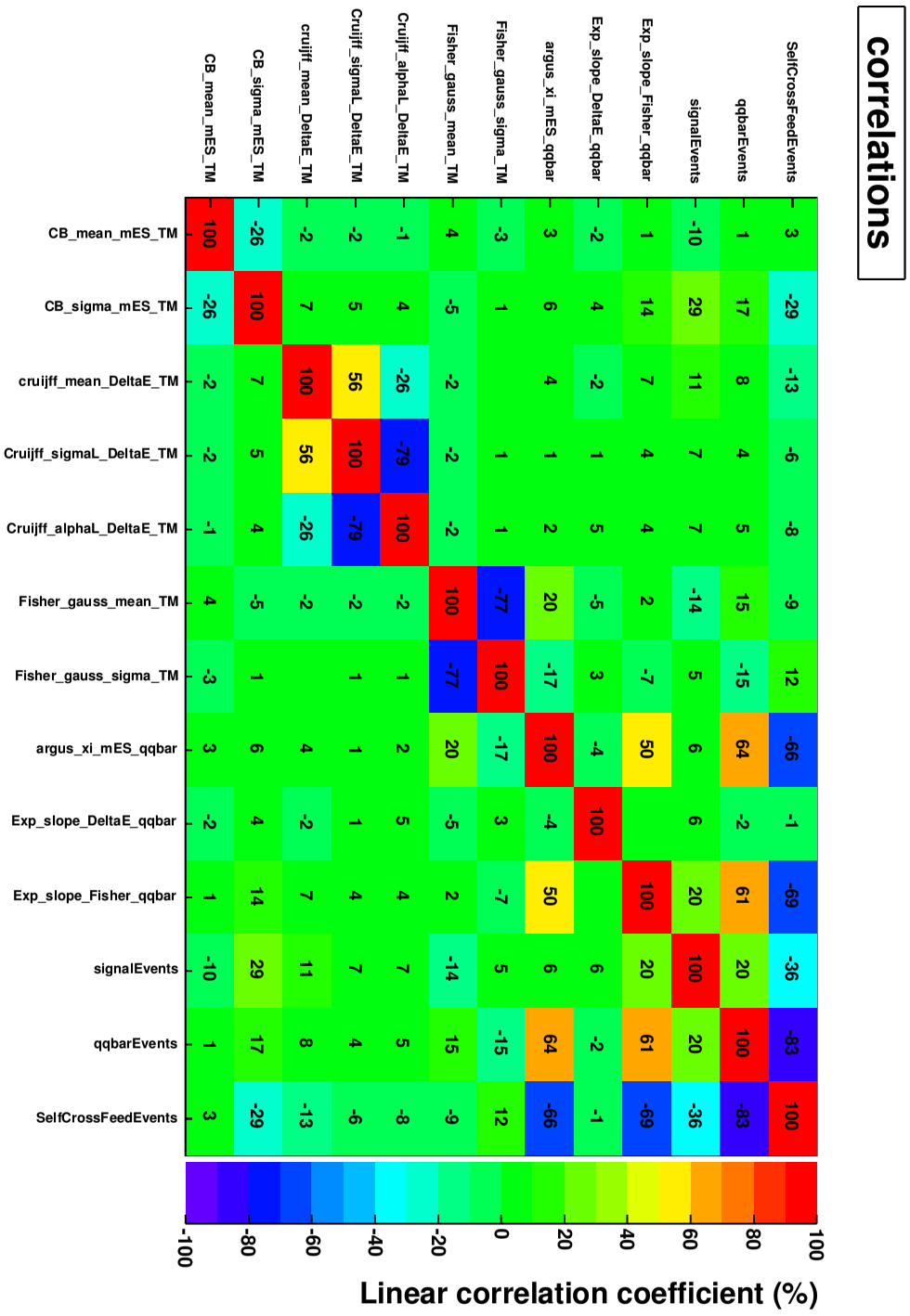

Figure E.6: Linear correlations between all floated parameters. Here the fitted components are the signal TM, the SCF and the continuum *udsc*. The SCF component is described as a separated category.

E.2 Pure toy studies

In this Section we present the shape parameter pull distributions of the pure toy studies described in Sec. 6.5.4.1

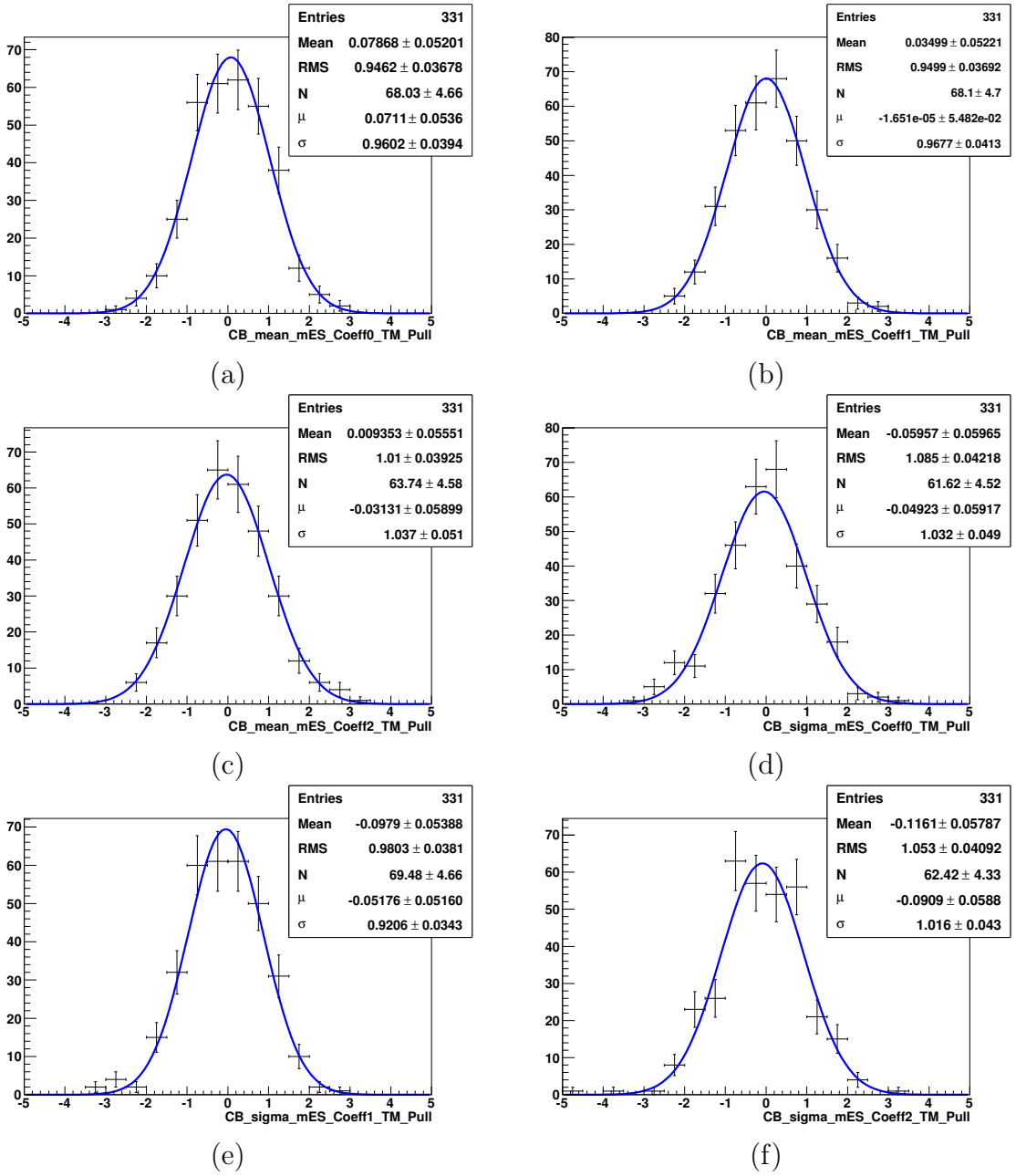

Figure E.7: Pull distributions of signal TM $m_{\rm ES}$ Crystal Ball $\mu_{\alpha 0}$ (a), $\mu_{\alpha 1}$ (b), $\mu_{\alpha 2}$ (c), $\sigma_{\alpha 1}$ (d), $\sigma_{\alpha 2}$ (e), $\sigma_{\alpha 3}$ (f) parameters for the pure toy studies with 331 toys.

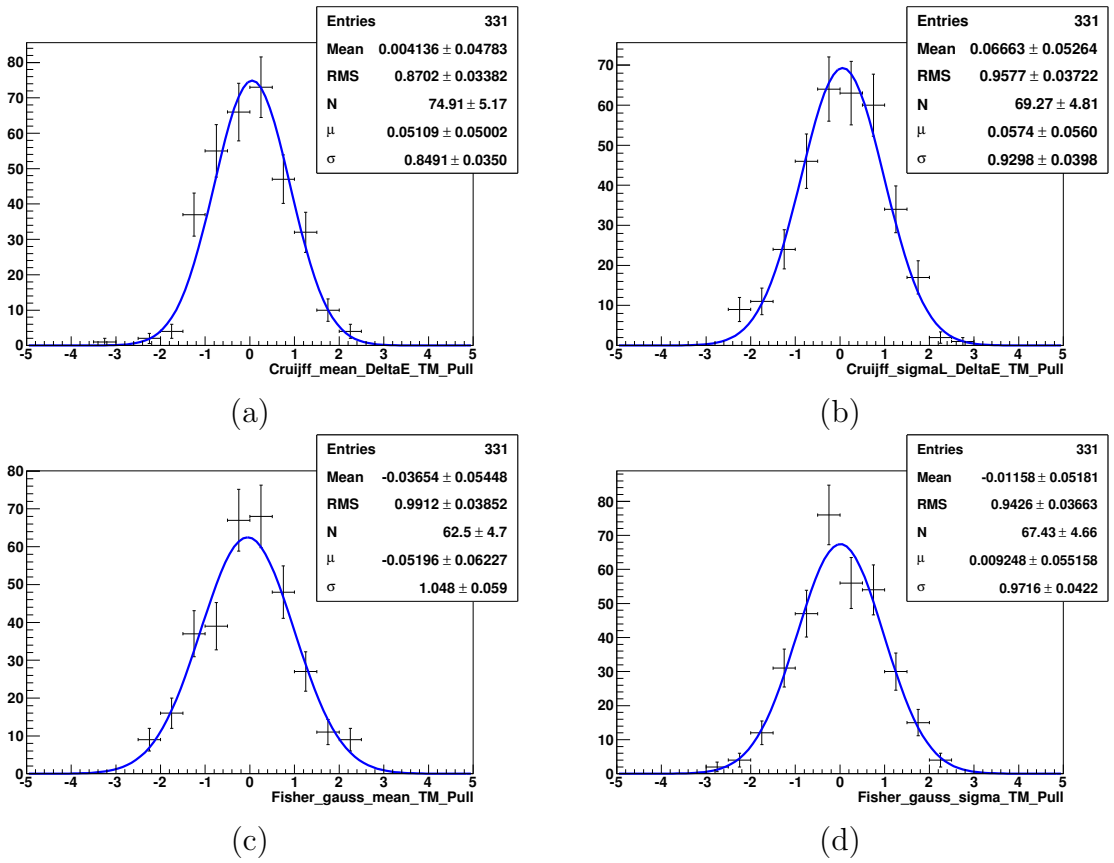

Figure E.8: Pull distributions of signal TM ΔE Cruijff μ (a), σ_L (b) and the Fisher discriminant Gaussian μ (c), σ (d) parameters for the pure toy studies with 331 toys.

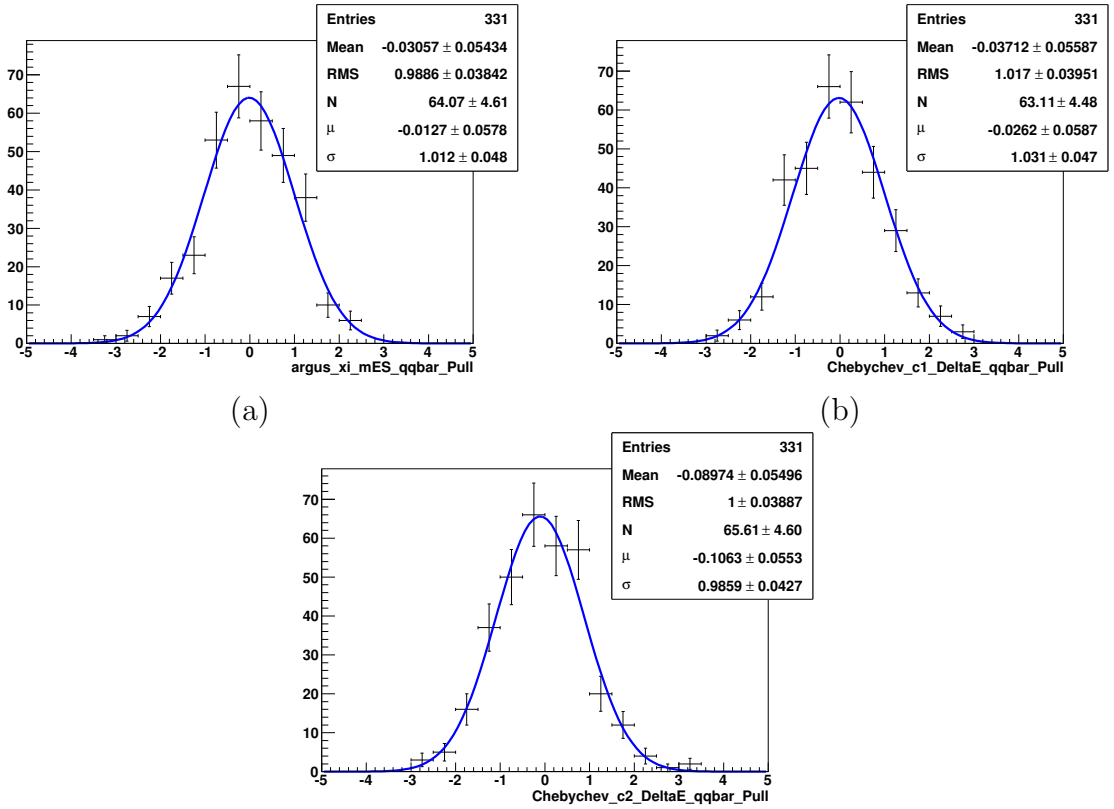

Figure E.9: Pull distributions of continuum *udsc* $m_{\rm ES}$ Argus ξ (a), ΔE Chebychev first coefficient (b) and ΔE Chebychev second coefficient (c) parameters for the pure toy studies with 331 toys.

E.3 Embedded toy studies

In this Section we present the shape parameter pull distributions of the embedded toy studies described in Sec. 6.5.4.2.

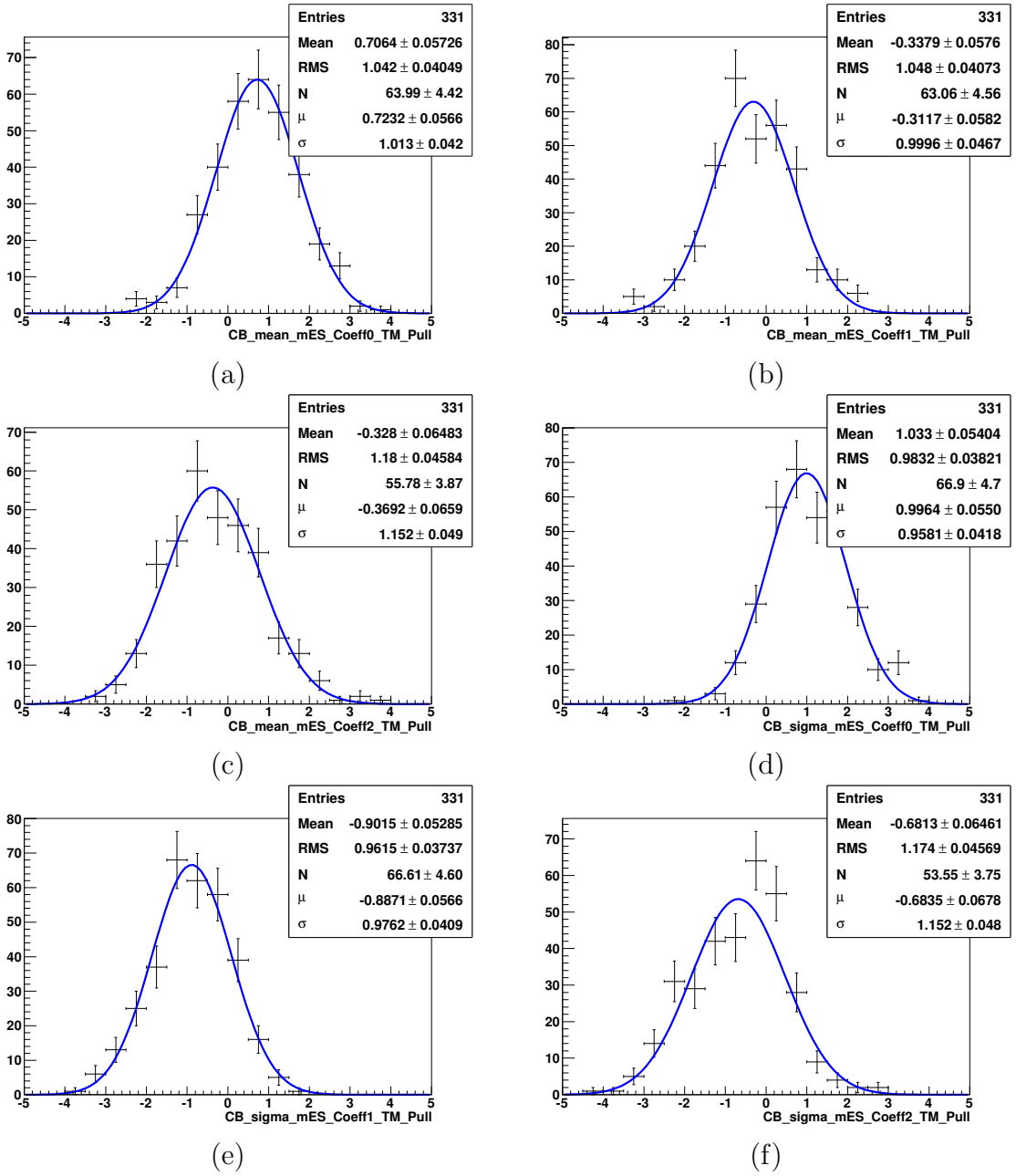

Figure E.10: Pull distributions of signal TM $m_{\rm ES}$ Crystal Ball $\mu_{\alpha 0}$ (a), $\mu_{\alpha 1}$ (b), $\mu_{\alpha 2}$ (c), $\sigma_{\alpha 1}$ (d), $\sigma_{\alpha 2}$ (e), $\sigma_{\alpha 3}$ (f) parameters for the embedded toy studies with 331 toys.

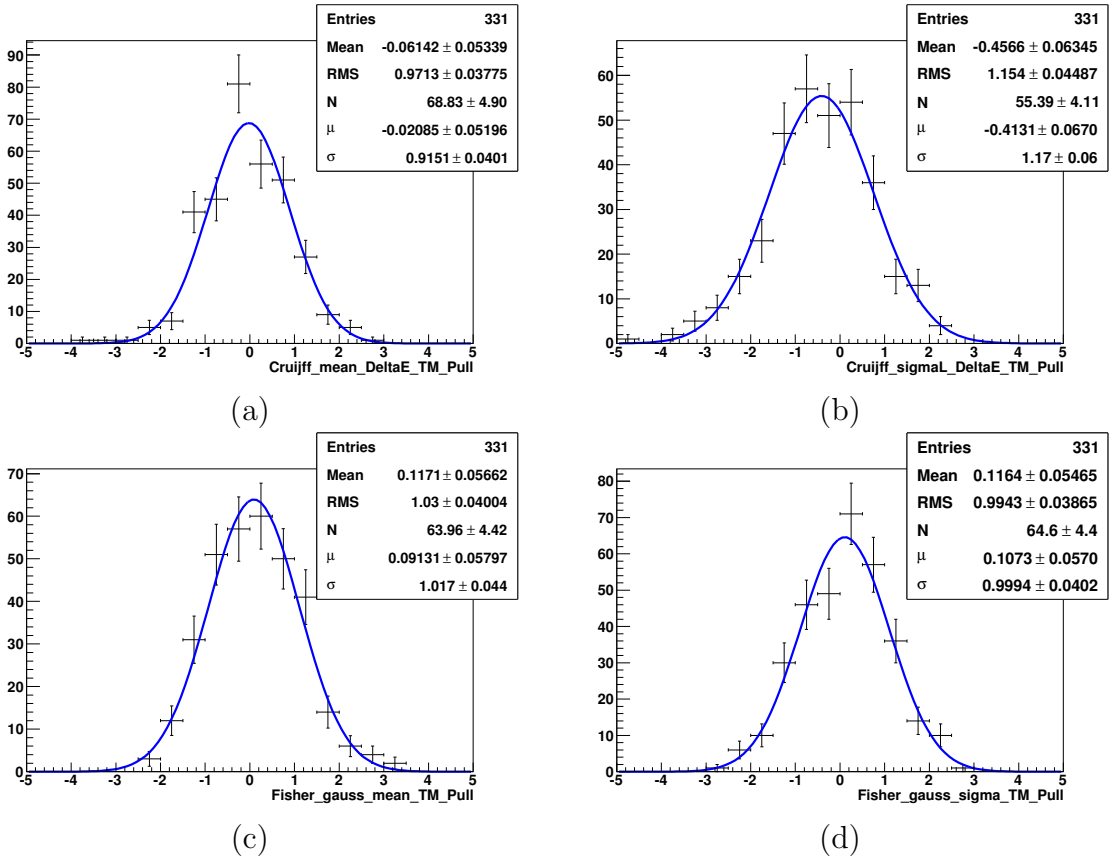

Figure E.11: Pull distributions of signal TM ΔE Cruijff μ (a), σ_L (b) and the Fisher discriminant Gaussian μ (c), σ (d) parameters for the embedded toy studies with 331 toys.

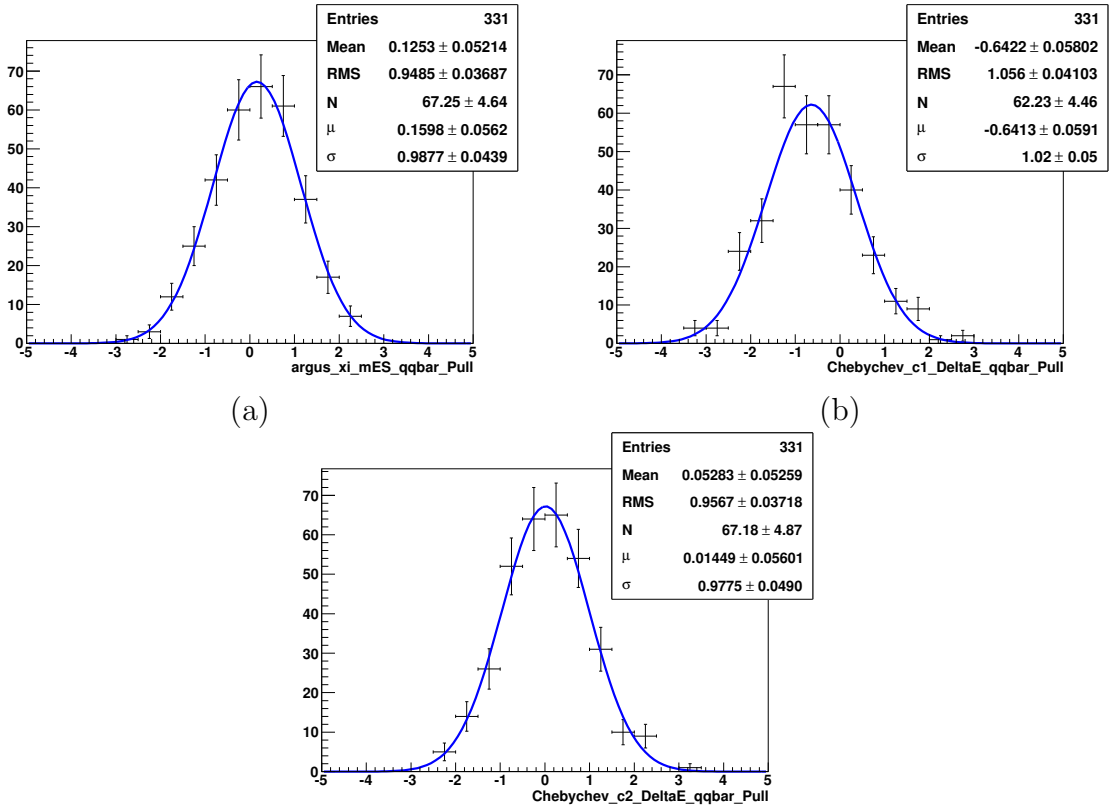

Figure E.12: Pull distributions of continuum *udsc* $m_{\rm ES}$ Argus ξ (a), ΔE Chebychev first coefficient (b) and ΔE Chebychev second coefficient (c) parameters for the embedded toy studies with 331 toys.

Appendix F

$B^+ \to K^+\pi^-\pi^+\gamma$ fit projection study

In order to study in more details the good behavior of the fit to $m_{\rm ES}$, DeltaE and the Fisher discriminant, especially in the signal region, we enriched the fit projections in signal events, as shown in App. F.1 for the $m_{\rm ES}$ and the Fisher discriminant fit projections. A more attentive study was performed in the case of the ΔE fit projection as described in App. F.2.

F.1 Study of the $m_{\rm ES}$ and the Fisher discriminant fit projections

Figures F.1 and F.2 show the $m_{\rm ES}$ fit projection in the entire fit region and in the signal region, respectively. Figures F.3 and F.4 show the Fisher discriminant fit projection in the entire fit region and in the signal region, respectively. Here the signal region is defined as $-0.15 \leq \Delta E \leq 0.10\,{\rm GeV}/c$ and $m_{\rm ES} > 5.27\,{\rm GeV}/c^2$.

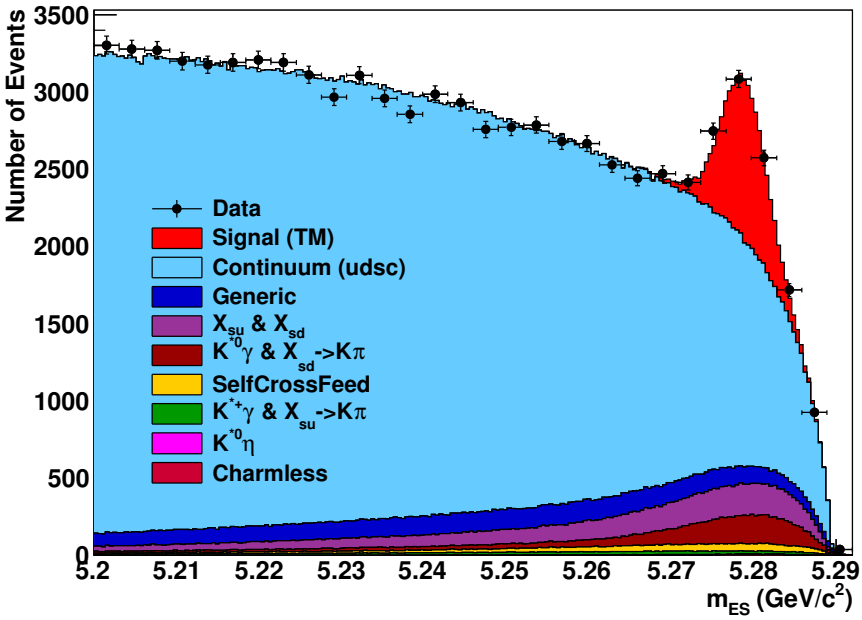

Figure F.1: $m_{\rm ES}$ fit projection in the whole fit region.

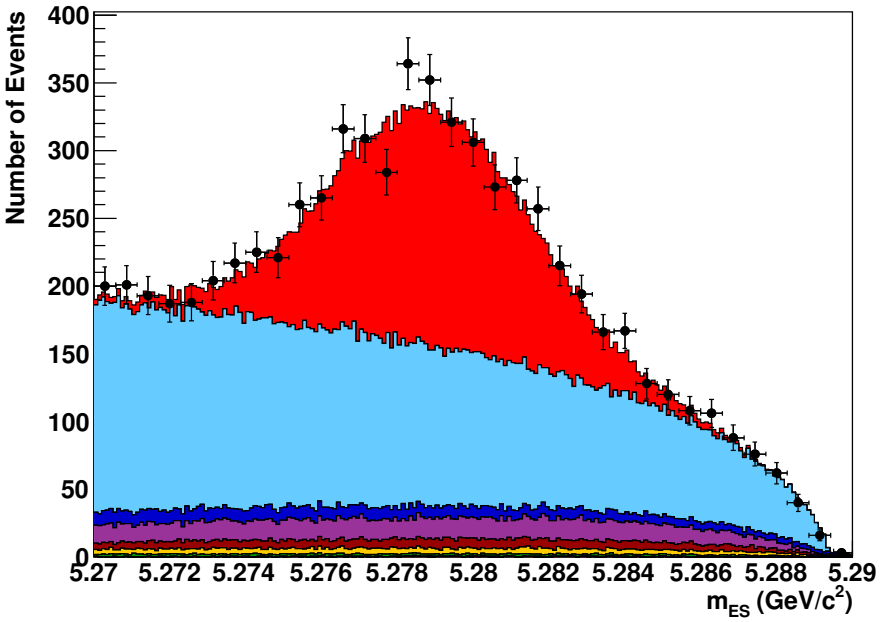

Figure F.2: $m_{\rm ES}$ fit projection in the signal region, where the following cuts have been applied in order to enrich the data sample in signal events: $-0.15 \leq \Delta E \leq 0.10\,\mathrm{GeV}/c$ and $m_{\rm ES} > 5.27\,\mathrm{GeV}/c^2$. Conventions are identical to those in Fig. F.1

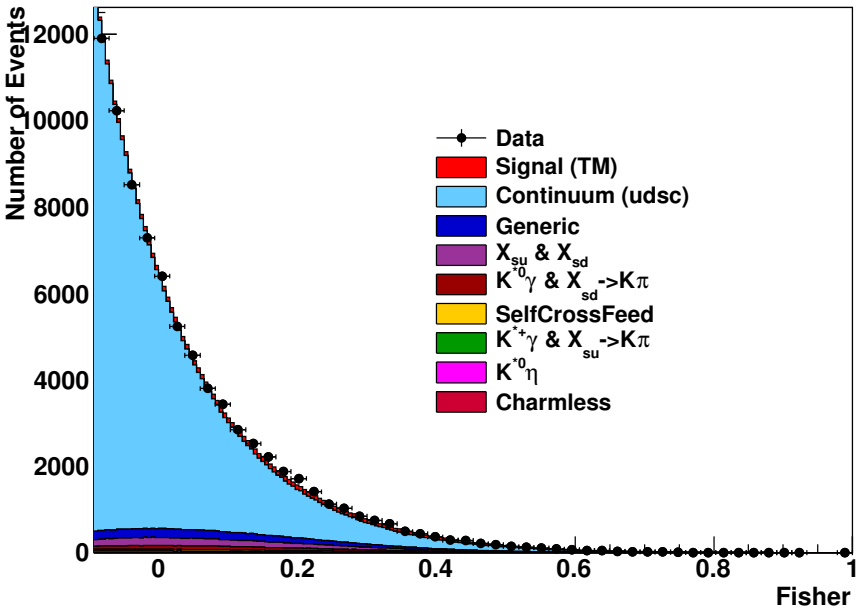

Figure F.3: The Fisher discriminant fit projection in the whole fit region.

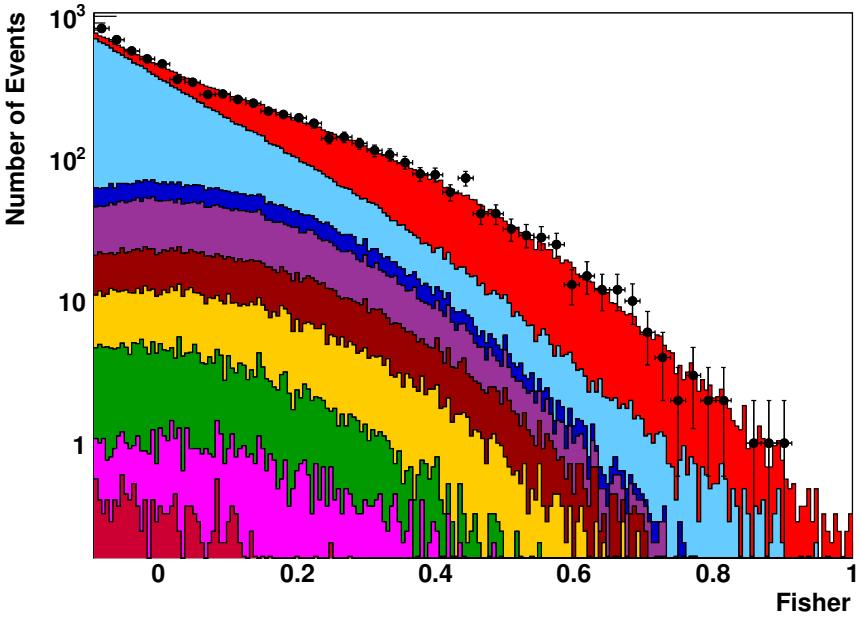

Figure F.4: The Fisher discriminant fit projection in the signal region, where the following cuts have been applied in order to enrich the data sample in signal events: $-0.15 \leq \Delta E \leq 0.10\,\mathrm{GeV}/c$ and $m_{\mathrm{ES}} > 5.27\,\mathrm{GeV}/c^2$. A log scale is applied to the y-axis. Conventions are identical to those in Fig. F.3

F.2 Study of the ΔE fit projection

Here we present the ΔE fit projection in terms of $m_{\rm ES}$ bins as described in Tab. F.1.

Table F.1: $m_{\rm ES}$ bins definition for the ΔE fit projection study.

$m_{\rm ES}$ bin number	$m_{\rm ES}$ range (GeV/c^2)
0	$5.200 \leq x < 5.270$
1	$5.270 \leq x < 5.272$
2	$5.272 \leq x < 5.274$
3	$5.274 \leq x < 5.275$
4	$5.275 \leq x < 5.276$
5	$5.276 \leq x < 5.278$
6	$5.278 \leq x < 5.280$
7	$5.280 \leq x < 5.282$
8	$5.282 \leq x < 5.284$
9	$5.284 \leq x \leq 5.292$

We observe comparing Fig. F.5 and F.6 that the little discrepancy in the whole $m_{\rm ES}$ region remains in the first bin in $m_{\rm ES}$ (bin 0) where lies almost no signal events. This shows that this is mainly due to a background fluctuation. Moreover in the other $m_{\rm ES}$ bins, except in bin 8, the agreement, within statistical errors is really good between data points and the fit projections.

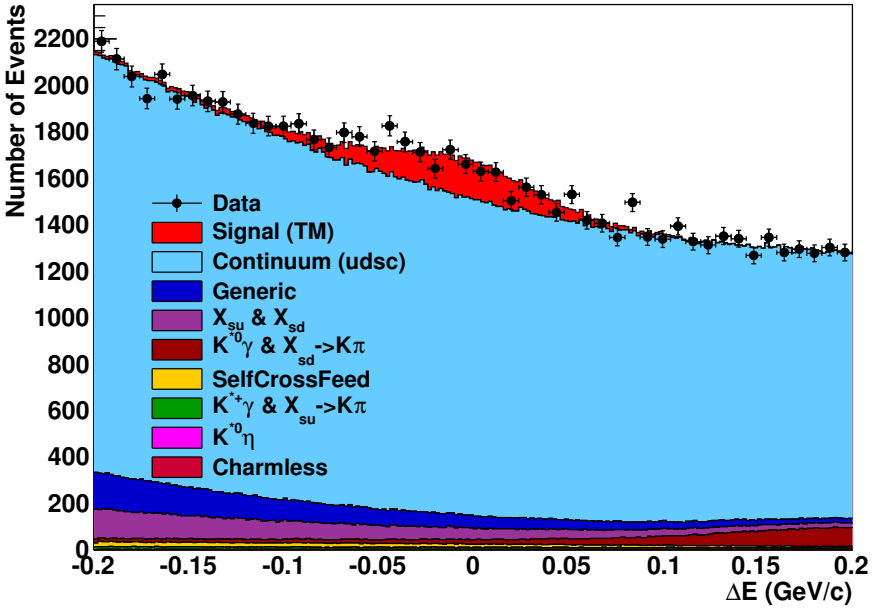

Figure F.5: ΔE fit projection in the whole $m_{\rm ES}$ range.

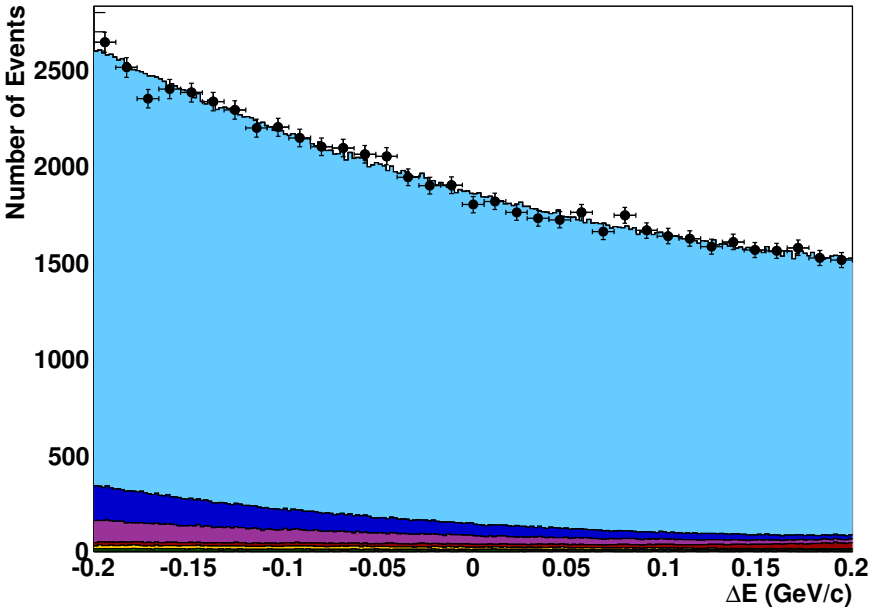

Figure F.6: ΔE fit projection in $m_{\rm ES}$ bin 0.

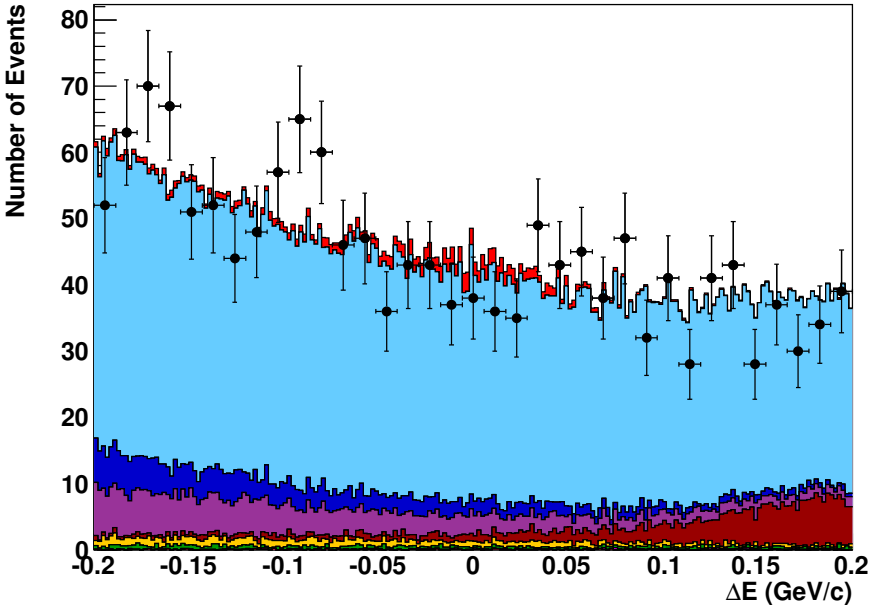

Figure F.7: ΔE fit projection in $m_{\rm ES}$ bin 1.

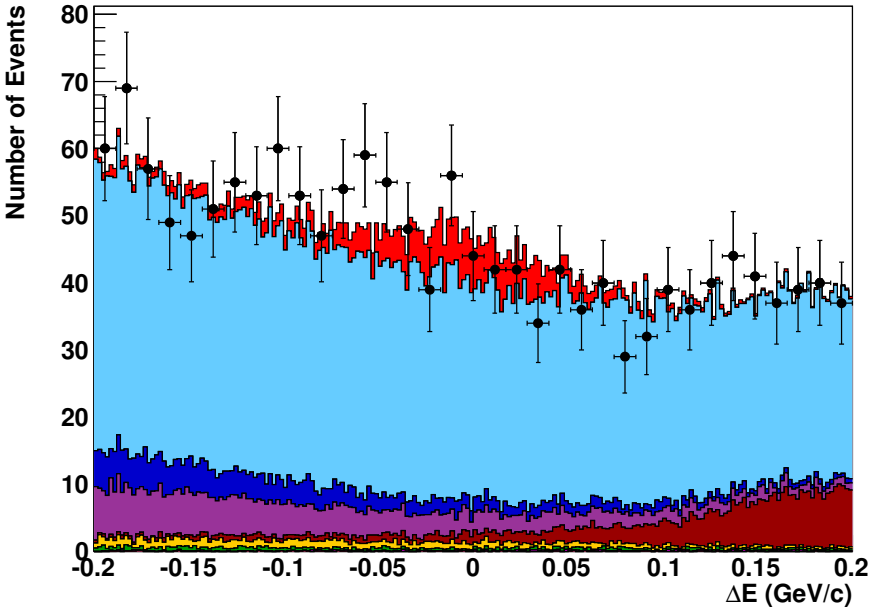

Figure F.8: ΔE fit projection in $m_{\rm ES}$ bin 2.

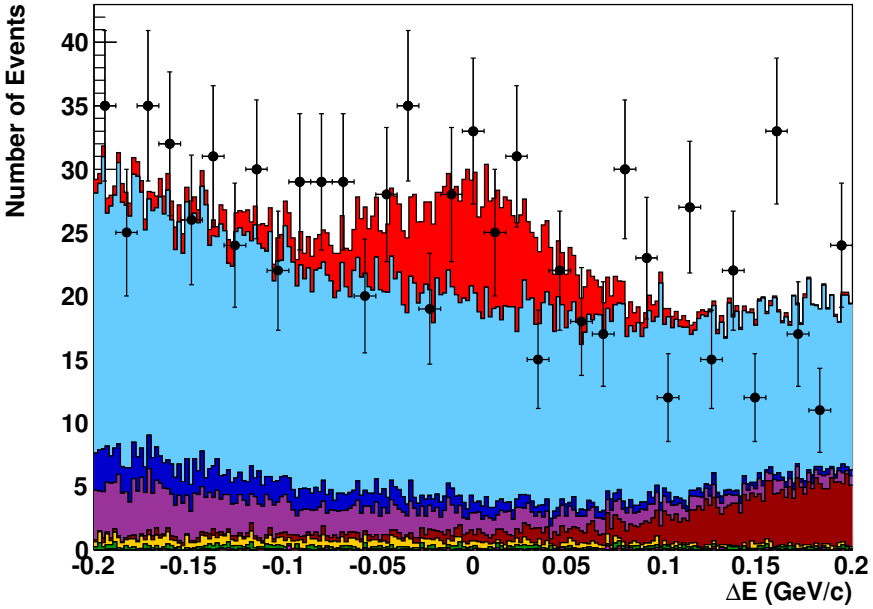

Figure F.9: ΔE fit projection in m_{ES} bin 3.

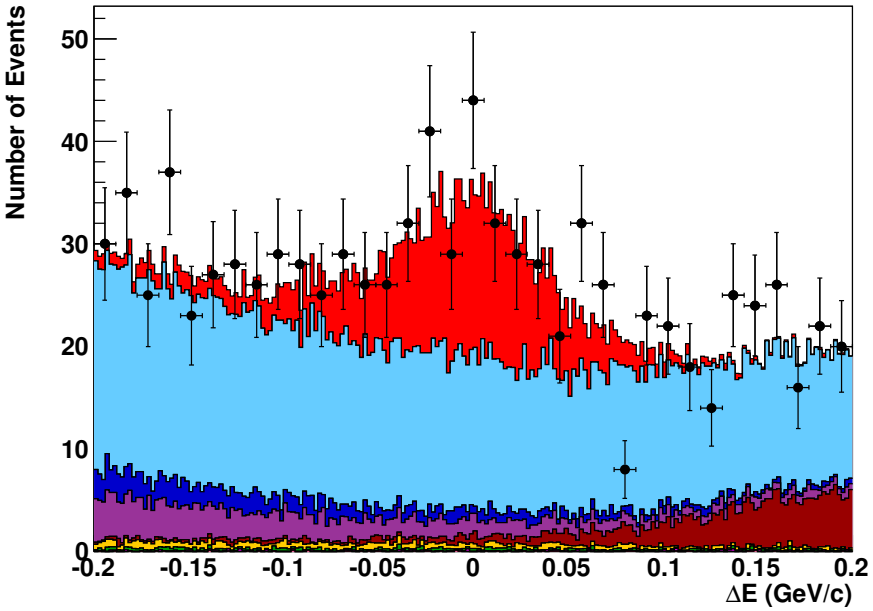

Figure F.10: ΔE fit projection in m_{ES} bin 4.

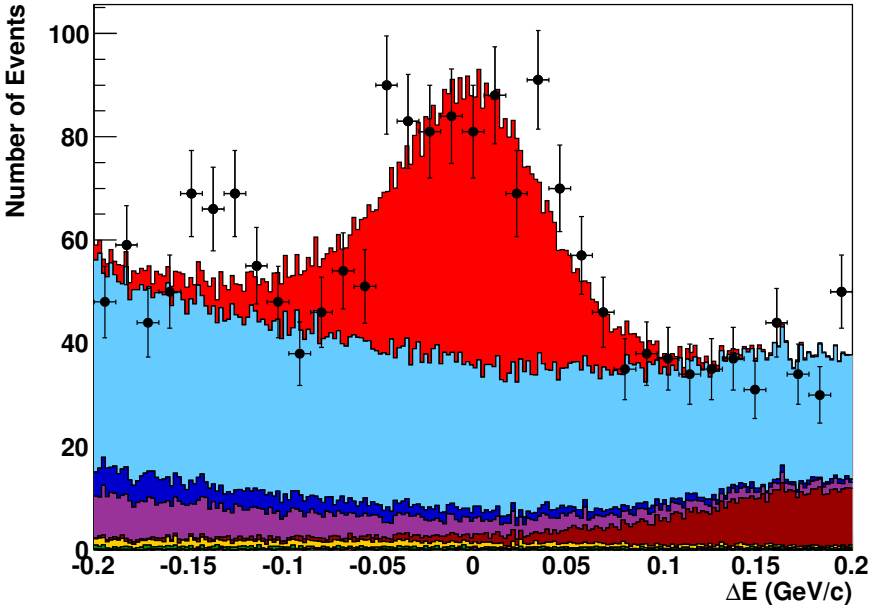

Figure F.11: ΔE fit projection in $m_{\rm ES}$ bin 5.

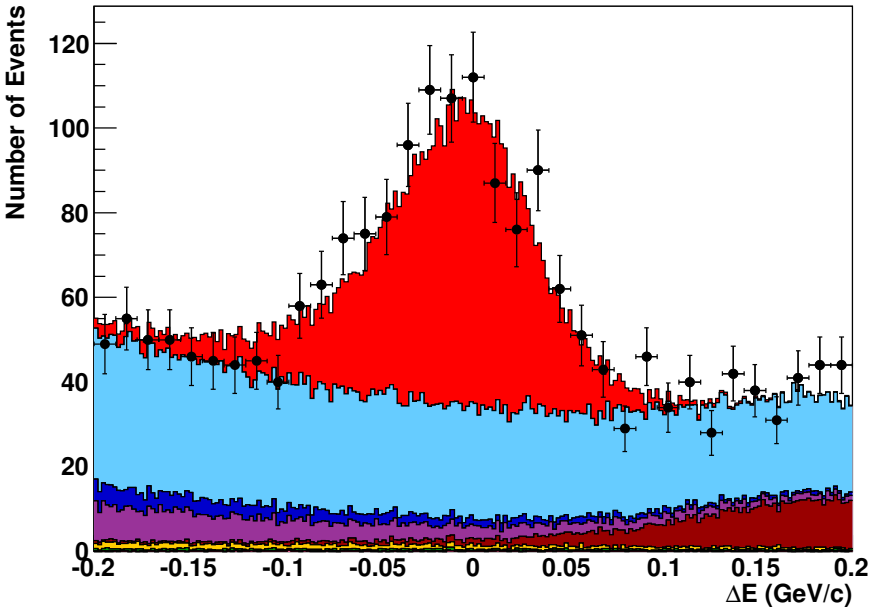

Figure F.12: ΔE fit projection in $m_{\rm ES}$ bin 6.

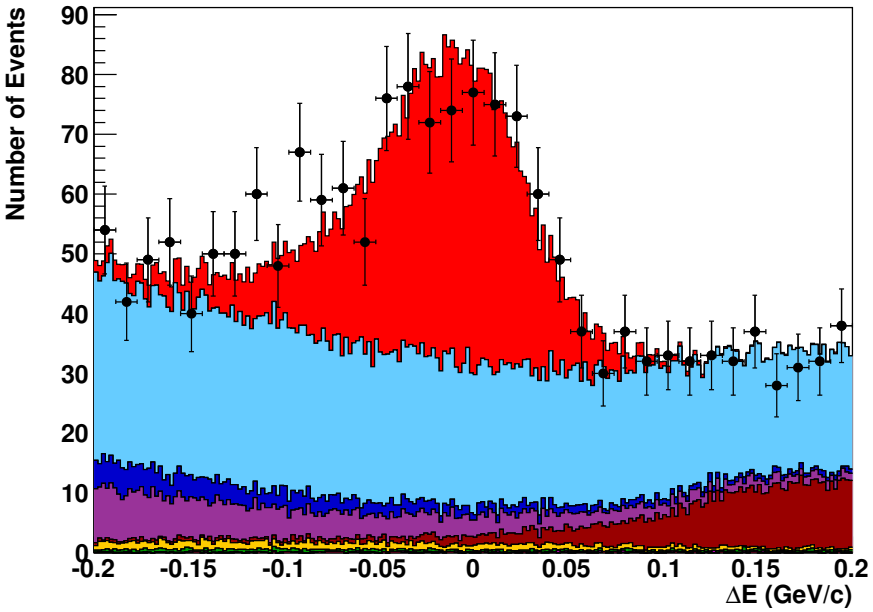

Figure F.13: ΔE fit projection in m_{ES} bin 7.

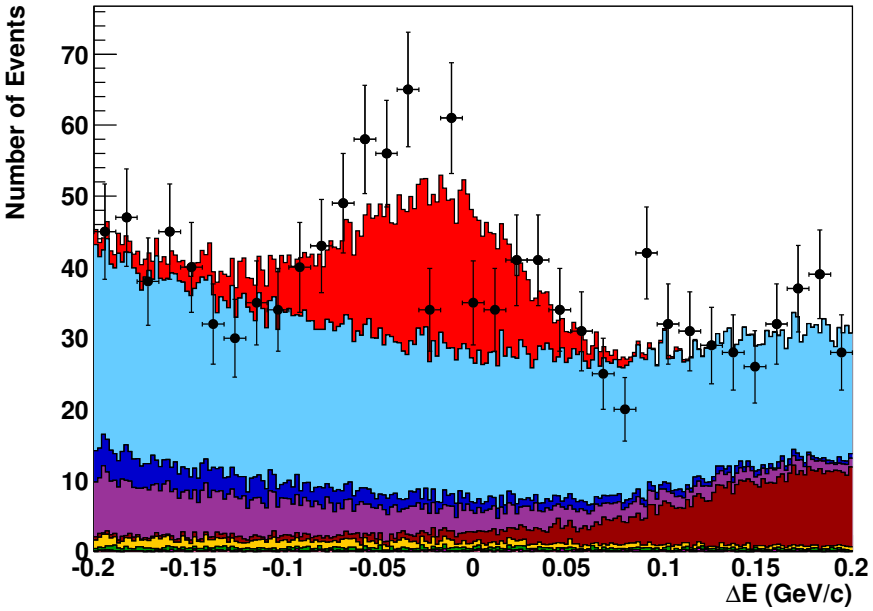

Figure F.14: ΔE fit projection in m_{ES} bin 8.

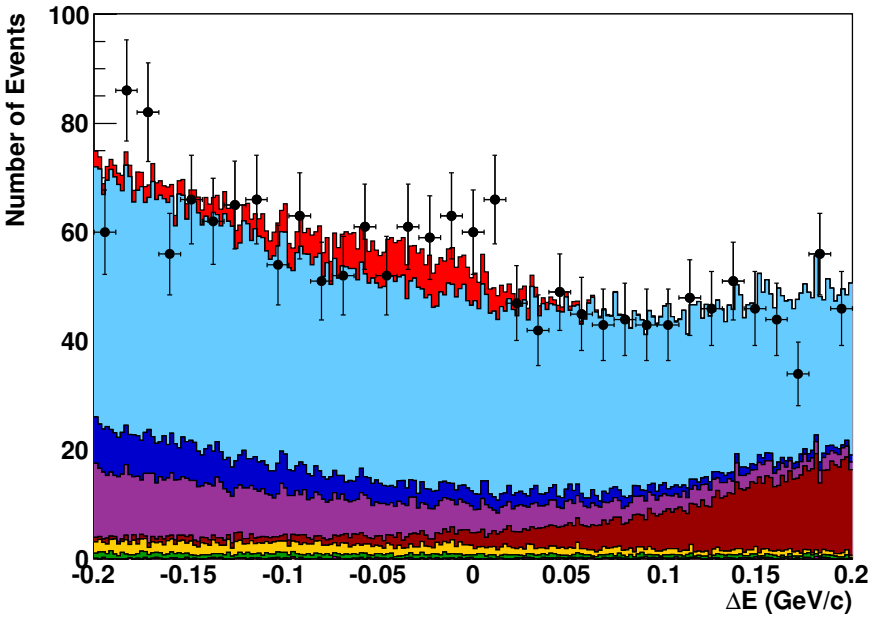

Figure F.15: ΔE fit projection in $m_{\rm ES}$ bin 9.

Appendix G

Toy studies for the time-dependent analysis

G.1 Pure toy studies

In this Section we present the shape parameter pull distributions of the pure toy studies described in Sec. 7.6.5.2

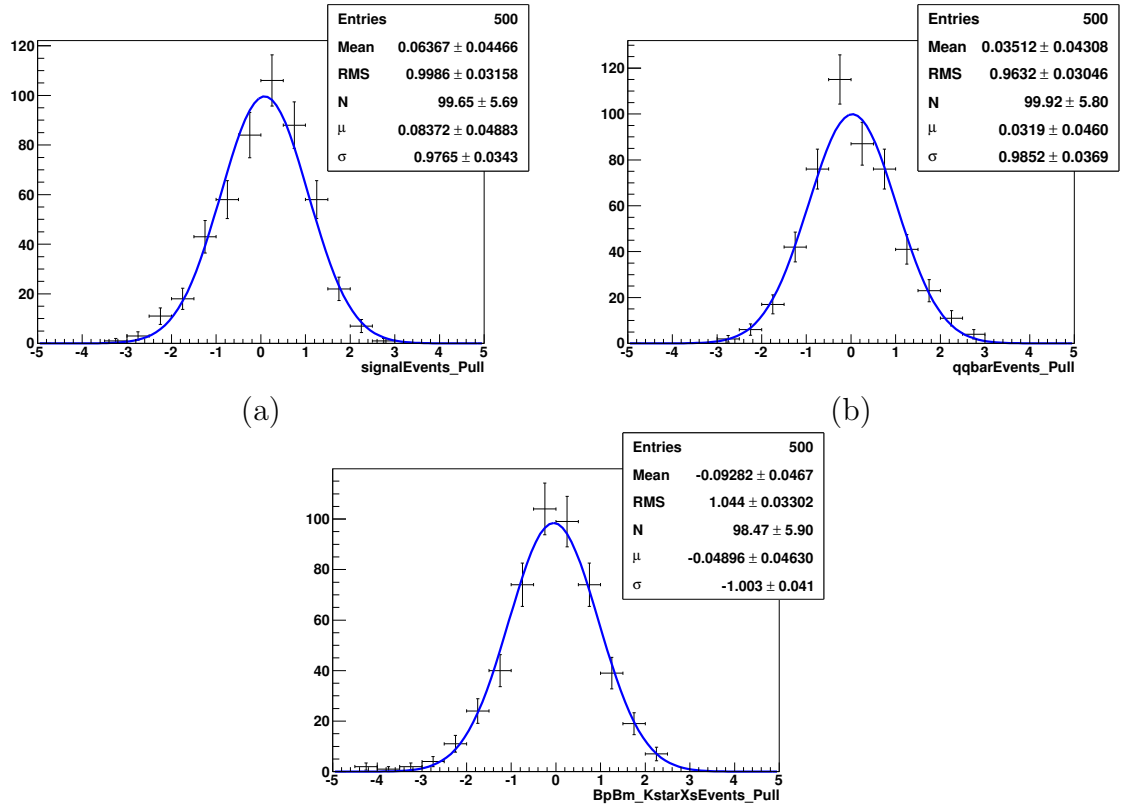

Figure G.1: Yields pull distributions of signal events category (a), continuum background (b) and $B^+ \to K^{*+}(\to K^0_S\pi^+)\gamma$ + $B^+ \to X_{su}(\to K^0_S\pi^+)\gamma$ B background (c) for the pure toy studies with 500 toys.

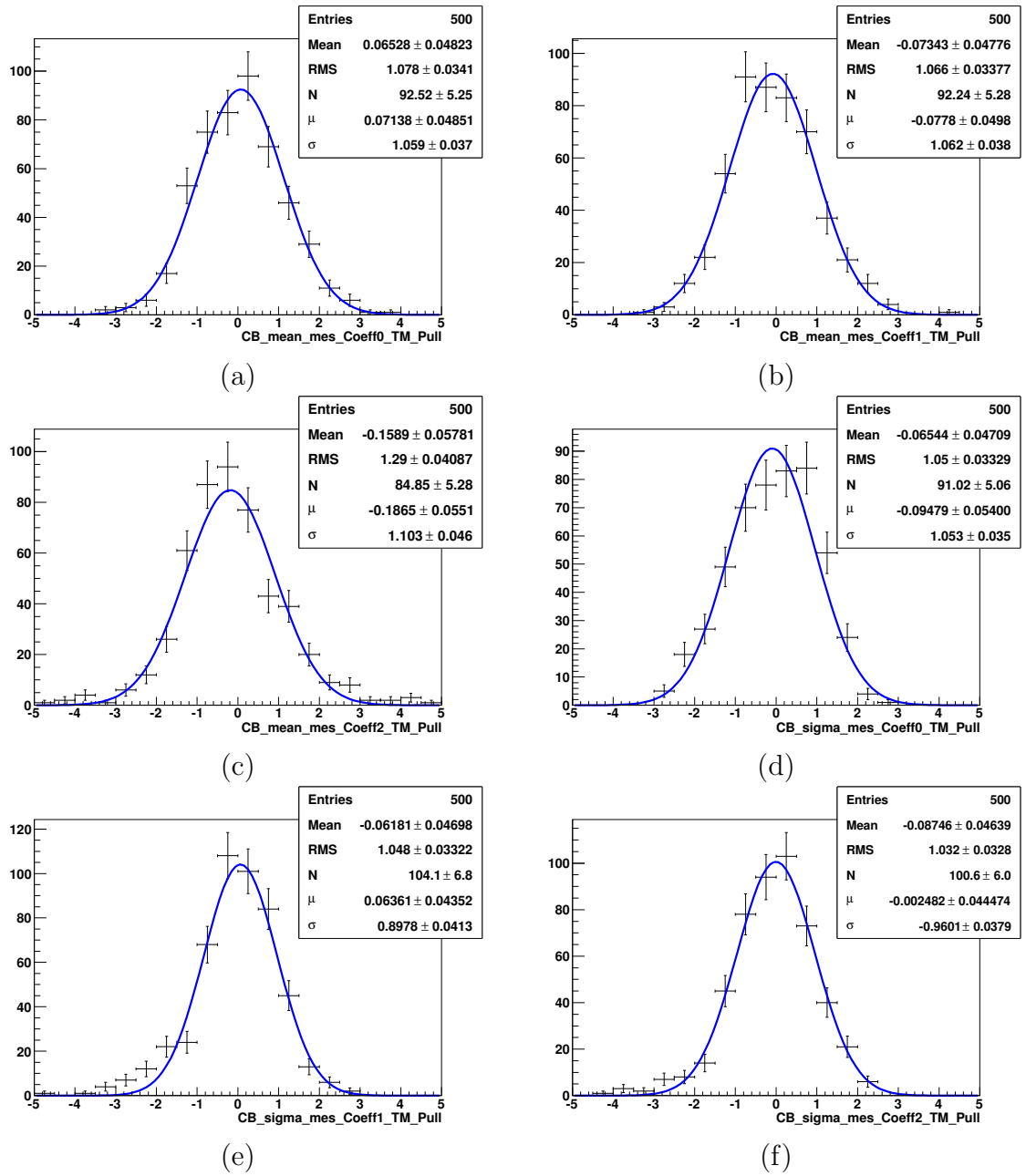

Figure G.2: Pull distributions of signal TM m_{ES} Crystal Ball $\mu_{\alpha 0}$ (a), $\mu_{\alpha 1}$ (b), $\mu_{\alpha 2}$ (c), $\sigma_{\alpha 1}$ (d), $\sigma_{\alpha 2}$ (e), $\sigma_{\alpha 3}$ (f) parameters for the pure toy studies with 500 toys.

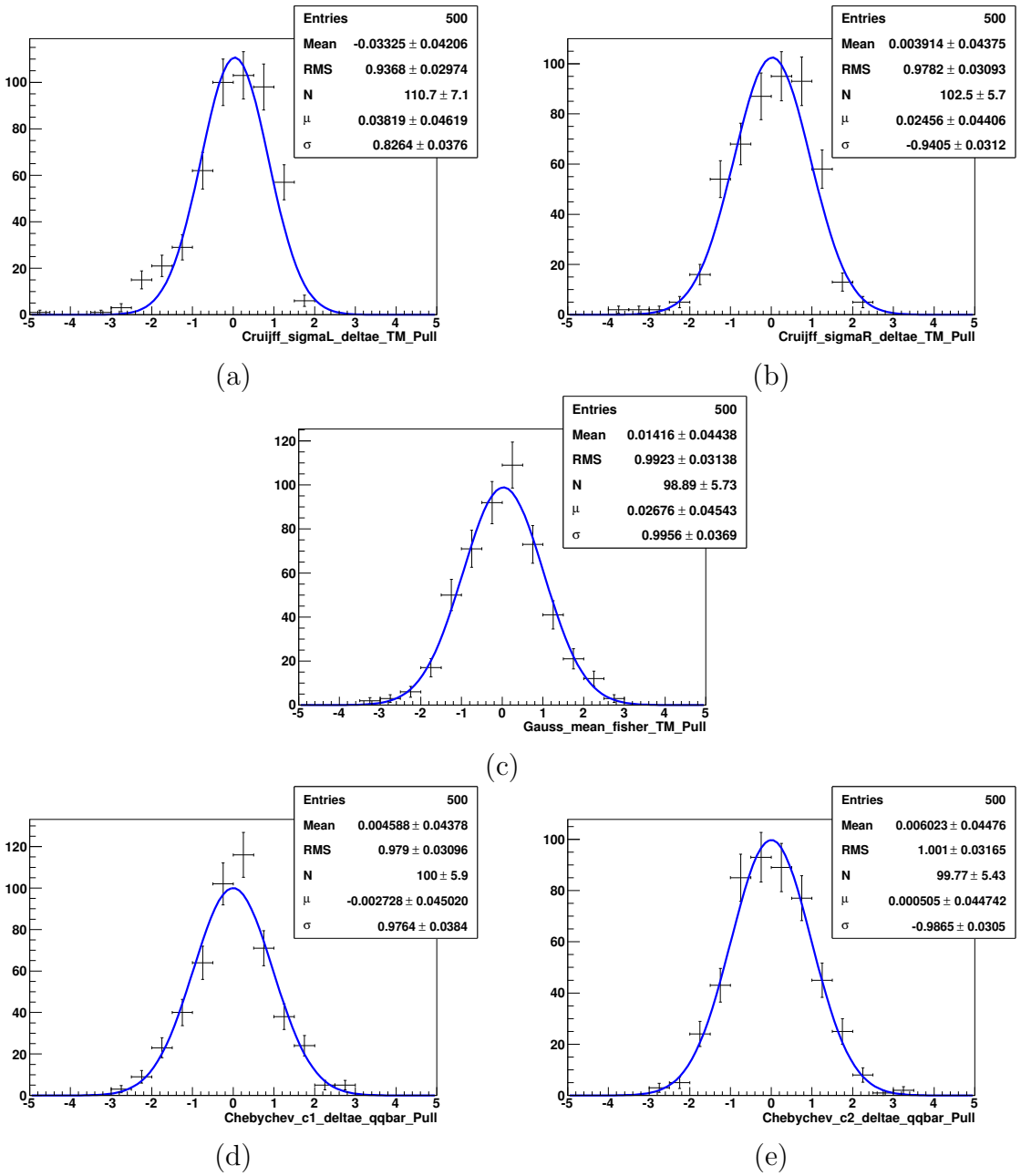

Figure G.3: Pull distributions of signal TM ΔE Cruijff and the Fisher discriminant Gaussian parameters: Cr_{σ_L} (a), Cr_{σ_R} (b) and G_{μ} (c), as well as the continuum background Fisher discriminant Chebychev polynomial parameters: Chebychevc_1 (d), Chebychevc_2 (e) for the pure toy studies with 500 toys.

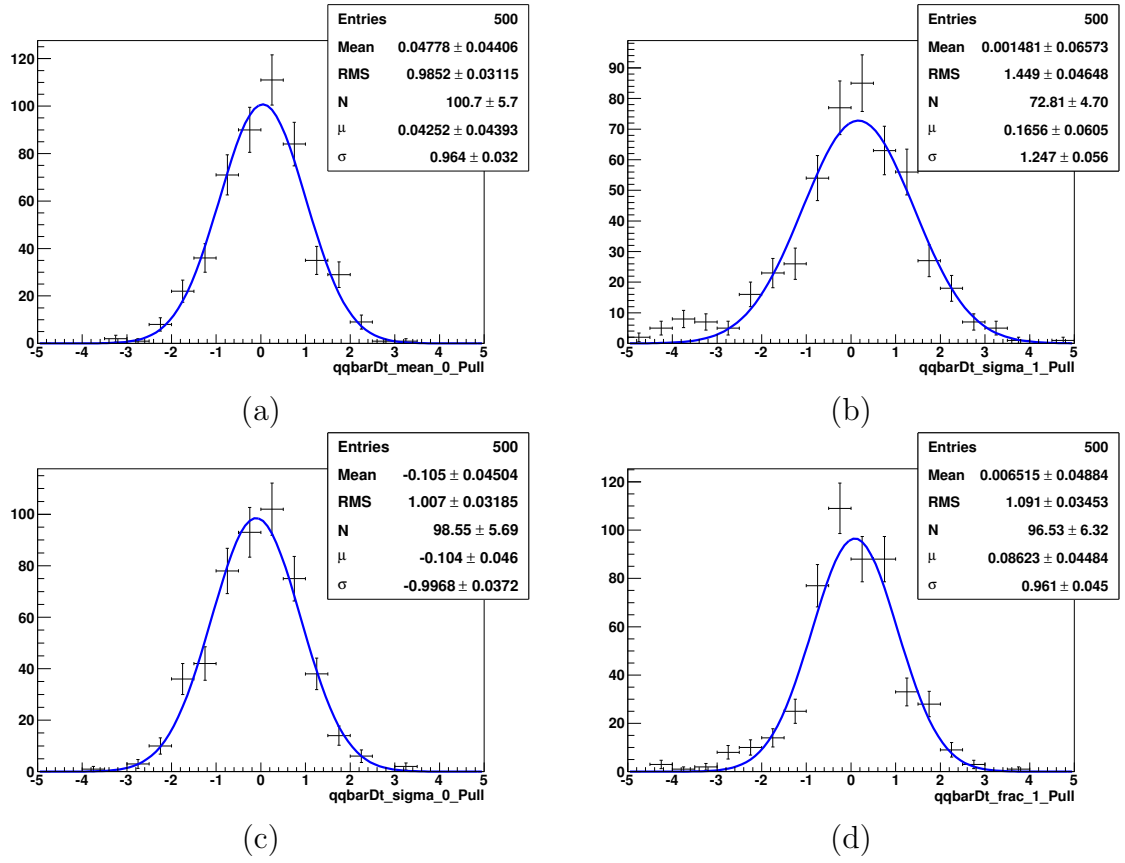

Figure G.4: Pull distributions of the continuum background resolution function ($\mathcal{R}_{\rm bg}$) parameters: $b_{\rm core}$ (a), $s_{\rm outlier}$ (b), $s_{\rm core}$ (c) and $f_{\rm outlier}$ (d) for the pure toy studies with 500 toys.

G.2 Embedded toy studies

In this Section we present the shape parameter pull distributions of the embedded toy studies described in Sec. 7.6.5.3.

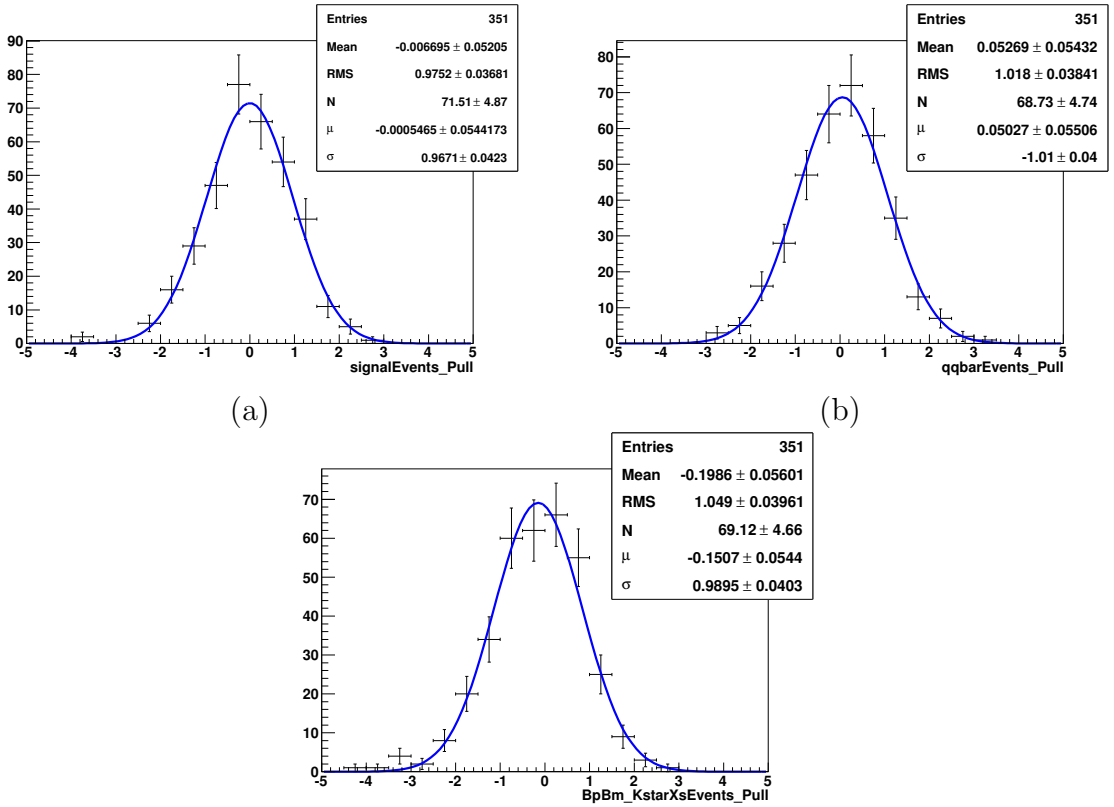

Figure G.5: Yields pull distributions of signal events category (a), continuum background (b) and $B^+ \to K^{*+}(\to K^0_S\pi^+)\gamma + B^+ \to X_{su}(\to K^0_S\pi^+)\gamma$ B background (c) for the embedded toy studies with 351 toys.

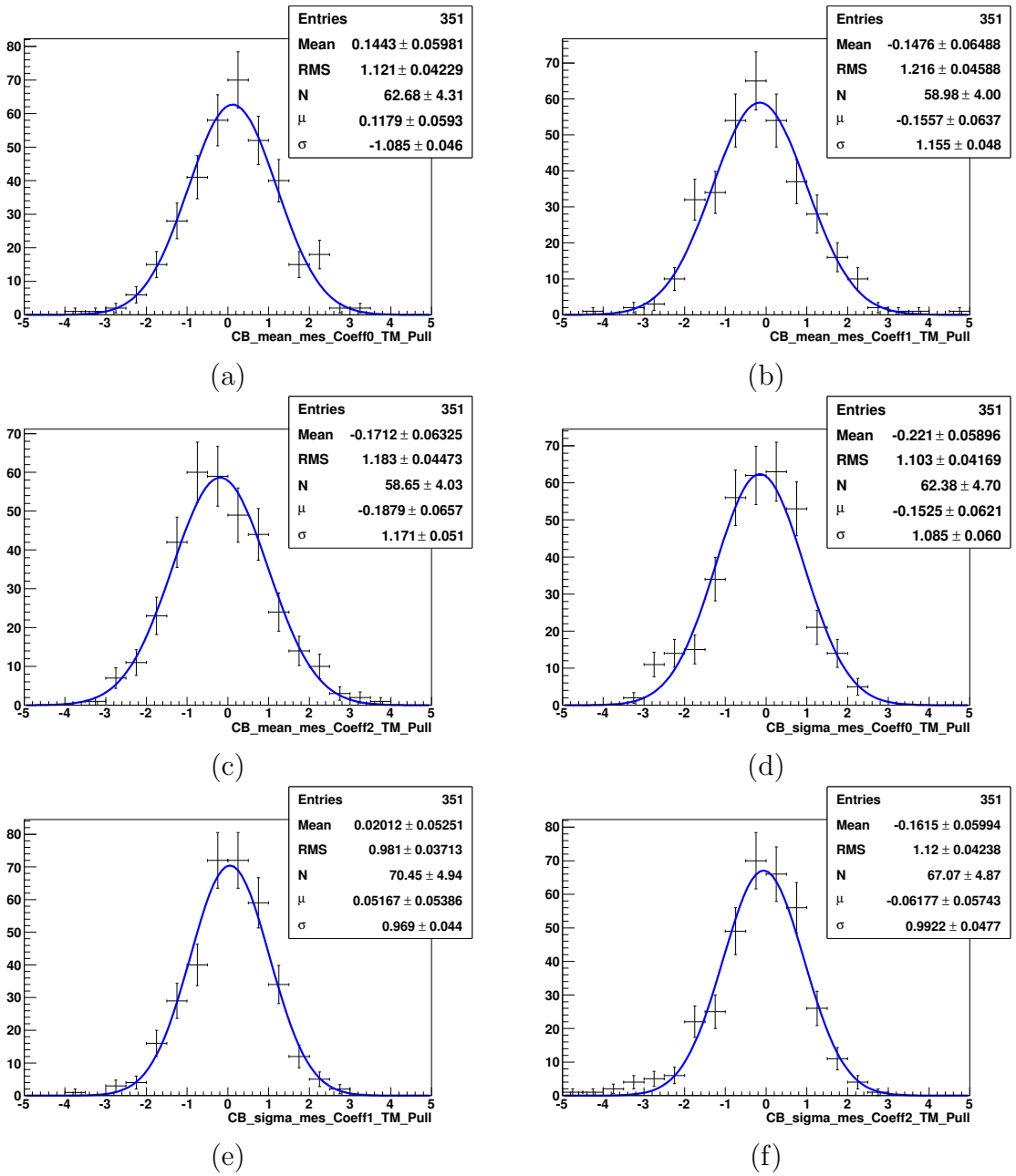

Figure G.6: Pull distributions of signal TM $m_{\rm ES}$ Crystal Ball $\mu_{\alpha 0}$ (a), $\mu_{\alpha 1}$ (b), $\mu_{\alpha 2}$ (c), $\sigma_{\alpha 1}$ (d), $\sigma_{\alpha 2}$ (e), $\sigma_{\alpha 3}$ (f) parameters for the embedded toy studies with 351 toys.

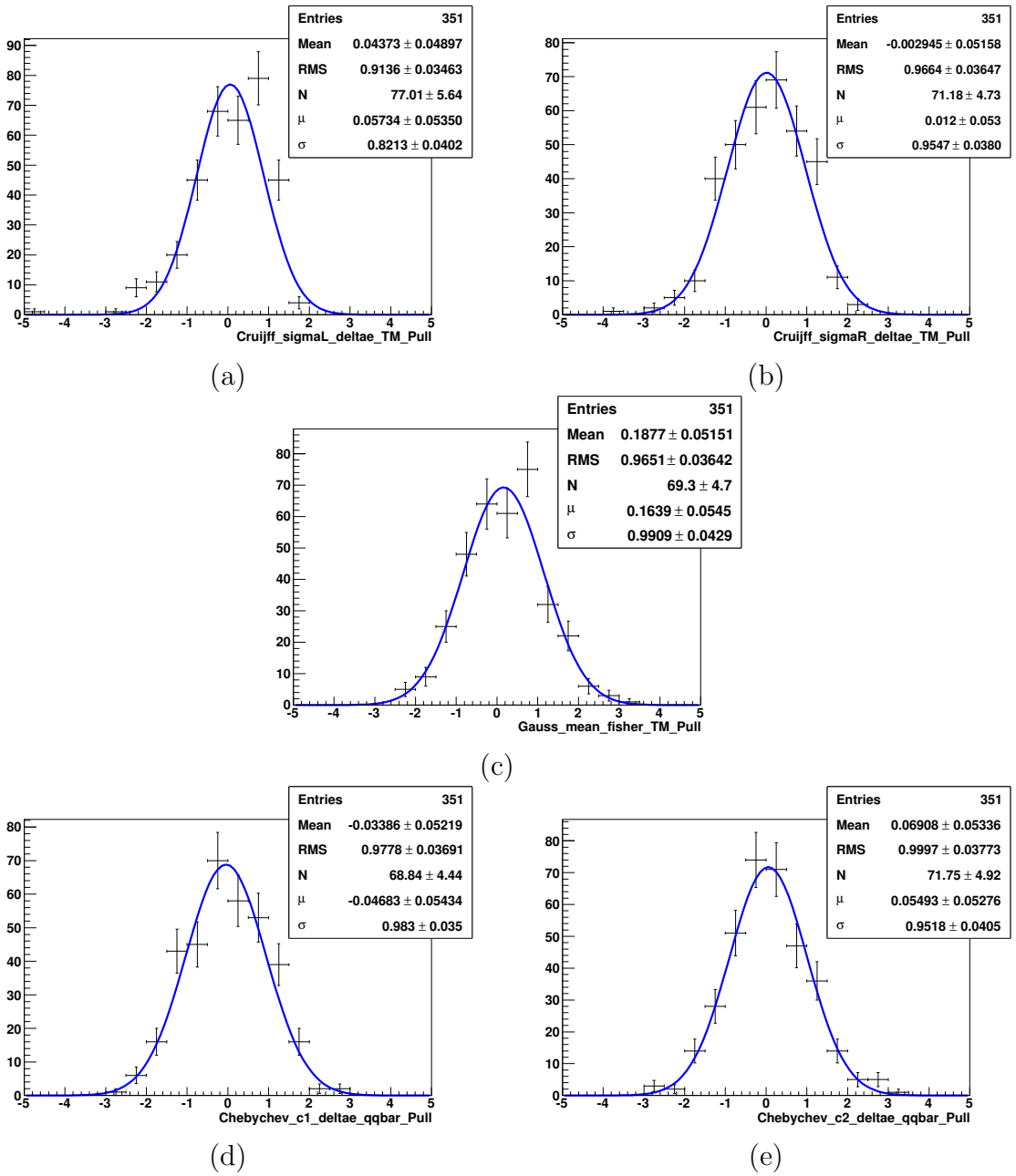

Figure G.7: Pull distributions of signal TM ΔE Cruijff and the Fisher discriminant Gaussian parameters: Cr_{σ_L} (a), Cr_{σ_R} (b) and G_{μ} (c), as well as the continuum background Fisher discriminant Chebychev polynomial parameters: Chebychevc_1 (d), Chebychevc_2 (e) for the embedded toy studies with 351 toys.

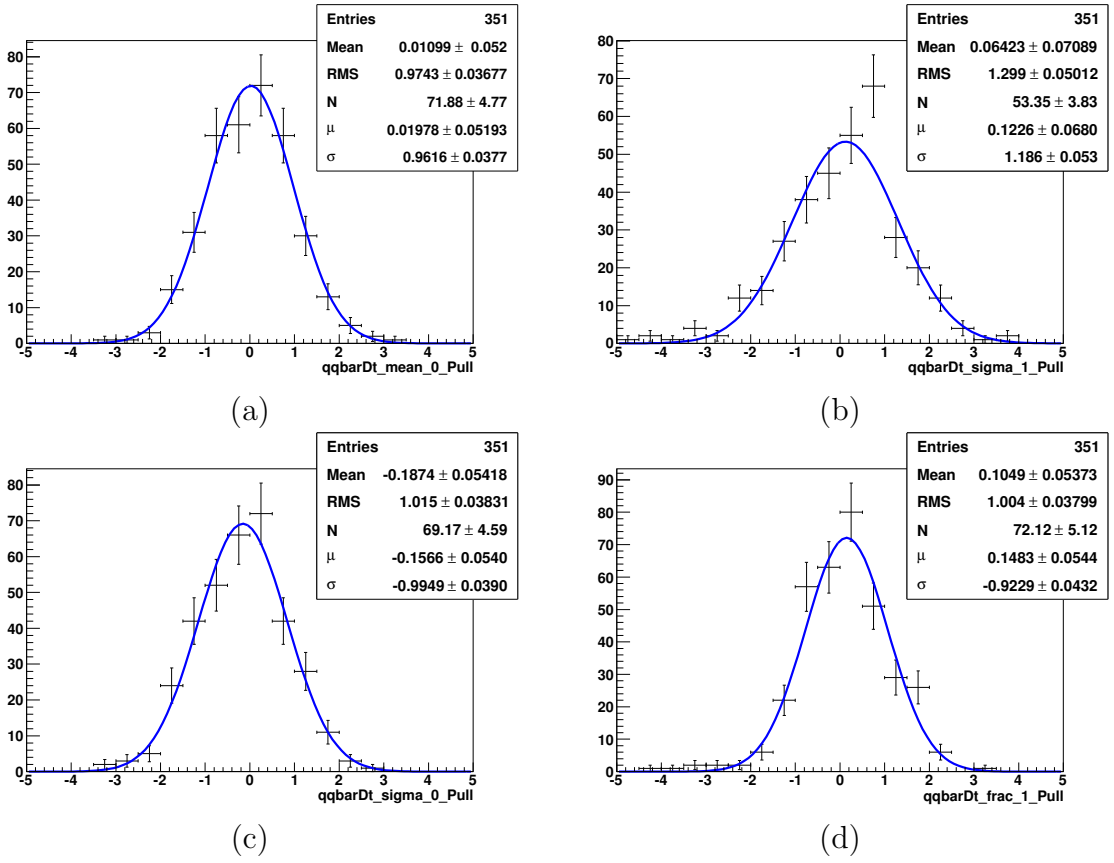

Figure G.8: Pull distributions of the continuum background resolution function ($\mathcal{R}_{\rm bg}$) parameters: $b_{\rm core}$ (a), $s_{\rm outlier}$ (b), $s_{\rm core}$ (c) and $f_{\rm outlier}$ (d) for the embedded toy studies with 351 toys.

Bibliography

[1] A. Sakharov, *Violation of CP Invariance, c Asymmetry, and Baryon Asymmetry of the Universe*, Pisma Zh.Eksp.Teor.Fiz. **5** (1967) 32–35.

[2] M. Gronau, Y. Grossman, D. Pirjol, and A. Ryd, *Measuring the photon polarization in $B \to K\pi\pi\gamma$*, Phys.Rev.Lett. **88** (2002) 051802, arXiv:hep-ph/0107254 [hep-ph].

[3] **Belle** Collaboration, J. Li et al., *Time-dependent CP Asymmetries in $B^0 \to K^0_S\rho^0\gamma$ Decays*, Phys.Rev.Lett. **101** (2008) 251601, arXiv:0806.1980 [hep-ex].

[4] ***BABAR*** Collaboration, B. Aubert et al., *Measurement of Time-Dependent CP Asymmetry in $B^0 \to K^0_S\pi^0\gamma$ Decays*, Phys.Rev. **D78** (2008) 071102, arXiv:0807.3103 [hep-ex].

[5] **Belle** Collaboration, Y. Ushiroda et al., *Time-Dependent CP Asymmetries in $B^0 \to K^0_S\pi^0\gamma$ transitions*, Phys.Rev. **D74** (2006) 111104, arXiv:hep-ex/0608017 [hep-ex].

[6] **Belle** Collaboration, H. Yang et al., *Observation of $B^+ \to K_1(1270)^+\gamma$*, Phys.Rev.Lett. **94** (2005) 111802, arXiv:hep-ex/0412039 [hep-ex].

[7] P. W. Higgs, *Broken Symmetries and the Masses of Gauge Bosons*, Phys.Rev.Lett. **13** (1964) 508–509.

[8] **ATLAS** Collaboration, G. Aad et al., *Observation of a new particle in the search for the Standard Model Higgs boson with the ATLAS detector at the LHC*, Phys.Lett. **B716** (2012) 1–29, arXiv:1207.7214 [hep-ex].

[9] **CMS** Collaboration, S. Chatrchyan et al., *Observation of a new boson at a mass of 125 GeV with the CMS experiment at the LHC*, Phys.Lett. **B716** (2012) 30–61, arXiv:1207.7235 [hep-ex].

[10] N. Cabibbo, *Unitary Symmetry and Leptonic Decays*, Phys.Rev.Lett. **10** (1963) 531–533.

[11] M. Kobayashi and T. Maskawa, *CP Violation in the Renormalizable Theory of Weak Interaction*, Prog.Theor.Phys. **49** (1973) 652–657.

[12] L. Wolfenstein, *Parametrization of the Kobayashi-Maskawa Matrix*, Phys.Rev.Lett. **51** (1983) 1945.

[13] **CKMfitter Group** Collaboration, J. Charles et al., *CP violation and the CKM matrix: Assessing the impact of the asymmetric B factories*, Eur.Phys.J. **C41** (2005) 1–131, arXiv:hep-ph/0406184 [hep-ph].

[14] **UTfit** Collaboration, M. Bona et al., *The 2004 UTfit Collaboration Report on the Status of the Unitarity Triangle in the Standard Model*, JHEP **07** (2005) 028, hep-ph/0501199. Updated results and plots available at: http://www.utfit.org/.

[15] K. Lande, E. Booth, J. Impeduglia, L. Lederman, and W. Chinowsky, *Observation of Long-Lived Neutral V Particles*, Phys.Rev. **103** (1956) 1901–1904.

[16] **ARGUS** Collaboration, H. Albrecht et al., *Observation of B0 - anti-B0 Mixing*, Phys.Lett. **B192** (1987) 245.

[17] **CDF** Collaboration, A. Abulencia et al., *Measurement of the $B_s^0 - \bar{B}_s^0$ Oscillation Frequency*, Phys.Rev.Lett. **97** (2006) 062003, arXiv:hep-ex/0606027 [hep-ex].

[18] **LHCb collaboration** Collaboration, R. Aaij et al., *Observation of B_s^0-$\bar{B}_s^0$ mixing and measurement of mixing frequencies using semileptonic B decays*, arXiv:1308.1302 [hep-ex].

[19] ***BABAR*** Collaboration, B. Aubert et al., *Evidence for D^0 -anti-D0 Mixing*, Phys.Rev.Lett. **98** (2007) 211802, arXiv:hep-ex/0703020 [HEP-EX].

[20] **Belle** Collaboration, M. Staric et al., *Evidence for D^0 - $\bar{D}^0$ Mixing*, Phys.Rev.Lett. **98** (2007) 211803, arXiv:hep-ex/0703036 [hep-ex].

[21] **LHCb collaboration** Collaboration, R. Aaij et al., *Measurement of D^0-$\overline{D}^0$ mixing parameters and search for CP violation using $D^0 \to K^+\pi^-$ decays*, arXiv:1309.6534 [hep-ex].

[22] I. Y. Bigi and A. I. Sanda, *CP Violation*. Cambridge, UK: Cambridge University Press, 2000.

[23] **Heavy Flavor Averaging Group** Collaboration, Y. Amhis et al., *Averages of B-Hadron, C-Hadron, and tau-lepton properties as of early 2012*, arXiv:1207.1158 [hep-ex].

[24] **Particle Data Group** Collaboration, J. Beringer et al., *Review of Particle Physics (RPP)*, Phys.Rev. **D86** (2012) 010001.

[25] ***BABAR*** Collaboration, B. Aubert et al., *A study of time dependent CP-violating asymmetries and flavor oscillations in neutral B decays at the $\Upsilon(4S)$*, Phys.Rev. **D66** (2002) 032003, arXiv:hep-ex/0201020 [hep-ex].

[26] J. Christenson, J. Cronin, V. Fitch, and R. Turlay, *Evidence for the 2 pi Decay of the k(2)0 Meson*, Phys.Rev.Lett. **13** (1964) 138–140.

[27] J. Charles, O. Deschamps, S. Descotes-Genon, R. Itoh, H. Lacker, et al., *Predictions of selected flavour observables within the Standard Model*, Phys.Rev. **D84** (2011) 033005, arXiv:1106.4041 [hep-ph].

[28] A. B. Carter and A. I. Sanda, *CP Nonconservation in Cascade Decays of B Mesons*, Phys. Rev. Lett. **45** (Sep, 1980) 952–954.

[29] A. B. Carter and A. I. Sanda, *CP violation in B-meson decays*, Phys. Rev. D **23** (Apr, 1981) 1567–1579.

[30] I. Y. Bigi and A. I. Sanda, *Notes on the Observability of CP Violations in B Decays*, Nucl. Phys. **B193** (1981) 85.

[31] A. Høcker and Z. Ligeti, *CP violation and the CKM matrix*, Ann. Rev. Nucl. Part. Sci. **56** (2006) 501–567, hep-ph/0605217.

[32] A. Einstein, B. Podolsky, and N. Rosen, *Can quantum mechanical description of physical reality be considered complete?*, Phys.Rev. **47** (1935) 777–780.

[33] D. J. Griffiths, *Introduction to Quantum Mechanics*. Benjamin Cummings, second ed.

[34] Y. Grossman and M. P. Worah, *CP asymmetries in B decays with new physics in decay amplitudes*, Phys.Lett. **B395** (1997) 241–249, arXiv:hep-ph/9612269 [hep-ph].

[35] Y. Nir, *B Physics and CP violation*, Lecture given at Les Houches Summer School (Session LXXXIV), 2005.

[36] S. L. Glashow, J. Iliopoulos, and L. Maiani, *Weak Interactions with Lepton-Hadron Symmetry*, Phys. Rev. **D2** (1970) 1285–1292.

[37] M. Misiak, H. Asatrian, K. Bieri, M. Czakon, A. Czarnecki, et al., *Estimate of* $\mathcal{B}(\overline{B} \to X_s\gamma)$ *at* $\mathcal{O}(\alpha_S^2)$, Phys.Rev.Lett. **98** (2007) 022002, arXiv:hep-ph/0609232 [hep-ph].

[38] K. Fujikawa and A. Yamada, *Test of the chiral structure of the top - bottom charged current by the process* $b \to s\gamma$, Phys.Rev. **D49** (1994) 5890–5893.

[39] K. Babu, K. Fujikawa, and A. Yamada, *Constraints on left-right symmetric models from the process* $b \to s\gamma$, Phys.Lett. **B333** (1994) 196–201, arXiv:hep-ph/9312315 [hep-ph].

[40] P. L. Cho and M. Misiak, $b \to s\gamma$ *decay in* $SU(2)_L \times SU(2)_R \times U(1)$ *extensions of the Standard Model*, Phys.Rev. **D49** (1994) 5894–5903, arXiv:hep-ph/9310332 [hep-ph].

[41] T. Inami and C. Lim, *Effects of Superheavy Quarks and Leptons in Low-Energy Weak Processes $K_L \to \mu^+\mu^-, K^+ \to \pi^+\nu\overline{\nu}$ and $K^0 \leftrightarrow \overline{K}^0$*, Prog.Theor.Phys. **65** (1981) 297.

[42] A. J. Buras, *Weak Hamiltonian, CP violation and rare decays*, arXiv:hep-ph/9806471 [hep-ph].

[43] S. W. Bosch and G. Buchalla, *Constraining the unitarity triangle with $B \to V\gamma$*, JHEP **0501** (2005) 035, arXiv:hep-ph/0408231 [hep-ph].

[44] M. Matsumori and A. Sanda, *The Mixing-induced CP asymmetry in $B \to K^*gamma$ decays with perturbative QCD approach*, Phys.Rev. **D73** (2006) 114022, arXiv:hep-ph/0512175 [hep-ph].

[45] B. Grinstein, Y. Grossman, Z. Ligeti, and D. Pirjol, *The Photon polarization in $B \to X\gamma$ in the standard model*, Phys.Rev. **D71** (2005) 011504, arXiv:hep-ph/0412019 [hep-ph].

[46] B. Grinstein and D. Pirjol, *The CP asymmetry in $B^0(t) \to K^0_S\pi^0\gamma$ in the standard model*, Phys.Rev. **D73** (2006) 014013, arXiv:hep-ph/0510104 [hep-ph].

[47] P. Ball and R. Zwicky, *Time-dependent CP asymmetry in $B \to K^*\gamma$ as a (quasi) null test of the Standard Model*, Phys.Lett. **B642** (2006) 478–486, arXiv:hep-ph/0609037 [hep-ph].

[48] A. Tayduganov, *Electroweak radiative B-decays as a test of the Standard Model and beyond*, PhD Thesis (2011), Unpublished . http://publication.lal.in2p3.fr/2011/thesis_TAYDUGANOV.

[49] S. P. Martin, *A Supersymmetry primer*, arXiv:hep-ph/9709356 [hep-ph].

[50] D. Atwood, M. Gronau, and A. Soni, *Mixing induced CP asymmetries in radiative B decays in and beyond the standard model*, Phys.Rev.Lett. **79** (1997) 185–188, arXiv:hep-ph/9704272 [hep-ph].

[51] **BABAR** Collaboration, B. Aubert et al., *Measurement of The Time-Dependent CP Asymmetry in $B^0 \to K^{*0}\ \gamma$ Decays*, arXiv:0708.1614 [hep-ex].

[52] **LHCb** Collaboration, R. Aaij et al., *Measurement of the ratio of branching fractions $\mathcal{B}(B^0 \to K^{*0}\gamma)/\mathcal{B}(B^0_S \to \phi\gamma)$ and the direct CP asymmetry in $B^0 \to K^{*0}\gamma$*, Nucl.Phys. **B867** (2013) 1–18, arXiv:1209.0313 [hep-ex].

[53] D. Atwood, T. Gershon, M. Hazumi, and A. Soni, *Mixing-induced CP violation in $B \to P(1)P(2)\gamma$ in search of clean new physics signals*, Phys.Rev. **D71** (2005) 076003, arXiv:hep-ph/0410036 [hep-ph].

[54] M. Gronau and D. Pirjol, *Photon polarization in radiative B decays*, Phys.Rev. **D66** (2002) 054008, arXiv:hep-ph/0205065 [hep-ph].

[55] T. Altomari, *Contribution of Exclusive Decays $B \to K^{(I)}\gamma$ to $B \to s\gamma$*, Phys.Rev. **D37** (1988) 677.

[56] A. Ali, T. Ohl, and T. Mannel, *Radiative rare B decays into higher K resonances*, Phys.Lett. **B298** (1993) 195–203, arXiv:hep-ph/9208207 [hep-ph].

[57] D. Atwood and A. Soni, *Influence of kaonic resonances on the CP violation in $B \to K^*\gamma$ like processes*, Z.Phys. **C64** (1994) 241–254, arXiv:hep-ph/9401347 [hep-ph].

[58] S. Veseli and M. Olsson, *Radiative rare B decays revisited*, Phys.Lett. **B367** (1996) 309–316, arXiv:hep-ph/9508255 [hep-ph].

[59] D. Ebert, R. Faustov, V. Galkin, and H. Toki, *Rare radiative B decay to the orbitally excited $K_2^*(1430)$ meson*, Phys.Lett. **B495** (2000) 309–316, arXiv:hep-ph/0009308 [hep-ph].

[60] D. Ebert, R. Faustov, V. Galkin, and H. Toki, *Rare radiative B decays to orbitally excited K mesons*, Phys.Rev. **D64** (2001) 054001, arXiv:hep-ph/0104264 [hep-ph].

[61] **LHCb** Collaboration, R. Aaij et al., *CP and up-down asymmetries in $B^\pm \to K^\pm\pi^\mp\pi^\pm\gamma$ decays*, LHCb-CONF-2013-009 (Jun, 2013) .

[62] F. Kruger and J. Matias, *Probing new physics via the transverse amplitudes of $B^0 \to K^{*0}(\to K^-\pi^+)\ell^+\ell^-$ at large recoil*, Phys.Rev. **D71** (2005) 094009, arXiv:hep-ph/0502060 [hep-ph].

[63] **LHCb** Collaboration, R. Aaij et al., *Measurement of the $B^0 \to K^{*0}e^+e^-$ branching fraction at low dilepton mass*, JHEP **1305** (2013) 159, arXiv:1304.3035 [hep-ex].

[64] **LHCb** Collaboration, R. Aaij et al., *Differential branching fraction and angular analysis of the decay $B^0 \to K^{*0}\mu^+\mu^-$*, JHEP **1308** (2013) 131, arXiv:1304.6325 [hep-ex].

[65] **CMS** Collaboration, S. Chatrchyan et al., *Angular analysis and branching fraction measurement of the decay $B^0 \to K^*\mu^+\mu^-$*, arXiv:1308.3409 [hep-ex].

[66] R. Carnegie, R. Cashmore, W. Dunwoodie, T. Lasinski, and D. W. Leith, *Q1 (1290) and Q2 (1400) Decay Rates and their SU(3) Implications*, Phys.Lett. **B68** (1977) 287–291.

[67] **ACCMOR** Collaboration, C. Daum et al., *Diffractive production of strange mesons at 63-GeV*, Nucl.Phys. **B187** (1981) 1.

[68] M. Suzuki, *Strange axial - vector mesons*, Phys.Rev. **D47** (1993) 1252–1255.

[69] **ALEPH** Collaboration, R. Barate et al., *Study of tau decays involving kaons, spectral functions and determination of the strange quark mass*, Eur.Phys.J. **C11** (1999) 599–618, arXiv:hep-ex/9903015 [hep-ex].

[70] **OPAL** Collaboration, G. Abbiendi et al., *A Study of three prong τ decays with charged kaons*, Eur.Phys.J. **C13** (2000) 197–212, arXiv:hep-ex/9908013 [hep-ex].

[71] **CLEO** Collaboration, D. Asner et al., *Resonance structure of $\tau^- \to K^-\pi^+\pi^-\nu_\tau$ decays*, Phys.Rev. **D62** (2000) 072006, arXiv:hep-ex/0004002 [hep-ex].

[72] H. Hatanaka and K.-C. Yang, *$B \to K_1\gamma$ Decays in the Light-Cone QCD Sum Rules*, Phys.Rev. **D77** (2008) 094023, arXiv:0804.3198 [hep-ph].

[73] **Belle** Collaboration, H. Guler et al., *Study of the $K^+\pi^+\pi^-$ Final State in $B^+ \to J/\psi K^+\pi^+\pi^-$ and $B^+ \to \psi - primeK^+\pi^+\pi^-$*, Phys.Rev. **D83** (2011) 032005, arXiv:1009.5256 [hep-ex].

[74] S. Descotes-Genon and B. Moussallam, *The $K_0^*(800)$ scalar resonance from Roy-Steiner representations of πK scattering*, Eur.Phys.J. **C48** (2006) 553, arXiv:hep-ph/0607133 [hep-ph].

[75] I. Aitchison, *K-matrix formalism for overlapping resonances*, Nucl.Phys. **A189** (1972) 417–423.

[76] N. Lockyer, J. Jaros, M. Nelson, G. Abrams, D. Amidei, et al., *Measurement of the Lifetime of Bottom Hadrons*, Phys.Rev.Lett. **51** (1983) 1316.

[77] P. Oddone, *An asymmetric B factory based on PEP*, Annals N.Y.Acad.Sci. **578** (1989) 237–247.

[78] ***BABAR*** Collaboration, P. F. Harrison and H. R. e. Quinn, *The BABAR physics book: Physics at an asymmetric B factory*, Papers from Workshop on Physics at an Asymmetric B Factory (*BABAR* Collaboration Meeting), Rome, Italy, 11-14 Nov 1996, Princeton, NJ, 17-20 Mar 1997, Orsay, France, 16-19 Jun 1997 and Pasadena, CA, 22-24 Sep 1997.

[79] ***BABAR*** Collaboration, C. Bozzi et al., *The design and construction of the BABAR silicon vertex tracker*, Nucl.Instrum.Meth. **A447** (2000) 15–25.

[80] A. Boucham, D. Boutigny, I. De Bonis, A. Jeremie, Y. Karyotakis, et al., *The BABAR drift chamber project*, Nucl.Instrum.Meth. **A409** (1998) 46–52.

[81] ***BABAR*** Collaboration, M. H. Kelsey, *Performance and aging of the BABAR drift chamber*, Nucl.Instrum.Meth. **A535** (2004) 206–211.

[82] ***BABAR*** Collaboration, B. Aubert et al., *The BABAR detector*, Nucl.Instrum.Meth. **A479** (2002) 1–116, arXiv:hep-ex/0105044 [hep-ex].

[83] ***BABAR*** Collaboration, B. Aubert et al., *Observation of CP violation in $B^0 \to K^+\pi^-$ and $B^0 \to \pi^+\pi^-$*, Phys.Rev.Lett. **99** (2007) 021603, arXiv:hep-ex/0703016 [HEP-EX].

[84] D. Lange, *The EvtGen particle decay simulation package*, Nucl.Instrum.Meth. **A462** (2001) 152–155.

[85] T. Sjostrand, *High-energy physics event generation with PYTHIA 5.7 and JETSET 7.4*, Comput.Phys.Commun. **82** (1994) 74–90.

[86] **GEANT4** Collaboration, S. Agostinelli et al., *GEANT4: A Simulation toolkit*, Nucl.Instrum.Meth. **A506** (2003) 250–303.

[87] P. Billoir, *Track fitting with multiple scattering: a new method*, Nucl.Instrum.Meth. **A225** (1984) 352–366.

[88] B. Lewandowski, *The BABAR electromagnetic calorimeter*, Nucl.Instrum.Meth. **A494** (2002) 303–307.

[89] B. Hartfiel, *PID using DIRC Global Likelihoods*, BABAR Analysis Document #649. Unpublished.

[90] W. Hulsbergen and A. Kalman, *Filter for BABAR decay chain fitting, internal documentation*, Unpublished . http://www.slac.stanford.edu/BFROOT/www/Physics/Tools/Vertex/treefitter/.

[91] W. Ford, *Choice of Kinematic Variables in B Meson Reconstruction*, BABAR Analysis Document #53. Unpublished.

[92] R. A. Fisher, *The use of multiple measurements in taxonomic problems*, Annals Eugen. **7** (1936) 179–188.

[93] G. Cowan, *Statistical Data Analysis*. Oxford University Press, 1998.

[94] R. T. T. Hastie and J. Friedman, *The Elements of Statistical Learning*. Springer, 2001.

[95] R. Barlow, *Statistics: A Guide to the Use of Statistical Methods in the Physical Sciences*. Wiley, 1989.

[96] P. Harrison et al., *LAURA++ - Likelihood Analysis Unbinned Reconstruction of Amplitudes*, BABAR Analysis Document #806. Unpublished.

[97] W. Verkerke and D. P. Kirkby, *The RooFit toolkit for data modeling*, eConf **C0303241** (2003) MOLT007, arXiv:physics/0306116 [physics].

[98] F. James and M. Roos, *Minuit: A System for Function Minimization and Analysis of the Parameter Errors and Correlations*, Comput.Phys.Commun. **10** (1975) 343–367.

[99] James, F., *MINUIT, Function Minimization and Error Analysis, Reference Manual*, wwwasdoc.web.cern.ch/wwwasdoc/minuit/minmain.html.

[100] I. Antcheva, M. Ballintijn, B. Bellenot, M. Biskup, R. Brun, et al., *ROOT: A C++ framework for petabyte data storage, statistical analysis and visualization*, Comput.Phys.Commun. **182** (2011) 1384–1385.

[101] M. Pivk and F. R. Le Diberder, *SPlot: A Statistical tool to unfold data distributions*, Nucl.Instrum.Meth. **A555** (2005) 356–369, arXiv:physics/0402083 [physics.data-an].

[102] S. Veseli and M. Olsson, *Radiative rare B decays revisited*, Phys.Lett. **B367** (1996) 309–316, arXiv:hep-ph/9508255 [hep-ph].

[103] H.-Y. Cheng and C.-K. Chua, *Covariant light front approach for $B \to K^* \gamma$, $K_1 \gamma$, $K_2^* \gamma$ decays*, Phys.Rev. **D69** (2004) 094007, arXiv:hep-ph/0401141 [hep-ph].

[104] F. Porter and A. Samuel, *Measurement of branching fractions and mass spectra of $B \to K \pi \pi \gamma$*, *BABAR* Analysis Document #1155 (2005). Unpublished.

[105] R. Bartoldus, A. Dvoretskii, A. Eisner, J. Harton, H. Paar, A. Ryd, U. Schwanke, D. Su, and J. Zhang, *Trigger and Filter Documentation for Run1*, *BABAR* Analysis Document #194. Unpublished.

[106] **BaBar Collaboration** Collaboration, J. Lees et al., *Exclusive Measurements of $b \to s\gamma$ Transition Rate and Photon Energy Spectrum*, Phys.Rev. **D86** (2012) 052012, arXiv:1207.2520 [hep-ex].

[107] C.-h. Cheng, D. Doll, D. Hitlin, and P. Ongmongkolkul, *Photon spectrum and transition rate of $b \to s\gamma$ based on a sum of exclusive final states*, *BABAR* Analysis Document #2178 (2011). Unpublished.

[108] Fang, Hitlin, Piatenko, Bright, Chandrasekaran, Koeneke, Sciolla, Yi, Convery, Yarritu, and Kroseberg, *Search for $B \to \rho\gamma$ and $B \to \omega\gamma$ in Run 1 - Run 5 data*, *BABAR* Analysis Document #1301 (2006). Unpublished.

[109] D. Dujmic, *Merged π^0 reconstruction: from cluster shape to mass*, *BABAR* Analysis Document #514 (2002). Unpublished.

[110] G. Choudalakis, *On hypothesis testing, trials factor, hypertests and the BumpHunter*, arXiv:1101.0390 [physics.data-an].

[111] D. Aston, N. Awaji, T. Bienz, F. Bird, J. D'Amore, et al., *A Study of $K^-\pi^+$ Scattering in the Reaction $K^-p \to K^-\pi^+n$ at 11 GeV/c*, Nucl.Phys. **B296** (1988) 493.

[112] W. M. Dunwoodie Private communication.

[113] D. Bugg, *Comments on the sigma and kappa*, Phys.Lett. **B572** (2003) 1–7.

[114] J. M. Blatt and V. F. Weisskopf, *Theoretical Nuclear Physics*. Springer-Verlag, 1952.

[115] G. Gounaris and J. Sakurai, *Finite width corrections to the vector meson dominance prediction for* $\rho \to e^+e^-$, Phys.Rev.Lett. **21** (1968) 244–247.

[116] V. Lombardo and A. Telnov, *Studies towards an improved tagging algorithm:* `Tag08`, *BABAR* Analysis Document #2082. Unpublished.

[117] D. Lange et al., *A B Flavour tagging algorithm for CP violation measurements with the BABAR experiment*, *BABAR* Analysis Document #1025. Unpublished.

[118] **BABAR** Collaboration, B. Aubert et al., *Improved measurement of CP asymmetries in* $B^0 \to (c\bar{c})K^{(*)0}$ *decays*, Phys.Rev.Lett. **94** (2005) 161803, arXiv:hep-ex/0408127 [hep-ex].

[119] **BABAR** Collaboration, B. Aubert et al., *Improved measurement of CP violation in neutral B decays to c anti-c s*, Phys.Rev.Lett. **99** (2007) 171803, arXiv:hep-ex/0703021 [hep-ex].

[120] A. V. Telnov and A. V. Gritsan, *Reconstruction efficiency in BABAR: Release 10 Data vs SP4 Monte Carlo*, *BABAR* Analysis Document #677 (2003). Unpublished.

[121] E. Kou Private communication.

[122] **LHCb** Collaboration, R. Aaij et al., *Measurement of form-factor independent observables in the decay* $B^0 \to K^{*0}\mu^+\mu^-$, arXiv:1308.1707 [hep-ex].

[123] **LHCb** Collaboration, R. Aaij et al., *Measurement of the ratio of branching fractions* $\mathcal{B}(B^0 \to K^{*0}\gamma)/\mathcal{B}(B_s^0 \to \phi\gamma)$, Phys.Rev. **D85** (2012) 112013, arXiv:1202.6267 [hep-ex].

[124] **ARGUS** Collaboration, H. Albrecht et al., *Exclusive hadronic decays of B mesons*, Z.Phys. **C48** (1990) 543–552.

Résumé: Une mesure de l'asymétrie de *CP* dépendante du temps des désintégrations radiatives $B^0 \to K^0_S\pi^+\pi^-\gamma$, est effectuée à partir d'un échantillon de 470.9 millions d'événements $\Upsilon(4S) \to B\overline{B}$ enregistrés par le détecteur *BABAR* auprès du collisionneur asymétrique PEP-II situé au SLAC. En utilisant les événements satisfaisant $m_{K\pi\pi} < 1.8\,\mathrm{GeV}/c^2$, $0.6 < m_{\pi\pi} < 0.9\,\mathrm{GeV}/c^2$, $m_{K\pi} < 0.845\,\mathrm{GeV}/c^2$ et $m_{K\pi} > 0.945\,\mathrm{GeV}/c^2$, les paramètres de violation de la symétrie de *CP* ainsi obtenus sont $\mathcal{S}_{K^0_S\pi^+\pi^-\gamma} = 0.137 \pm 0.249^{+0.042}_{-0.033}$ et $\mathcal{C}_{K^0_S\pi^+\pi^-\gamma} = -0.390 \pm 0.204^{+0.045}_{-0.050}$. À partir de ces résultats la valeur de l'asymétrie de *CP* dépendante du temps reliée aux états propres de *CP* $\rho^0 K^0_S$, est extraite: $\mathcal{S}_{K^0_S\rho\gamma} = 0.249 \pm 0.455^{+0.076}_{-0.060}$. Cette observable apporte de l'information relative aux états de polarisation du photon dans les processus sous-jacents de transitions radiatives $b \to s\gamma$. En utilisant l'hypothèse de conservation de la symétrie d'isospin, l'extraction de $\mathcal{S}_{K^0_S\rho\gamma}$ à partir $\mathcal{S}_{K^0_S\pi^+\pi^-\gamma}$ est effectuée à partir de l'étude des désintégrations $B^+ \to K^+\pi^+\pi^-\gamma$, où les amplitudes des différentes résonances intermédiaires $\rho^0 K^+$, $K^{*0}\pi^+$ et $(K\pi)_{\mathrm{S-wave}}\pi^+$, contribuant au système $K\pi\pi$, sont mesurées. Cette étude, en plus de l'information nécessaire à l'extraction de $\mathcal{S}_{K^0_S\rho\gamma}$, a permis d'extraire les contributions relatives des résonances kaoniques au système $K\pi\pi$, ainsi que les fractions globales des modes résonants $\rho^0 K^+$, $K^{*0}\pi^+$ et $(K\pi)_{\mathrm{S-wave}}\pi^+$, constituant une source d'information utile à d'autres études sur la polarisation du photon.

Mots-clés: *BABAR*, méson B, pinguoin radiatif, asymétrie de CP dépendante du temps, polarisation du photon, résonances kaonique

Abstract: We present a measurement of the time-dependent *CP* asymmetry in the radiative-penguin decay $B^0 \to K^0_S\pi^+\pi^-\gamma$, using a sample of 470.9 million $\Upsilon(4S) \to B\overline{B}$ events recorded with the *BABAR* detector at the PEP-II e^+e^- storage ring at SLAC. Using events with $m_{K\pi\pi} < 1.8\,\mathrm{GeV}/c^2$, $0.6 < m_{\pi\pi} < 0.9\,\mathrm{GeV}/c^2$ and with $m_{K\pi} < 0.845\,\mathrm{GeV}/c^2$ and $m_{K\pi} > 0.945\,\mathrm{GeV}/c^2$, we obtain the *CP*-violating parameters $\mathcal{S}_{K^0_S\pi^+\pi^-\gamma} = 0.137 \pm 0.249^{+0.042}_{-0.033}$ and $\mathcal{C}_{K^0_S\pi^+\pi^-\gamma} = -0.390 \pm 0.204^{+0.045}_{-0.050}$, where the first quoted errors are statistical and the second are systematic. We extract from this measurement the time-dependent *CP* asymmetry related to the hadronic *CP* eigenstate $\rho^0 K^0_S$ and obtain $\mathcal{S}_{K^0_S\rho\gamma} = 0.249 \pm 0.455^{+0.076}_{-0.060}$. This observable provides information on the photon polarization in the underlying $b \to s\gamma$ transition. To extract $\mathcal{S}_{K^0_S\rho\gamma}$ from $\mathcal{S}_{K^0_S\pi^+\pi^-\gamma}$, assuming isospin symmetry, we study $B^+ \to K^+\pi^+\pi^-\gamma$ decays and measure intermediate resonant amplitudes of different resonances decaying to $K\pi\pi$ through the intermediate states $\rho^0 K^+$, $K^{*0}\pi^+$ and $(K\pi)_{\mathrm{S-wave}}\pi^+$. In addition to the need of this information for the extraction of $\mathcal{S}_{K^0_S\rho\gamma}$, it provides input on the $B \to K\pi\pi$ system, which is useful for other studies of the photon polarization. The fractions of the different $K_{\mathrm{res}} \to K\pi\pi$ states as well as the overall fractions of the $\rho^0 K^+$, $K^{*0}\pi^+$ and $(K\pi)_{\mathrm{S-wave}}\pi^+$ components are also measured.

Key words: *BABAR*, B meson, radiative penguin, time-dependent *CP* asymmetry, photon polarization, kaonic resonances